Swansea University
Prifysgol Abertawe

Cronfa
Setting Research Free

Swansea University E-Theses

# New generation advanced high strength steels for automotive hot stamping technologies.

Taylor, Thomas James

How to cite:

Taylor, Thomas James (2014) *New generation advanced high strength steels for automotive hot stamping technologies..* thesis, Swansea University.
http://cronfa.swan.ac.uk/Record/cronfa43085

Use policy:

This item is brought to you by Swansea University. Any person downloading material is agreeing to abide by the terms of the repository licence: copies of full text items may be used or reproduced in any format or medium, without prior permission for personal research or study, educational or non-commercial purposes only. The copyright for any work remains with the original author unless otherwise specified. The full-text must not be sold in any format or medium without the formal permission of the copyright holder. Permission for multiple reproductions should be obtained from the original author.

Authors are personally responsible for adhering to copyright and publisher restrictions when uploading content to the repository.

Please link to the metadata record in the Swansea University repository, Cronfa (link given in the citation reference above.)

http://www.swansea.ac.uk/library/researchsupport/ris-support/

# New Generation Advanced High Strength Steels for Automotive Hot Stamping Technologies

Thomas James Taylor

Submitted to Swansea University in fulfilment of the requirements for the Degree of Doctor of Engineering

College of Engineering
Swansea University

2014

ProQuest Number: 10821477

All rights reserved

INFORMATION TO ALL USERS
The quality of this reproduction is dependent upon the quality of the copy submitted.

In the unlikely event that the author did not send a complete manuscript
and there are missing pages, these will be noted. Also, if material had to be removed,
a note will indicate the deletion.

ProQuest 10821477

Published by ProQuest LLC (2018). Copyright of the Dissertation is held by the Author.

All rights reserved.
This work is protected against unauthorized copying under Title 17, United States Code
Microform Edition © ProQuest LLC.

ProQuest LLC.
789 East Eisenhower Parkway
P.O. Box 1346
Ann Arbor, MI 48106 – 1346

# DECLARATIONS

I declare that the work presented in this thesis has not previously been accepted in substance for any degree and is not being concurrently submitted in candidature for any degree.

Signed ___ (candidate)

Date 7/6/14

I declare that the work presented in this thesis is the result of my own investigations, except where otherwise stated and that other sources are acknowledged by footnotes giving explicit references and that a bibliography is appended.

Signed ___ (candidate)

Date 7/6/14

I declare consent for this thesis, if accepted, to be available for photocopying and for inter-library loan, and for the title and summary to be made available to outside organisations.

Signed ___ (candidate)

Date 7/6/14



SWANSEA LIBRARY UNIVERSITY

# ACKNOWLEDGEMENTS

The author would like to acknowledge and thank those organisations and individuals who have contributed to the research reported in this thesis. Professor David Worsley (Engineering Doctorate Director) and Doctor David Penney (Engineering Doctorate Project Manager) for accepting the author onto the Engineering Doctorate scheme and in doing so, providing the author with so many fantastic opportunities, for which the author will be eternally grateful. The European Social Fund, Tata Steel and Swansea University for funding the research project. Professor George Fourlaris (academic supervisor) for his rich knowledge of physical metallurgy and moreover, for his valuable time spent reviewing draft journal publications and this thesis. Peter Evans (industrial supervisor) of Tata Steel Strip Products UK RD&T Port Talbot for his relentless knowledge of physical metallurgy and product development. Numerous members of the Tata Steel Strip Products UK RD&T Port Talbot team (past and present) including Geraint Gladwyn, Andrew Brown and Lee Jones for their assistance with laboratory experimentation; and Brian Jones and Doctor Gary Bright for their support as Products & Applications Theme Leaders. Workshop staff both at Swansea University and Tata Steel for machining the 624 tensile specimens tested throughout the research project. Peter Davies of Swansea University for his support with microscopy and energy dispersive X-ray spectroscopy. Doctor Yi Gao and especially Doctor Janka Cafolla of Tata Steel Automotive Engineering for their support with finite element modelling. Finally, Steve Danks of Tata Steel R&D Rotherham for his support with dynamic tensile testing.

# ABSTRACT

The automotive industry is under increasing legislative pressure to: 1) reduce vehicle weight so to improve fuel efficiency; and 2) improve crash performance. Ultrahigh strength 'hot stamped' martensitic 'boron steel' 22MnB5 has become common-place in the automotive body structure over the past 10 to 15 years, where it has superseded conventional cold formed carbon-manganese, high strength low alloy and even dual phase steels. However, it is reported by experts within the automotive steel industry that hot stamped 22MnB5 is now widely regarded as a 'commodity product' and that demand exists for steels that exhibit higher tensile strength and/or higher elongation values following hot stamping. For these reasons, novel grades for automotive hot stamping technologies must be developed. Laboratory hot stamping was performed with ten experimental grades, in addition to the 22MnB5 control grade. The ten experimental grades included seven bespoke trial grades (laboratory produced) and three existing commercial grades (industrially produced). During laboratory hot stamping, nine soak time-temperature conditions were investigated for each grade. Following evaluation, the optimal hot stamping soak condition for each grade was determined. Subsequently, the three most successful outcomes from laboratory hot stamping were selected, including the three experimental grades treated to their optimal hot stamping soak conditions that collectively met the three objectives of: 1) higher tensile strength; 2) higher elongation; and 3) higher tensile strength-higher elongation, compared to the 22MnB5 control grade. The three selected experimental grades, in addition to the 22MnB5 control grade, were further evaluated with dynamic tensile testing, three-point bend testing and finite element modelling crash simulation. Highlights included: 38MnB5 which demonstrated ultimate tensile strength in excess of 2000 MPa and total elongation in excess of 6 % under quasi-static tensile testing, in addition to a significant increase to both tensile strength and elongation with increased strain rate; increased tensile strength and elongation resulting from the addition of molybdenum, vanadium or nickel to boron steel; and the suitability of dual phase steels to hot stamping, providing substantially higher elongation, yet with a relatively small loss to ultimate tensile strength compared to 22MnB5.

# LIST OF FIGURES

# LIST OF TABLES

# CONTENTS

# INTRODUCTION

During the 1990s, the automotive industry worldwide dramatically accelerated programmes to meet intensifying legislation to reduce greenhouse gas (particularly carbon dioxide ($CO_2$)) exhaust emissions [1]. While many automotive manufacturers have pursued alternative low carbon fuels such as electric, petrol-electric hybrid, liquid petroleum gas (LPG) and hydrogen (fuel cells); and have also pursued technologies such as variable valve timing, turbo charging, cylinder deactivation, idling stop-start systems and energy recovery systems [2]; the primary, most practical and most effective method of complying with such exhaust emission legislation continues to be reduced vehicle body weight [1] [2]. Reduced vehicle body weight enables equivalent automotive performance while using smaller engines of greater fuel efficiency. Reduced vehicle body weight can also permit smaller and thus lighter mechanical components, such as those of the suspension and braking systems [3]. Hence, the weight saving can be multi-fold. Further, for those alternative low carbon fuels and technologies to be successful, reduced vehicle body weight is also important, since most of those concepts involve a weight penalty (e.g. batteries for electric powered vehicles).

Weight reduction remains the most important goal in modern car body engineering, mainly driven by $CO_2$ exhaust emission reduction legislation [2]. On 23$^{rd}$ April 2009, the European Union (EU) specified that 65 % of the 'fleet average' $CO_2$ exhaust emission must be $\leq$ 130 g/km by 2012 [4]. Moreover, EU legislation specified that the 130 g/km $CO_2$ exhaust emission limit applying to 65 % of the fleet average in 2012, would apply to 75 % by 2013, 80 % by 2014 and 100 % by 2015 [4]. Further, the EU has set a target of $\leq$ 95 g/km by 2021 [4]. The incentive to reduce vehicle body weight is clear: a 100 kg weight reduction can achieve up to 12.5 g/km $CO_2$ reduction [4].

In addition to reducing $CO_2$ exhaust emissions, greater fuel efficiency is attractive for the reduced demand on non-renewable energy resources (sustainable development) and is financially attractive to the automotive consumer: firstly, for the direct cost saving from lower fuel consumption; and secondly, for the cost

saving from lower vehicle excise duty and company car excise duty, which are partially based on $CO_2$ exhaust emissions [5]. Moreover, vehicle body weight reduction can improve automotive performance (superior braking, handling and acceleration characteristics).

Reduced vehicle body weight can be achieved by utilising materials of lower density, down gauging (thinner material) and by employing consolidated (monolithic) components rather than assemblies consisting of multiple welded components [1]. However, while implementing these weight reduction methods, sufficient mechanical strength, crash performance and occupant safety; economy; and manufacturing reproducibility, must be maintained.

While reducing vehicle body weight, automotive manufacturers simultaneously strive for improved crash performance to achieve the coveted European New Car Assessment Programme (EURO NCAP) 5 Star safety rating (and non-European equivalent), which can be used to raise the commercial value of their vehicles further, as automotive consumers become increasingly expectant of optimal safety. Additionally, automotive manufacturers may target increased structural/torsional rigidity (chassis stiffness) in order to improve handling characteristics.

Thus, the automotive industry has two major targets: 1) reduce vehicle body weight; and 2) improve crash performance. In order to meet these two (conflicting) targets, the demands from the automotive industry have been for materials exhibiting lower density and/or greater formability in the 'as-delivered' condition, yet greater strength and/or impact toughness in the final component [1]. Greater formability in the as-delivered condition can provide weight reduction by: 1) down gauging while not compromising forming limits; and 2) component consolidation, where assemblies consisting of multiple, individually formed components, are consolidated in one single, geometrically complex forming operation. Greater strength and/or impact toughness in the final component provide equivalent or improved crash performance while down gauging.

Steel has been the primary material used by the automotive industry since the invention of the automobile and continues to be the main material used in the mass production of automobiles [6], with more than 80 % of the typical passenger vehicle body composed of steel [2]. However, in recent years, certain automotive manufacturers have turned to alterative, non-ferrous materials [7], such as aluminium alloys[1] [8], magnesium alloys, titanium alloys, plastics and carbon fibre reinforced plastic (CFRP)[2] [9]. For complex geometries of low weight, these non-ferrous alternatives are a suitable solution owing to ductility (non-ferrous alloys), their manufacturing route (CFRP) and low density. However, compared to steel, these non-ferrous alternatives are expensive and create greater environmental implications when considering the entire life cycle assessment including extraction, production, utilisation and disposal.

The steel industry needed to respond to the demands from the automotive industry and also to the competition posed by the non-ferrous materials. Thus, in 1994, a consortium of 35 steel manufacturers worldwide began the UltraLight Steel Auto Body (ULSAB) programme, with the aim to design a lightweight steel automotive body structure that would meet the demands from the automotive industry and that would also face the competition posed by the non-ferrous materials [1] [10]. The result was unveiled in 1998 and unleashed a new family of steels: 'advanced high strength steels (AHSS)'.

---

[1] The 2000 Audi A2 was the first aluminium intensive mass produced vehicle.

[2] In 2011, BMW unveiled two concept vehicles (the i3 and i8); both utilising CFRP body construction technology and both intended as mass produced vehicles. The CFRP technology was developed in the USA in partnership with SGL Group, which focuses on producing affordable CFRP components for various industries. In the same year, Daimler announced a joint venture with Toray Industries to produce CFRP components.

AHSS are a group of 'high strength steels' (HSS) and 'ultrahigh strength steels' (UHSS)[3] [11] characterised by unique chemical compositions and/or forming & processing techniques, giving rise to unique microstructures and mechanical properties compared to conventional automotive steels [1].

AHSS were introduced to the mainstream steel and automotive industries in the late 1990s and have evolved to include three generations (Table 1.1), with each generation encompassing a collection of types [e.g. dual phase (DP), transformation induced plasticity (TRIP) and martensitic (M)] and then grades within each type (e.g. DP 600, DP 800 and DP 1000) [1].

Table 1.1: Three generations of AHSS

| *First generation* | *Second generation* | *Third generation* |
|---|---|---|
| Dual phase | Twinning induced plasticity | Hot stamped |
| Transformation induced plasticity | | |
| Ferritic-bainitic | | |
| Complex phase | | Post-forming heat treatable |
| Martensitic | | |

Ultimate tensile strength and total elongation are often used to rank automotive steels [1]. Figure 1.1 [1] illustrates ultimate tensile strength-total elongation ranges of AHSS (colour) compared to conventional automotive steels (grey).

[3] Low strength steels (LSS): yield strength < 210 MPa, ultimate tensile strength < 270 MPa.
High strength steels (HSS): yield strength 210-550 MPa, ultimate tensile strength 270-700 MPa.
Ultrahigh strength steels (UHSS): yield strength > 550 MPa, ultimate tensile strength > 700 MPa.

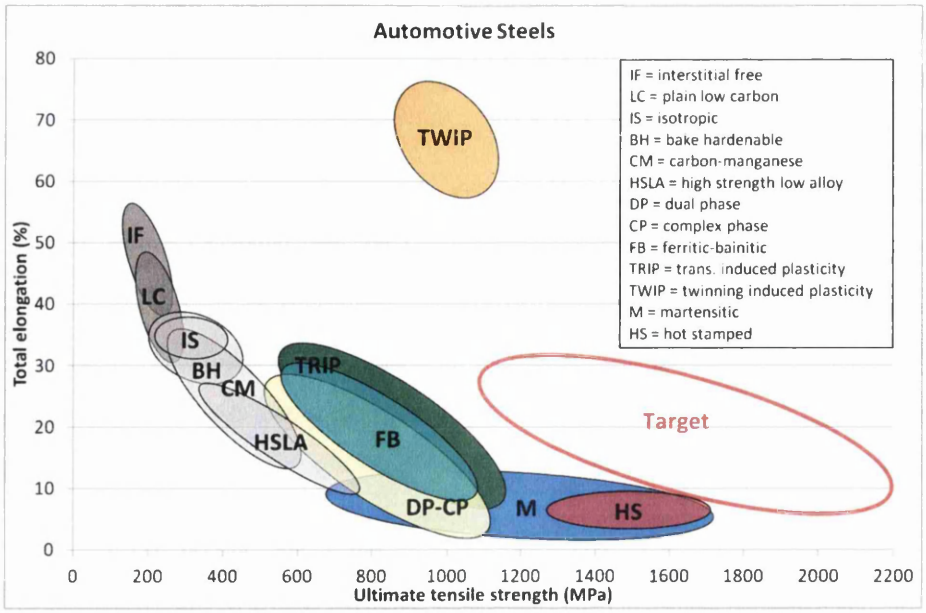


Figure 1.1: Automotive steels (adapted from [1])

As of 2010, the quest of the steel industry worldwide was to develop the fourth generation AHSS so to meet escalating demands from the automotive industry for materials exhibiting yet greater sophistication, as summarised by Table 1.2 [12]. The ultimate tensile strength-total elongation range targeted by the steel and automotive industries [10] is illustrated in Figure 1.1.

Table 1.2: Demands from the automotive industry [12]

| *Demands* |
|---|
| Increased tensile strength for a given elongation in the final component so to permit further down gauging and vehicle body weight reduction while improving crash performance |
| Increased formability (elongation, work hardening exponent, lateral anisotropy-non-thinning, planar isotropy etc.) for a given tensile strength in the as-delivered condition so to permit further down gauging and vehicle body weight reduction by means of greater forming limits |
| Increased formability for a given tensile strength in the as-delivered condition so to permit further component consolidation, giving rise to reduced process time (cost), reduced weight, increased manufacturing reproducibility, increased geometric accuracy and increased structural strength |
| Lower density for a given tensile strength so to permit further vehicle body weight reduction while improving crash performance |
| Increased weldability |
| Increased corrosion resistance |
| Increased manufacturing reproducibility |
| Increased geometric accuracy (reduced springback and forming & processing errors) |
| Lower cost |
| Increased elastic modulus (stiffness) for improved anti-intrusive crash performance and for improved structural/torsional rigidity (chassis stiffness) and in turn, for improved handling performance |

Figure 1.2 illustrates how the demands from the automotive industry inter-relate together with the corresponding material, forming and processing properties.

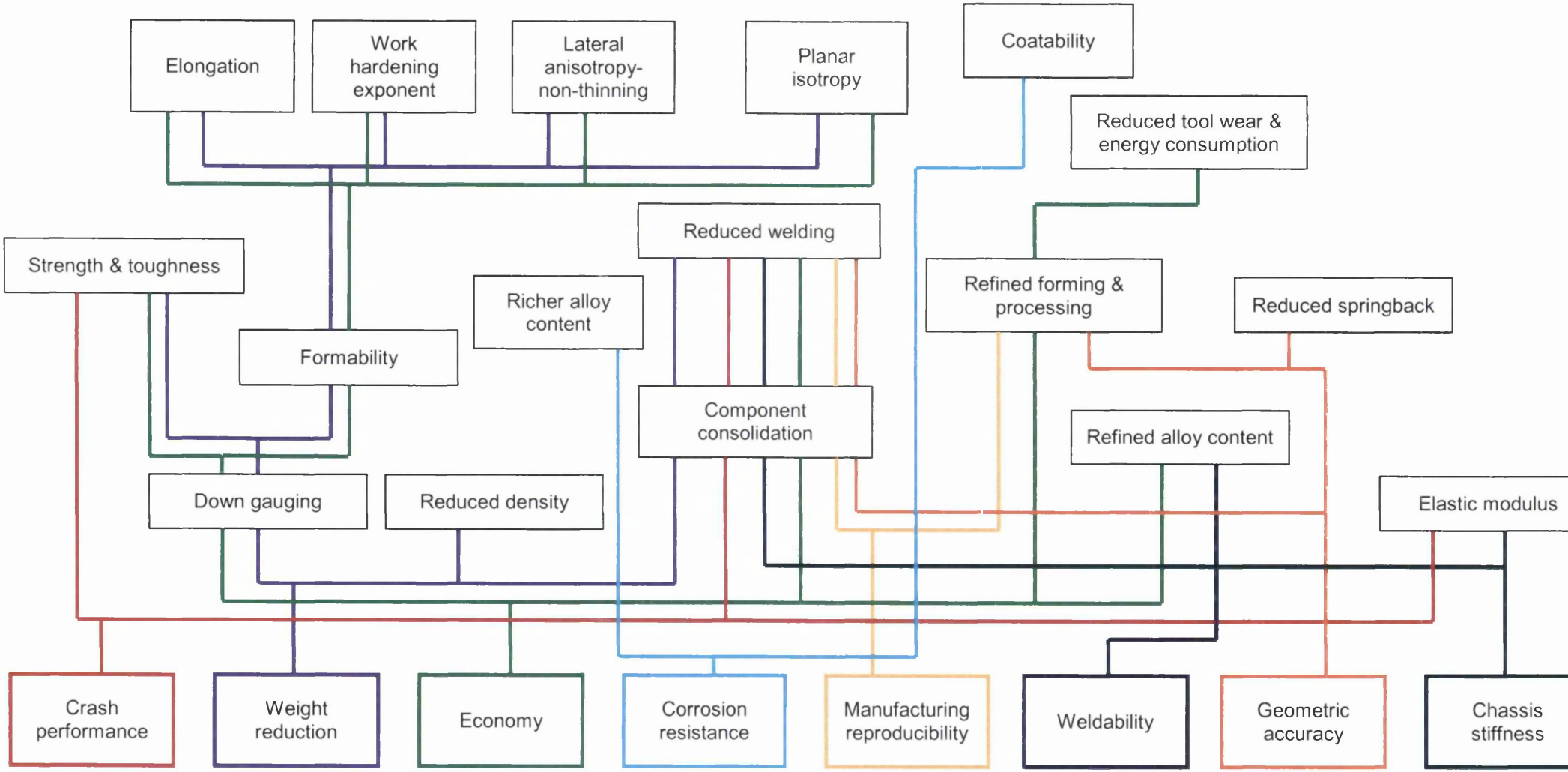


Figure 1.2: Demands from the automotive industry and corresponding material, forming and processing properties

The demands from the automotive industry are to combine what may be considered as mutually exclusive material, forming and/or processing properties. The prime example of this is the demands for: 1) increased tensile strength for a given elongation in the final component; and 2) increased formability for a given tensile strength in the as-delivered condition.

To appreciate the complications of the above demands, consider the following example [1]. Component consolidation may combine three small and simple component geometries to form one large and complex component geometry. Take three separate components, each deep drawn individually from individual blanks of sheet steel, with extensive flange flow at the perimeter of the blank feeding the interior so to provide maximum drawing depth (Figure 1.3a). Lay the three components side-by-side and join them with welds (Figure 1.3b) to form a finished component (assembly). Now attempt to form the same assembly from one blank, in one die and in one deep drawing operation (Figure 1.3c). There is no flange flow to feed the interior region of this consolidated component. Instead, forming of the interior region must occur completely by excessive stretch forming, with the exterior regions of the component stretched excessively so to feed the interior region, before conventional flange flow from the perimeter of the blank feeds and replenishes the exterior regions. This excessive stretch forming places immense strains on the blank. To make matters worse, increasing strength of the blank generally reduces stretch capability since elongation and work hardening capacity generally decrease with increased strength. As strength increases, a greater forming force must be applied, which increases energy consumption and tool wear. Reducing blank thickness so to down gauge reduces stretch capability and increases springback. Moreover, springback increases with increased yield strength as the degree of elastic deformation and potential elastic recovery intensifies. All the while, the automotive industry demands stiffness (which is generally contradictory to formability), lower density (which is generally contradictory to strength), increased weldability, increased corrosion resistance and all for lower cost. Indeed, it is worthy to note that while the first and second generation AHSS (particularly TRIP and TWIP steels) have been able to meet the strength and formability demands from the automotive industry, 'rich' chemical

compositions have limited weldability, coatability (corrosion resistance) and economy; and therefore, have limited mass utilisation.

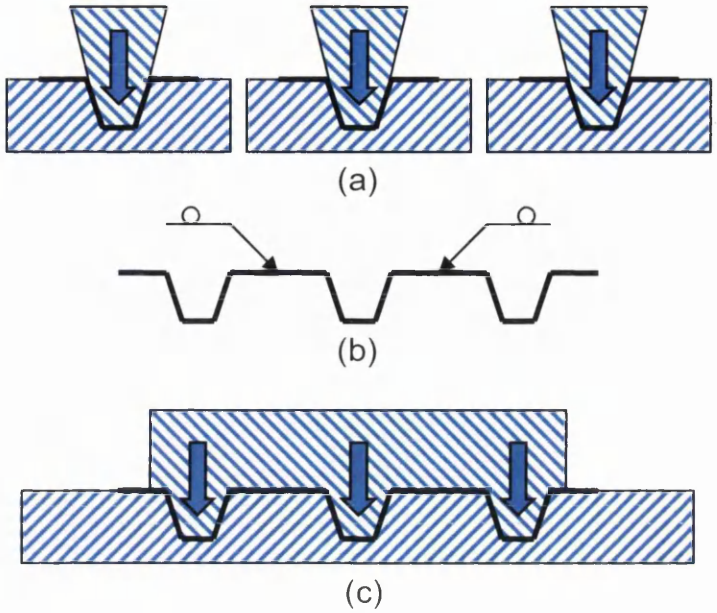


Figure 1.3: Component consolidation

'Hot stamped boron steels' and their corresponding 'hot stamping' forming process can alleviate or even completely remove all the above complications.

Hot stamped boron steels represented the third generation AHSS, were introduced to the mainstream steel and automotive industries in the late 1990s and were intended for automotive 'anti-intrusive' structural body component applications, such as roof pillars; door, floor and roof reinforcements; and bumper beams [1]. Development of hot stamped boron steels and their corresponding hot stamping forming process has since gained much interest. As of 2010, hot stamped boron steels were the most rapidly growing steels in the automotive industry [13]. It was anticipated [12] [14] [15] that hot stamped boron steels would hold the second largest market share of all AHSS in the coming years (after DP); growing three-fold from 2010 to 2015 and on average accounting for at least 10 % of all steel used in the European vehicle.

Figure 1.4 [16] illustrates the increasing application of hot stamped boron steels to select European automotive body structures from 2003 to 2014. Moreover, VW Group's 2012 Modularer Querbaukasten (MQB) universal platform that provided 43 different models across the VW Group range was composed of 21.7 % hot stamped boron steel [17]. Amongst the automotive manufacturers exhibiting at the EuroCarBody show, average hot stamped boron steel usage increased from 4.0 % in 2011 to 7.9 % in 2012 [17].

Figure 1.5 [18] [19] illustrates the increasing number of hot stamped boron steel components produced per year worldwide from 1987 to 2010 and predicted by 2015. Figure 1.6 [14] [20] illustrates hot stamped boron steel market evolution from 2006 to 2013 (supplied by multinational steel manufacturer ArcelorMittal). In 2003 there were just 15 hot stamping lines in Europe; by 2009 this increased to 42 lines [15]. In 2012 there were 159 hot stamping lines worldwide [16].

The above data clearly illustrate the growing importance of the hot stamped boron steel market to the steel industry and therefore, the importance of developing new generation advanced high strength steels for automotive hot stamping technologies.

In brief, the main objectives and achievements of the research reported in this thesis were as follows:

- Development of novel advanced high strength steel grades for automotive hot stamping technologies that demonstrated novel mechanical properties following hot stamping, namely: 1) higher tensile strength; 2) higher elongation; and 3) higher tensile strength-higher elongation, compared to the benchmark grade used throughout laboratory experimentation; and also compared to novel grades presented in the literature.
- Characterisation of the dynamic (high strain rate) tensile properties of hot stamped steels – novel research that was not available in the literature.
- Characterisation of the automotive crash performance of hot stamped steels via finite element modelling (FEM) crash simulation – novel research that was not available in the literature.

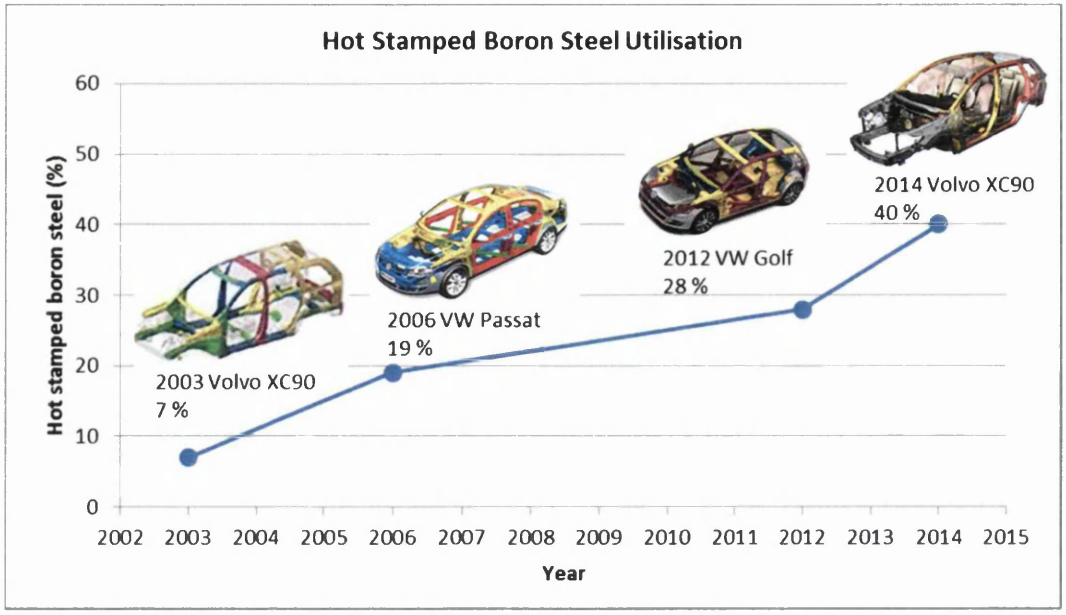


Figure 1.4: Hot stamped boron steel utilisation (adapted from [16])

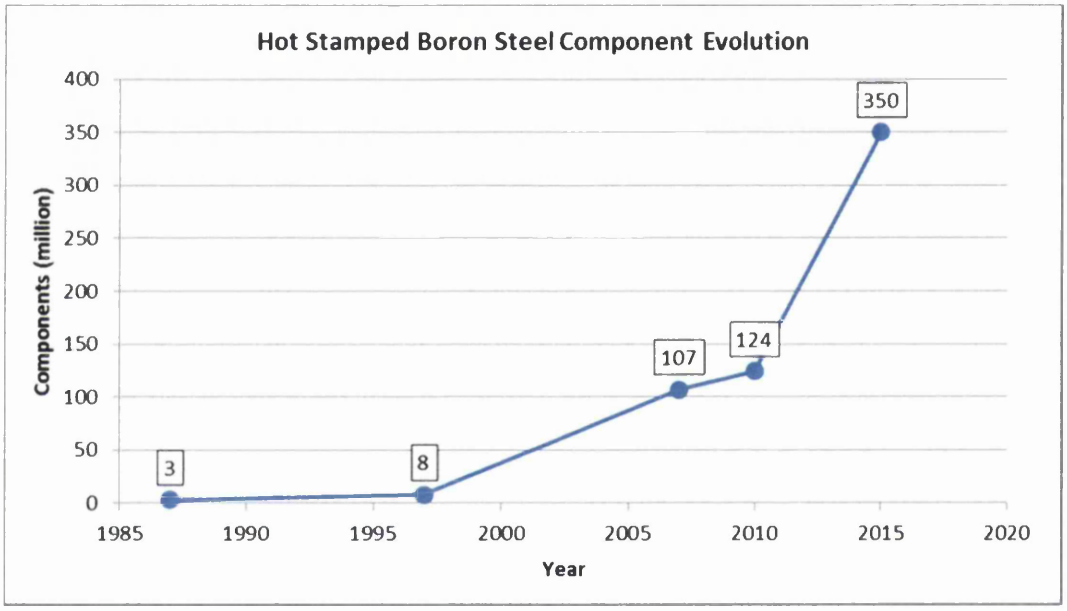


Figure 1.5: Hot stamped boron steel component evolution worldwide (adapted from [18] [19])

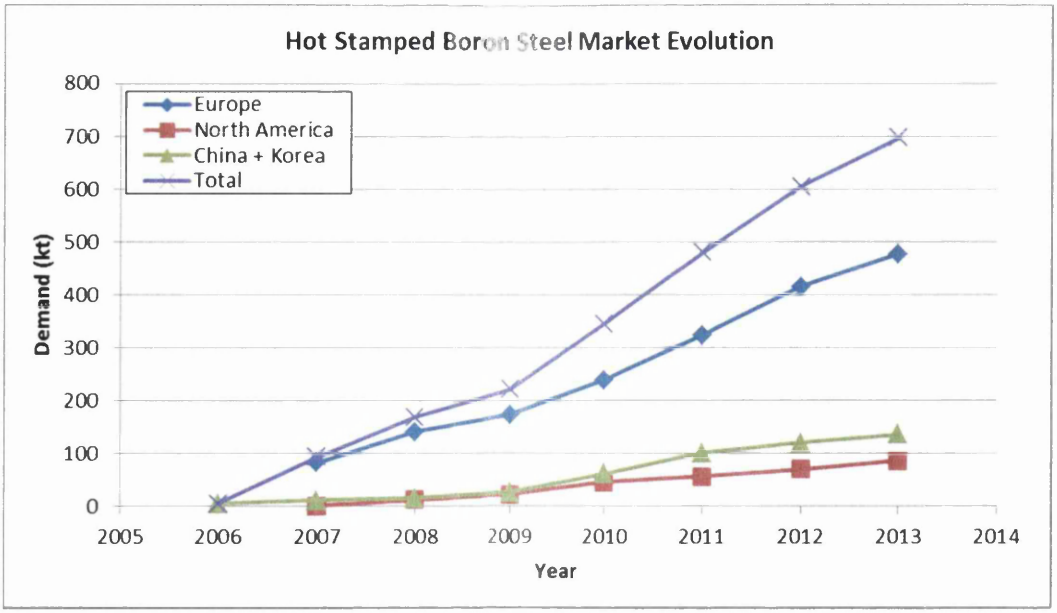


Figure 1.6: Hot stamped boron steel market evolution (adapted from [14] [20])

## Hot Stamping

### *History of Hot Stamping*

The hot stamping process was pioneered and applied for patenting by Carl-Erik Ridderstrale of Swedish steel manufacturer Norrbottens Järnverk[4] [18] in 1973. The patent [21] was approved in 1974:

*GB1490535 Alloys NORRBOTTENS JARNVERK AB 6 Nov 1974 [6 Nov 1973] 48077/74 Heading C7A [Also in Division B3]: A hardened steel article is formed by heating a hardenable steel blank to hardening temperature and then placing it in a forming apparatus in which the blank is deformed and simultaneously rapidly cooled to obtain a martensitic and/or bainitic structure while the blank remains in the apparatus which serves as a gauge for preventing distortion. Bearing shells, vehicle bumpers etc. may be formed by pressing between tools or between a tool and pressure medium. The hardened pressing may be used without tempering. It is also stated that the process is applicable to forming by extrusion, drop forging and explosion. Cooling is by cooling parts of the forming device and/or by direct cooling with salt water or oil. The steel used may have the following composition, percentage by weight: C less than 0.4 %, Mn 0.5-2.0 %, P > 0.05 %, S 0.05 %, Cr 0.1-0.5 % and/or Mo 0.05-0.5 %, Ti 0.1 %, B 0.005-0.01 %, Al 0.1 %, balance Fe and impurities including Si. The steel is heated to above $Ac_3$ e.g. 775-1000 °C, preferably 900 °C.*

Following patent approval, the hot stamping technology was initially used for forming agricultural tooling such as saw and mower blades, before it was further developed by the first major research project in 1975 [18]. This involved collaboration between Norrbottens Järnverk, Volvo Trucks and Luleå University of Technology. In 1984, Saab became the first automotive manufacturer to adopt hot stamped boron steel components [18] – door reinforcement beams for the Saab 9000 (Figure 2.1) [22].

[4] In 1978 the three independent Swedish steel manufacturers: 1) Domnarvets Järnverk in Borlänge; 2) Oxelösunds Järnverk in Oxelösund; and 3) Norrbottens Järnverk in Luleå; merged to form the united Swedish Steel AB (SSAB).

First hot stamped boron steel automotive components: door reinforcement beams for the 1984 Saab 9000

Figure 2.1: 1984 Saab 9000 (adapted from [22])

***Hot Stamping Process***

Hot stamping can be defined as a 'high temperature anisothermal deformation process'. Details of the original [1] [14] [15] [23] [24] [25] [26] [27] [28] [29] [30] hot stamping process[5] shall now be explored. The term 'original' is used as there have been several developments to the process over the years since its patenting in 1974 and introduction to the mainstream automotive industry in the late 1990s. These developments and latest variants of hot stamping are detailed in the later section: Hot Stamping Process Parameters.

It should be noted that during the following discussion of the hot stamping process, there is considerable reference to metallurgical principles such as phases and phase transformations. The reader is directed to the later section: Microstructure, for background information regarding such principles.

There are two types of hot stamping [15]: 1) direct hot stamping; and 2) indirect hot stamping.

*Direct Hot Stamping*

Figure 2.2 illustrates the stages of the direct hot stamping process. Figure 2.3 illustrates a hypothetical heat treatment cycle of blank to hot stamped component [31]. Figure 2.4 illustrates the exploitation of phase transformation phenomena and maintenance of different phases with different mechanical properties prior to forming (the pre-hot stamping condition), during forming (the hot stamping condition) and in the hot stamped component following forming (the post-hot stamping condition) [1].

---

[5] As applied to the 'conventional' hot stamped boron steel 22MnB5 – see section: Boron Steels.

*Stage 1 – blanking:* The as-delivered cold rolled sheet steel, typically with width ≤ 1500 mm and thickness 1-2 mm; a microstructure of proeutectoid α-ferrite and pearlite; and yield/proof strength ($R_e$/$R_{p0.2}$) 340-480 MPa, ultimate tensile strength ($R_m$) 550-600 MPa and total elongation (A) ~ 25 %, is cut to suitable geometry by the process of blanking. Blanking is a 'cold' cutting/shearing operation in which a workpiece (blank) is cut and removed from the sheet by applying a sufficient shearing force at ambient temperature. The blank thus represents the removed part that goes on to be hot stamped into the component, while the remainder of the sheet represents scrap that is recycled.

Blanking requires a press consisting of a hydraulic ram, punch and die. The sheet is placed over the die, with the latter exhibiting a cut-out with geometry of the desired blank, plus an additional clearance margin of 10-20 % the sheet thickness [1]. Above the sheet resides the punch which also exhibits geometry of the desired blank. Both the die and punch are typically fabricated from hardened tool & die steels and their geometries (and thus the geometry of the blank) may be standard (i.e. a standard circle or oblong), or customised depending on the desired hot stamped component geometry (e.g. an outline of a roof pillar or bumper beam). The hydraulic ram drives the punch downwards at high speed into the sheet, resulting in bending and eventually shear fracture of the sheet within the clearance margin. The blank which is sheared from the sheet falls freely into the cut-out in the die. Blanking is extremely rapid, reaching as high as 1000 strokes/minute [15]. Moreover, multiple sheets can sometimes be stacked and blanked simultaneously [15].

*Stage 2 – austenisation:* The blank is austenised by radiant and convective heating in a continuous electric or gas fired roller hearth furnace [1]. The heating rate is typically < 12 °C/s [20] to a target 'soak' temperature of 900-950 °C (with $Ac_3$ ~ 850 °C)[6] [11]. The soak temperature is then maintained for a soak time of 3-5 minutes to ensure complete and homogenous austenisation [20].

During austenisation of a ferritic-pearlitic microstructure, cementite begins to transform to γ-austenite (corresponding to the $Ac_1$ temperature), which is followed by transformation of eutectoid and proeutectoid α-ferrite to γ-austenite (with completion of the transformation corresponding to the $Ac_3$ temperature) [32] [33].

The roller hearth furnace includes a multiplicity of independently and externally controlled rollers, extending across 30-40 meters [15]. Rotation of the rollers transports the blank through the heating section (with these rollers rotating at relatively high speed) and then into the soaking section (with these rollers rotating at relatively low speed or even paused so to achieve the soak time). Total furnace time including heating and soaking is usually ≤ 10 minutes [20].

Due to the high temperature, uncoated steel is austenised in an inert gas atmosphere of nitrogen, hydrogen and/or argon to avoid oxidation (and thus accumulation of surface oxide scale) and decarburisation, with these phenomena occurring particularly dramatically on the sheared edges resulting from blanking [31]. Oxide scale is undesirable primarily due to its hardness which increases tool wear during hot stamping. Moreover, oxide scale inhibits welding and the

---

[6] Critical phase transformation temperatures:

$Ae_1$: pearlite <> γ-austenite under equilibrium heating/cooling.

$Ae_3$: proeutectoid α-ferrite <> γ-austenite under equilibrium heating/cooling.

$Ac_1$: pearlite > γ-austenite under superheating.

$Ac_3$: proeutectoid α-ferrite > γ-austenite under superheating.

$Ar_3$: γ-austenite > proeutectoid α-ferrite under supercooling.

$Ar_1$: γ-austenite > pearlite under supercooling.

Bs: γ-austenite > bainite under supercooling.

Ms: γ-austenite > martensite (start) under supercooling.

Mf: γ-austenite > martensite (finish) under supercooling.

adhesion of organic coatings (paint), where painting may be necessary [1]. Decarburisation (segregation of carbon within the cross-section interior and away from the surfaces; and/or formation of carbon dioxide due to oxygen presence) which reduces surface carbon concentration is undesirable since austenitic homogeneity is essential for homogenous stamping (deformation), homogenous quench hardening and ultimately, homogenous mechanical properties in the hot stamped component [34]. Coated steel (the leading coating being an aluminium-silicon example [14]) however can be austenised without the need of the inert gas atmosphere, since the coating precludes oxidation and decarburisation.

*Stage 3 – transfer:* The austenised blank at 900-950 °C is transferred by a robotic system from the austenisation furnace to the blank holder of the press in 3-8 seconds [1]. During this time, the temperature of the blank can drop by up to 100 °C due to natural air cooling [20]. Natural air cooling also presents an opportunity for surface oxidation and decarburisation in uncoated steel. Thus, it is essential that the transfer time is as short as possible so to minimise surface oxidation and decarburisation (in uncoated steel) and most importantly, so that temperature does not drop below ~ 700 °C ($Ar_3$), in turn to ensure that the microstructure remains entirely austenitic (stable or metastable) at the commencement of the hot stamping and quench hardening stages. If the $Ar_3$ temperature is reached before quenching begins, proeutectoid α-ferrite will form and thus, the microstructure will only partially harden to martensite. Moreover, the presence of proeutectoid α-ferrite (as opposed to exclusive γ-austenite) during the hot stamping stage, will compromise formability.

*Stage 4 – hot stamping:* The press consists of a hydraulic ram, punch, die and blank holder. The hydraulic ram descends the punch to meet its mating die, with the combined punch and die geometry equal to the desired component geometry (the punch is a protrusion which embosses the blank, while the die is an intrusion/cavity which accepts the blank). Highly intricate components may require a more complex arrangement of punch, die and counter punch; with the counter punch a protrusion rising from the die cavity [1].

With the blank constrained in the blank holder and between the punch and die, the blank is rapidly stamped/deformed in 2-3 seconds [1] into the combined geometry of the punch and die and thus, acquires the desired component geometry.

With the punch and die maintained at ambient temperatures by an 'active cooling system' [15], the temperature of the blank at the beginning of the hot stamping stage is dictated by the austenisation temperature and the exact degree of cooling during transfer. Typical temperature at the beginning of the hot stamping stage is ~ 850 °C, which decreases to ~ 650 °C by the end of the hot stamping stage [1].

As the hot blank systematically contacts the punch and die surfaces during hot stamping, quenching effectively begins immediately and intensifies as more of the blank contacts the punch and die surfaces during the punch descent and as the force on the blank increases. Thus, some say hot stamping and quench hardening take place simultaneously [15].

Since the blank is maintained in the (metastable) austenitic phase and moreover, in a narrow temperature band (~ 850-650 °C) during the 2-3 seconds of hot stamping, true strength is reasonably constant at just ~ 200 MPa [35] and with true strain > 50 % [35]. Furthermore, with homogenous austenisation which eliminates any texture developed during cold rolling of the sheet steel, plastic isotropy is found, with r-value ~ 1 and Δr-value ~ 0 [34]. These mechanical properties are optimal for formability, permitting down gauging while maintaining adequate forming limits and/or permitting geometric complexity leading to component consolidation. Moreover, tool energy consumption and tool wear from force requirements are minimised, thereby aiding economy [1].

Forming at elevated temperature, above the proeutectoid α-ferrite recrystallisation temperature of ~ 750 K (477 °C), has also been shown [36] to be a critical factor for the elimination of springback. In turn, the elimination of springback caused by forming above the proeutectoid α-ferrite recrystallisation temperature has been related to the occurrence of high temperature transient creep deformation [37].

*Stage 5 – quench hardening:* The punch and die are cooled by an active cooling system, consisting of an intricacy of internal cooling channels (mains from which coils deviate) through which the quench medium (water or liquid nitrogen) circulates [15]. Thus, when the hot stamping stage is complete (defined by the punch reaching the bottom of its decent so to mate with the die) and with every surface of the component (at ~ 650 °C) in contact with either the punch or the die surfaces, the 'true' quench hardening stage begins with rapid quenching to ~ 150 °C (with Ms ~ 410 °C and Mf ~ 200 °C) [1] [20]. However, this quenching is 'indirect' since the quench medium and component do not make contact. Quenching is achieved by conductive heat transfer from the component to the cooled punch and die surfaces.

The punch is retained at the lowest (dead) point with a hold down force until the entirety of the constrained component has cooled sufficiently, which takes 15-20 seconds [1]. In this fashion, the component is rapidly quenched through the Ms-Mf range and hardened to an entirety of martensite. The martensitic transformation which releases stress imposed during forming has been shown to be a contributory factor to the elimination of springback [38]. Moreover, geometric constraint on the component throughout quenching also contributes to the elimination of springback [26].

The critical cooling rate[7] [11] for complete quench hardening (transformation to martensite) with 22MnB5 is approximately -30 °C/s [20], although actual quench rates can be two or three times higher than this [15]. With carbon content << 0.6 wt %, the martensite resulting from quenching is predominantly of the lath character [39].

---

[7] The critical cooling rate can be defined as the minimal rate of cooling (or typically quenching) that is required from an austenitic temperature (i.e. from a temperature > $Ar_3$) to a temperature below Bs in order to achieve a complete transformation to martensite. Essentially, the critical cooling rate is the minimal cooling rate over the reconstructive/semi-reconstructive phase transformation temperature range that is necessary to prevent the reconstructive/semi-reconstructive phase transformations from taking place and thus, to permit the displacive γ-austenite > martensite phase transformation to take place exclusively.

Following quenching, the hot stamped component at ~ 150 °C is entirely martensitic (below Mf) and free from springback. Slow cooling from this temperature to ambient temperature does not initiate a phase transformation or springback [1]. Thus, the hot stamped component is ejected from the press and cooled to ambient temperature by natural air cooling.

Final tensile properties in the hot stamped component are typically elastic modulus (E) ~ 200 GPa, $R_e/R_{p0.2}$ 1000-1250 MPa, $R_m$ 1400-1700 MPa and A 4-8 % [1] [20]. These tensile properties are optimal for automotive anti-intrusive structural body component applications (see section: Automotive Applications), providing excellent anti-intrusive crash performance, simultaneously while down gauging [15].

*Stage 6 – post-hot stamping processing:* Post-hot stamping processing includes shot blasting or pickling of uncoated steel in order to remove surface oxide scale [1]. Machining such as cutting, trimming and/or piercing may be in order to refine geometry (remove flanges, add intricate details etc.), although this is usually unnecessary since all but the most intricate geometries are obtainable immediately from hot stamping [1]. The ultrahigh strength of the hot stamped component limits ambient temperature machining. Machining is usually conducted with laser tooling rather than conventional mechanical tooling [1]. Painting and paint baking which involves heating to ~ 170 °C for ~ 10 minutes may also be required. In addition to the primary objective of curing the paint, an additional 100 MPa to yield/proof strength can be achieved through the strain aging phenomenon [1].

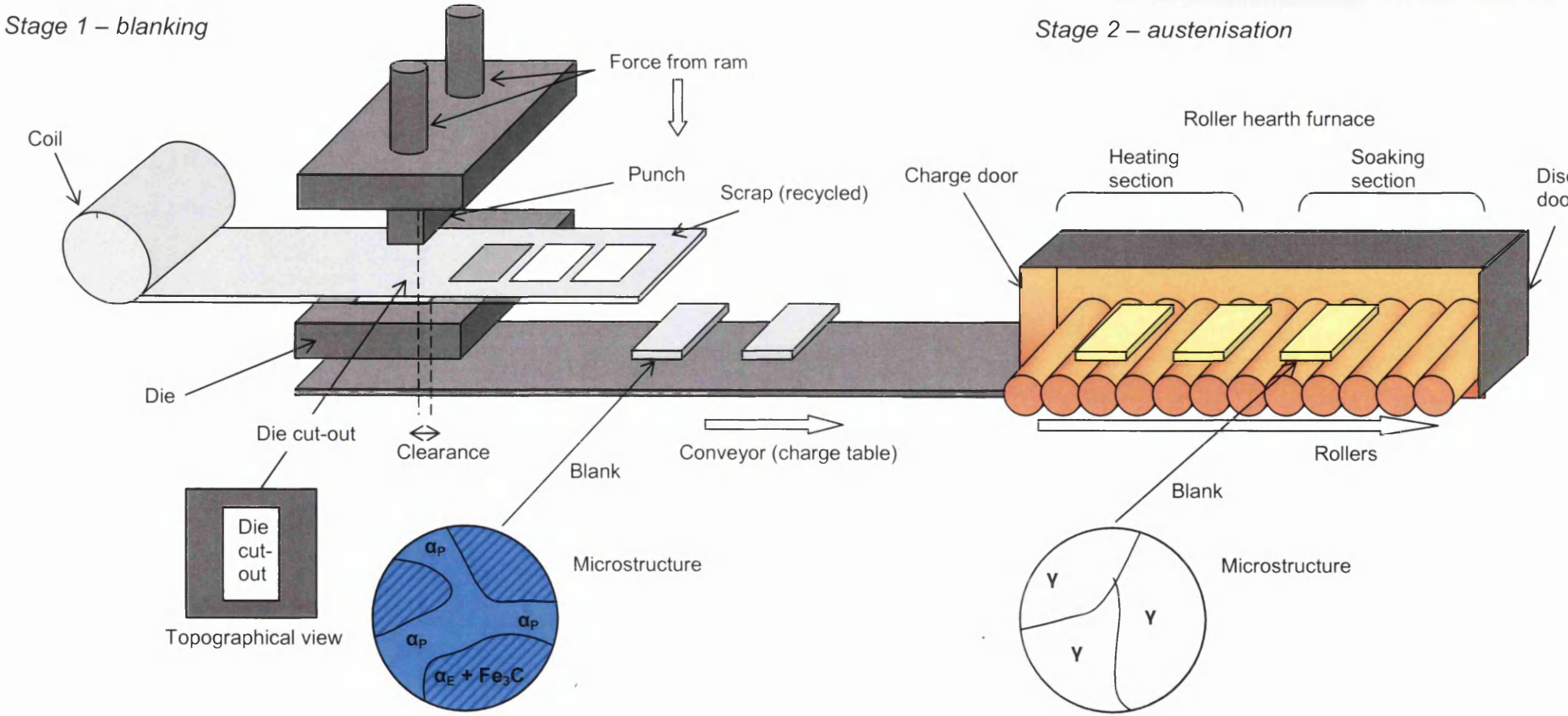


*Blanking:*

- Sheet (width ≤ 1500 mm, thickness 1-2 mm) cut into suitably sized blanks.
- Temperature: ~ 20 °C.
- $R_e$: 340-480 MPa.
- $R_m$: 550-600 MPa.
- A: ~ 25 %.
- Microstructure: proeutectoid α-ferrite + pearlite.

*Austenisation:*

- Heating rate: < 12 °C/s.
- Soak temperature: 900-950 °C.
- Soak time: 3-5 min.
- Total furnace time: ≤ 10 min.
- Atmosphere: inert gas for uncoated sheet.
- Phase transformation: proeutectoid α-ferrite + pearlite > γ-austenite.

Figure 2.2: Direct hot stamping

*Stage 3 – transfer*

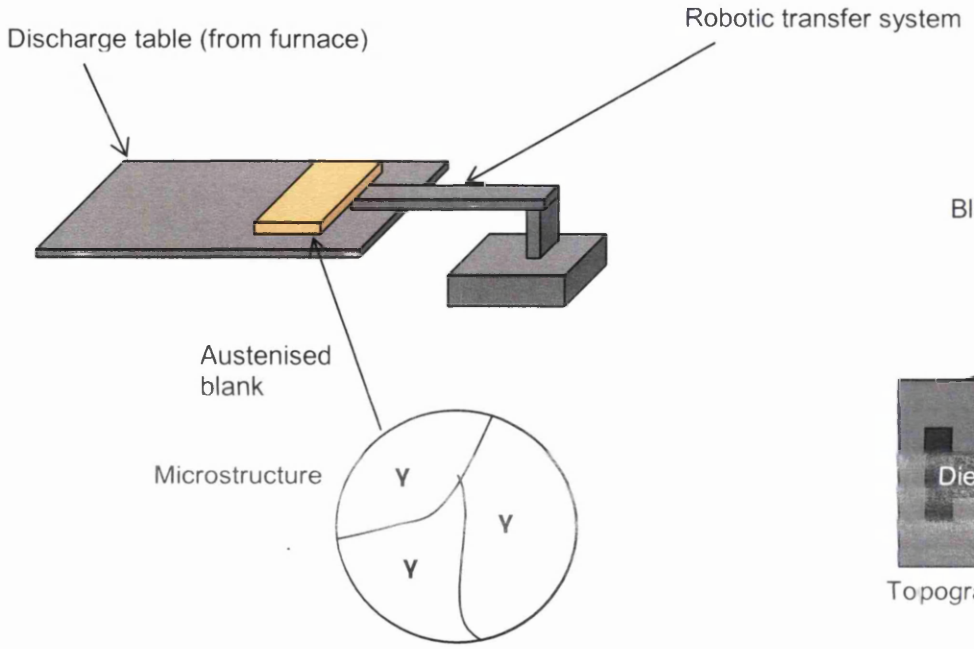


*Transfer:*

- Austenised blank from furnace to press by robotic transfer system.
- Time: 3-8 sec.
- Start temperature: 900-950 °C (austenisation temperature).
- Finish temperature: 800-850 °C.
- Microstructure: γ-austenite.

*Stage 4 – hot stamping*

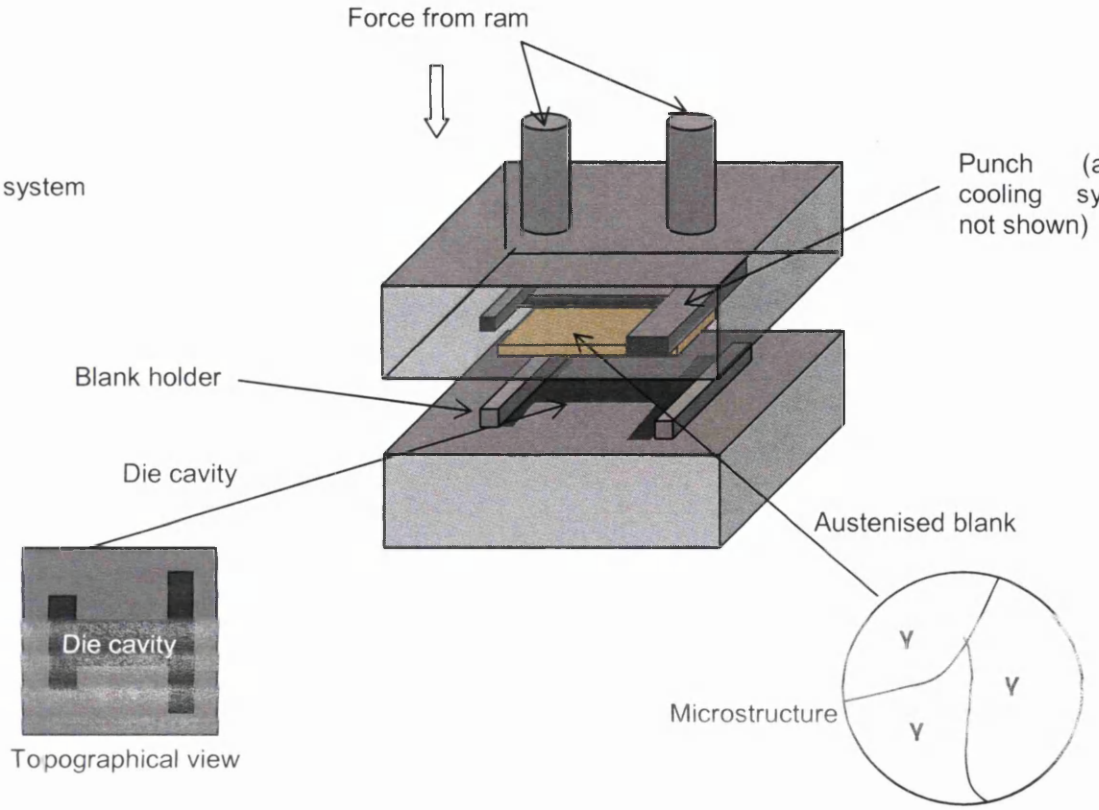


*Hot stamping:*

- Austenised blank stamped into component geometry with force from ram.
- Start temperature: 800-850 °C.
- Finish temperature: 600-650 °C.
- Time: 2-3 sec.
- True strength: ~ 200 MPa.
- True strain: > 50 %.
- Microstructure: γ-austenite.

Figure 2.2: Direct hot stamping (continued)

*Stage 5 – quench hardening*

*Stage 6 – post-hot stamping processing*

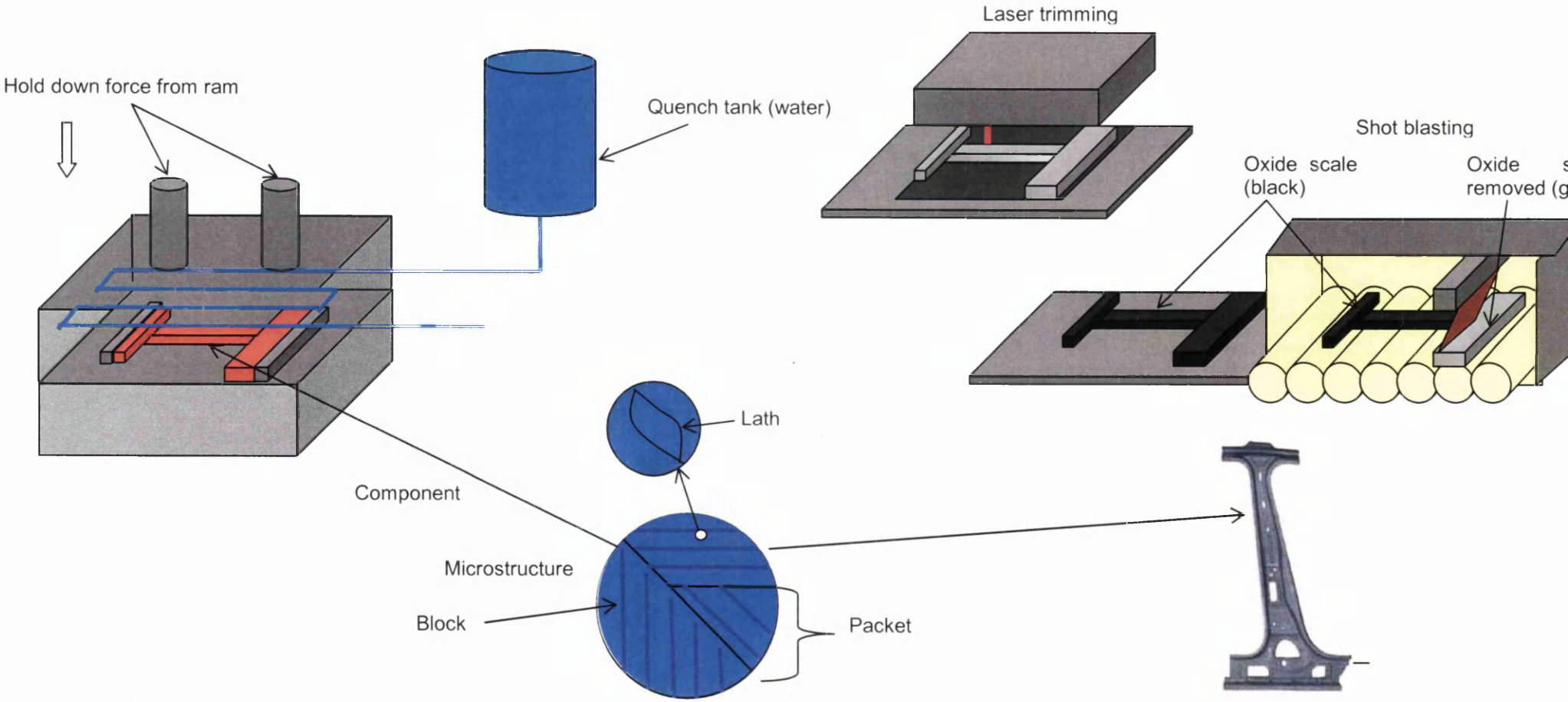


*Quench hardening:*

- Indirect quenching in the press.
- Quench rate: > -30 °C/s.
- Start temperature: 600-650 °C.
- Finish temperature: 100-200 °C.
- $R_e$ (final): 1000-1250 MPa.
- $R_m$ (final): 1400-1700 MPa.
- A (final): 4-8 %.
- Phase transformation: γ-austenite > martensite.

*Post-hot stamping processing:*

- Shot blasting or pickling (for uncoated steel to remove oxide scale).
- Cutting/trimming/piercing with laser tooling.
- Painting and paint baking ($R_e$: 1000-1250 MPa + 10 %).

Figure 2.2: Direct hot stamping (continued)

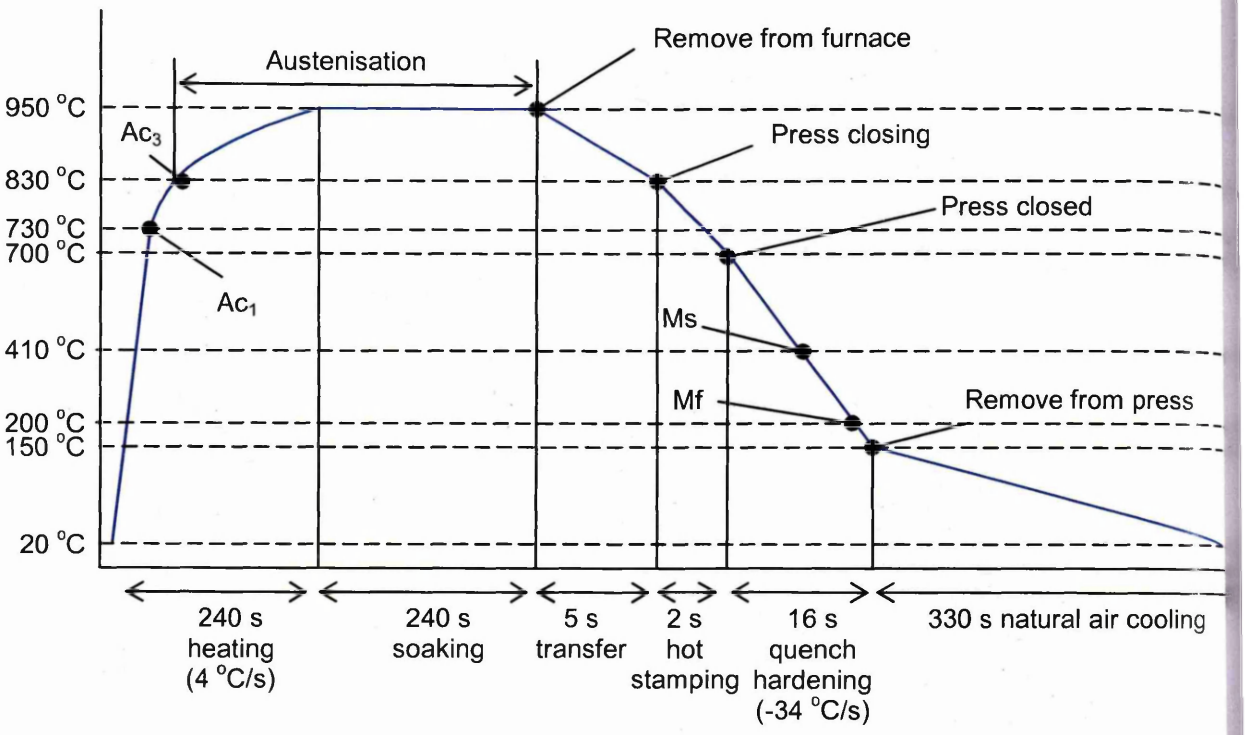


Figure 2.3: Heat treatment cycle of blank to hot stamped component (adapted from [3

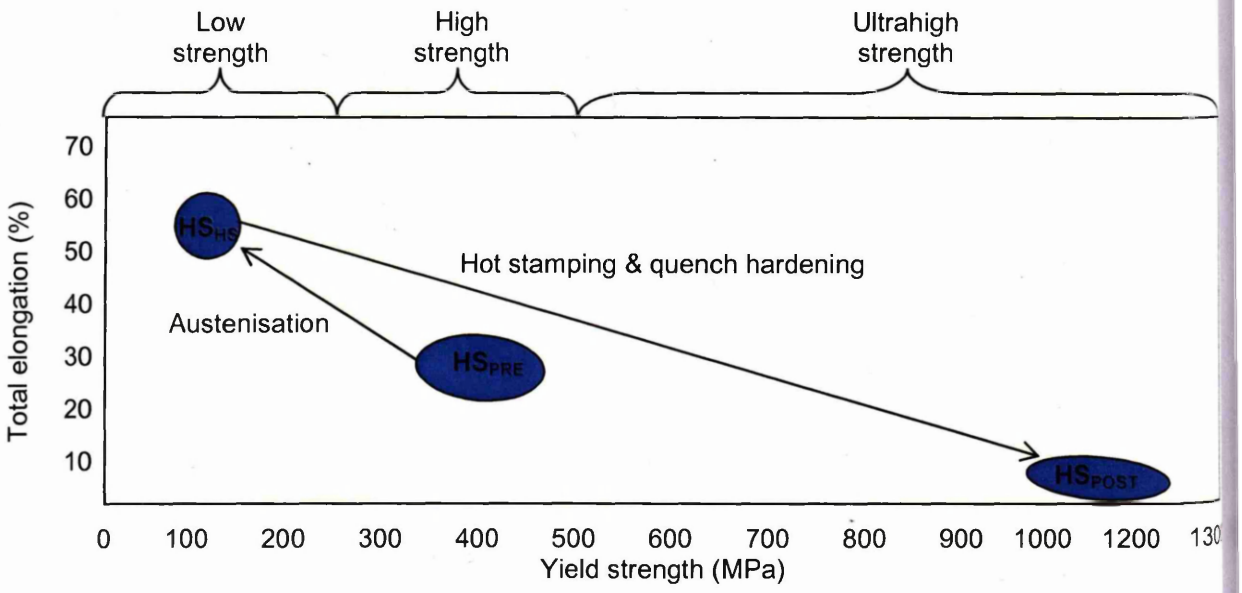


Figure 2.4: Yield strength-total elongation ranges of hot stamped boron steels in the pre-hot stamping ($HS_{PRE}$), hot stamping ($HS_{HS}$) and post-hot stamping ($HS_{POST}$) conditions (adapted from [1])

*Indirect Hot Stamping*

Indirect hot stamping is exactly as direct hot stamping, except for the addition of a 'preform' stage between blanking and austenisation [15]. During the preform stage, a significant portion of forming so to attain 90-95 % the final component geometry is carried out 'cold' to produce a 'preform', before final forming (sometimes termed 'calibration') is carried out 'hot'. Quenching in the press then follows.

The advantages and disadvantages of indirect hot stamping relative to direct hot stamping are summarised in Table 2.1 [1] [15] [20].

Table 2.1: Advantages and disadvantages of indirect hot stamping relative to direct hot stamping (adapted from [1] [15] [20])

| *Advantages* | *Disadvantages* |
|---|---|
| Reduced hot stamping tool wear: when uncoated steel blanks are austenised, hard oxide scale forms on the surfaces. The relative movement between the punch/die and hard oxide scale during hot stamping escalates tool wear. Since only 5-10 % of the final geometry need be hot stamped in the indirect type, hot stamping tool wear from oxide scale is minimised. | Cold stamping capital cost: two separate presses are required rather than just one (one for cold stamping of the preform and another for hot stamping of the final component), thereby creating an additional capital cost and adding to floor space demand. |
| Lower austenisation temperatures and times: since only 5-10 % of the final geometry need be formed 'hot', austenisation temperatures and times can be lower. Thus, the indirect type is more suitable for pre-galvanised steels where the zinc coating cannot withstand the higher temperatures and/or longer times of austenisation associated with direct hot stamping (zinc has a melting point of just 420 $^{o}$C and the conventional austenisation temperature and time for direct hot stamping are 900-950 $^{o}$C and 3-5 minutes respectively). The lower austenisation temperatures and times also reduce cost from energy demand. | Cold stamping running cost: cold stamping gives rise to significant tool energy consumption and tool wear. |
| Aided machining and finishing: post-hot stamping processing made difficult in the martensitic condition can be carried out prior to quench hardening, where the ferritic-pearlitic microstructure is much softer and more ductile. | Reduced efficiency: the process is longer and less efficient, including more stages that also introduce greater room for manufacturing error and loss of reproducibility. |

The choice between direct and indirect hot stamping comes down to production size, floor space, coating type, and/or component geometry [23]. Direct hot stamping is preferred by the automotive industry [20] and will be the focus of further discussions.

### *Automotive Applications*

*Body in White*

The structural body components constituting the automotive body structure[8] [40], termed 'body in white' (BIW), account for ~ 60 % of the average passenger vehicle's total weight [41]. Moreover, 80 % of the BIW is typically composed of steel [2]. Besides the BIW, the remainder of the vehicle is then constituted by the mechanical, electrical, interior and closure components [41]. Thus, the BIW presents the greatest potential for vehicle weight reduction (particularly for the steel industry). Further, the BIW is most important in terms of crash performance and associated occupant safety, since it forms a barrier between the occupant

---

[8] The foundation of an automobile is termed 'chassis' to which the various components are attached, including the mechanical components (engine, driveshaft, gearbox, clutch, axles, wheels, steering column, suspension, brakes, exhaust etc.), structural body components (roof pillars; roof, floor and door reinforcements; engine-bay beams; body panels, floorpan etc.), electrical components (sensors, wiring, lights etc.), interior components (seats, upholstery, instrument panel etc.) and closure components (doors, bonnet and boot-lid).

There are chiefly two types of chassis design distinguished by different utilisation of the structural body components/BIW: 1) body on frame; and 2) unibody.

The body on frame was the original chassis design. The chassis is the frame element of 'body on frame'. All other components, including the structural body components/BIW, attach to the frame.

As of 2010, ~ 99.9 % of passenger vehicles utilised the unibody, which has largely superseded the body on frame. The unibody integrates the structural body components into a single welded unit, which then represents the chassis. Thus, in the unibody, the chassis and BIW are equivalent. The mechanical, electrical, interior and closure components are then attached to the chassis/BIW.

The term 'body in white' is derived from manufacturing practice in the days that the body on frame dominated and before the appearance of the unibody. Body assemblies (wooden structures coated with sheet steel and painted white) were often produced by outside contractor firms and imported by the automotive manufacturer. The automotive manufacturer then bolted the acquired 'white' body to their frame.

and the collision object. For these reasons, AHSS have been applied most intensively to the structural body components [1].

The BIW is composed of many individual structural body components. The essential structural body components that are most load bearing under normal driving situations (non-crash events), that are imperative during crash events and/or that represent those components to which AHSS have been applied as of 2014, are illustrated by the generic example of Figure 2.5 [14] [17] [42] [43]. The anti-intrusive structural body components to which hot stamped boron steels have been applied as of 2014 are highlighted [20].

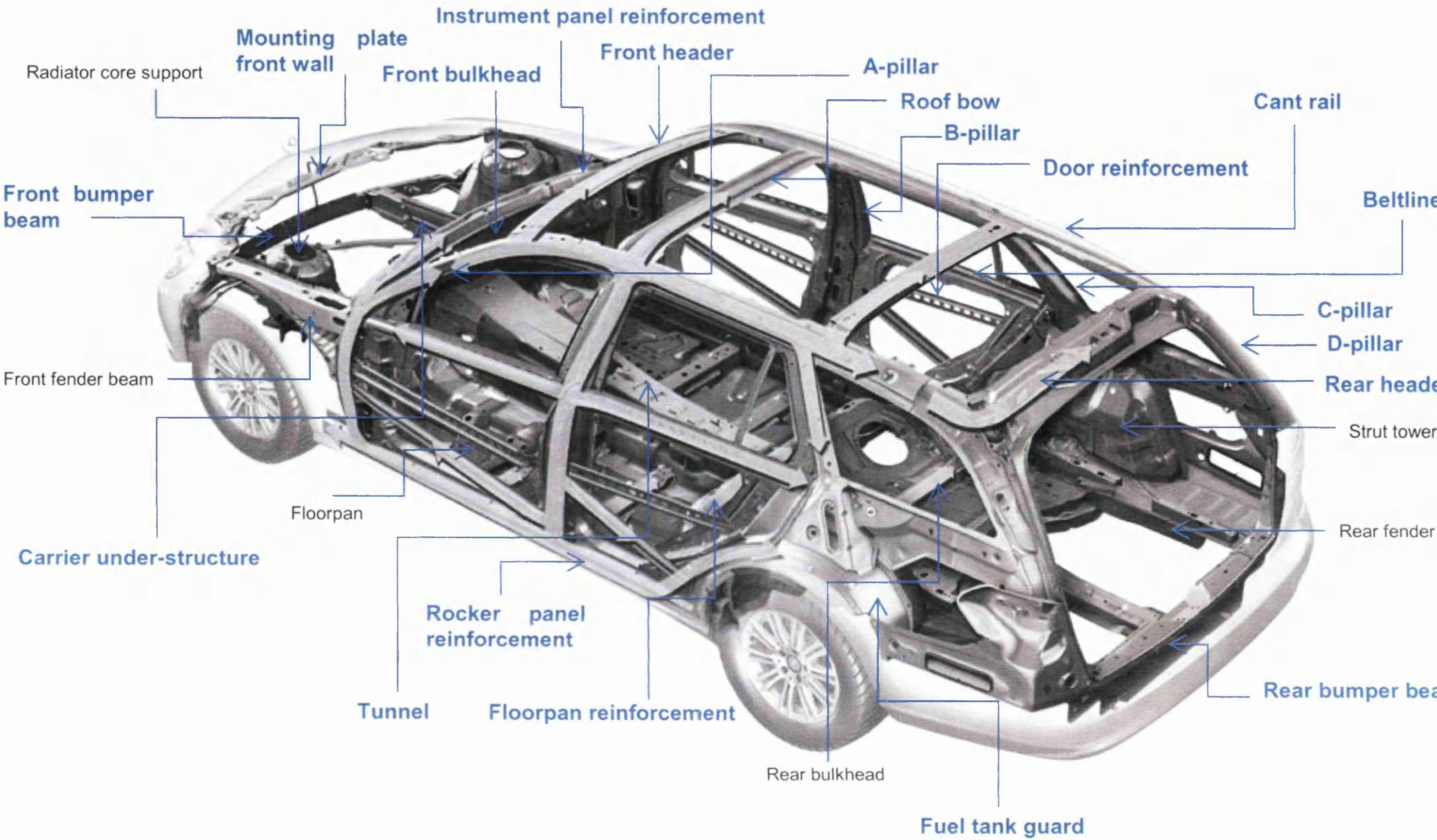


Figure 2.5: Essential structural body components of the BIW (anti-intrusive components to which hot stamped boron steels have been applied as of 2014 are highlighted) (adapted from [14] [17] [42] [43])

In 1951, Béla Barényi of Mercedes-Benz patented the 'safety cell and crumple zones' concept: a rigid passenger safety cell enclosed by crumple zones at front and rear [44]. The crumple zones were designed to deform during impact, thus absorbing the kinetic/impact energy and in turn, reducing load transferred to vehicle occupants. Meanwhile, the rigid safety cell prevented intrusion into the passenger compartment and crushing of vehicle occupants. The Mercedes-Benz W 111 series of 1959 was the first production vehicle to be equipped with the safety cell and crumple zones concept; a concept that has since become common-place in essentially all vehicles.

Based on Barényi's concept and in turn, deformation behaviour in a crash event, structural body components can broadly be classified as one of two types:

*Impact energy absorptive (deformable):* Those that are designed to deform, absorb impact energy and thus prevent transfer of impact energy to vehicle occupants. This translates into materials with moderate elastic modulus, moderate yield strength, ultrahigh ultimate tensile strength, high total elongation and high impact toughness. The impact energy absorptive components are usually situated at relatively far distance from the passenger compartment, or at a height or in an orientation so to be out of line with the passenger compartment, so that deformation does not result in intrusion into the passenger compartment and crushing of occupants. An example is the lower region of the B-pillar, which is designed to deform substantially in side impact so to absorb significant impact energy and thus, prevent impact energy transfer to occupants. However, this region is below the passenger compartment, so anti-intrusion is not necessary. Figure 2.6a illustrates how this concept functions, in terms of the component at the macroscopic scale [45] [46] and in terms of the material stress-strain response.

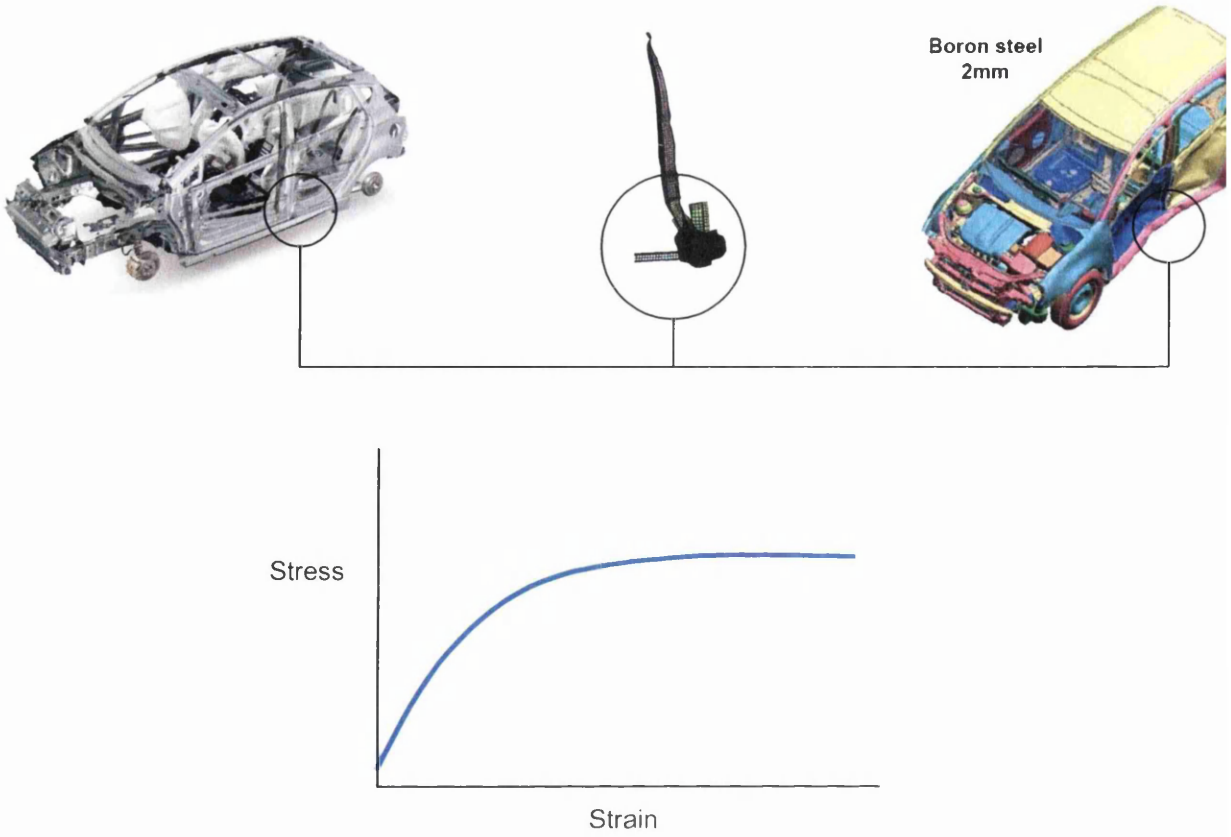


Figure 2.6a: Impact energy absorptive structural body components (adapted from [45] [46])

*Anti-intrusive (non-deformable):* Those that are designed to form a rigid cage or safety cell around the passenger compartment by sustaining impact with little deformation, thus avoiding intrusion into the passenger compartment and crushing of vehicle occupants. This translates into materials with high elastic modulus, ultrahigh yield strength, ultrahigh ultimate tensile strength and limited total elongation. The anti-intrusive components are usually situated in close proximity to the passenger compartment. An example of an anti-intrusive component is the centre region of the B-pillar in side impact – if this region of the B-pillar was to deform excessively, it would buckle and bend with intrusion into the passenger compartment, potentially resulting in crushing of occupants. On the contrary, if the component was to fracture, less impact energy would be transferred to adjacent impact energy absorptive components and moreover, sharp edges of the fracture surface would be exposed, leading to exacerbated danger. Figure 2.6b illustrates how this concept functions, in terms of the

component at the macroscopic scale [45] [46] and in terms of the material stress-strain response.

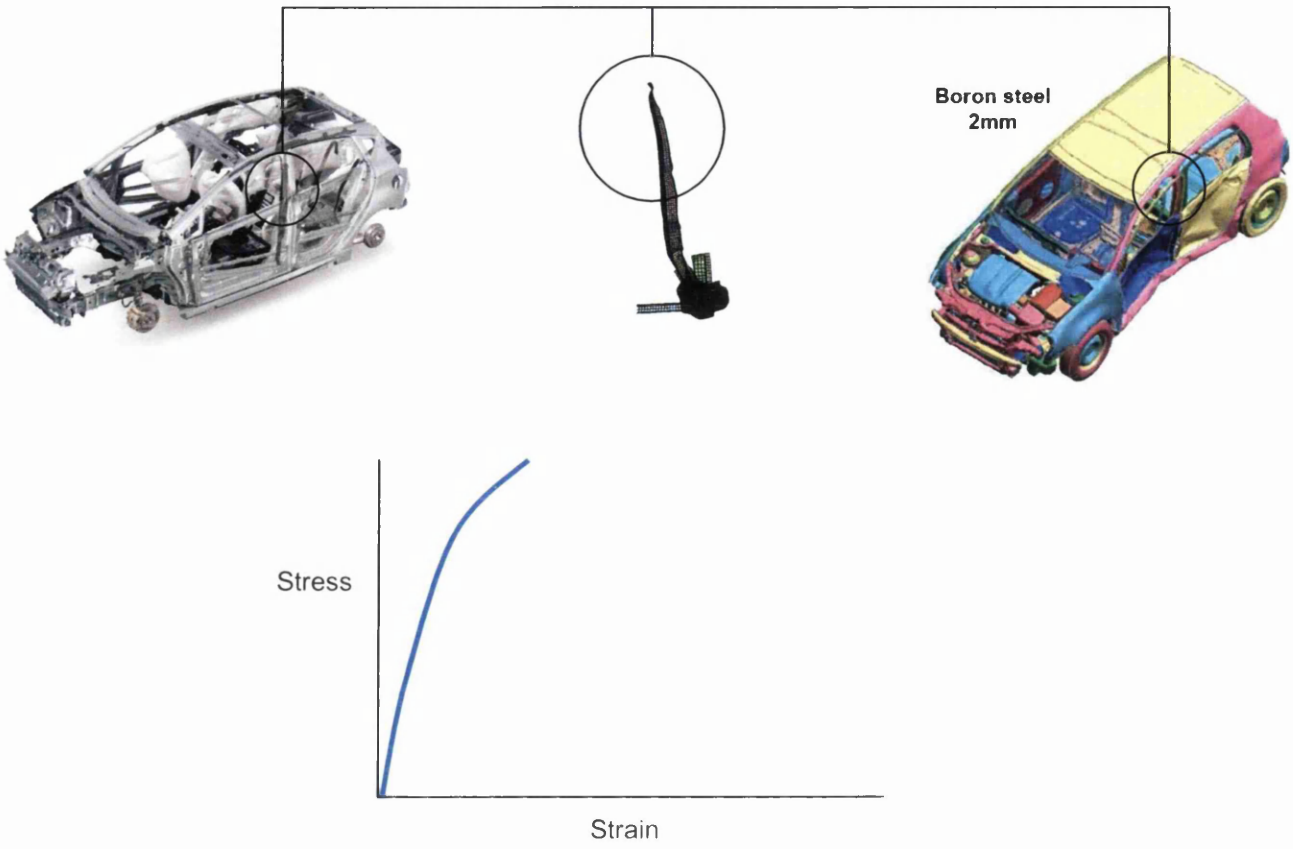


Figure 2.6b: Anti-intrusive structural body components (adapted from [45] [46])

*Tailor Welded Blank*

The 'tailor welded blank' concept was invented by German steel manufacturer Thyssen Stahl (predecessor to ThyssenKrupp) in 1983 [47]. Two or more sheet steels of different chemical composition/grade (e.g. a HSS grade and an UHSS grade), of different heat treatment/thermal history, with different coating type and/or of different thickness, are laser welded to form a blank. The tailor welded blank is then formed into the component, which inherits the different properties of the sheet steels in different regions. This is illustrated by the hot stamped B-pillar of Figure 2.6c [48], where the green (HSLA), yellow (DP) and red (boron) regions represent different steel grades, with the tensile properties of the three grades transitioning from lower tensile strength-higher elongation, to higher tensile strength-lower elongation, respectively. Combined with the thickness of the three grades increasing from the HSLA grade, to the DP grade and to the boron grade, this provides maximum impact energy absorption (while reducing weight) and superior weldability (to assist joining of the hot stamped component to adjacent components of the automotive body structure) in the upper and lower regions, with maximum anti-intrusion in the centre region. The tailor welded blank ensures that the most appropriate material is in the correct place for the application [47].

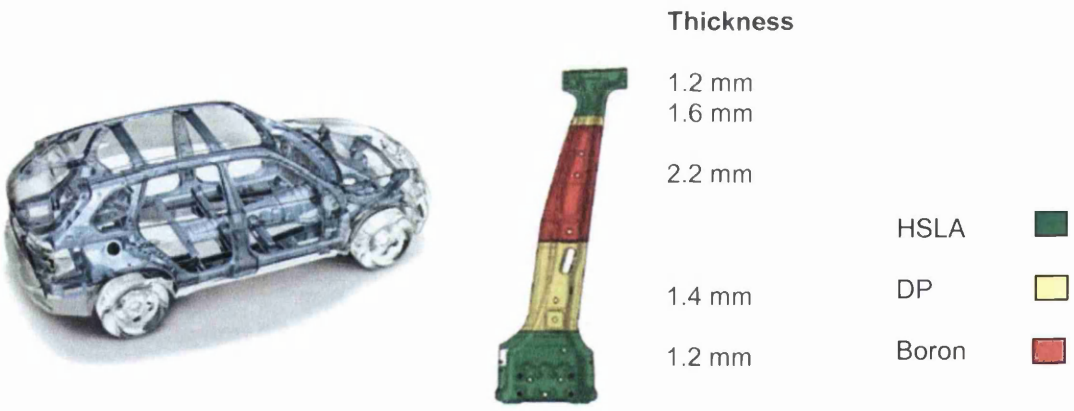


Figure 2.6c: B-pillar from tailor welded blank (adapted from [48])

*Geometric Requirements*

Hot stamping can meet the geometric intricacy, reproducibility and accuracy requirements of automotive structural body components. Figure 2.7 [49] illustrates a door reinforcement beam, B-pillar and tunnel, together with the common locations in each where cracking, distortion and springback are encountered when manufactured by conventional cold forming processes. The large amount of springback following forming with HSS and particularly UHSS is a major limitation of cold forming processes [37]. Forming above the proeutectoid α-ferrite recrystallisation temperature of ~ 750 K (477 °C) [36] where high temperature transient creep deformation is permitted [37]; the martensitic transformation which releases the stress imposed during forming [38]; and geometric constraint on the component throughout quenching [26], all contribute to the elimination of springback via hot stamping.


Figure 2.7: Limitations of cold forming that are overcome by hot stamping (adapted from [49])

***Hot Stamping Summary***

The highly formable, high temperature austenitic microstructure that is maintained throughout the forming stage of the hot stamping process permits down gauging while not compromising forming limits. Moreover, the high formability permits component consolidation, where welded assemblies consisting of multiple, individually cold formed components, can be consolidated in one single, geometrically complex hot forming operation. Component consolidation reduces process time (cost), reduces weight and increases structural strength. The ultrahigh strength martensitic microstructure resulting in the final component permits down gauging while not compromising anti-intrusive crash performance. Forming above the proeutectoid α-ferrite recrystallisation temperature of ~ 750 K (477 $^{o}$C) where high temperature transient creep deformation is permitted; the martensitic transformation which releases the stress imposed during forming; and geometric constraint on the component throughout quenching, all contribute to the elimination of springback. Further, the above can be achieved with mild carbon low alloy steels (see section: Boron Steels), thereby aiding economy, formability, weldability and coatability.

Extensive application of hot stamped boron steel (28 %) to the 2012 VW Golf VII gave rise to a direct weight reduction of 10.2 kg from down gauging of anti-intrusive structural body components and a further indirect weight reduction of 2.9 kg from down gauging of adjacent components such as floor panels [17]. The weight reduction achieved from the application of hot stamped boron steel helped the 2012 VW Golf VII increase fuel efficiency by 23.0 % and reduce carbon dioxide exhaust emissions by 13.9 % compared to its predecessor [50]. Application of hot stamped boron steel to the 2012 Skoda Rapid tunnel assembly gave rise to an assembly consisting of 2 individual components rather than 7 individual components, 14 welding points rather than 115 welding points, a weight reduction of 4 kg and a total cost saving of 30 % compared to its predecessor [17]. Moreover, both of these vehicles achieved the maximum EURO NCAP 5 Star safety rating [51].

Although the hot stamping line demands a large initial capital investment and moreover, running costs are greater than those of cold forming processes, principally due to the heating requirement; the ability to down gauge compared to cold formed components gives rise to a cost saving from less material usage. Further, component consolidation gives rise to fewer processing stages, as fewer individual components need be formed and moreover, fewer individual components need be joined to produce an assembly. This consideration also gives rise to a cost saving compared to cold forming processes.

The virtues of hot stamped boron steels can be summarised by relating back to the demands from the automotive industry, as presented in Table 2.2.

Table 2.2: Demands from the automotive industry met by hot stamped boron steels

| *Demands* | *Hot stamped boron steels* |
|---|---|
| Increased tensile strength for a given elongation in the final component so to permit further down gauging and vehicle body weight reduction while improving crash performance | Ultrahigh strength ($R_e$ ~ 1200 MPa and $R_m$ ~ 1500 MPa post-hot stamping) plus 10 % increase to $R_e$ following paint baking |
| Increased formability (elongation, work hardening exponent, lateral anisotropy-non-thinning, planar isotropy etc.) for a given tensile strength in the as-delivered condition so to permit further down gauging and vehicle body weight reduction by means of greater forming limits | High formability (true strength ~ 200 MPa and true strain > 50 % during hot stamping) |
| Increased formability for a given tensile strength in the as-delivered condition so to permit further component consolidation, giving rise to reduced process time (cost), reduced weight, increased manufacturing reproducibility, increased geometric accuracy and increased structural strength | |
| Increased weldability | Mild carbon, low alloy steels |
| Increased corrosion resistance | Coatability |
| Increased manufacturing reproducibility | Simplistic and automatable forming & processing with little room for manufacturing error<br><br>Components are close to plastic isotropy with little crystallographic texture, giving rise to reliable, predictable and reproducible mechanical properties in various orientations of measurement |
| Increased geometric accuracy (reduced springback and forming & processing errors) | Springback is eliminated<br><br>Simplistic and automatable forming & processing with little room for manufacturing error<br><br>Component consolidation permits less welding and in turn, fewer welding errors |
| Lower cost | Rapid forming & processing times, little tool energy consumption and little tool wear (with coated steel)<br><br>Mild carbon, low alloy steels<br><br>Component consolidation |
| Increased elastic modulus (stiffness) for improved anti-intrusive crash performance and for improved structural/torsional rigidity (chassis stiffness) and in turn, for improved handling performance | E ~ 200 GPa post-hot stamping |

## Steels for Hot Stamping

### *Boron Steels*

'Boron steels' are carbon-manganese-boron, low to high carbon[9] [52], low alloy[10] [52] steels. Hot rolled and cold rolled annealed boron steels were first produced in the mid-1900s by Norrbottens Järnverk [18] – the same Swedish steel manufacturer that pioneered the hot stamping process. Initially, the as-delivered boron steels were cold formed, furnace austenised and quench hardened in the conventional unconstrained manner and applied to agricultural machinery requiring abrasion resistance, such as cutting discs, mower blades, plough folks and mould boards [15] [23]. In 1974, with the introduction of the hot stamping process, boron steels found an exclusive niche when Norrbottens Järnverk brought boron steels and the hot stamping process together.

In 2014, applications of boron steels continue to include agricultural machinery, in addition to other abrasion resistant demanding applications, such as earth moving machinery, engine and transmission components, mining drills and folk lift truck arms [15] [23]. Moreover, boron steels have remained in association with hot stamping – the convention has become grade 22MnB5[11] [15] [20] [23]. The supremacy of 22MnB5 has been due to the combination of relative economy, cold and hot formability, weldability and coatability owing to the relatively 'lean' chemical composition, yet ultrahigh strength tensile properties of typically 1200 MPa yield/proof strength, 1500 MPa ultimate tensile strength and 6.0 % total elongation exhibited by the entirely martensitic microstructure following hot stamping.

---

[9] Low carbon steels: 0.05-0.14 wt % C.
Mild carbon steels: 0.15-0.29 wt % C.
Medium carbon steels: 0.30-0.59 wt % C.
High carbon steels: 0.60-2.13 wt % C.

[10] Low alloy steels: alloying elements in individual concentrations of $\leq$ 2 wt % (except for nickel which may be $\leq$ 4 wt %) and in a combined concentration $\leq$ 8 wt %.

[11] 22MnB5 approximate chemical composition (wt %): 0.230 C, 1.180 Mn, 0.220 Si, 0.025 P, 0.008 S, 0.160 Cr, 0.120 Ni, 0.030 Al, 0.040 Ti, 0.002 B, 0.005 N (Fe balanced).

The origin of the desirable characteristics is related to the relatively low alloy content (particularly carbon and transition metals) combined with the minute boron addition of just 0.003-0.005 wt % (30-50 ppm). The boron addition yields exceptional quench hardenability[12] [11] [39] and a very low critical cooling rate in the order of just -30 °C/s [15] [20] [23]. This critical cooling rate is less than the hot stamping quench rate and thus, eases the attainment of complete and homogenous martensite formation and the corresponding ultrahigh strength properties post-hot stamping. This is demonstrated by the hypothetical continuous cooling transformation (CCT) diagram of Figure 2.8, where the dashed proeutectoid α-ferrite region represents a mild carbon-manganese steel (without

---

[12] Quench hardenability is a depth measurement to which a steel specimen may be hardened by martensite formation.

The displacive γ-austenite > martensite phase transformation is dependent on a minimal/critical cooling rate, below which the displacive transformation is gradually surpassed by semi-reconstructive and reconstructive transformations to bainite and proeutectoid α-ferrite/pearlite, respectively.

As a steel specimen is rapidly cooled from an austenisation temperature, the surfaces of the specimen experience the greatest cooling rate, with the cooling rate diminishing with increasing depth below the surfaces and into the interior regions, as heat must transfer increasing distance in order to be dissipated from the surfaces and into the surrounding medium. If this diminishing cooling rate falls below the critical for martensite formation, the semi-reconstructive and reconstructive transformations will take place in the interior regions. As the cooling rate gradually diminishes further below the critical with increasing depth below the surfaces, the ratio of martensite to other microconstituents will gradually decrease further, until eventually, with a low enough cooling rate in the inner-most regions, martensite formation will be eclipsed completely. Thus, a martensite volume fraction gradient will result – richest at the surfaces and gradually diminishing with increasing depth below the specimen surfaces. Corresponding to this martensite volume fraction gradient will be a hardness gradient.

Quench hardenability then is a measure of hardness declination with increasing depth below the specimen surfaces and into the interior as a result of diminished martensite volume fraction. The steel with high quench hardenability is that which forms martensite (and thus exhibits high hardness) throughout its cross-section and moreover, with a relatively low cooling rate.

boron) and where the solid proeutectoid α-ferrite region represents the equivalent mild carbon-manganese steel, but with the minute boron addition.

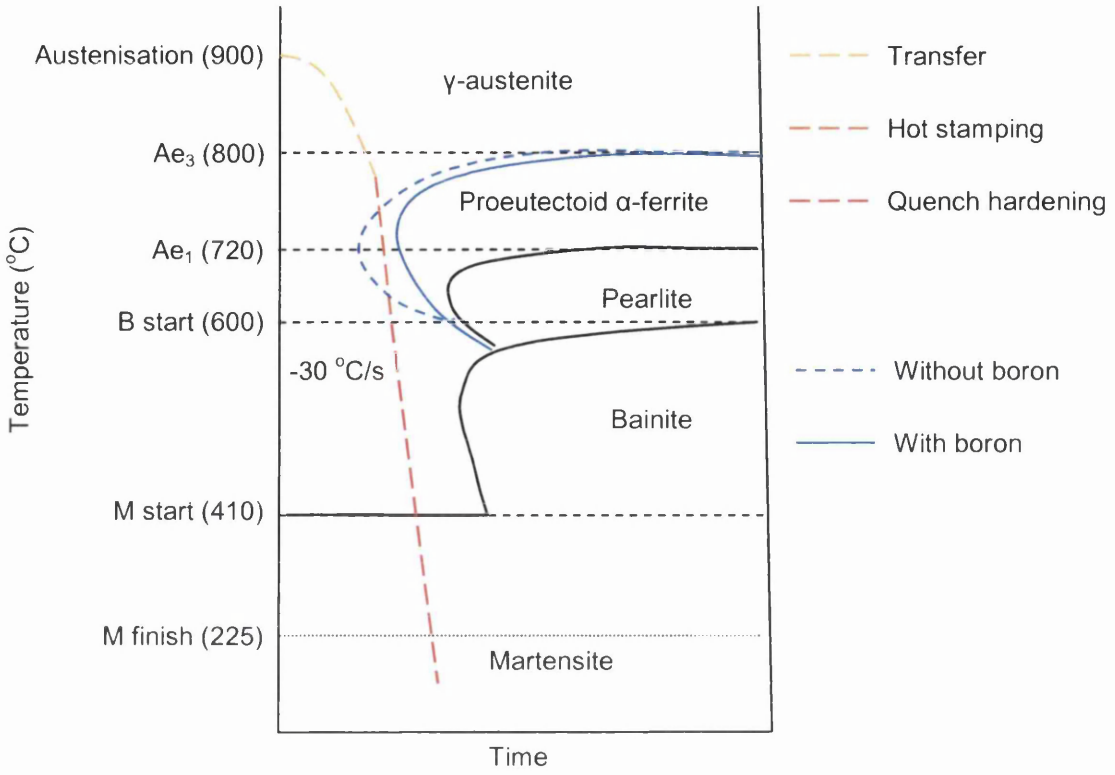


Figure 2.8: Influence of boron on the CCT diagram

The necessity for a low critical cooling rate is that the actual cooling rate during the quench hardening stage of hot stamping is primarily determined by press design (active cooling system, boundary conditions between component and punch/die, geometry etc.). Thus, the alloy that presents a lower critical cooling rate permits complete martensite formation with a less complicated (and costly) press design. Moreover, the lower critical cooling rate provides greater assurance of complete and homogenous martensite formation across a wider range of components with different geometries that experience different quench rates. Finally, quenching at a rate somewhat greater than the critical cooling rate has been found [31] to provide a finer lath martensitic microstructure, which can increase strength without decreasing impact toughness (see section: Microstructure).

It is also worth noting that boron is a relatively abundant and economical element [53], does not compromise cold formability in the ferritic-pearlitic pre-hot stamping condition (when used in the minute quantity) [53], can increase hot formability [53] and the boron quench hardenability effect is greater with lower carbon content [15], which is a happy circumstance since lower carbon content promotes greater ductility, homogeneity, formability, weldability, coatability and economy [11].

22MnB5 exhibits quench hardenability equivalent to plain carbon steels of much richer carbon contents and alloy steels (e.g. HSLA steels and DP steels) containing greater quantities of transition metals. The additional alloy content of these steels then results in inferior formability (due to unwanted solid solution strengthening and/or precipitation hardening), weldability, coatability, possibly ductility in the final component and economy.

The boron addition of just 0.003 wt % to mild carbon-manganese steel can induce an equivalent increase to quench hardenability [31] as 0.7 wt % Cr, 0.5 wt % Mo, 1.5 wt % Ni or an additional 0.6 wt % Mn.

In summary, boron is economical, not very much is necessary, it has a very profound effect on quench hardenability and there are few drawbacks. Thus, boron steels can exhibit ultrahigh strength martensitic microstructures with highly economical chemical compositions.

In 2007 it was stated [41]:

*'The ideal material for side impact protection would be a low cost, high strength grade that can be formed, joined and coated easily'.*

It can be seen that hot stamped 22MnB5 has made significant progress towards this criteria.

***Microstructure***

Microstructure is characterised by three factors [11]: 1) the number of phases present; 2) the concentration (volume fraction) of each phase; and 3) the manner in which multiple phases are distributed or arranged (microconstituent structure/morphology, grain structure and grain size). Microstructure is then dependent on four principal variables [11], as these variables directly influence those three factors that characterise microstructure: 1) the alloying elements present; 2) the concentration of each alloying element; 3) the heat treatment to which the alloy has been exposed; and 4) pressure (usually assumed to be a constant).

*Phase Transformations*

Before delving into discussion of the possible phases [13] [11] and microconstituents [14] [11] of steels, an understanding of the principles behind microstructure should be sought. Perhaps the most important of all microstructural principals is 'equilibrium'.

In a general grammatical context, equilibrium can be defined as 'a state of rest or balance due to the equal action of opposing forces'. In the context of engineering material systems, this definition of equilibrium is best related to thermodynamics and free energy [11]. In brief, free energy is a thermodynamic parameter and a function of thermodynamic measurements including system internal energy (enthalpy) and atomic/molecular randomness (entropy) – a system is at equilibrium if its free energy is at the minimum value attainable under a given combination of conditions, such as chemical composition, temperature and pressure. The equilibrium state within a system is thus defined by constant physical and chemical characteristics: the microstructure (characterised by the number of phases present, their concentrations and arrangement) persists indefinitely provided that the given combination of conditions is maintained.

---

[13] The phase can be defined as a homogenous portion of a system (e.g. the iron-carbon system) with uniform physical (state and crystal structure) and chemical characteristics.

[14] The microconstituent can be defined as a portion of a microstructure with an identifiable and characteristic crystal structure.

However, a change to the combination of conditions (such as an alteration of chemical composition, temperature and/or pressure) may raise the free energy and thus the system will respond by adjusting to another state (that is, the equilibrium state under the new combination of conditions) which will be defined by different physical and/or chemical characteristics; and hence a different microstructure consisting of a different number of phases, different concentrations of phases and/or a different arrangement of phases. Phase transformations thus represent one method by which a system can respond to a change of conditions in order to adjust to the new equilibrium state.

Phase transformations involve the formation of a new product phase (or new product phases) with different physical and/or chemical characteristics from the parent phase(s). Phase transformations may then be classified as either 'reconstructive' or 'displacive', where the primary distinction between the two types lays in atomic diffusion dependence [54].

The reconstructive (diffusional) transformation [54] can be envisaged as the breakdown of atomic bonds in the parent phase (Figure 2.9a), the movement via diffusion of atoms into new positions (Figure 2.9b) and then the reconstruction of atomic bonds in the product phase (Figure 2.9c). Conversely, the displacive (diffusionless) transformation [54] can be envisaged as the cooperative movement of atoms from the parent phase into the product phase via a shear displacement; that is, there is no breakdown of atomic bonds, no atomic diffusion and no reconstruction of atomic bonds (Figure 2.10).

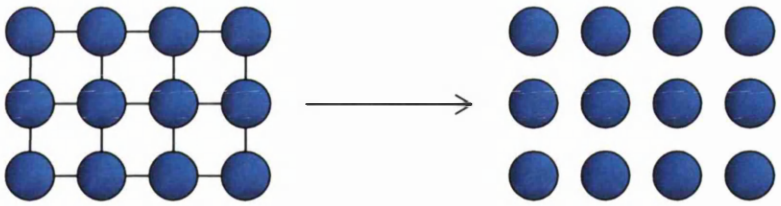

(a) Breakdown of atomic bonds in parent phase

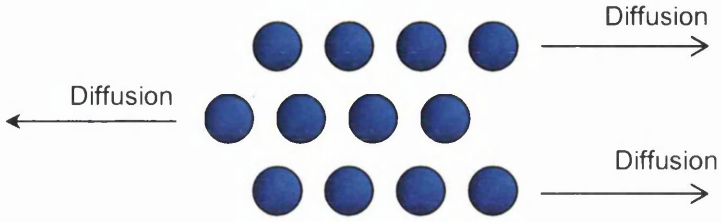


(b) Diffusion of atoms into new positions

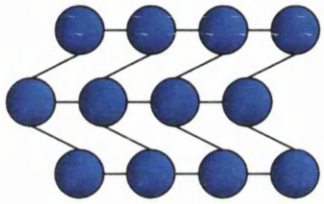

(c) Reconstruction of atomic bonds in product phase

Figure 2.9: Reconstructive transformation (adapted from [54])

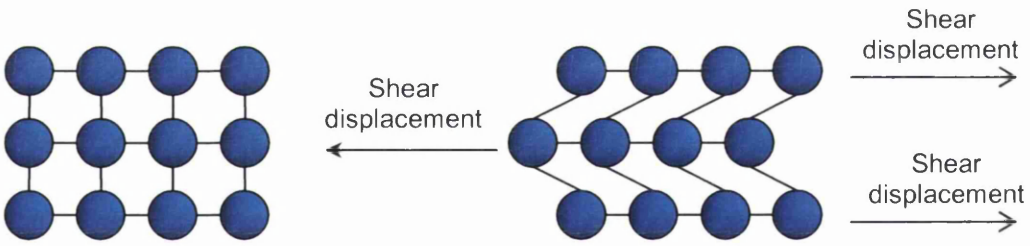


Figure 2.10: Displacive transformation (adapted from [54])

Reconstructive transformations can then be sub-divided into congruent and incongruent, giving rise to three broad categories of phase transformations [55]:

1) *Reconstructive-congruent:* defined by atomic diffusion, no change to either the chemical composition or number of phases between parent and product; and the formation of stable (equilibrium) phases.
2) *Reconstructive-incongruent:* defined by atomic diffusion, a change to the chemical composition and often the number of phases between parent and product; and the formation of stable (equilibrium) phases.
3) *Displacive:* defined by the absence of atomic diffusion, no change to either the chemical composition or number of phases between parent and product; and the formation of metastable (non-equilibrium) phases.

The reconstructive transformations and equilibrium phases attainable in iron-carbon alloys given different alloy composition and temperature combinations, are graphically represented by the iron-iron carbide metastable equilibrium phase diagram[15] (Figure 2.11) [11]. The equilibrium phase diagram is a plot of one variable condition against another variable condition (commonly chemical composition against temperature). The equilibrium phase diagram can be used to anticipate the microstructure in terms of phases present, their chemical compositions and their concentrations for a given combination of conditions. Moreover, the equilibrium phase diagram can be used to anticipate the adjustments that the system will make in response to a change to the combination of conditions, which may involve a phase transformation from one phase to another phase and/or the appearance or disappearance of a phase. However, it is important to recognise that equilibrium phase diagrams only provide such information under the circumstance that the equilibrium state is maintained.

[15] It may be noted that the term 'metastable equilibrium phase diagram' has been used rather than 'equilibrium phase diagram'. The reason for this is that iron carbide is not a true equilibrium/stable compound, but rather is a metastable compound that will exist indefinitely at ambient temperature, however will decompose permanently into the constituents iron and carbon (graphite) if maintained between 650-700 °C for many years. However, since decomposition is both extremely slow and in practice, unlikely given the temperature and time dependence, iron carbide can be considered stable for most practical purposes and thus, the metastable equilibrium phase diagram can be considered as a conventional equilibrium phase diagram.

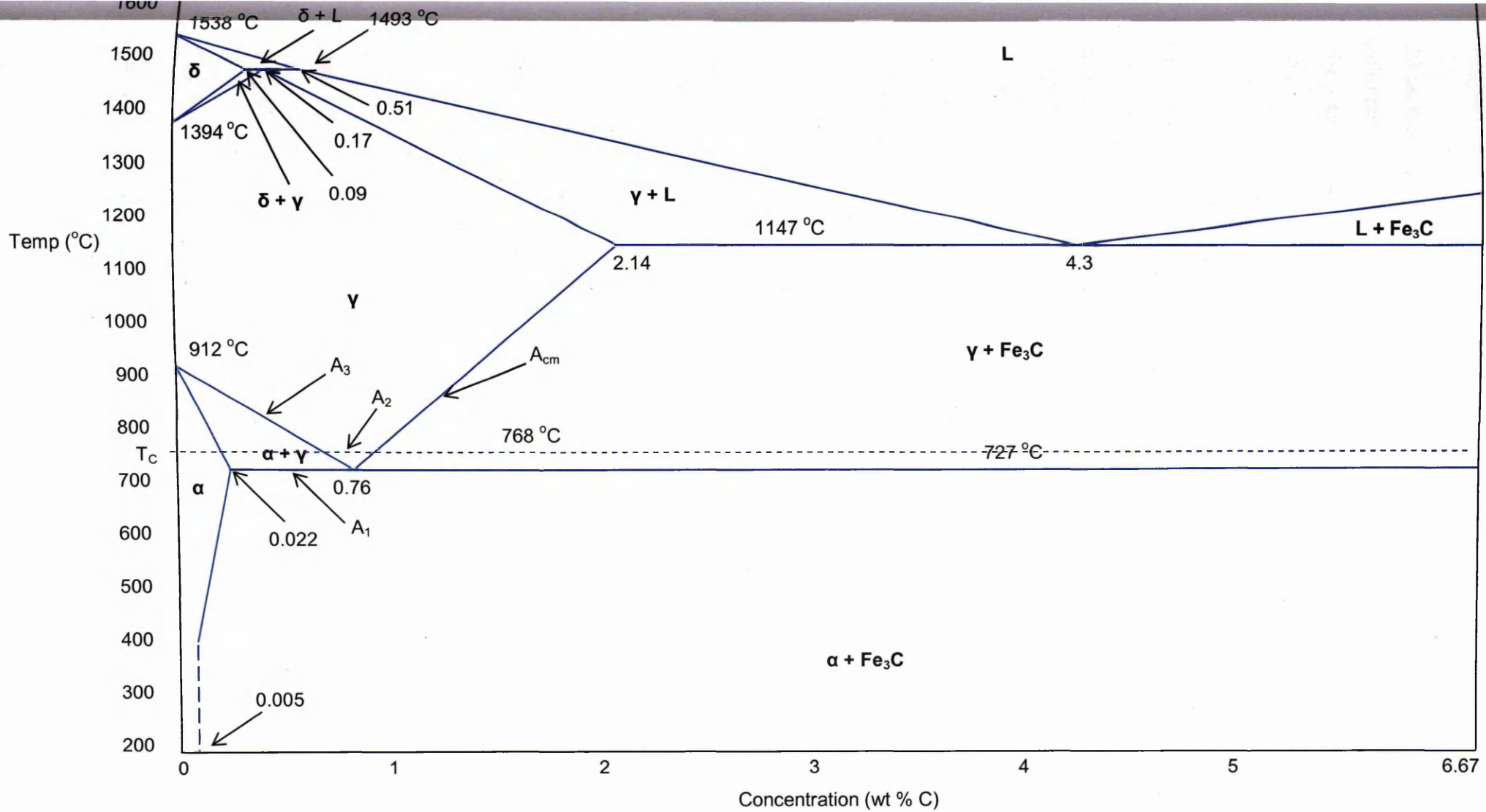


Figure 2.11: Iron-iron carbide metastable equilibrium phase diagram (adapted from [11])

The equilibrium and non-equilibrium phases and microconstituents that may form in 22MnB5 on cooling from an austenisation temperature shall now be explained. Note that many of the following principles apply to low, mild and medium carbon low alloy steels in general.

*Proeutectoid α-Ferrite*

The proeutectoid phase can be defined as the phase to form first during austenitic transformation on equilibrium cooling in hypoeutectoid or hypereutectoid steels[16] [54], before (pro) pearlite (eutectoid) or the metastable equivalent (bainite and/or martensite). In hypoeutectoid steels, the proeutectoid phase is α-ferrite[17] [54] and formation is initiated on cooling through the $Ae_3$ (~ 800 °C) or $Ar_3$ temperature [54].

Proeutectoid α-ferrite precipitates from the γ-austenite[18] [54] phase and moreover, generally from γ-austenite grain boundaries since these represent areas of high free energy and thus, are favourable transformation sites as the system seeks to lower free energy [55].

Proeutectoid α-ferrite formation is generally considered to be of the reconstructive-incongruent type [55], involving diffusional nucleation and growth processes and resulting in an alteration to chemical composition between parent (γ-austenite) and product (proeutectoid α-ferrite) phases.

Due to the diffusion dependence, proeutectoid α-ferrite formation is only possible on the condition that the cooling rate through the $Ae/r_3$ temperature is limited, so

---

[16] Eutectoid steels: 0.76 wt % C (there is no proeutectoid phase). Hypoeutectoid steels: < 0.76 wt % C (the proeutectoid phase is α-ferrite). Hypereutectoid steels: > 0.76 wt % C (the proeutectoid phase is cementite). Note these values apply to plain carbon steels only, which essentially contain just iron and carbon, with only minor concentrations of other elements. The introduction of alloying elements can change the 'eutectoid point'.

[17] α-ferrite is an interstitial solid solution of carbon (solute) in the body centred cubic (BCC) allotropic phase of α-iron (solvent).

[18] γ-austenite is an interstitial solid solution of carbon (solute) in the face centred cubic (FCC) allotropic phase of γ-iron (solvent).

that in turn, sufficient time is permitted at each temperature decrement for the necessary atomic rearrangement and maintenance (or approach) of the equilibrium state [55].

Proeutectoid α-ferrite may precipitate with a variety of forms[19] [55], distinguished primarily by morphology, in addition to the location of nucleation and/or growth in the γ-austenite phase, crystallographic orientation relationship with respect to the γ-austenite phase and kinetics (transformation rate as a function of time) [55].

The forms of proeutectoid α-ferrite include the following [55]:

- *Allotriomorphic inter-granular:* crystals that nucleate directly from the γ-austenite grain boundary and grow preferentially and smoothly along this grain boundary, giving rise to a morphology that reflects the γ-austenite grain boundary contours (Figure 2.12a).
- *Widmanstätten:* crystals that nucleate and/or grow with a needle-like cross-sectional morphology:
    - *Primary Widmanstätten inter-granular:* nucleate and grow directly from the γ-austenite grain boundary (Figure 2.12b).
    - *Secondary Widmanstätten inter-granular:* grow from another form of the same phase (usually allotriomorphic inter-granular), with the latter located on the γ-austenite grain boundary (Figure 2.12c).
    - *Widmanstätten intra-granular:* nucleate and grow in the γ-austenite grain interior (Figure 2.12d).
- *Idiomorphic:* crystals that nucleate and grow uniaxially, forming equiaxed morphologies:
    - *Idiomorphic intra-granular:* nucleate and grow in the γ-austenite grain interior (Figure 2.12e).
    - *Idiomorphic inter-granular:* nucleate and grow directly from the γ-austenite grain boundary (Figure 2.12f).

[19] The various forms of proeutectoid α-ferrite were first recognised by C A Dubé, giving rise to the 'Dubé morphological classification scheme'.

- *Massive:* may be considered a secondary form that results from impingement by crystals of the above forms during growth; thus is a polycrystalline, essentially equiaxed mass located randomly in the γ-austenite grain (Figure 2.12g).

The form of proeutectoid α-ferrite that results is primarily a function of chemical composition and formation temperature (supercooling) [55]. For conditions of continuous cooling, the cooling rate is also influential [55]. For as-delivered 22MnB5, allotriomorphic inter-granular is dominant [15].

Figure 2.13 [55] demonstrates approximate chemical composition-temperature ranges (in terms of the iron-iron carbide metastable equilibrium phase diagram) in which select forms of proeutectoid α-ferrite are dominant after near complete γ-austenite transformation under isothermal conditions: (a) assumes a coarser γ-austenite grain size; while (b) assumes a finer γ-austenite grain size.

(a) Allotriomorphic inter-granular

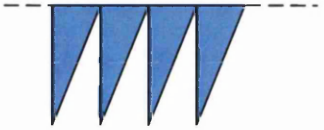

(b) Primary Widmanstätten inter-granular

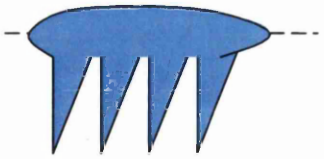

(c) Secondary Widmanstätten inter-granular

(d) Widmanstätten intra-granular

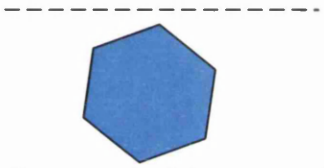

(e) Idiomorphic intra-granular

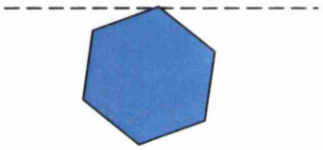

(f) Idiomorphic inter-granular

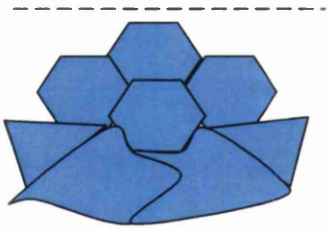

(g) Massive

Figure 2.12: Dubé morphological classification scheme (adapted from [55])

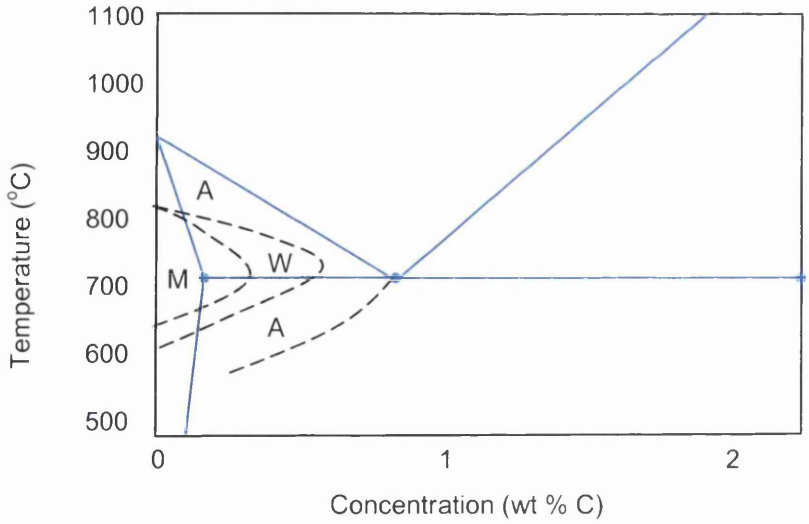


(a) Coarser γ-austenite grain size (ASTM G: 0-1)

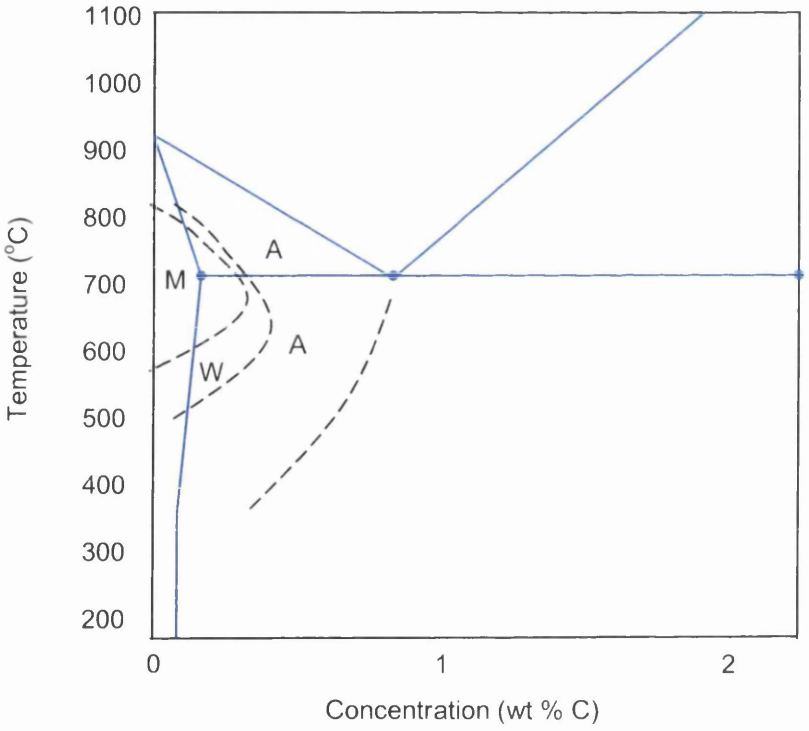


(b) Finer γ-austenite grain size (ASTM G: 7-8)

Figure 2.13: Approximate chemical composition-temperature ranges in which select forms of proeutectoid α-ferrite are dominant at late γ-austenite transformation times (A = allotriomorphic. W = Widmanstätten (mixed variants). M = massive) (adapted from [55])

*Pearlite*

The γ-austenite > pearlite[20] [54] transformation is the eutectoid transformation and corresponds to the $Ae_1$ (~ 720 °C) or $Ar_1$ temperature [54].

As is generally the case for proeutectoid α-ferrite, pearlite formation is of the reconstructive-incongruent type and nucleation of pearlite is dominant on γ-austenite grain boundaries [55].

The pearlite microconstituent consists of alternating lamellae of the (eutectoid) α-ferrite and (eutectoid) cementite[21] [54] phases with an approximate lamellae thickness ratio of 8:1 [54], as depicted by the schematic micrograph of Figure 2.14a [11].

During the γ-austenite > pearlite transformation, a significant redistribution of carbon must take place between the product phases (α-ferrite and cementite) constituting the product microconstituent, pearlite. This is since the equilibrium carbon concentration of parent and product phases is distinctly different. The equilibrium carbon concentration of the γ-austenite parent phase at the point of transformation is ~ 0.76 wt %, while the equilibrium carbon concentration of the α-ferrite product phase is much less at just ~ 0.022 wt % and the equilibrium carbon concentration of the cementite product phase is much more at 6.67 wt %. Thus, the carbon concentration of the α-ferrite product phase, inherited from the γ-austenite parent phase, is initially in excess of the α-ferrite equilibrium; while the carbon concentration of the cementite product phase, inherited from the γ-austenite parent phase, is initially below the cementite equilibrium. These non-equilibrium carbon concentrations of the product phases are corrected by carbon redistribution: as the two product phases simultaneously nucleate and grow into the γ-austenite grain interior, α-ferrite liberates excess carbon, which travels via

---

[20] Pearlite was discovered by H C Sorby in 1864 and initially named 'sorbite'. However, the 'mother of pearl' appearance under microscopy made the name 'pearlite' more popular.

[21] Cementite (sometimes termed 'θ-carbide') is an orthorhombic structured inter-metallic compound with the distinct chemical composition 93.33 wt % Fe-6.67 wt % C, which can be expressed by the chemical formula $Fe_3C$.

diffusion immediately ahead of the transformation front to the cementite phase, where this excess carbon is absorbed. Carbon diffusion distance from α-ferrite to cementite is then minimised by the two phases forming in the alternating lamellae arrangement [11].

On the condition that cooling through the $Ae_1$ temperature is extremely slow in order for the equilibrium state to be continually maintained, the pearlite that results can be considered as 'equilibrium' pearlite, which has a particular lamellae thickness. However, with supercooling through the $Ae_1$ temperature to an $Ar_1$ temperature, the lamellae thickness decreases from that of equilibrium pearlite. At transformation ($Ar_1$) temperatures closer to the $Ae_1$ (~ 720-650 °C) [55] the pearlite is termed 'coarse' pearlite (Figure 2.14b) [11]. At transformation ($Ar_1$) temperatures further from the $Ae_1$ (~ 650-600 °C) [55] the pearlite is termed 'fine' pearlite (Figure 2.14c) [11].

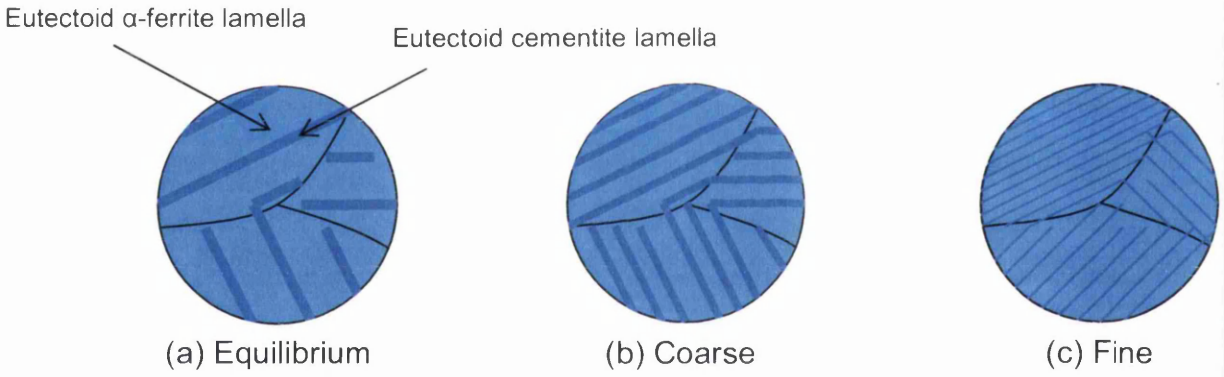


Figure 2.14: Schematic of pearlite (adapted from [11])

Decreasing lamellae thickness with decreasing transformation temperature relates to nucleation and growth rates (Figure 2.15) [11]. In the temperature range of ~ 720-650 °C, the growth rate of the α-ferrite and cementite nuclei exceeds the nucleation rate [55]. The differential between growth rate and nucleation rate decreases with decreasing transformation temperature, so that at ~ 650 °C the growth rate and nucleation rate equate to each other [55]. With decreasing transformation temperature below ~ 650 °C, the nucleation rate exceeds the

growth rate [55]. This phenomenon relates to 'activation free energy of nucleation' and 'activation free energy of long range atomic diffusion' parameters [11].

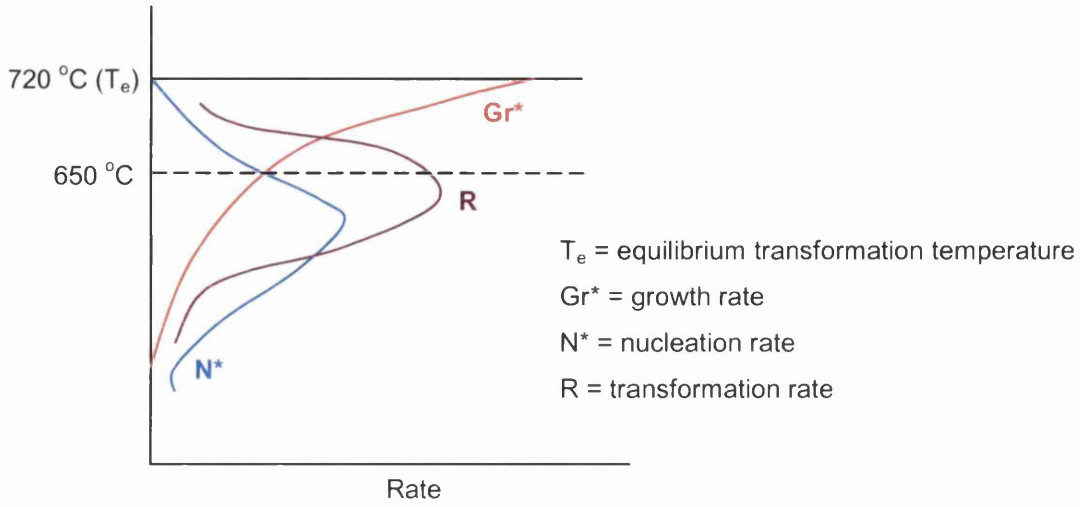


Figure 2.15: Rate-temperature of reconstructive transformation (adapted from [11])

*Bainite*

With greater supercooling through the $Ae_1$-$Ar_1$ range to the Bs temperature (~ 575 °C) [55], the nature of the γ-austenite transformation changes significantly. Instead of pearlite formation, the microconstituent termed 'bainite'[22] [56] forms.

Bainite formation is of the semi-reconstructive-incongruent and semi-displacive type, involving both diffusional and diffusionless nucleation and growth processes and resulting in different and equal chemical compositions between parent and product phases [55]. Accordingly, bainite may be termed a 'paraequilibrium' microconstituent [54] between pearlite (considered as equilibrium) and martensite (considered as non-equilibrium).

The phase has been defined as a homogenous portion of a system with uniform physical and chemical characteristics. Thus, during a phase transformation, an alteration must take place to the crystal structure and/or the chemical composition between parent and product phases. Such alterations occur via atomic

[22] Bainite was discovered by E S Davenport and E C Bain in the 1920s. Initially, the microconstituent was named 'troostite' before it was renamed 'bainite'.

movement, which in turn can be achieved via two processes: 1) atomic diffusion; or 2) atomic displacement.

The process of atomic diffusion gives rise to what has been termed a 'reconstructive' phase transformation, which can be envisaged as the breaking of atomic bonds in the parent phase and the rearrangement of those atoms, which may involve: 1) an alteration to the atomic arrangement in order to conform to the alteration to crystallinity; and/or 2) a redistribution of atomic species between two product phases in order to conform to the alteration to chemical composition. These alterations are then followed by the formation of new atomic bonds so to complete the product phase. In this fashion, atomic movement can be considered as 'voluntary' [54], with the driving force for such voluntary atomic movement (diffusion) being maintenance of the equilibrium (lowest free energy) state.

The process of atomic displacement gives rise to what has been termed a 'displacive' phase transformation, which can be envisaged as a uniform deformation of the parent phase, in which atoms are displaced via shear force from that atomic arrangement (crystal structure) of the parent phase, into that atomic arrangement of the product phase. In this fashion, atomic movement can be considered as 'involuntary' [54]. Moreover, a chemical correspondence exists between parent and product phases.

When the specimen is not geometrically constrained at the macroscopic level, the crystallographic deformation alters the macroscopic shape of the specimen: there is a macroscopic shape deformation [54]. When the specimen is geometrically constrained, the macroscopic shape deformation is accommodated by elastic and plastic strains in the microstructure [54]. The accumulation of such strains increases the system's free energy. Consequently, the system attempts to minimise the accumulation of strain and in turn, free energy, by the product phase(s) forming with thin needle-like or plate-like morphologies [56].

*Lath and lenticular bainite*

Bainite features an aggregate arrangement of thin α-ferrite crystals and elongated cementite crystals [56]. The α-ferrite crystals are either in the form of long and narrow needles termed 'laths' (equivalent to Widmanstätten proeutectoid α-ferrite) which are approximately 10 μm long and 0.2 μm wide, or in the form of very thin but wider plates termed 'lenses' [56].

The α-ferrite crystals form the bulk of the microconstituent and group together, connected in three-dimensions, into wedge-shaped units termed 'sheaves' [56]. Each sheaf generally grows from the γ-austenite grain boundary, with the tip of the wedge culminating in the γ-austenite grain interior. Within a sheaf, α-ferrite crystals grow in a parallel fashion (end-to-end or side-by-side) with identical crystallographic orientations. This occurs since each consecutive α-ferrite crystal nucleates from the tip or edge of the previous α-ferrite crystal. Thus, a sheaf may be considered a bainitic unit containing a given number of connected α-ferrite sub-units and a dispersion of cementite sub-units.

Bainite featuring α-ferrite crystals in the form of laths is termed 'lath' bainite, while bainite featuring α-ferrite crystals in the form of lenses is termed 'lenticular' bainite [56]. The bainite that forms during the γ-austenite transformation is dependent on several factors, including [56]: 1) temperature (supercooling); 2) carbon concentration; and 3) yield strength of the γ-austenite phase. Generally, lath bainite forms preferentially at higher temperatures (~ 575-500 $^{o}$C) while lenticular bainite forms preferentially at lower temperatures (~ 500-410 $^{o}$C). Lower carbon concentration and/or a γ-austenite phase exhibiting lower yield strength also favour lath bainite formation [56].

*Upper and lower bainite*

In addition to the lath-lenticular division of bainite, there has been considerable effort to simplify the various forms of bainite. The prevailing simplifying division is into the forms termed 'upper' bainite and 'lower' bainite [56].

Upper bainite is associated with a formation temperature in accordance with that in which the lath morphology is preferential, while lower bainite is associated with a formation temperature in accordance with that in which the lenticular morphology is preferential [56]. Thus, upper bainite is generally characterised by α-ferrite laths, while lower bainite is generally characterised by α-ferrite lenses (although this is not mandatory).

The defining distinction between upper and lower bainite is the presence of additional and extremely fine carbide crystals termed 'blades' that are present inside the α-ferrite crystals for lower bainite, but not for upper bainite [56]. The carbide blades of lower bainite are not necessarily cementite, but more commonly transition carbide precursors to cementite, such as ε-carbide ($Fe_{2.4}C$) and are orientated at an angle of ~ 60 ° to the α-ferrite crystal longitudinal axis [56].

Thus, upper bainite is definitively characterised by homogenous α-ferrite crystals (generally in the form of laths), connected in three-dimensions and contained within a sheaf, together with a dispersion of elongated cementite crystals. In contrast, lower bainite is definitively characterised by heterogeneous α-ferrite crystals (generally in the form of lenses), containing a fine dispersion of carbide blades (at ~ 60 ° to the α-ferrite crystal longitudinal axis), with the α-ferrite crystals connected in three-dimensions, all contained within a sheaf, together with a dispersion of elongated cementite crystals.

Figures 2.16a and 2.16b respectively depict schematic three-dimensional representations of the morphologies of upper bainite (featuring α-ferrite laths) and lower bainite (featuring α-ferrite lenses).

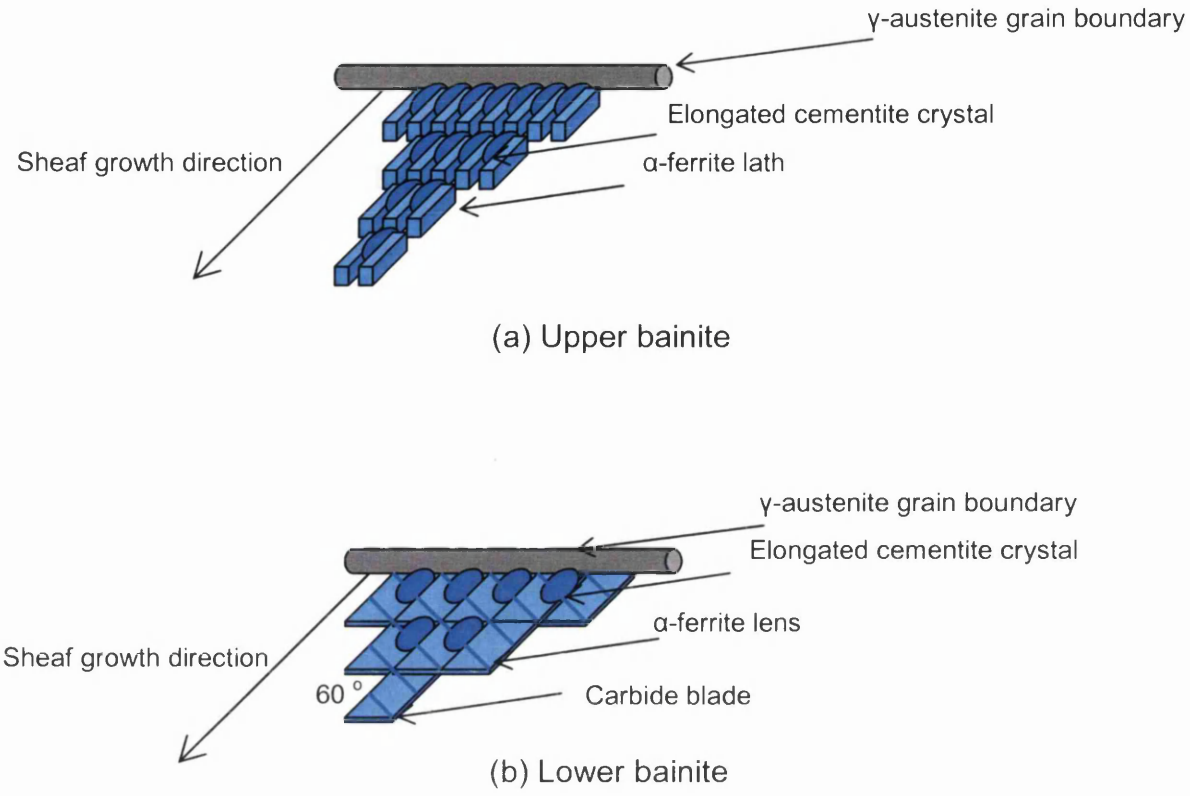


Figure 2.16: Schematic of bainite (adapted from [56])

In common with pearlite formation, with decreasing formation temperature through the bainitic range, the microstructure becomes finer; that is, α-ferrite and cementite crystals become smaller [11]. This is since the temperature range in which the γ-austenite > bainite transformation occurs is in the region in which decreasing temperature (greater supercooling) results in increasing nucleation rate and decreasing growth rate. For this reason combined with the additional carbide blades, lower bainite (associated with lower formation temperature) can be expected to be stronger and tougher than upper bainite, owing to a microstructural refinement mode [56].

*Bainite formation*

The γ-austenite > bainite transformation can be broken down into two stages for upper bainite and three stages for lower bainite [56]:

1) The displacive first stage that is consistent between both upper and lower bainite.
2) The reconstructive second stage that is consistent between both upper and lower bainite.
3) The reconstructive third stage that is unique to lower bainite.

The first stage is believed to involve the formation of a carbon supersaturated α-ferrite plate which can be considered as a Widmanstätten α-ferrite crystal much like that which may form for proeutectoid α-ferrite [56]. The carbon supersaturated α-ferrite plate is then surrounded by the γ-austenite matrix. This γ-austenite > carbon supersaturated α-ferrite plate transformation is displacive involving the cooperative movement via a shear displacement of atoms from the FCC structured γ-austenite to the BCC structured α-ferrite. The displacive transformation occurs in this fashion since the carbon concentration of the γ-austenite parent phase (~ 0.76 wt % C) is in excess of the equilibrium carbon solubility limit of the α-ferrite product phase (~ 0.022 wt % C) and the rate of temperature change through and below the equilibrium transformation ($Ae_1$) temperature is too rapid to enable the necessary atomic diffusion and adjustment of carbon concentration between phases so to precipitate cementite and conform to the carbon solubility limit of α-ferrite. Effectively, the α-ferrite is forced to accommodate a concentration of carbon that is in excess of its equilibrium solubility limit.

Since the BCC α-ferrite is less dense than the FCC γ-austenite (atomic packing factors 68 and 74 % respectively), there is a volumetric expansion (dilatation) and accordingly, growth of each carbon supersaturate α-ferrite plate is accompanied by a change to the geometry of the transformed region [56]. Large strains associated with the shape change cannot be sustained by the surrounding γ-austenite matrix. Thus, localised plastic deformation escalates and eventually halts growth of the carbon supersaturated α-ferrite plate so that it achieves a

limited size and explains why each plate is of equal geometry and moreover, why each bainitic sheaf culminates in the γ-austenite grain interior rather than continuing to the γ-austenite grain boundary.

The plate-like geometry leading to very fine lath and lenticular bainitic morphologies is the result of a minimisation of strain energy (as explained previously). Further, there exists a special crystallographic orientation relationship between a given carbon supersaturated α-ferrite plate and the surrounding γ-austenite matrix; that is, of the Kurdjumov-Sachs character, in which the close packed planes of each crystal align in parallel, together with a corresponding pair of close packed directions [56]. The Kurdjumov-Sachs crystallographic orientation relationship can be expressed as $\{111\}_\gamma$ / $\{110\}_\alpha$ and $<110>_\gamma$ / $<111>_\alpha$. This is illustrated for one set of planes and directions from each family of equivalents by Figure 2.17.

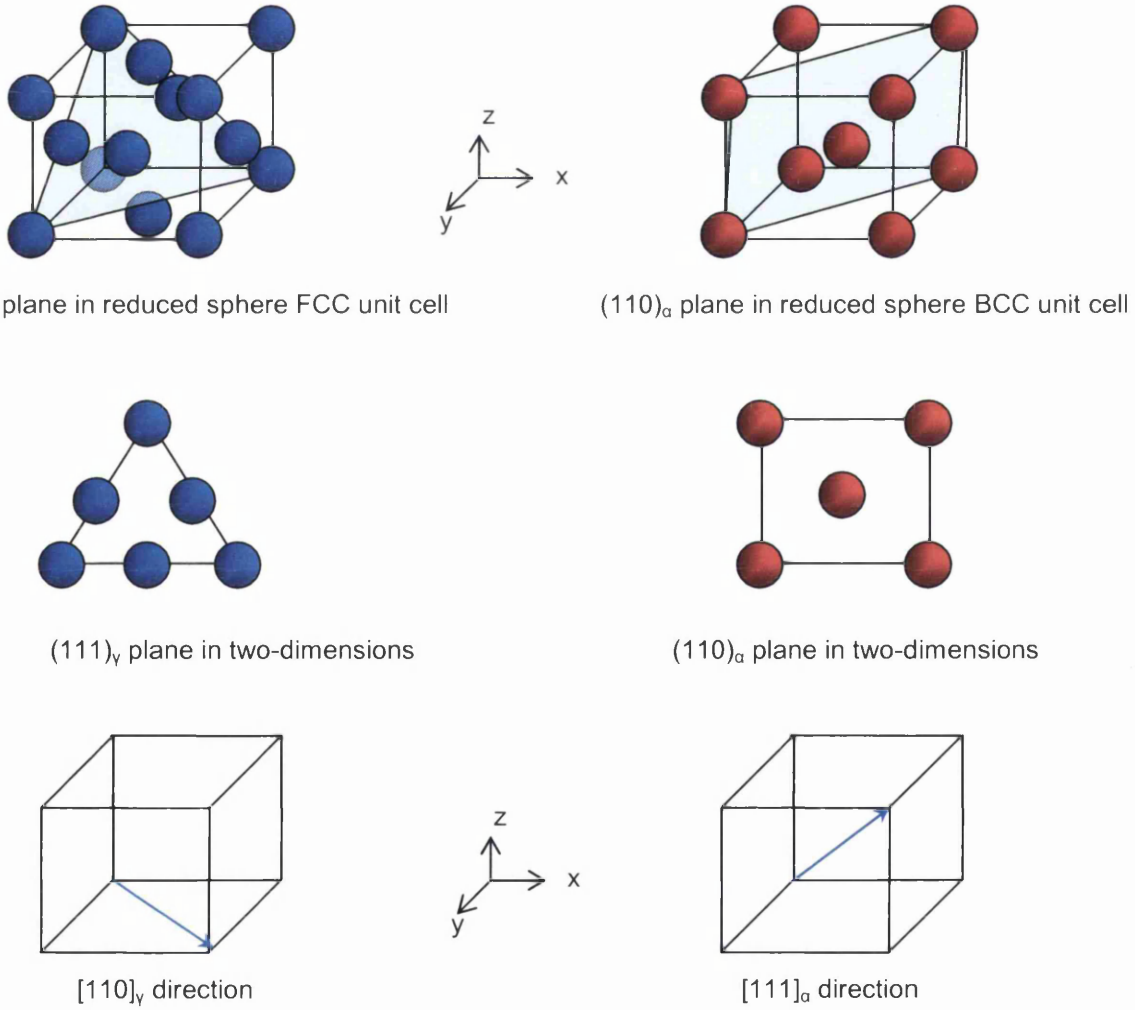


$(111)_\gamma$ plane in reduced sphere FCC unit cell

$(110)_\alpha$ plane in reduced sphere BCC unit cell

$(111)_\gamma$ plane in two-dimensions

$(110)_\alpha$ plane in two-dimensions

$[110]_\gamma$ direction

$[111]_\alpha$ direction

Figure 2.17: Kurdjumov-Sachs crystallographic orientation relationship

Thus, the first stage of bainite formation can be considered displacive; expressed as: γ-austenite > carbon supersaturated α-ferrite; and is schematically illustrated by Figure 2.18a [56].

The beginning of the second stage involves carbon diffusion from the carbon supersaturated α-ferrite plate, across the γ-austenite-α-ferrite phase boundary; and into the γ-austenite matrix immediately surrounding the carbon supersaturated α-ferrite plate [56]. In this region of the γ-austenite matrix, the carbon concentration clearly increases which initiates cementite precipitation in the manner of very fine elongated crystals that assume positions in between the α-ferrite plates. For high carbon steels, prolific cementite precipitation can give rise to continuous cementite layers surrounding isolated α-ferrite plates [56].

In the process of carbon diffusion, carbon is said to 'partition' from the carbon supersaturated α-ferrite plate to the γ-austenite matrix [56]. The partitioning phenomenon reflects the interstitial solute's affinity to migrate through a crystal where the substitutional atoms (including iron) are immobile.

The second stage of bainite formation can be considered semi-reconstructive-incongruent; can be expressed as: γ-austenite > cementite; and is schematically illustrated by Figure 2.18b [56].

In the case of upper bainite formation, the entirety of the excess carbon in the carbon supersaturated α-ferrite plate partitions to the γ-austenite matrix, which then transforms to cementite. This gives rise to an aggregate arrangement of α-ferrite plates with the equilibrium carbon concentration; and elongated cementite crystals, as demonstrated by Figure 2.18c [56].

In the case of lower bainite formation, there exists a third stage in which extremely fine carbide blades precipitate within the carbon supersaturated α-ferrite plate before the entirety of the excess carbon has partitioned into the γ-austenite matrix [56]. In other words, a portion of the excess carbon is relieved from the carbon supersaturated α-ferrite plate through carbon partitioning to the γ-austenite matrix

which then initiates cementite precipitation, while the remaining portion of excess carbon is relived from the carbon supersaturated α-ferrite plate through carbide precipitation within the plate itself.

The third stage of lower bainite formation involving carbide precipitation (considered as cementite for simplicity) within the carbon supersaturated α-ferrite plate can be considered reconstructive-incongruent; can be expressed as: carbon supersaturated α-ferrite > α-ferrite + cementite; and is schematically illustrated by Figure 2.18d [56].

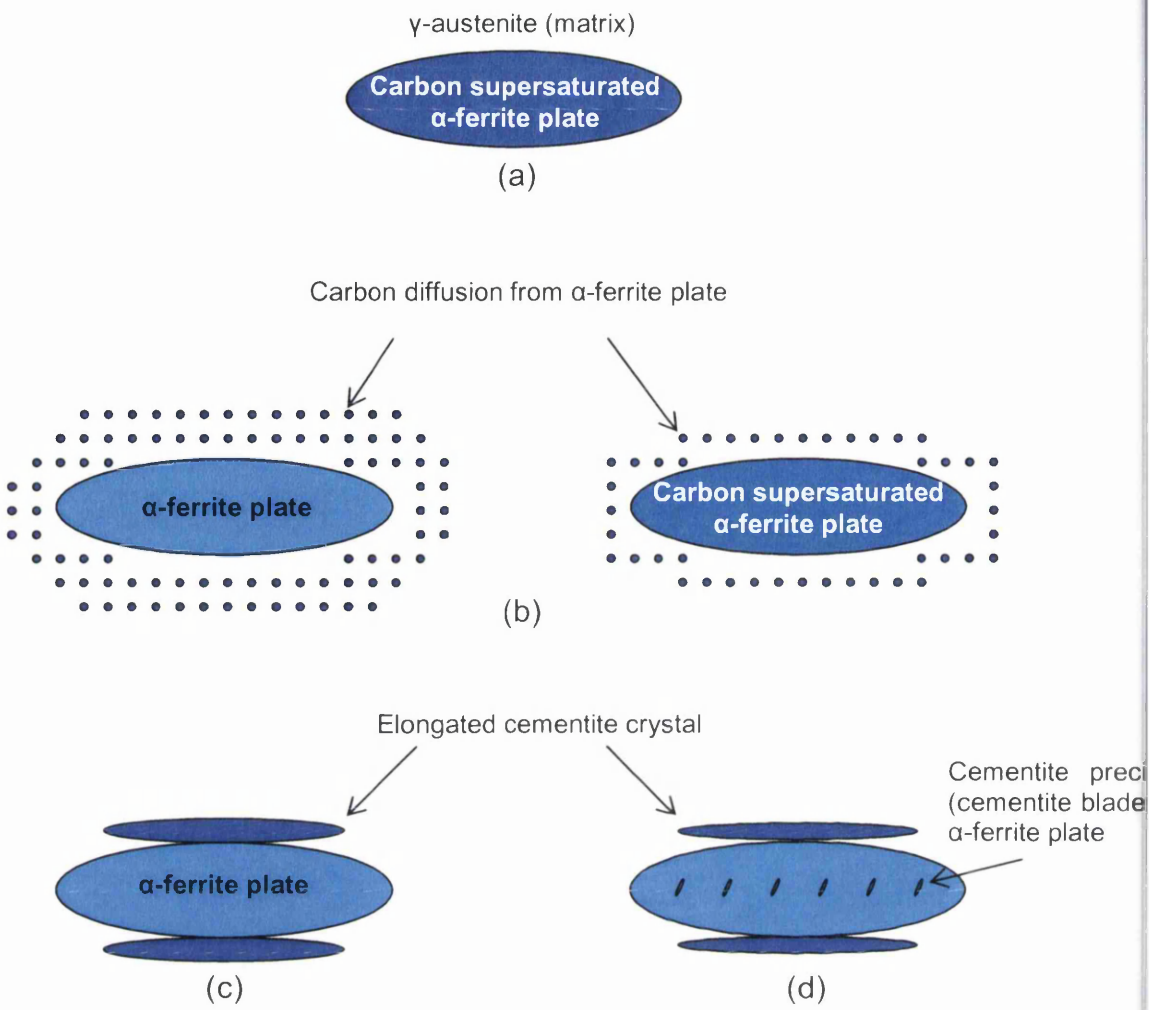


Figure 2.18: Bainite formation (adapted from [56])

The partitioning and intra-α-ferrite precipitation of carbides, are considered to be competitive processes. If the entirety of the excess carbon within the carbon supersaturated α-ferrite plate partitions out of the α-ferrite plate and into the retained γ-austenite matrix rapidly enough; that is, before carbide precipitation within the α-ferrite plate takes place, upper bainite characterised by homogenous α-ferrite crystals will result. Alternatively, if the carbon diffusion rate is not rapid enough, carbide precipitation will commence within the α-ferrite plate giving rise to lower bainite, characterised by α-ferrite crystals containing a dispersion of precipitated carbide blades.

Due to the influence of temperature on atomic diffusion rates, this parameter is highly influential on the upper bainite-lower bainite transition. At higher

transformation temperatures, atomic diffusion rates are greater; thus upper bainite characterised by complete diffusion of excess carbon from the carbon supersaturated α-ferrite plate to the γ-austenite matrix is preferential [56]. Conversely, at lower transformation temperatures, atomic diffusion rates are lower; thus lower bainite characterised by incomplete diffusion of excess carbon from the carbon supersaturated α-ferrite plate to the γ-austenite matrix, resulting in precipitation of carbide blades within the α-ferrite plate is preferential [56].

Carbon concentration is also believed to contribute an influence, with higher carbon concentration favouring lower bainite formation and lower carbon concentration favouring upper bainite formation [57]. It has been demonstrated [57] that upper bainite formation is not possible in highly pure iron-carbon alloys with a carbon concentration of more than ~ 0.4 wt %. The explanation for this preferential formation of upper bainite with lower carbon concentration and lower bainite with higher carbon concentration can be hypothesised to be a greater requirement for rapid carbon diffusion as carbon concentration is increased. In other words, with a greater carbon concentration, the degree of carbon supersaturation of a given α-ferrite plate is likely to be greater, thus there is need for more carbon diffusion in a given time period to prevent the onset of carbide precipitation in the α-ferrite plate and lower bainite formation.

*Martensite*

With yet greater supercooling through the $Ae_1$-Bs range to the Ms temperature (~ 410 °C) [55], the nature of the γ-austenite transformation changes once more. Instead of pearlite or bainite formation, the phase and microconstituent termed 'martensite'[23] [58] forms.

---

[23] Martensite (α') was discovered by A Martens in the 1890s. Martensite is not exclusive to the iron-carbon system as to a certain extent it is just the displacive nature of formation that defines the phase. Such displacive phase formation has been observed in other systems.

Iron-carbon martensite is a supersaturated interstitial solid solution of carbon (solute) in the elongated body centred cubic (BCC) allotropic phase of α-iron (solvent), most commonly giving rise to a body centred tetragonal (BCT) crystal structure; although a hexagonal close packed (HCP) crystal structure is also possible.

There are several characteristics of the γ-austenite > martensite transformation [58]:

- The transformation is displacive. Thus, parent and product phases are chemically equivalent and there exists a crystallographic correspondence.
- The transformation begins after considerable supercooling to the Ms temperature.
- Above a certain quench rate, Ms is generally constant for a given alloy irrespective of quench rate. Below that certain quench rate, Ms shares an inverse correlation with quench rate (greater quench rate equals lower Ms).
- Ms is affected by prior heat treatments.
- The volume fraction of martensite obtained is dependent only on the temperature supercooled to below Ms and is not dependent on time – with more supercooling below Ms, the fraction of martensite increases. The maximum volume fraction of martensite attainable (theoretically 100 vol. %) is achieved when the quench temperature is to or below Mf. The transformation is thus time independent and solely a function of the temperature supercooled to.
- Ms varies with γ-austenite grain size; vacancy, impurity, precipitate and dislocation concentrations; but most notably with chemical composition. Increased γ-austenite grain size generally raises Ms, while alloy additions usually depress Ms. However, interactions between substitutional solutes can change the effect of a given element alone on Ms. For example, Si-Mo interactions strongly decrease Ms, while Si-Mn interactions strongly increase Ms (and with all three of these elements in isolation decreasing Ms).
- The transformation is usually athermal (it continues only on cooling) and the volume fraction of martensite formed is not linearly related to temperature depression between Ms and Mf.
- The transformation does not proceed to completion in all cases; that is, a certain volume fraction of retained γ-austenite will occur even with maximum supercooling to the theoretical Mf.

- Martensite growth is generally extremely rapid with the γ-austenite-martensite phase boundary exhibiting a velocity in the order of $10^6$ $mm/s^{-1}$ and approaching the speed of sound through the parent phase.
- The transformation may be induced at temperatures above Ms by mechanical deformation (strain) up to a limiting temperature Md. However, deformation at temperatures above Md can have the opposite effect via mechanical stabilisation of γ-austenite, inhibiting subsequent transformation to martensite when quenching to Ms is initiated.
- Thermal stabilisation occurs when the alloy is slowly cooled between Ms and Mf or held for a given time at a temperature between Ms and Mf. In these cases, further rapid cooling does not yield immediate transformation to martensite. In other words, a critical degree of consistent supercooling is necessary.
- The transformation is usually reversible with a temperature hysteresis (the temperature at which the martensite > γ-austenite transformation occurs on heating depends on the previous γ-austenite > martensite transformation temperature). For plain carbon and low alloy steels, the reverse transformation temperature (As) lays in a region where diffusion of carbon becomes appreciable. Consequently, decomposition of martensite to α-ferrite and cementite occurs before γ-austenite can reform.
- Martensite occurs by a process of shear atomic displacement which forms crystals with needle-like (lath) or plate-like morphologies and are coherent with the γ-austenite parent phase. Needle-like morphologies (laths) become more prominent as the transformation temperature falls.
- Crystal shear and volume changes between parent and product phases produce microstructural distortions.
- As parent and product phases are coherent, the coherent phase boundary must be restricted to certain crystallographic planes which give a good fit between atoms in each crystal. There are two crystallographic data of interest: 1) the habit plane (the plane of the γ-austenite parent phase that lays parallel to the phase boundary (if planar)); and 2) the relationship between the planes & directions of the martensite product phase; and the parallel planes & directions of the γ-austenite parent phase. This

crystallographic relationship allows for the crystal shear and furthermore, gives rise to the coordinated movement of atoms that results in individual atoms moving only small inter-atomic distances while producing large macroscopic strains.

*Martensite formation*

The definitive characteristic of the displacive γ-austenite > martensite transformation is a crystallographic correspondence between the parent and product phases since atoms move in a highly coordinated fashion without any reordering or great movement relative to other atoms [58]. In consequence, the precise atomic order in the parent phase is translated into the product phase. This can be illustrated by Figure 2.19 which presents a hypothetical parent crystal (in two-dimensions) containing a precise atomic order; and a hypothetical product crystal (following the displacive transformation) which contains that same precise atomic order. The correspondence between the two crystals means that crystallographic directions and planes with particular atomic order in the parent phase are translated into crystallographic directions and planes with the same atomic order in the product phase. The displacive transformation may be regarded physically as a homogenous deformation of one crystal into the other.

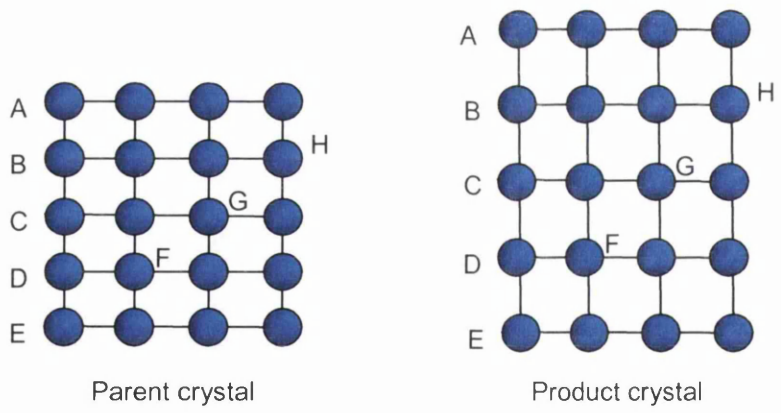


Figure 2.19: Crystallographic correspondence of homogenous deformation

Figure 2.20 [59] demonstrates how the FCC structured γ-austenite parent phase is homogenously deformed into the BCT structured martensite product phase. Essentially, deformation can be considered to consist of two adjacent FCC

structured γ-austenite unit cells (marked by the blue reduced spheres in the figure) that experience a compression of ~ 17 % along the $[001]_\gamma$ direction and with an expansion of ~ 12 % in all directions of the $(001)_\gamma$ plane. The BCT structured martensite unit cell (marked by the red reduced spheres in the figure) results and can be envisaged as an alternative representation of the two FCC structured γ-austenite unit cells. The crystallographic correspondence between the martensite and γ-austenite crystals is termed the 'Bain correspondence', while the associated homogenous deformation (strain) is termed the 'Bain strain' [59].

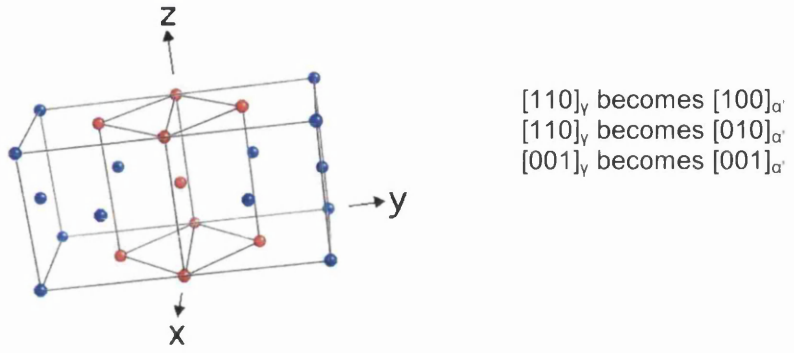


Figure 2.20: Bain correspondence between FCC structured γ-austenite and BCT structured martensite [59]

The BCT crystal structure can also be envisaged as a distorted BCC crystal structure – elongated along one axis due to carbon supersaturation. During the rapid quench, the FCC structured γ-austenite can be considered to attempt transformation to the BCC structured α-ferrite (such as in pearlite formation). However, due to the lack of time permitted for atomic diffusion, atoms experience a shear displacement and move cooperatively into their new positions characterised by the BCC structure, with little displacement of atoms relative to their neighbours (inter-atomic separation remains fairly constant). Further, there is no precipitation of a second phase (e.g. cementite such as in pearlite formation). Thus, martensite is supersaturated with carbon and is forced to occupy a greater carbon content than is theoretically possible for the BCC structure under equilibrium conditions. It is this supersaturation which then forces the BCC structure into a BCT structure.

*Lath and plate martensite*

There are two morphologies of iron-carbon martensite: lath and plate [58]. Lath martensite (also called 'massive' martensite), which is dominant in iron-carbon alloys with < 0.6 wt % C and exclusive with < 0.15 wt % C [31], is characterised by very narrow needle-like crystals termed 'laths' (similar in morphology to the α-ferrite laths of lath bainite) [58]. The laths contain a high dislocation density and are aligned side-by-side, parallel to each other; separated by low angle grain boundaries. The collection of parallel laths in this fashion is termed a 'block'. The collection of parallel blocks is termed a 'packet'. Numerous packets, with each packet containing blocks in different orientations compared to adjacent packets, are then separated by high angle grain boundaries, with each packet originating from an individual γ-austenite grain. Thus, a packet can be considered a martensitic 'primary unit' originating from the γ-austenite grain; a block can be considered a martensitic 'secondary unit'; and a lath can be considered a martensitic 'tertiary unit'. Figure 2.21a [11] provides a schematic micrograph of lath martensite.

Plate martensite is exclusive in iron-carbon alloys with $\geq$ 0.6 wt % C [31] and is characterised by randomly arranged thin, but long crystals termed 'plates' (similar in morphology to the α-ferrite lenses of lenticular bainite) [58]. Each martensitic plate is a complex arrangement of a crystallographically twinned region termed a 'midrib', a partially twinned region and an un-twinned region formed by dislocations. Figure 2.21b [11] provides a schematic micrograph of plate martensite.

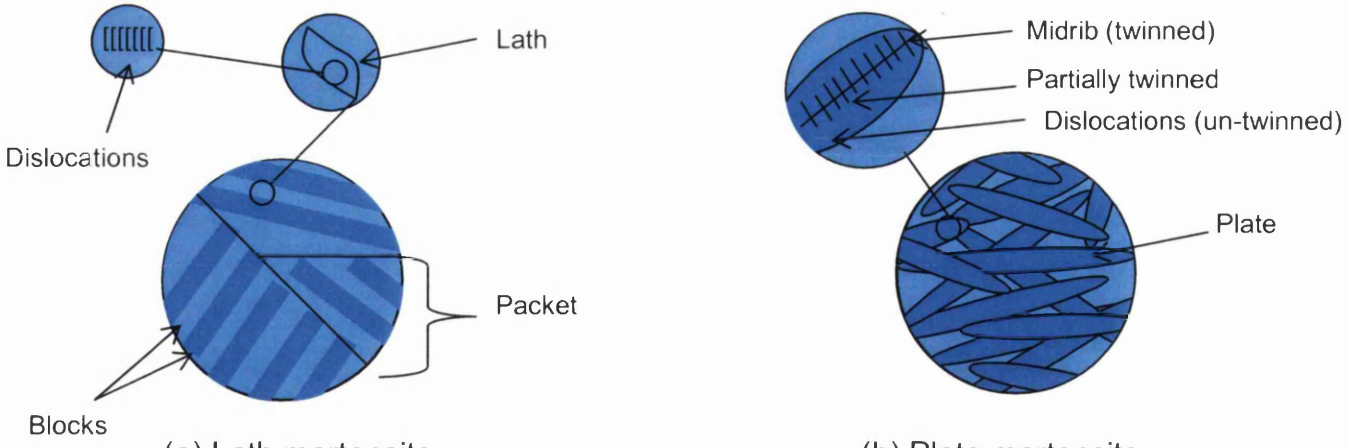


(a) Lath martensite (b) Plate martensite

Figure 2.21: Schematics of lath and plate martensite (adapted from [11])

*Strength*

Iron-carbon martensite is the strongest microconstituent known [58]. The exceptional strength is primarily attributed to the interstitial solute carbon, with nitrogen also playing a similar role (see section: Chemical Compositions).

There are several possible mechanisms by which the interstitial solutes carbon and nitrogen dramatically aid the strength of martensite [58]:

- *Interstitial solid solution strengthening:* interstitial solutes pin and/or block dislocations.
- *Microstructural refinement from solutes:* interstitial solutes segregate to and pin phase boundaries and martensitic boundaries (packet, block and lath boundaries in lath martensite and plate boundaries in plate martensite), which then inhibit dislocation movement.
- *Precipitation hardening:* inter-metallic compounds (carbides and nitrides) inhibit dislocation movement.
- *Microstructural refinement from precipitates:* precipitates segregate to and pin phase boundaries and martensitic boundaries, which then inhibit dislocation movement.

Other strengthening mechanisms in martensite include [58]:

- *Substitutional solid solution strengthening:* substitutional solutes pin and/or block dislocations.
- *Substructures in martensite:* the packet, block and lath morphology of lath martensite; and the twinned, partially twinned and un-twinned morphology of plate martensite, creates many boundaries which inhibit dislocation movement.
- *Work hardening:* the introduction of dislocations that inhibit the movement of other dislocations. Iron-carbon martensite exhibits a very high dislocation density in the order of $10^{11}$-$10^{12}$ $cm^{-2}$, which is similar to that of a very heavily worked hardened alloy.

*Microstructural Refinement*

It is common knowledge [11] that microstructural refinement (usually considered as grain size refinement) increases strength and impact toughness, but generally decreases ductility. Grain size can be extrapolated to the packet, block and lath morphology of lath martensite, which is dominant in quench hardened steels with < 0.6 wt % C (such as 22MnB5) and exclusive with < 0.15 wt % C [31]. Moreover, it has been reported that microstructural refinement of lath martensite increases strength without decreasing impact toughness [31]. Thus, an ultrafine lath martensite may be optimal. The microstructural size of lath martensite is proportional to the prior γ-austenite grain size, where a finer γ-austenite grain size results in a finer martensitic microstructure following quench hardening [56]. Thus, a fine γ-austenite grain size at the moment of quench hardening may be optimal.

It is possible to influence γ-austenite grain size through the proeutectoid α-ferrite and pearlite grain size in the as-delivered sheet (pre-hot stamping condition), since a finer proeutectoid α-ferrite-pearlite grain size results in a finer γ-austenite grain size. It is then possible to control the proeutectoid α-ferrite-pearlite grain size by the hot rolling, cold rolling (work hardening) and/or annealing parameters. However, it has been found [60] that these parameters bare little influence on the post-hot stamping condition. Rather, these parameters influence cold formability ahead of hot stamping. Thus, low tensile strength-high elongation should be

strived for in the as-delivered sheet, corresponding to a coarse, equiaxed and deformation-free proeutectoid α-ferrite-pearlite microstructure. This maximises cold formability ahead of hot stamping with little influence on the post-hot stamping condition. Conversely, it has been stated [61] that the cold rolled sheet that has not been annealed (and is thus severely work hardened), provides higher tensile strength post-hot stamping compared to the cold rolled and annealed sheet post-hot stamping, yet without elongation sacrifice.

Alloying elements (either dissolved in solid solution or bound in compounds) that pin γ-austenite grain boundaries during austenisation can maintain a fine austenitic grain size ahead of hot stamping and quench hardening. In other words, the proeutectoid α-ferrite-pearlite microstructure is austenised (transformation and recrystallisation resulting in fine γ-austenite grains) but with little austenitic grain growth. The fine γ-austenite then transforms into a fine lath martensite on quenching. However, this must be pursued with caution since a finer austenitic microstructure exhibiting more γ-austenite grain boundaries can reduce quench hardenability since grain boundaries provide potential nucleation sites for reconstructive phase transformations [62] [63] [64].

It has been stated [31] that a finer martensitic microstructure results with increased deformation rate and quench rate. These factors are considered further in sections: Hot Stamping and Quench Hardening, respectively.

With specific regard to DP steels, it has been stated [15] that a coarse and non-uniform ferritic-martensitic dual phase microstructure with poor tensile strength, elongation and impact toughness is obtained from controlled cooling (complete austenisation followed by cooling to a temperature between the $Ar_3$ and $Ar_1$ which is maintained to yield a volume fraction of proeutectoid α-ferrite, before quenching to below Mf). In contrast, a fine and uniform dual phase microstructure with improved tensile strength, elongation and impact toughness is obtained from inter-critical annealing (partial austenisation between the $Ac_1$ and $Ac_3$, followed by continuous quenching to below Mf). These concepts are discussed further in section: Dual Phase.

*Homogeneity*

Microstructural homogeneity is important so to avoid stress concentrations from localised defects such as inclusions, voids and dislocations. Stress concentrations reduce the theoretical tensile strength, elongation and impact toughness [11]. High temperatures during sheet forming & processing (hot rolling or annealing) and during blank austenisation ahead of hot stamping can lead to greater microstructural homogeneity, as the high temperature 'anneals out' the defects. However, excessive temperature can lead to decarburisation (in uncoated steel) and segregation of inclusions and thus, microstructural heterogeneity. Higher temperature also introduces added cost.

It is believed [15] that the forming mode of UHSS is mainly bending rather than pure and total elongation, because of limited total elongation, or simply because the formability of UHSS is governed by the local elongation (and then, local elongation can be evaluated by bendability). The relationship between bendability and microstructural homogeneity in UHSS has been investigated [34]. It was found that bendability is strongly dependent on microstructure homogeneity and not on total elongation. In other words, increased microstructural homogeneity increases bendability, which indicates increased local elongation and in turn, increased formability. In contrast, increased total elongation has random influences on bendability and thus formability. This can be attributed to microstructural homogeneity leading to fewer stress concentrations in which micro-cracks can nucleate and that deteriorate local elongation and bendability. This conclusion was established with what was defined as the 'homogeneity index'. The homogeneity index was obtained from 10 (Rockwell) hardness measurements, with each taken at one of five points separated by 2 mm intervals in both the rolling (0 $^{o}$) and transverse (90 $^{o}$) directions on sheet specimens (i.e. 5 points in the rolling direction and 5 points in the transverse direction). The standard deviation of the 10 hardness measurements then defined the homogeneity index. In conclusion, microstructural homogeneity results in significantly improved formability in UHSS.

***Chemical Compositions***

The common alloying elements and their functions in low alloy steels shall be reviewed.

*Carbon*

Carbon is the primary (interstitial solid solution) strengthening element in all steels and especially martensitic steels, where the strength of martensite is essentially governed by carbon content alone [58]. Increased carbon content up to ~ 0.85 wt % increases quench hardenability by delaying proeutectoid α-ferrite and bainite formation [39], with the maximum quench hardenability potential greater than for any other alloying element. Carbon provides post-quench tempering and precipitation hardening potential as carbon diffuses out of solid solution to form carbides.

With carbon content below the high range (< 0.6 wt %), martensite is predominantly of the lath character, with the remaining martensite of the plate character [31]. With carbon content in the low range (0.05-0.14 wt %), exclusive lath martensite results [31]. Lath martensite, characterised by 'packets' containing smaller 'blocks' and in turn yet smaller 'laths', exhibits a very fine microstructure consisting of many boundaries (packet boundaries, block boundaries and lath boundaries) which provide strength and impact toughness in a microstructural refinement mode [11]. Moreover, is has been stated [31] that microstructural refinement of lath martensite increases strength while not decreasing impact toughness.

During rapid quenching with < 0.2 wt % C, the majority of carbon (up to 90 %) segregates to dislocations and boundaries in the martensitic microstructure, where it remains in supersaturated solid solution and provides optimal strength [31]. With richer carbon contents and/or lower quench rates, precipitation of carbides (mainly cementite) during quenching (termed 'auto-tempering') becomes more probable, which compromises strength at the gain of elongation and impact toughness [31].

For the substitutional alloying elements dissolved in martensitic supersaturated solid solution to be of significance to martensitic hardness, two prerequisites [39] are necessary: 1) carbon content must be below ~ 0.35 wt %; and 2) a complete transformation to martensite must be achieved.

Carbon lowers the $Ac_3$ temperature [39] which can permit easier/faster and thus more economical austenisation; and lowers the Ms temperature while the $Ar_1$ temperature remains unchanged [39], which can provide a longer austenitic hot stamping window.

Carbon degrades coatability and weldability [39]. For automotive welding techniques to be practicable, low and mild carbon steels are dominant in automotive structural body components [1], with medium and especially high carbon steels seldom used.

*Manganese*

Under most circumstances, manganese is a non-carbide former[24] [39] and dissolves into solid solution.

In a concentration of up to ~ 1.5 wt %, manganese increases quench hardenability by inhibiting γ-austenite transformations, with the effect stronger for reconstructive transformations to proeutectoid α-ferrite and pearlite than for semi-displacive and displacive transformations to bainite and martensite [31]. This effect is non-linear with respect to manganese content – at higher manganese contents up to ~ 1.5 wt %, increasing content has a larger inhibiting effect on γ-austenite transformations and thereby, increasing manganese content up to ~ 1.5 wt % has an exponential effect of increasing quench hardenability [31].

Substitutional solid solution strengthening is an important feature of manganese addition. The loss of elongation for a given strength gain is less severe compared

[24] Although the term 'carbide former' is used, this term can be considered to also include 'nitride former', since those alloying elements that form carbides also exhibit a tendency to form nitrides. Thus, in this context (unless otherwise stated), 'carbide' and 'nitride' may be used interchangeably.

to interstitial solid solution strengthening by carbon [65]. Further, the strength increase from manganese addition is dependent on carbon content, with the strength increase from a given manganese addition raised by greater carbon presence [65].

Manganese aids surface finish, stabilises carbides which may increase strength in tempered or precipitation hardened steels, degrades weldability (but less so than carbon), is a deoxidising agent and readily forms manganese sulphides that reduce grain boundary embrittlement by removing sulphur from solid solution [65].

*Silicon*

In a concentration of 1-2 wt %, silicon is a non-carbide former and furthermore, inhibits nucleation and growth of carbides – this is termed a 'graphitising' effect [39]. Thus, silicon aids quench hardenability by inhibiting the transformation of γ-austenite to pearlite and bainite (but does not inhibit transformation to proeutectoid α-ferrite). For the graphitising behaviour, silicon is a standard addition to steels in which tempering is to be avoided for ultrahigh strength un-tempered martensite [39]; and is also an imperative addition to TRIP steels [1].

Silicon is a deoxidising agent, assists corrosion resistance, introduces substitutional solid solution strengthening and can aid grain growth [65] (austenitic grain growth increases quench hardenability).

The formation of manganese-silicon oxides can affect the surface chemistry and make hot dip galvanising impossible [66].

*Chromium*

Chromium is a carbide former [39]. Chromium carbides dissolve into γ-austenite solid solution slowly. Therefore, reasonably high austenisation temperatures and/or long austenisation times must be permitted in order to achieve hot formability and quench hardenability, as un-dissolved carbides can provide unwanted precipitation hardening and remove carbon and chromium from γ-

austenite solid solution, where both of these alloying elements increase quench hardenability when dissolved in γ-austenite solid solution [39].

Dissolved in γ-austenite solid solution, chromium can encourage grain growth and in turn, increase quench hardenability by inhibiting the beginning of proeutectoid α-ferrite and bainite formation [39]. Due to austenitic grain coarsening, decreased strength and increased elongation can result which increases hot formability. However, the austenitic grain coarsening can be transferred into the martensitic microstructure on quenching. Conversely, combined in carbide, chromium can restrict recrystallisation and austenitic grain coarsening so to achieve a fine martensitic microstructure on quenching [65]. Moreover, chromium carbides may maintain boron in solid solution (rather than boron carbide formation), thereby indirectly aiding quench hardenability by enhancing the boron quench hardenability effect. Manipulation of chromium's carbide forming affinity can thus present a diverse range of benefits.

*Molybdenum*

Molybdenum exhibits a stronger affinity for forming carbides than chromium [39]. Thus, high austenisation temperatures and/or long austenisation times may be necessary in order to dissolve molybdenum carbides into γ-austenite solid solution and thereby, achieve hot formability and quench hardenability. However, when dissolved in γ-austenite solid solution, molybdenum increases quench hardenability strongly (more so than chromium) by delaying proeutectoid α-ferrite and bainite formation [39].

Also when dissolved in γ-austenite solid solution, molybdenum increases the $Ar_3$ temperature and decreases the Bs temperature so to extend the $Ar_3$-Bs range, which increases the possibility of strain induced proeutectoid α-ferrite or granular bainite formation [67].

German steel and automotive component manufacturer Benteler has reported [68] that molybdenum addition to boron steel increases fatigue strength.

*Vanadium*

Vanadium exhibits a stronger affinity for forming carbides than chromium and molybdenum [39].

When dissolved in γ-austenite solid solution at ~ 0.5 wt %, vanadium inhibits the formation of proeutectoid α-ferrite and pearlite more so than the formation of bainite and increases quench hardenability very strongly – more so than chromium and molybdenum [39].

*Niobium*

Niobium is a potent carbide former (more so than chromium, molybdenum and vanadium) and forms stable carbides that can be dissolved in γ-austenite solid solution only at high temperatures, but remain at temperatures just above the $Ac_3$ [31]. Thus, high austenisation temperatures are needed to achieve dissolution, hot formability and quench hardenability. Moreover, maintenance of niobium carbides can significantly reduce the carbon content of martensite on quenching, reducing martensitic strength [39]. However, also due to the high carbide forming affinity, niobium carbides are adept at slowing recrystallisation and subsequent γ-austenite grain growth, leading to grain size refinement. This feature is often exploited in DP steels so to reduce quench hardenability and thereby, produce the ferritic-martensitic dual phase microstructure on cooling [68].

*Titanium*

Titanium is essential for promoting quench hardenability in boron steels since titanium, as one of the most potent nitride formers [39], forms titanium nitride preferentially to boron forming boron nitride. This ensures that boron remains in solid solution which is believed to be essential for the boron quench hardenability effect [31].

The hyperstoichiometric Ti/N ratio (more titanium atoms than nitrogen atoms) is required to stabilise nitrogen [31]. The Ti/N ratio of 5/4 with the lowest possible levels of titanium and nitrogen is desirable so to achieve the optimal tensile strength-elongation combination and in turn, impact toughness following quench

hardening [31]. This is because titanium nitrides (and carbides) can also be used to promote precipitation hardening and grain size refinement, but a hyperstoichiometric Ti/N ratio (while favourable for the boron quench hardenability effect) causes formation of coarse titanium nitrides which can be detrimental to impact toughness. Thereby, the hyperstoichiometric Ti/N ratio of 5/4 (only marginally more titanium than nitrogen) and with as little titanium and nitrogen as possible, achieves optimal boron induced quench hardenability while maintaining titanium nitrides reasonably fine. Furthermore, excess titanium nitrides are undesired due to the detriment to hot formability.

Titanium causes globularisation of manganese sulphide inclusions so to aid planar isotropy, improves corrosion resistance and can restrict grain growth both when combined as nitrides and when dissolved in γ-austenite solid solution [65].

*Nickel*

Nickel does not form carbides, but is a powerful substitutional solid solution strengthening and toughening element and increases quench hardenability by delaying pearlite formation [39]. Nickel is a common element in quench hardened steels as it reduces quench distortion and cracking [39].

*Aluminium*

Aluminium is an essential deoxidising agent [66] and is the most effective (dissolved) alloying element at restricting γ-austenite grain growth, as it is more easily dissolved than other grain refiners [65].

Aluminium is imperative in TWIP steels where in concentrations approaching 10 wt % it increases the stacking fault energy and promotes deformation by twinning rather than plasticity [1]. Thereby, γ-austenite can be retained rather than strain-induce transformed to martensite [69].

*Boron*

The addition of just 0.001-0.003 wt % boron to low-mild carbon, low alloy steels, increases quench hardenability by delaying the nucleation of proeutectoid α-ferrite, pearlite and bainite. The theory behind this occurrence is debated, although the leading two theories agree on the involvement of γ-austenite grain boundaries. There is general agreement that solute boron dissolved in γ-austenite solid solution segregates to γ-austenite grain boundaries, reduces the γ-austenite grain boundary surface energy, reduces the thermodynamic driving force for a reconstructive phase transformation, retards proeutectoid α-ferrite nucleation and ultimately, increases quench hardenability [70] [71] [72] [73] [74]. The second theory is that iron-boron carbides [$Fe_{23}(CB)_6$] precipitated on γ-austenite grain boundaries may hinder the nucleation of α-ferrite by providing site competition [75].

As illustrated by Figure 2.22 [15] for a variety of alloy steels, the boron quench hardenability effect decreases with increasing carbon content and has no affect at ~ 0.85 wt % C. Moreover, beyond ~ 0.85 wt % C the effect of boron on quench hardenability can be negative. This has been postulated [15] to be due to precipitation of grain boundary boron carbides in such a quantity that promotes cementite formation. Boron oxides and nitrides may also decrease quench hardenability since these compounds remove boron from solid solution [31].

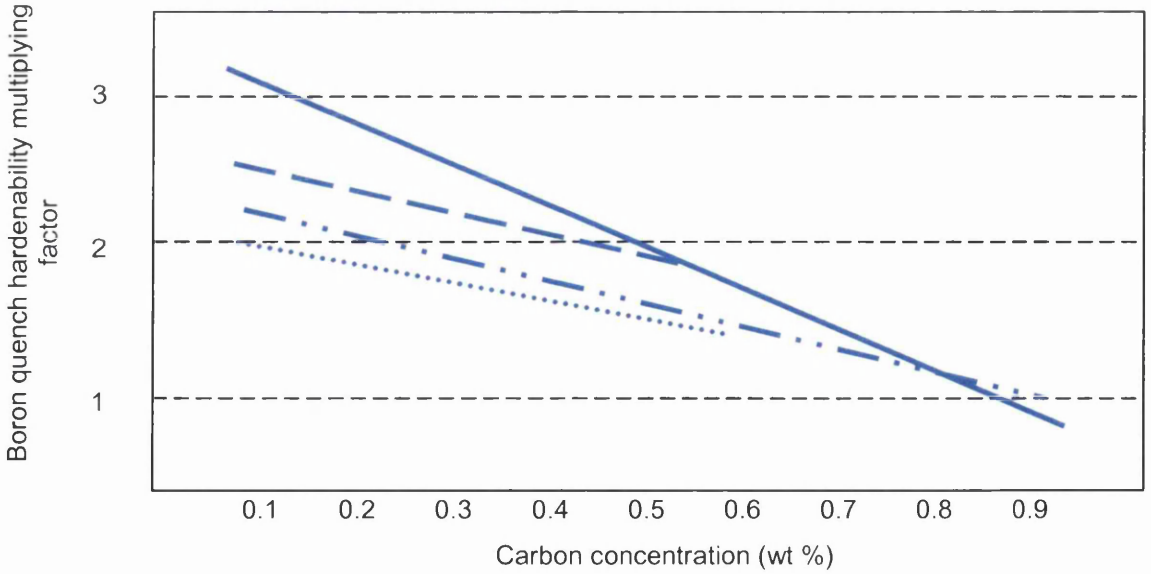


Figure 2.22: Boron quench hardenability effect as a function of carbon content (adapted from [15])

*Nitrogen*

Nitrogen is an extremely economical source of interstitial solid solution strengthening and precipitation hardening. Dissolved in solid solution (in a concentration > 0.01 wt %), nitrogen introduces the interstitial-related strain aging and bake hardening effects [31] which may be capitalised on during post-quench heat treatment. Combined as nitrides, nitrogen can be exploited to refine grain size [39].

Excess nitrogen can cause gaseous porosity during casting, degrade weldability and decrease the boron quench hardenability effect through boron nitride formation [31].

*Influences of Alloying Elements*

Equations 2.1 to 2.9 [3] [31] [76] [77] [78] estimate the influences of the most common alloying elements in low alloy steels, on the critical phase transformation temperatures including the $Ae_3$, $Ae_1$, Bs and Ms. The influences of select alloying elements on the hypothetical CCT diagram are illustrated by Figure 2.23 [31] [77].

$$Ae_3 = 912 - 203\sqrt{C} - 15.2Ni + 44.7Si - 104V + 31.5Mo + 13.1W - 30Mn - 11Cr - 20Cu700P + 400Al + 120As + 400Ti \quad \text{(Eq. 2.1)}$$

$$Ae_1 = 723 - 10.7\text{Mn} - 16.9\text{Ni} + 29.1\text{Si} + 16.9\text{Cr} + 290\text{As} + 6.38\text{W} \quad \text{(Eq. 2.2)}$$

$$Bs = 656 - 58C - 35Mn - 75Si - 15Ni - 34Cr - 41Mo \quad \text{(Eq. 2.3)}$$

$$Ms = 499 - 308\text{C} - 32.4\text{Mn} - 27\text{Cr} - 16.2\text{Ni} - 10.8(\text{Si} + \text{Mo} + \text{W}) + 10\text{Co} \quad \text{(Eq. 2.4)}$$

$$Ms = 499 - 292C - 32.4Mn - 22Cr - 16.2Ni + 10.8(Si + Mo) + 10Co10\text{Co} \quad \text{(Eq. 2.5)}$$

$$Ms = 539 - 423C - 30.4Mn - 17.7Ni - 12.2Cr - 7.5Mo10\text{Co} \quad \text{(Eq. 2.6)}$$

$$Ms = 539 - 423C - 30.4Mn - 7.5Si + 30Al10\text{Co} \quad \text{(Eq. 2.7)}$$

$$Ms = 539 - 423C - 30.4Mn - 6.6Si - 59.9P + 43.6Al10\text{Co} \quad \text{(Eq. 2.8)}$$

$$Ms = 561 - 474C - 35Mn - 17Ni - 17Cr - 21Mo10\text{Co}$$ (Eq. 2.9)

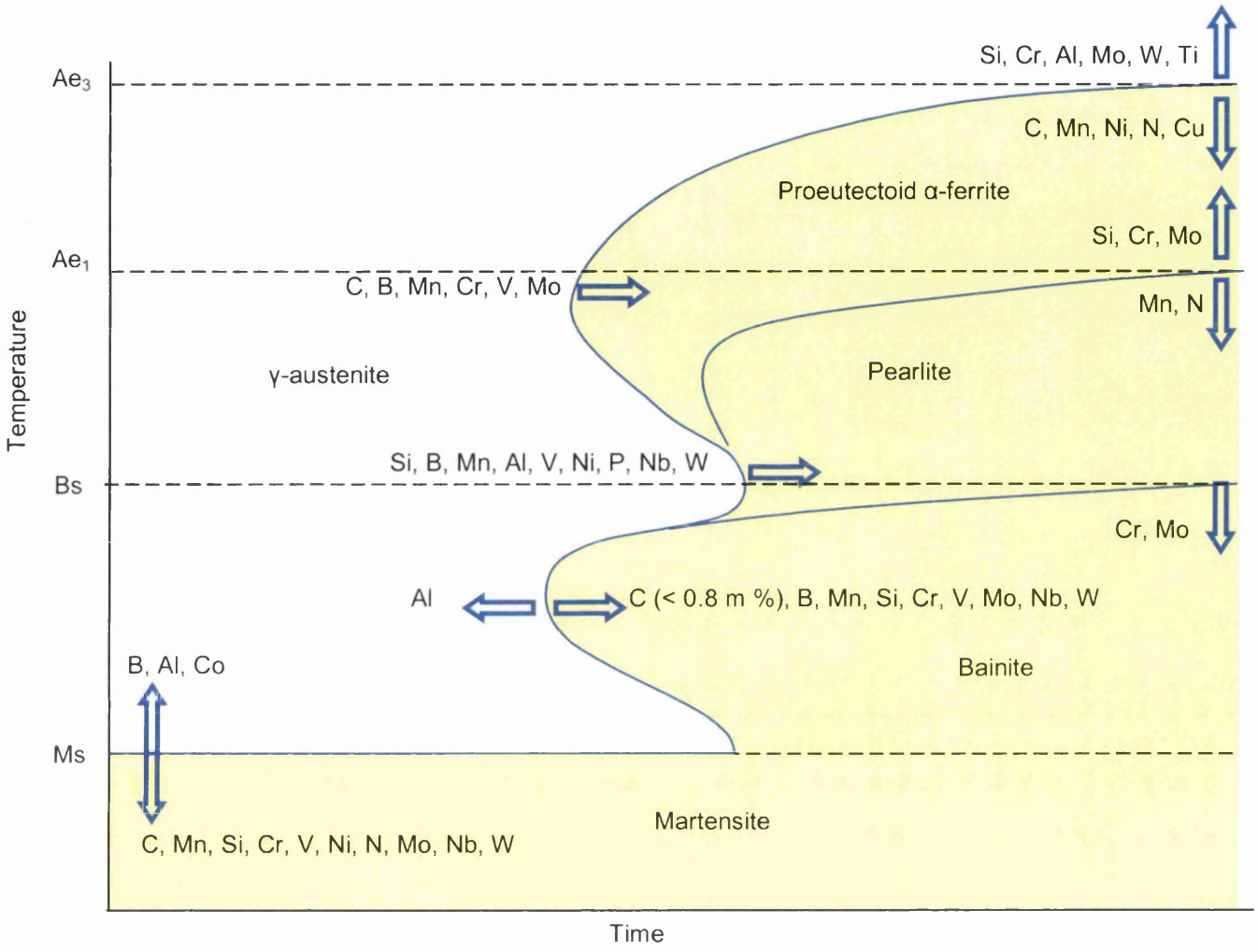


Figure 2.23: Influences of select alloying elements on the CCT diagram (adapted from [31] [77])

*Carbon Equivalent*

The carbon equivalent (CE) parameter aims to express the chemical composition of alloy steel in terms of a single carbon concentration. This carbon concentration (carbon equivalent) can then be used to predict behaviour of the steel [11].

Originally, CE was developed to predict quench hardenability and in turn, weldability of non-martensitic steels. The theory was that if quench hardenability was too high, martensite would form unintentionally during cooling of the weld cycle, giving rise to 'brittle spots' in the weld area that were prone to premature fracture [79].

CE was later extended to predict susceptibility to hydrogen embrittlement. CE can also be used to gauge strength, hardness and impact toughness [79].

There are several established formulae for calculating CE [80] [81] [82] [83] [84] [85] [79] [86]:

In 1967, the International Institute of Welding (IIW) developed their formula (Equation 2.10). The $CE_{IIW}$ parameter was developed for structural steels of relatively high carbon content and has since been incorporated into a number of industry standards.

$$CE_{IIW} = C + \frac{Mn}{6} + \frac{Cr+Mo+V}{5} + \frac{Ni+Cu}{15} \quad \text{(Eq. 2.10)}$$

The Japanese Welding Institute (JWI) developed the 'critical metal parameter' ($P_{cm}$), as calculated by Equation 2.11.

$$P_{cm} = C + \frac{Si}{30} + \frac{Mn+Cu+Cr}{20} + \frac{Ni}{60} + \frac{Mo}{15} + \frac{V}{10} + 5B \quad \text{(Eq. 2.11)}$$

Düren developed an alternative carbon equivalent (CEq), as calculated by Equation 2.12.

$$CEq = C + \frac{Si}{25} + \frac{Mn+Cu}{16} + \frac{Ni}{40} + \frac{Cr}{10} + \frac{Mo}{15} + \frac{V}{10} \quad \text{(Eq. 2.12)}$$

Both $P_{cm}$ and CEq were developed for low carbon steels (ideally less than ~ 0.11 wt % C).

Yet another carbon equivalent (CEN) was developed to include a wider variety of steels (Equation 2.13).

$$CEN = C + A(C) \times \left(\frac{Si}{24} + \frac{Mn}{6} + \frac{Cu}{15} + \frac{Ni}{60} + \frac{Cr + Mo + Nb + V}{5} + 5B\right)$$
$$Where\ A(C) = 0.75 + 0.25tanh[20 \times (C - 0.12)] \quad \text{(Eq. 2.13)}$$

For low and mild carbon steel, CEN has been shown to correlate closely with $P_{cm}$ and CEq. For higher carbon steels, CEN has been shown to correlate closely with $CE_{IIW}$ [79].

***Commercially Produced Boron Steels for Hot Stamping***

22MnB5 is produced by many steel manufacturers worldwide under various trade names. For example, 'MBW 1500' by ThyssenKrupp and 'BTR 165' by Benteler. These grades are intended for hot stamping and otherwise (e.g. conventionally cold formed agricultural machinery). Moreover, several steel manufacturers produce 22MnB5 specifically for hot stamping. These grades are essentially pre-coated 22MnB5. For example, MBW+AS by ThyssenKrupp, which is an Al coated 22MnB5; and Usibor 1500 by ArcelorMittal, which is an Al-Si coated 22MnB5. The pre-coating is principally designed to protect the steel substrate from oxidation and decarburisation during the high temperatures of hot stamping [20].

Further from the above, ThyssenKrupp reports [87] the development of boron steel grade MBW 1900 that exhibits ultimate tensile strength in excess of 1900 MPa, combined with total elongation of more than 4 % following hot stamping.

Another product that warrants discussion is Ductibor 500 by ArcelorMittal. Ductibor 500 is suspected by experts [68] within the steel industry to be a low

carbon-manganese-niobium grade (no boron), exhibiting proof strength ~ 400 MPa, ultimate tensile strength ~ 500 MPa and total elongation ~ 17 % following hot stamping. Ductibor 500 is not completely quench hardened to martensite during hot stamping, but rather is partially quench hardened to exhibit a 'partially martensitic' microstructure [1] of proeutectoid α-ferrite and (~ 10 vol. %) martensite. The two grades Usibor 1500 and Ductibor 500 are intended for use in the hot stamped tailor welded blank concept [20], where the former grade provides localised anti-intrusion and where the latter grade provides localised impact energy absorption. Moreover, Ductibor 500 with its partially martensitic microstructure and lower carbon equivalent, exhibits superior weldability to Usibor 1500. This is exploited to assist joining of the hot stamped component to adjacent components of the automotive body structure, with the attachment points of the hot stamped component constituted by Ductibor 500 [20].

ArcelorMittal also reports [20] the development of Ductibor 1000 and Ductibor 1300, with the former grade exhibiting proof strength in excess of 800 MPa, ultimate tensile strength in excess of 1000 MPa and total elongation in excess of 12 % following hot stamping; and with the latter grade exhibiting proof strength in excess of 950 MPa, ultimate tensile strength in excess of 1300 MPa and total elongation in excess of 8 % following hot stamping.

### *Other Commercially Produced Boron Steels*

Many steel manufacturers produce other boron steels besides 22MnB5, which were not originally intended for hot stamping. Most notably, these boron steels exhibit lower or higher carbon contents. However, these boron steels are now under consideration for hot stamping, as shall be explored in the next section: Investigations into Experimental Steels for Hot Stamping.

Table 2.3 lists chemical compositions[25] of boron steels commercially produced by select steel manufacturers worldwide as of 2014 [88].

[25] Certain chemical compositions are listed as ranges, while others are listed as absolute values. It is common practice for ranges to be presented. Precise chemical compositions within those ranges are then decided by discussions between the steel manufacturer and the customer and also by the manufacturer's refining capability (specification of a range or a maximum rather than a precise value allows for a degree of unavoidable industrial variability). However, other manufacturers choose to be more economical with the information they share for reasons of commercial sensitivity and rather present an example chemical composition with possible absolute values. Certain data have also been sourced from secondary references (i.e. not directly from the manufacturer itself) that have acquired steels from the manufacturers and then carried out their own chemical analyses so to provide possible absolute values. Importantly, the data presented in Table 2.3 (and throughout Literature Review unless otherwise stated) should be considered as incomplete since the complete chemical compositions of these steels cannot be confirmed – acknowledgement of certain alloying elements may have been withheld by the manufacturer, again for reasons of commercial sensitivity. Therefore, if a given steel grade appears not to contain a certain alloying element, this should not be considered to be absolute. Rather, the grade may contain a concentration of that alloying element, but the information has not been supplied by the manufacturer.

Table 2.3: Boron steels commercially produced by select steel manufacturers (chemical compositions in wt % with Fe balanced)

| Manu. | Grade | C | | Mn | | Si | | P | | S | | Cr | | Mo | | Ni | | Al | | Ti | | Cu | | B | | N | |
|---|---|---|---|---|---|---|---|---|---|---|---|---|---|---|---|---|---|---|---|---|---|---|---|---|---|---|---|
| | | Min | Max | Min | Max | Min | Max | Min | Max | Min | Max | Min | Max | Min | Max | Min | Max | Min | Max | Min | Max | Min | Max | Min | Max | Min | |
| Arcelor Mittal | Usibor 1500 (22MnB5) | 0.20 | 0.25 | 1.10 | 1.40 | 0.15 | 0.35 | | 0.025 | | 0.008 | 0.15 | 0.35 | | | | | 0.015 | | 0.02 | 0.05 | | | 0.002 | 0.005 | | 0 |
| | 22MnB5 AM FCE | 0.20 | 0.25 | 1.10 | 1.40 | 0.15 | 0.35 | | 0.025 | | 0.008 | | | | | | | 0.015 | | 0.02 | 0.05 | | | 0.002 | 0.005 | | |
| | 30MnB5 AM FCE | 0.27 | 0.33 | 1.15 | 1.45 | 0.17 | 0.35 | | 0.025 | | 0.005 | | | | | | | 0.015 | | 0.02 | 0.05 | | | 0.001 | 0.005 | | |
| | 30MnB5 EN 10083 | 0.27 | 0.33 | 1.15 | 1.45 | 0.17 | 0.35 | | 0.025 | | 0.035 | | | | | | | | | | | | | 0.001 | 0.005 | | |
| | 30MnB5 DRUM AM FCE | 0.27 | 0.33 | 1.15 | 1.45 | 0.17 | 0.35 | | 0.025 | | 0.020 | | | | | | | 0.015 | | 0.02 | 0.05 | | | 0.001 | 0.005 | | |
| | 38MnB5 AM FCE | 0.36 | 0.42 | 1.15 | 1.45 | 0.17 | 0.35 | | 0.025 | | 0.005 | | | | | | | 0.015 | | 0.02 | 0.05 | | | 0.001 | 0.005 | | |
| | Ductibor 1500P | | | | | | | | | | | | | | | | | | | | | | | | | | |
| Salzgitter Flachstahl | 22MnB5 (yr 2005) | 0.22 | 0.25 | 1.20 | 1.40 | 0.20 | 0.30 | | 0.020 | | 0.005 | 0.11 | | 0.1 | 0.1 | 0.1 | 0.1 | 0.020 | 0.05 | 0.02 | 0.05 | 0.1 | 0.1 | 0.002 | 0.005 | | |
| | 22MnB5 (yr 2007) | 0.19 | 0.25 | 1.10 | 1.40 | 0.10 | 0.40 | | 0.025 | | 0.010 | 0.10 | 0.30 | | | | | 0.015 | 0.08 | 0.02 | 0.05 | | | 0.001 | 0.005 | | 0 |
| | 24MnB5 (yr 2007) | 0.21 | 0.26 | 1.15 | 1.50 | 0.10 | 0.40 | | 0.025 | | 0.010 | 0.10 | 0.30 | | | | | 0.015 | 0.08 | 0.02 | 0.05 | | | 0.001 | 0.005 | | 0 |
| | 26MnB5 (yr 2007) | 0.22 | 0.28 | 1.10 | 1.50 | 0.10 | 0.40 | | 0.025 | | 0.010 | 0.10 | 0.30 | | | | | 0.015 | 0.08 | 0.02 | 0.05 | | | 0.001 | 0.005 | | 0 |
| | 30MnB5 (yr 2007) | 0.27 | 0.33 | 1.15 | 1.45 | 0.10 | 0.40 | | 0.025 | | 0.010 | 0.10 | 0.30 | | | | | 0.015 | 0.08 | 0.02 | 0.05 | | | 0.001 | 0.005 | | 0 |

Table 2.3: (Continued)

| Manu. | Grade | C | | Mn | | Si | | P | | S | | Cr | | Mo | | Ni | | Al | | Ti | | Cu | | B | | N |
|---|---|---|---|---|---|---|---|---|---|---|---|---|---|---|---|---|---|---|---|---|---|---|---|---|---|---|
| | | Min | Max | Min | Max | Min | Max | Min | Max | Min | Max | Min | Max | Min | Max | Min | Max | Min | Max | Min | Max | Min | Max | Min | Max | Min |
| China Steel Cooperation | 10B20 | 0.18 | 0.23 | 0.30 | 0.60 | | 0.10 | | 0.03 | | 0.035 | | | | | | | | | | | | | 0.0005 | | |
| | 10B21/10B22 | 0.18 | 0.23 | 0.70 | 1.00 | | 0.10 | | 0.03 | | 0.035 | | | | | | | | | | | | | 0.0005 | | |
| | 10B29 | 0.26 | 0.3 | 0.70 | 1.00 | 0.15 | 0.35 | | 0.03 | | 0.035 | | | | | | | | | | | | | 0.0005 | | |
| | 10B30 | 0.28 | 0.34 | 0.70 | 1.00 | 0.15 | 0.35 | | 0.03 | | 0.035 | | | | | | | | | | | | | 0.0005 | | |
| | 10B33 | 0.32 | 0.36 | 0.70 | 1.00 | 0.15 | 0.35 | | 0.03 | | 0.035 | | | | | | | | | | | | | 0.0005 | | |
| | 10B38 | 0.35 | 0.42 | 0.70 | 1.00 | 0.15 | 0.35 | | 0.03 | | 0.035 | | | | | | | | | | | | | 0.0005 | | |
| | 50BV18 | 0.15 | 0.20 | 0.70 | 1.00 | | 0.10 | | 0.03 | | 0.035 | 0.30 | 0.50 | 0.10 | 0.15 | | | | | | | | | 0.0005 | | |
| | 50BV21 | 0.18 | 0.23 | 0.70 | 1.00 | | 0.10 | | 0.03 | | 0.035 | 0.30 | 0.50 | 0.10 | 0.15 | | | | | | | | | 0.0005 | | |
| | 50BV30 | 0.27 | 0.33 | 0.70 | 1.00 | | 0.10 | | 0.03 | | 0.035 | 0.30 | 0.50 | 0.10 | 0.15 | | | | | | | | | 0.0005 | | |
| | 50BV31 | 0.32 | 0.36 | 0.70 | 1.00 | 0.15 | 0.35 | | 0.03 | | 0.035 | 0.30 | 0.50 | 0.10 | 0.15 | | | | | | | | | 0.0005 | | |
| | 50B40H | 0.37 | 0.44 | 0.65 | 1.10 | 0.15 | 0.35 | | 0.03 | | 0.040 | 0.30 | 0.70 | | 0.06 | | 0.25 | | | | | | 0.35 | 0.0005 | 0.003 | |
| | 50B44H | 0.42 | 0.49 | 0.65 | 1.10 | 0.15 | 0.35 | | 0.03 | | 0.040 | 0.30 | 0.70 | | 0.06 | | 0.25 | | | | | | 0.35 | 0.0005 | 0.003 | |
| | 50B46H | 0.43 | 0.50 | 0.65 | 1.10 | 0.15 | 0.35 | | 0.03 | | 0.040 | 0.13 | 0.43 | | 0.06 | | 0.25 | | | | | | 0.35 | 0.0005 | 0.003 | |
| | 50B50H | 0.47 | 0.54 | 0.65 | 1.10 | 0.15 | 0.35 | | 0.03 | | 0.040 | 0.30 | 0.70 | | 0.06 | | 0.25 | | | | | | 0.35 | 0.0005 | 0.003 | |
| | 50B60H | 0.55 | 0.65 | 0.65 | 1.10 | 0.15 | 0.35 | | 0.03 | | 0.040 | 0.30 | 0.70 | | 0.06 | | 0.25 | | | | | | 0.35 | 0.0005 | 0.003 | |
| | 81B45H | 0.42 | 0.49 | 0.70 | 1.05 | 0.15 | 0.35 | | 0.03 | | 0.040 | 0.30 | 0.60 | 0.08 | 0.15 | 0.15 | 0.45 | | | | | | 0.35 | 0.0005 | 0.003 | |
| | 86B30H | 0.27 | 0.33 | 0.60 | 0.95 | 0.15 | 0.35 | | 0.03 | | 0.040 | 0.35 | 0.65 | 0.15 | 0.25 | 0.35 | 0.75 | | | | | | 0.35 | 0.0005 | 0.003 | |
| | 86B45H | 0.42 | 0.49 | 0.70 | 1.05 | 0.15 | 0.35 | | 0.03 | | 0.040 | 0.35 | 0.65 | 0.15 | 0.25 | 0.35 | 0.75 | | | | | | 0.35 | 0.0005 | 0.003 | |
| | 94B15H | 0.12 | 0.18 | 0.70 | 1.05 | 0.15 | 0.35 | | 0.03 | | 0.040 | 0.25 | 0.55 | 0.08 | 0.15 | 0.25 | 0.65 | | | | | | 0.35 | 0.0005 | 0.003 | |
| | 94B17H | 0.14 | 0.20 | 0.70 | 1.05 | 0.15 | 0.35 | | 0.03 | | 0.040 | 0.25 | 0.55 | 0.08 | 0.15 | 0.25 | 0.65 | | | | | | 0.35 | 0.0005 | 0.003 | |
| | 94B30H | 0.27 | 0.33 | 0.70 | 1.05 | 0.15 | 0.35 | | 0.03 | | 0.040 | 0.25 | 0.55 | 0.08 | 0.15 | 0.25 | 0.65 | | | | | | 0.35 | 0.0005 | 0.003 | |
| Bromford Iron and Steel | 30CCrB | 0.28 | 0.33 | 1.00 | 1.40 | 0.15 | 0.35 | | 0.04 | | 0.035 | 0.30 | 0.60 | | | | | 0.02 | 0.06 | 0.02 | | | | 0.0010 | 0.005 | |
| | 43CMnB | 0.40 | 0.45 | 1.30 | 1.50 | 0.15 | 0.35 | | 0.03 | | 0.035 | 0.15 | 0.30 | | | | | 0.02 | 0.06 | 0.02 | | | | 0.0020 | 0.005 | |
| Swedish Steel AB | Docal 20MnB5 | 0.17 | 0.23 | 1.10 | 1.40 | | 0.40 | | 0.03 | | 0.015 | 0.10 | 0.30 | | | | | | | | | | | 0.0008 | 0.005 | |
| | Docal 30MnB5 | 0.27 | 0.33 | 1.15 | 1.45 | | 0.40 | | 0.03 | | 0.015 | 0.10 | 0.30 | | | | | | | | | | | 0.0008 | 0.005 | |
| | Docal 38MnB5 | 0.36 | 0.42 | 1.15 | 1.45 | | 0.40 | | 0.03 | | 0.015 | 0.10 | 0.30 | | | | | | | | | | | 0.0008 | 0.005 | |
| | Docal 27MnCrB5 | 0.24 | 0.30 | 1.10 | 1.40 | | 0.40 | | 0.03 | | 0.015 | 0.30 | 0.60 | | | | | | | | | | | 0.0008 | 0.005 | |
| | Docal 33MnCrB5 | 0.30 | 0.36 | 1.20 | 1.50 | | 0.40 | | 0.03 | | 0.015 | 0.30 | 0.60 | | | | | | | | | | | 0.0008 | 0.005 | |
| | Docal 39MnCrB5 | 0.36 | 0.42 | 1.40 | 1.70 | | 0.40 | | 0.03 | | 0.015 | 0.30 | 0.60 | | | | | | | | | | | 0.0008 | 0.005 | |

***Investigations into Experimental Steels for Hot Stamping***

It is reported by experts within the automotive steel industry that hot stamped 22MnB5 is now widely regarded as a 'commodity product' [68]. Moreover, it is reported [8] [12] that demand exists for steels that exhibit higher tensile strength and/or higher elongation values following hot stamping compared to 22MnB5 (Figure 1.1), where higher tensile strength can provide improved anti-intrusive crash performance and thus enable down gauging of anti-intrusive structural body components; and where higher tensile strength and/or higher elongation can provide higher impact toughness, improved impact energy absorptive crash performance and thus, enable down gauging of impact energy absorptive structural body components.

Related to higher tensile strength, there is also demand for greater quench hardenability intrinsic to the chemistry. When down gauging, the blank cools more quickly during the transfer stage of hot stamping. If the blank cools below the critical $Ar_3$ temperature before reaching the hot stamping and quench hardening stages, proeutectoid α-ferrite will be present in the final microstructure, which will compromise strength. Austrian steel manufacturer Voestalpine has reported [17] such problems of insufficient quench hardenability when attempting to down gauge 22MnB5. The completely martensitic microstructure with a gauge of 0.8 mm was found to be achievable only with small components, since larger components (with larger surface area) were difficult to transfer quickly enough so to prevent over-cooling and proeutectoid α-ferrite formation. Larger components are therefore mostly of thicker gauges, such as 1.2 to 1.5 mm.

For the above reasons, novel grades for automotive hot stamping technologies must be developed.

Besides other commercially produced boron steels, consideration for hot stamping has also been given to further removed chemical compositions from 22MnB5, including derivatives of DP, CP and TRIP steels; and even, austenitic stainless steels. There have been several proposed chemical compositions that are

pending patents, while other proposals seek further investigation. These experimental steels for hot stamping shall now be reviewed.

Most of the following references include a commercially produced 22MnB5 for benchmarking purposes. However, when an appropriate 22MnB5 benchmark has not been included by the reference, cross-referencing shall be employed in order to compare all experimental chemical compositions and corresponding mechanical properties to a suitable 22MnB5 benchmark treated to equivalent (or similar) forming and/or processing conditions.

When comparing chemical compositions and properties, significant improvements over the 22MnB5 benchmark that may be worth further investigation shall be highlighted.

*Investigation One: Naderi*

The applicability of ten commercial UHSS grades to hot stamping; and conventional cold stamping followed by austenisation and direct water quenching, has been reported [15].

Hot stamping with indirect water quenching (a water cooled punch maintained at ambient temperature at the commencement of hot stamping) was referred to as 'hot stamping-WCP'. Hot stamping with indirect liquid nitrogen quenching (a liquid nitrogen cooled punch maintained at approximately -50 $^{o}$C at the commencement of hot stamping) was referred to as 'hot stamping-NCP'. Conventional cold stamping followed by austenisation and direct water quenching (submersion in a water bath) was referred to as 'cold stamping-WQH'. In all cases, the stamped component was of U-bend geometry.

Experimental austenisation conditions included a series of durations and temperatures (50 and 80 $^{o}$C above the grade specific $Ac_3$). The austenisation conditions employed during the stamping experiments were then those that yielded maximum hardness resulting from standardised quenching.

Chemical compositions and specimen (sheet) thicknesses of the investigated grades are given in Table 2.4a.

Table 2.4a: Investigated grades from Naderi (chemical compositions in wt % with Fe balanced) [15]

| *Grade* | *Thickness (mm)* | *C* | *Si* | *Mn* | *Cr* | *Ni* | *Al* | *Ti* | *B* | *N* |
|---|---|---|---|---|---|---|---|---|---|---|
| 22MnB5 | 1.0 1.5 2.8 | 0.230 | 0.220 | 1.180 | 0.160 | 0.120 | 0.030 | 0.040 | 0.002 | 0.005 |
| 8MnCrB3 | 3.5 | 0.070 | 0.210 | 0.750 | 0.370 | 0.010 | 0.050 | 0.048 | 0.002 | 0.006 |
| 20MnB5 | 2.7 | 0.160 | 0.400 | 1.050 | 0.230 | 0.010 | 0.040 | 0.034 | 0.001 | - |
| 27MnCrB5 | 3.0 | 0.250 | 0.210 | 1.240 | 0.340 | 0.010 | 0.030 | 0.042 | 0.002 | 0.004 |
| **37MnB4** | **3.0** | **0.330** | **0.310** | **0.810** | **0.190** | **0.020** | **0.030** | **0.046** | **0.001** | **0.006** |
| MSW 1200 | 1.5 | 0.140 | 0.120 | 1.710 | 0.550 | 0.060 | 0.020 | 0.002 | 0.000 | - |
| DP 1400 | 1.0 | 0.190 | 0.550 | 1.610 | 0.020 | 0.050 | 0.040 | 0.003 | 0.000 | 0.006 |
| DP 1000 | 1.5 | 0.150 | 0.570 | 1.450 | 0.010 | 0.030 | 0.040 | 0.003 | 0.000 | 0.003 |
| **DP 800** | **1.0** | **0.120** | **0.240** | **1.450** | **0.020** | **0.040** | **0.030** | **0.002** | **0.000** | **0.004** |
| **TRIP 800** | **1.0** | **0.200** | **1.810** | **1.480** | **0.040** | **0.030** | **0.040** | **0.006** | **0.000** | **-** |

The reoccurring theme was the supremacy of direct water quenching in order to achieve maximum tensile strength. This is believed to have risen from the greater quench rate provided by direct water quenching compared to the lower quench rates provided by indirect water or liquid nitrogen quenching. Thus, there is an ambition to introduce severe direct water quenching to hot stamping.

DP 800 was found to be a lower tensile strength-higher elongation improvement over 22MnB5. Hot stamping of DP 800 with indirect water or liquid nitrogen quenching did not result in complete martensite formation, even with a blank thickness of just 1 mm (and thus, high quench rate). In contrast, hot stamping of 22MnB5 resulted in (essentially) complete martensite formation, regardless of experimented austenisation conditions, indirect water or liquid nitrogen quenching and experimented blank thickness (even to a blank thickness of 2.8 mm). Consequently, hot stamped DP 800 consistently exhibited lower tensile strength than hot stamped 22MnB5. This suggests that DP 800 does not compare favourably to 22MnB5 for the intention of producing hot stamped components of maximum tensile strength. However, complete martensite formation in DP 800 was possible via direct water quenching and accordingly, tensile strength increased. This suggests that if the hot stamping quench rate could be increased to that of direct water quenching, or if quench hardenability of DP 800 could be increased (perhaps by a boron addition), the potential for complete martensite

formation and increased tensile strength similar to that of 22MnB5, may be realised.

When comparing hot stamped DP 800 to hot stamped 22MnB5 treated to the same conditions, DP 800 consistently offered lower tensile strength-higher elongation. This underlines the hot stamping potential of DP 800 as a lower tensile strength-higher elongation improvement over 22MnB5. Further, when comparing directly water quenched DP 800 to directly water quenched 22MnB5; DP 800 offered similar tensile strength yet with much improved elongation. In fact, total elongation was nearly doubled. Thus, to refer back to the previous statement that if the hot stamping quench rate could be increased to that of direct water quenching, or if quench hardenability of DP 800 could be increased, the hot stamping potential of DP 800 may be even wider; offering not only higher elongation compared to 22MnB5, but also similar tensile strength.

TRIP 800 was also highlighted as a potential lower tensile strength-higher elongation improvement over 22MnB5. Moreover, 37MnB4 was highlighted as a potential higher tensile strength-lower elongation improvement.

The highlighted grades, their sheet thicknesses, optimal austenisation and hot stamping conditions, resulting tensile properties post-hot stamping and potential advantages over 22MnB5, are summarised in Table 2.4b.

Table 2.4b: Results from Naderi (adapted from [15])

| Grade | Thickness (mm) | Condition | E (GPa) | $R_{p0.2}$ (MPa) | $R_m$ (MPa) | $A_u$ (%) | $A_{25}$ (%) | $R_m \times A_{25}$ | Comments |
|---|---|---|---|---|---|---|---|---|---|
| 22MnB5 | 1.0 | 10 min at 950 °C-WCP | 198 | 1024 | 1418 | 2.6 | 3.7 | 5247 | High $R_m$-low $A_{25}$ benchmark |
| | | 15 min at 900 °C-WCP | 198 | 987 | 1397 | 2.6 | 3.8 | 5309 | Low $R_m$-high $A_{25}$ benchmark |
| | 1.5 | 15 min at 900 °C-WCP | 194 | 1035 | 1485 | 3.4 | 6.7 | 9950 | High $R_m$-high $A_{25}$ benchmark |
| | 2.8 | 15 min at 950 °C-WCP | 208 | 987 | 1493 | 3.6 | 8.1 | 12093 | High $R_m$-high $A_{25}$ benchmark |
| **37MnB4** | **3.0** | **10 min at 900 °C-WCP** | **197** | **1378** | **2040** | **2.2** | **2.5** | **5100** | **Higher $R_m$-lower $A_{25}$** |
| **DP 800** | **1.0** | **15 min at 900 °C-WCP** | **208** | **750** | **1058** | **2.6** | **5.3** | **5607** | **Lower $R_m$-higher $A_{25}$** |
| | | **15 min at 900 °C-NCP** | **278** | **904** | **1257** | **2.9** | **4.5** | **5657** | |
| **TRIP 800** | **1.0** | **15 min at 950 °C-WCP** | **184** | **787** | **1190** | **4.6** | **5.3** | **6307** | **Lower $R_m$-higher $A_{25}$** |

*Investigation Two: Naderi et al*

Hot stamping with indirect water quenching (a water cooled punch) has been performed [89] on TRIP 800 of 1 mm sheet thickness and 37MnB4 of 3 mm sheet thickness. 22MnB5 of 1 and 2.8 mm sheet thickness was included for benchmarking against TRIP 800 and 37MnB4 respectively (so to compare the experimental grades against 22MnB5 of equal or approximately equal thickness). The chemical compositions are presented in Table 2.5a. Sheet thicknesses, austenisation and hot stamping conditions, mechanical properties in the as-delivered (pre-hot stamping) and post-hot stamping conditions; and microconstituent volume fractions in the post-hot stamping condition, are provided in Table 2.5b. Austenisation conditions were not presented for 22MnB5.

Table 2.5a: Investigated grades from Naderi et al (chemical compositions in wt % with Fe balanced) [89]

| Grade | C | Mn | Si | Cr | Ni | Al | Ti | B | N |
|---|---|---|---|---|---|---|---|---|---|
| 22MnB5 | 0.230 | 0.180 | 0.220 | 0.160 | 0.120 | 0.030 | 0.040 | 0.002 | 0.005 |
| **TRIP 800** | **0.200** | **1.500** | **1.800** | **0.040** | **0.030** | **0.040** | **0.006** | **0.000** | **0.005** |
| **37MnB4** | **0.330** | **0.810** | **0.310** | **0.190** | **0.020** | **0.030** | **0.046** | **0.001** | **0.006** |

Table 2.5b: Results from Naderi et al [89]

| Grade | Thickness (mm) | Condition | | $R_{p0.2}$ (MPa) | $R_m$ (MPa) | $A_u$ (%) | $A_{50}$ (%) | $R_m \times A_{50}$ | Micro. ± 5 % | Vickers hardness ($Hv_{10}$) |
|---|---|---|---|---|---|---|---|---|---|---|
| 22MnB5 | 1.0 | As-delivered | | 410 | 555 | 15.2 | 26.3 | 14597 | 78F+22P | 170 |
| | | Hot stamped | | 1024 | 1418 | 2.6 | 4.6 | 6523 | 99M+1B | 556 |
| | 2.8 | As-delivered | | 490 | 650 | 12.1 | 26 | 16900 | 75F+25P | 210 |
| | | Hot stamped | | 987 | 1493 | 3.6 | 8.8 | 13138 | 100M | 475 |
| **TRIP 800** | **1.0** | As-delivered | | 514 | 836 | 22.9 | 27.8 | 23241 | 65F+35A | 312 |
| | | **10 min at 1000 °C-hot stamped** | | **970** | **1360** | **3.1** | **6.1** | **8296** | **100M** | **525** |
| **37MnB4** | **3.0** | As-delivered | | 580 | 810 | 10.6 | 21.7 | 17577 | 47F+53P | 260 |
| | | 10 min at 950 °C-hot stamped | | 1378 | 2040 | 2.2 | 4.4 | 8976 | 100M | 610 |
| | | Tempered at 200 °C | 5 min | 1311 | 1960 | 4.1 | 8.6 | 16856 | 100TM | 420 |
| | | | 10 min | 1330 | 1955 | 2.7 | 9.4 | 18377 | 100TM | 490 |
| | | | 15 min | 1400 | 1970 | 3.8 | 8.3 | 16351 | 100TM | 360 |
| | | | 30 min | 1595 | 1850 | 2.8 | 9.8 | 18130 | 100TM | 590 |
| | | | 45 min | 1625 | 1860 | 3.4 | 9.2 | 17112 | 100TM | 560 |
| | | | 60 min | 1615 | 1850 | 3.0 | 8.0 | 14800 | 100TM | 540 |
| | | **Tempered at 250 °C** | 5 min | 1380 | 2015 | 4.1 | 9.6 | 19344 | 100TM | 390 |
| | | | 10 min | 1430 | 1965 | 4.0 | 10.2 | 20043 | 100TM | 430 |
| | | | **15 min** | **1570** | **1960** | **3.6** | **10.3** | **20188** | **100TM** | **490** |
| | | | 30 min | 1605 | 1820 | 2.8 | 9.4 | 17108 | 100TM | 575 |
| | | | 45 min | 1600 | 1775 | 2.3 | 9.5 | 16863 | 100TM | 545 |
| | | | 60 min | 1585 | 1745 | 2.4 | 9.1 | 15880 | 100TM | 545 |
| | | **Tempered at 300 °C** | 5 min | 1545 | 1980 | 4.4 | 9.7 | 19206 | 100TM | 550 |
| | | | 10 min | 1580 | 1890 | 3.2 | 8.9 | 16821 | 100TM | 400 |
| | | | **15 min** | **1645** | **1880** | **3.4** | **9.0** | **16920** | **100TM** | **405** |
| | | | 30 min | 1630 | 1770 | 2.1 | 8.6 | 15222 | 100TM | 490 |
| | | | 45 min | 1575 | 1720 | 2.1 | 9.0 | 15480 | 100TM | 550 |
| | | | 60 min | 1510 | 1670 | 2.9 | 9.8 | 16366 | 100TM | 515 |

The TRIP 800 specimen of 1 mm thickness should be compared to the benchmark 22MnB5 of equal (1 mm) thickness. In the post-hot stamping condition, TRIP 800 exhibited inferior hardness (525 $Hv_{10}$ compared to 556 $Hv_{10}$), $R_{p0.2}$ (970 MPa compared to 1024 MPa) and $R_m$ (1360 MPa compared to 1418 MPa), but superior $A_u$ (3.1 % compared to 2.6 %), $A_{50}$ (6.1 % compared to 4.6 %) and $R_m \times A_{50}$ (8296 compared to 6523). These results correlate with those presented previously [15] and underline the potential of TRIP 800 as a lower tensile strength-higher elongation improvement over 22MnB5.

The 37MnB4 specimen of 3 mm thickness should be compared to the benchmark 22MnB5 of similar (2.8 mm) thickness. In the post-hot stamping condition, 37MnB4 exhibited significantly superior hardness (610 $Hv_{10}$ compared to 475 $Hv_{10}$), $R_{p0.2}$ (1378 MPa compared to 987 MPa) and $R_m$ (2040 MPa compared to 1493 MPa), but with significantly inferior $A_u$ (2.2 % compared to 3.6 %), $A_{50}$ (4.4 % compared to 8.8 %) and $R_m \times A_{50}$ (8976 compared to 13138). These results also correlate with those presented previously [15] and underline the potential of 37MnB4 as a higher tensile strength-lower elongation improvement over 22MnB5.

In order to improve elongation of 37MnB4 while maintaining the superior tensile strength compared to 22MnB5, post-quench tempering was conducted at the temperatures and times presented in Table 2.5b. Following the majority of tempering treatments, $R_{p0.2}$ was equal to or even higher than the $R_m$ of un-tempered 22MnB5 (1493 MPa). Moreover, in all but two tempering treatments (5 and 10 minutes at 200 °C), $R_{p0.2}$ of tempered 37MnB4 not only failed to decrease relative to un-tempered 37MnB4 (1378 MPa), but actually increased (although $R_m$ decreased). This was interpreted to be due to the role of carbon. Following rapid quenching, carbon is trapped in martensitic supersaturated solid solution where it increases $R_m$. During tempering, carbon is released from supersaturated solid solution as carbides are precipitated; a portion of the released carbon atoms inhibits dislocations with Cottrell atmospheres and $R_{p0.2}$ accordingly increases as a greater stress must be applied to initiate dislocation movement. However, once the dislocation breaks free from the Cottrell atmosphere, the potential for lower $R_m$ is realised.

The highest $R_{p0.2}$ of all specimens combined with very respectable $R_m$, $A_u$ and $A_{50}$ was achieved with 37MnB4 tempered for 15 minutes at 300 °C. Compared to un-tempered 22MnB5, mechanical property modifications included higher $R_{p0.2}$ (1645 MPa compared to 987 MPa), higher $R_m$ (1880 MPa compared to 1493 MPa), similar $A_u$ (3.4 % compared to 3.6 %) and $A_{50}$ (9.0 % compared to 8.8 %), higher $R_m \times A_{50}$ (16920 compared to 13138) and slightly lower hardness (405 $Hv_{10}$ compared to 475 $Hv_{10}$). 37MnB4 tempered for 15 minutes at 300 °C can be considered the optimal higher tensile strength-lower elongation combination.

The optimal tensile strength-elongation combination overall (expressed by $R_m \times A_{50}$) was achieved with 37MnB4 tempered for 15 minutes at 250 °C. Moreover, apart from $A_u$ which remained equal, every mentioned mechanical property was improved over the un-tempered 22MnB5 benchmark.

It was concluded that by introducing a post-quench tempering stage to the hot stamping process, ultrahigh strength hot stamped 37MnB4 could be produced with improved tensile strength and elongation compared to the conventional 22MnB5.

*Investigation Three: Benteler*

The grade to be termed 'EP 1881083-A1' has been claimed [90] to be an 'air hardenable' grade that can be used with regular hot stamping and 'semi-hot stamping' where the blank is stamped below 400 °C, austenised and air cooled.

Claimed chemical composition ranges and mechanical properties are given in Tables 2.6a and 2.6b respectively and in comparison to Benteler's commercial BTR 165 grade. Specimen thicknesses and austenisation conditions are unknown. 22MnB5 treated to known conditions is also presented for benchmarking [15].

Table 2.6a: Investigated grades from Benteler (chemical compositions in wt % with Fe balanced) (adapted from [15] [90])

| *Grade* | *C* | *Si* | *Mn* | *P* | *S* | *Cr* | *Nb* | *Ni* | *Al* | *Ti* | *B* | *N* |
|---|---|---|---|---|---|---|---|---|---|---|---|---|
| 22MnB5 | 0.230 | 0.220 | 1.180 | - | - | 0.160 | - | 0.1200 | 0.030 | 0.040 | 0.002 | 0.005 |
| BTR 165 | 0.250 | 0.270 | 1.140 | 0.015 | 0.001 | 0.150 | - | 0.037-0.120 | - | 0.036 | 0.003 | - |
| **EP 1881083-A1** | **0.110-0.180** | **0.100-0.300** | **1.800-2.200** | **0.002** | **0.010** | **1.000-2.000** | **0.020-0.060** | **-** | **-** | **0.001-0.050** | **0.001-0.004** | **-** |

Table 2.6b: Results from Benteler (adapted from [15] [90])

| *Grade* | *Thickness (mm)* | *Condition* | *E (GPa)* | $R_{p0.2}$ *(MPa)* | $R_m$ *(MPa)* | $A_u$ *(%)* | *A (%)* | $R_m \times A$ |
|---|---|---|---|---|---|---|---|---|
| 22MnB5 | 1.0 | 10 min at 950 °C-water quenched | 243 | 1060 | 1590 | 2.4 | 3.8 ($A_{25}$) | 6052 |
| | 1.5 | 15 min at 900 °C-water quenched | 210 | 1202 | 1647 | 2.4 | 4.5 ($A_{25}$) | 7412 |
| | 2.8 | 15 min at 950 °C-water quenched | 208 | 1250 | 1649 | 2.8 | 8.1 ($A_{25}$) | 13357 |
| BTR 165 | - | Water quenched | - | - | 1500 | - | 9.0 ($A_{50}$) | 13500 |
| **EP 1881083-A1** | **-** | **Air cooled** | **-** | **-** | **1200-1500** | **-** | **8.0-16.0 ($A_{50}$)** | **12000-19200** |

Following air cooling, $R_m$ is claimed to be 1200-1500 MPa with $A_{50}$ 8-16 %. This $R_m$ claim is similar to BTR 165 and the referenced 22MnB5, but with potentially higher elongation. Hot dip galvanising has been claimed to decrease $R_m$ by 100-200 MPa, while $A_{50}$ remains at 8-16 %. Of interest is that the phosphorous content is very low, which is thought to be beneficial for elongation and results from electric arc re-melting. The contents of chromium and manganese are high which lower the critical cooling rate to air cooling conditions. The carbon content is rather low when compared to BTR 165 and the referenced 22MnB5.

*Investigation Four: POSCO*

The chemical compositions of the grades to be termed 'IMO 2007/064172-A1' [91] and 'C22C38/00' [92] are presented in Table 2.7a. Mechanical properties claimed for both grades are presented in Table 2.7b. Specimen thicknesses and austenisation conditions are unknown. 22MnB5 treated to known conditions is also presented for benchmarking [15].

Table 2.7a: Investigated grades from POSCO (chemical compositions in wt % with Fe balanced) (adapted from [15] [91] [92])

| Grade | IMO 2007/064172-A1 | | C22C38/00 | | 22MnB5 | |
|---|---|---|---|---|---|---|
| | Min | Max | Min | Max | | |
| C | 0.100 | 0.500 | 0.500 | 1.000 | 0.230 | |
| Mn | 0.500 | 4.000 | 0.010 | 2.000 | 1.180 | |
| Si | 0.010 | 1.000 | 1.000 | 2.000 | 0.220 | |
| P | - | 0.010 | - | - | - | |
| S | - | 0.030 | - | 0.012 | - | |
| Cr | Option 1 | | - | - | 0.160 | |
| Nb | Option 2 | | - | - | - | |
| Ni | Option 3 | | - | - | 0.120 | |
| Mo | Option 1 | | - | - | - | |
| V | Option 2 | | - | - | - | |
| Cu | Option 3 | | - | - | - | |
| W | - | 0.300 | - | - | - | |
| Al | 0.100 | - | 0.010 | 2.000 | 0.030 | |
| Ti | Option 2 | | - | - | 0.040 | |
| B | Option 4 | | - | - | 0.002 | |
| N | 0.010 | 0.100 | - | - | 0.005 | |
| Option 1 | Cr and/or Mo 0.010-2.000 | | - | - | - | - |
| Option 2 | Nb, V and/or Ti 0.001-0.100 | | - | - | - | - |
| Option 3 | Cu 0.005-1.000 or Ni 0.005-2.000 | | - | - | - | - |
| Option 4 | B 0.000-0.010 | | - | - | - | - |

Table 2.7b: Results from POSCO (adapted from [15] [91] [92])

| Grade | Thickness (mm) | Condition | E (GPa) | $R_{p0.2}$ (MPa) | $R_m$ (MPa) | $A_u$ (%) | A (%) | $R_m$ |
|---|---|---|---|---|---|---|---|---|
| 22MnB5 | 1.0 | 10 min at 950 °C-water quenched | 243 | 1060 | 1590 | 2.4 | 3.8 ($A_{25}$) | 60 |
| | 1.5 | 15 min at 900 °C-water quenched | 210 | 1202 | 1647 | 2.4 | 4.5 ($A_{25}$) | 74 |
| | 2.8 | 15 min at 950 °C-water quenched | 208 | 1250 | 1649 | 2.8 | 8.1 ($A_{25}$) | 13 |
| IMO 2007/064172-A1 | - | Water quenched | - | 1200 | 1490 | - | 7.9 ($A_{50}$) | 11 |
| | - | Water quenched-paint baked | - | > 1320 | 1690 | - | 7.9 ($A_{50}$) | 13 |
| C22C38/00 | - | Air cooled | - | > 700 | > 920 | - | > 20.0 ($A_{50}$) | 18 |

Claimed mechanical properties for IMO 2007/064172-A1 following water quenching are similar to the referenced 22MnB5. However, with the wide range of possible chemical compositions, a wide range of tensile strength-elongation combinations should be achievable. It is claimed that an enhanced paint bake effect is possible with an additional 120 MPa or more to $R_{p0.2}$ and an additional 200 MPa to $R_m$, but without a sacrifice to elongation. This is thought to be caused mainly by the large nitrogen content.

C22C38/00 has been referred to as a 'high strength elongation sheet steel'. The microstructure is of lath bainite and retained γ-austenite, with the relatively large aluminium and silicon contents giving rise to the latter. With $R_{p0.2}$ > 700 MPa, $R_m$ > 920 MPa and $A_{50}$ > 20 %, this is a very promising lower tensile strength-higher elongation combination compared to 22MnB5. Carbon content is relatively high and manganese content ranges from relatively very low to high. These potentially rich concentrations (giving rise to solid solution strengthening) could account for the ultrahigh strength in the absence of martensite and significant concentrations of other strengthening elements.

*Investigation Five: Yi et al*

The 'dual phase-press forming' (DP-PF) grade was designed [93] that yielded a mixture of allotriomorphic proeutectoid α-ferrite and γ-austenite in the hot stamping condition (i.e. following inter-critical annealing) and that subsequently transformed to an allotriomorphic proeutectoid α-ferrite-martensite dual phase microstructure on quenching. The potential advantage of this dual phase microstructure was cited to be that martensite occurs in a finer morphology compared to exclusive martensite and therefore should improve tensile strength and impact toughness. The concept of dual phase is discussed further in section: Dual Phase.

The chemical composition of the investigated grade is shown in Table 2.8a. The chemical composition of 22MnB5 is presented for benchmarking [15].

Table 2.8a: Investigated grade from Yi et al (chemical compositions in wt % with Fe balanced) (adapted from [15] [93])

| *Grade* | *C* | *Si* | *Mn* | *P* | *S* | *Cr* | *Ni* | *Al* | *Ti* | *B* | *N* |
|---|---|---|---|---|---|---|---|---|---|---|---|
| 22MnB5 | 0.23 | 0.22 | 1.18 | - | - | 0.16 | 0.12 | 0.03 | 0.04 | 0.002 | 0.0050 |
| **DP-PF** | **0.40** | **0.26** | **2.02** | **0.018** | **0.0036** | **-** | **-** | **2.50** | **-** | **-** | **0.0048** |

Compared to 22MnB5, carbon and manganese contents are higher; silicon and nitrogen contents are similar; there are no transition elements present (except manganese); there is no boron; but aluminium content is much higher which assists in maintaining proeutectoid α-ferrite during inter-critical annealing by raising the $Ac_3$ temperature.

Blanks obtained from cold rolled 1.2 mm thick sheet were inter-critically annealed in a nitrogen rich atmosphere at 840, 860, 880 and 900 °C for 3 minutes with the heating rate of 20 °C/s, followed by direct liquid nitrogen quenching at -40 °C/s.

The microstructural results including proeutectoid α-ferrite volume fraction, carbon concentration in martensite, average proeutectoid α-ferrite grain size and average martensite packet size following quenching, are summarised by Table 2.8b. With increased inter-critical annealing temperature, the proeutectoid α-ferrite volume fraction following quenching decreased (a greater volume fraction of pre-existing proeutectoid α-ferrite transformed to γ-austenite, which then hardened to martensite on quenching); the carbon concentration in martensite decreased (this can be attributed to a greater martensite volume fraction, thus the carbon content is more dispersed and the martensite is less concentrated with carbon in any given region); and the proeutectoid α-ferrite grain size increased (due to greater grain growth at elevated temperatures), while the martensite packet size decreased. The microstructural scale of the two phases was said to be remarkably fine given the simple heat treatment and the absence of thermo-mechanical processing. The advantages of a fine dual phase microstructure are explained in the later section: Grain Size.

Table 2.8b: Microstructural results from Yi et al [93]

| *Inter-critical annealing temperature (°C)* | *Proeutectoid α-ferrite (vol. %)* | *Carbon (%) in martensite* | *Average grain diameter (μm) proeutectoid α-ferrite* | *Average packet diameter (μm) martensite* |
|---|---|---|---|---|
| 840 | 38 ± 5 | 64 ± 0.05 | 1.7 ± 0.3 | 1.2 ± 0.1 |
| 860 | 34 ± 9 | 60 ± 0.07 | 1.9 ± 0.1 | 1.1 ± 0.1 |
| 880 | 32 ± 6 | 58 ± 0.05 | 2.4 ± 0.2 | 1.1 ± 0.2 |
| 900 | 26 ± 6 | 54 ± 0.05 | 2.5 ± 0.4 | 1.0 ± 0.1 |

Tensile properties are presented in Table 2.8c. 22MnB5 with comparable thickness of 1 and 1.5 mm and treated to similar conditions (direct water quenching) is presented for benchmarking [15].

Table 2.8c: Tensile results from Yi et al (adapted from [15] [93])

| *Grade* | *Thickness (mm)* | *Condition* | $R_{p0.2}$ *(MPa)* | $R_m$ *(MPa)* | $A_u$ *(%)* | *A (%)* | $R_m \times A$ |
|---|---|---|---|---|---|---|---|
| 22MnB5 | 1.0 | 10 min at 950 °C-water quenched | 1060 | 1590 | 2.4 | 3.8 ($A_{25}$) | 6052 |
| | 1.5 | 15 min at 900 °C-water quenched | 1202 | 1647 | 2.4 | 4.5 ($A_{25}$) | 7412 |
| **DP-PF** | **1.2** | **3 min at 840 °C-nitrogen quenched** | **600** | **1550** | **-** | **8.8 ($A_{50}$)** | **13563** |
| | | 3 min at 860 °C-nitrogen quenched | 600 | 1500 | - | 6.3 ($A_{50}$) | 9375 |
| | | 3 min at 880 °C-nitrogen quenched | 550 | 1475 | - | 6.0 ($A_{50}$) | 8850 |
| | | 3 min at 900 °C-nitrogen quenched | 550 | 1475 | - | 5.5 ($A_{50}$) | 8113 |

Compared to 22MnB5, $R_{p0.2}$ is considerably lower ($\leq$ 600 MPa compared to $\geq$ 1060 MPa) and $R_m$ is slightly lower ($\leq$ 1550 MPa compared to $\geq$ 1590 MPa). The greater difference between $R_{p0.2}$ and $R_m$ (characterised by a smaller $R_{p0.2}/R_m$ ratio) signifies greater work hardening (n-value) intrinsic to the DP-PF grade. If the n-value could be determined, it would be relatively high. This intense work hardening behaviour is expected of dual phase steels [1], with two phases that demonstrate quite different yield strengths. The application of stress at first causes yielding in the weaker/softer proeutectoid α-ferrite matrix only, while the stronger/harder martensite dispersion remains far from yielding, but because the proeutectoid α-ferrite does not occupy the entire microstructure, the specimen as a whole does not reach its $R_m$ as rapidly as it would if entirely of proeutectoid α-ferrite. Thus, the $R_{p0.2}$ signifies yielding of ferritic regions, while the martensitic dispersion effectively 'holds' the microstructure together as the ferritic regions work harden to a great degree. It is only after the ferritic regions have work hardened sufficiently so to transfer adequate stress to the stronger/harder martensite that the latter begins to deform plastically. It is in this fashion that high $R_m$ with relatively low $R_{p0.2}$ is achieved [93].

Following all inter-critical annealing conditions, the DP-PF grade exhibited higher elongation than 22MnB5.

Amongst the DP-PF grade treated to the various conditions, inter-critical annealing at 840 °C yielded the equal highest $R_{p0.2}$ (600 MPa), highest $R_m$ (1550 MPa), highest $A_{50}$ (8.8 %) and thus, highest $R_m \times A$ (13563); with this final property somewhat higher than that of 22MnB5 ($\leq$ 7412).

With lower inter-critical annealing temperature, elongation increased (expectedly as the proeutectoid α-ferrite/martensite ratio increased), but tensile strength also increased (un-expectedly as the proeutectoid α-ferrite/martensite ratio increased). One theory for the tensile strength increase despite a lower martensite volume fraction is reduced grain growth at the lower inter-critical annealing temperature, giving rise to a finer dual phase microstructure post-quenching. The second theory is that of crack percolation [93] – failure occurs when crack percolation is lost through the ductile proeutectoid α-ferrite phase and instead, the crack must breach the brittle martensite phase which leads to catastrophic failure. It was found that a minimum of 29 vol. % proeutectoid α-ferrite is required in the microstructure so that this ductile phase can establish a continuous matrix without interruption by brittle martensite, so that in turn crack percolation through the former phase is maintained and catastrophic failure is avoided. This is demonstrated schematically by Figure 2.24 [93].

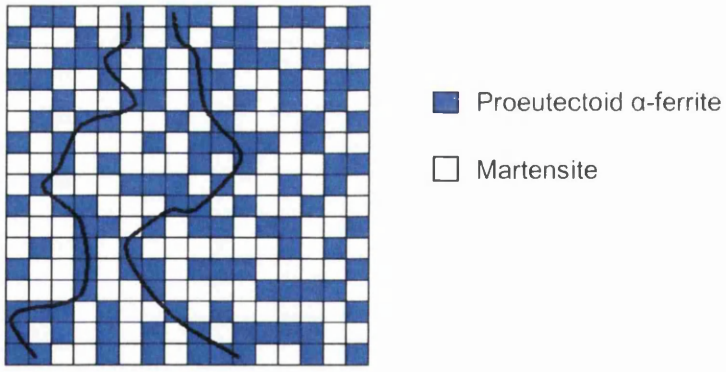


Figure 2.24: Crack percolation theory [93]

It was concluded that it should be possible to improve the DP-PF grade with yet higher elongation by reducing the carbon concentration to 0.3 wt % in order to make the martensite somewhat softer and to yield a higher proeutectoid α-ferrite volume fraction above the crack percolation threshold of 29 vol. %. However, this would involve a compromise for reduced tensile strength.



SWANSEA LIBRARY UNIVERSITY

**Hot Stamping Process Parameters**

***Austenisation***

*Temperature & Time*

When selecting the austenisation temperature, the first task should be to establish the $Ac_3$ since this represents the absolute minimum austenisation temperature possible. The $Ac_3$ mainly depends on chemical composition, where certain alloying elements (γ-austenite stabilisers) have the effect of lowering the $Ac_3$; while other alloying elements (α-ferrite stabilises) have the opposite effect of increasing the $Ac_3$ (Figure 2.23). Besides chemical composition, greater heating rate gives rise to superheating and in turn, a higher $Ac_3$; and heavily deformed microstructures primed for recrystallisation exhibit a lower $Ac_3$ than equiaxed microstructures that have been annealed and are in a closer to equilibrium state [11].

Time-temperature-austenisation (TTA) diagrams [32] and continuous heating transformation (CHT) [33] diagrams graphically represent the above influences, under isothermal conditions and continuous heating conditions respectively. Figure 2.25 [32] presents the 22MnB5 (ThyssenKrupp MBW) TTA diagram from which it can be seen that the completely austenitic microstructure is achieved after $10^3$ seconds with isothermal heat treatment at 800 °C, after $10^1$ seconds with isothermal heat treatment at 850 °C and after 10 seconds with isothermal heat treatment at 875 °C.

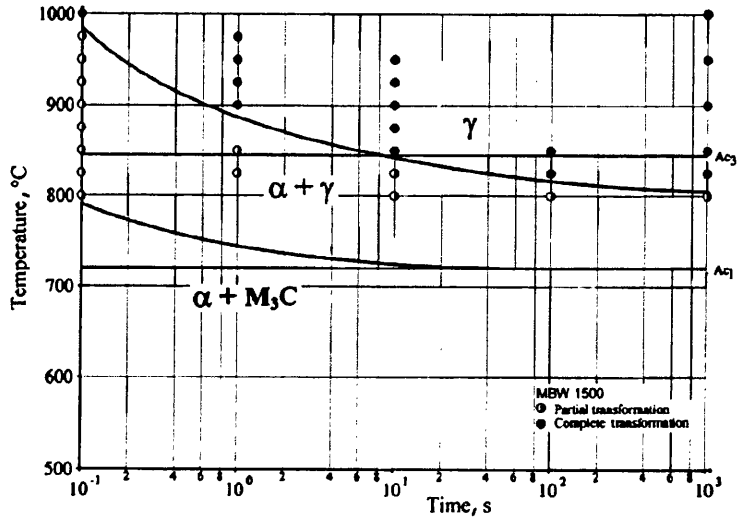


Figure 2.25: 22MnB5 (ThyssenKrupp MBW) TTA diagram [32]

It is desired to maintain the $Ac_3$ as low as possible; chiefly for the energy, time and cost savings (a lower $Ac_3$ can be achieved with a lower soak temperature, which in turn requires less energy to maintain and can be reached more quickly for a given heating rate). Thus, employing a chemical composition rich in γ-austenite stabilisers may be advantageous in this respect. Moreover, γ-austenite stabilisers generally lower the Ms [39] which could preclude auto-tempering [31] (giving rise to higher tensile strength, although lower elongation and impact toughness). However, this would have to be carefully balanced with consideration of the Mf temperature so to ensure that complete martensite formation takes place. As the Ms decreases, generally the Mf also decreases [39]. Thus, if the concentration of Ms depressing alloying elements is too great, Mf will be depressed to a sub-ambient temperature at which complete martensite formation becomes impractical, and rather γ-austenite will be retained. Further, many γ-austenite stabilisers increase quench hardenability [39]. Thus, by employing γ-austenite stabilisers first and foremost so to achieve a lower $Ac_3$ and austenisation temperature, other benefits including avoiding auto-tempering, gaining microstructural refinement and gaining quench hardenability, may be obtained. Furthermore, a lower heating rate is desirable for a lower $Ac_3$, but a lower heating rate increases process time (cost). Heavily deformed microstructures in the as-delivered sheet are desirable for lowering the $Ac_3$, but work hardening inhibits cold formability ahead of hot stamping.

Once the $Ac_3$ has been established, it is then necessary to consider the consequences of exceeding this minimum austenisation temperature. Most consequences can be considered as only beneficial or only detrimental (e.g. greater carbon homogeneity in γ-austenite solid solution can only be considered as beneficial, while greater surface oxidation of uncoated steel can only be considered as detrimental); while others may be considered as beneficial or detrimental depending on the desired mechanical properties in the hot stamped component (e.g. greater auto-tempering during quenching to decrease tensile strength, but increase elongation and impact toughness may be considered as beneficial or detrimental depending on the component and its application). These consequences are summarised in Table 2.9a [14] [15] [31] [62] [63] [64].

Table 2.9a: Consequences of higher austenisation temperature (adapted from [14] [15] [31] [62] [63] [64])

| *Beneficial* | *Detrimental* | *Beneficial or detrimental* |
|---|---|---|
| Greater carbon homogeneity in γ-austenite solid solution, more homogeneous deformation during hot stamping, more homogenous hardening during quenching and more homogenous mechanical properties in the hot stamped component. | Greater γ-austenite grain growth, giving rise to a coarser lath martensite of lower tensile strength and impact toughness. | Higher Ms temperature, potential auto-tempering of martensite during quenching and in turn, lower tensile strength, but higher elongation and impact toughness in the hot stamped component. |
| Greater dissolution of inter-metallic compounds, giving rise to lower tensile strength-higher elongation and greater formability during hot stamping; and greater quench hardenability. | Greater boron homogeneity (intra-granularly) in γ-austenite solid solution, depleting γ-austenite grain boundaries of (inter-granular) boron, which reduces quench hardenability as boron is only effective in increasing quench hardenability if it resides on γ-austenite grain boundaries. | Greater austenitic grain growth, decreasing austenitic grain boundary surface area where the heterogeneous nucleation of reconstructive phase transformations is dominant and thereby, increasing quench hardenability. |
| Greater homogeneity of defects such as voids, inclusions and dislocations, giving rise to more homogenous deformation during hot stamping, more homogenous hardening during quenching and more homogenous mechanical properties with minimal stress concentrations in the hot stamped component. | Greater surface oxidation of uncoated steel, greater tool wear and reduced post-hot stamping coating adhesion and weldability. | |
| Greater transfer window to hot stamping and in turn, greater quench hardenability. | Greater surface decarburisation of uncoated steel. | |
| | Greater energy, time and cost consumption. | |

Austenisation time shares similar characteristics with austenisation temperature. Longer austenisation time for a given austenisation temperature yields the consequences summarised in Table 2.9b [14] [15] [31] [62] [63] [64].

Table 2.9b: Consequences of longer austenisation time (adapted from [14] [15] [31] [62] [63] [64])

| *Beneficial* | *Detrimental* | *Beneficial or detrimental* |
|---|---|---|
| Greater carbon homogeneity in γ-austenite solid solution, more homogeneous deformation during hot stamping, more homogenous hardening during quenching and more homogenous mechanical properties in the hot stamped component. | Greater γ-austenite grain growth, giving rise to a coarser lath martensite of lower tensile strength and impact toughness. | Higher Ms temperature, potential auto-tempering of martensite during quenching and in turn, lower tensile strength, but higher elongation and impact toughness in the hot stamped component. |
| Greater dissolution of inter-metallic compounds, giving rise to lower tensile strength-higher elongation and greater formability during hot stamping; and greater quench hardenability. | Greater boron homogeneity (intra-granularly) in γ-austenite solid solution, depleting γ-austenite grain boundaries of (inter-granular) boron, which reduces quench hardenability as boron is only effective in increasing quench hardenability if it resides on γ-austenite grain boundaries. | Greater austenitic grain growth, decreasing austenitic grain boundary surface area where the heterogeneous nucleation of reconstructive phase transformations is dominant and thereby, increasing quench hardenability. |
| Greater homogeneity of defects such as voids, inclusions and dislocations, giving rise to more homogenous deformation during hot stamping, more homogenous hardening during quenching and more homogenous mechanical properties with minimal stress concentrations in the hot stamped component. | Greater surface oxidation of uncoated steel, greater tool wear and reduced post-hot stamping coating adhesion and weldability. | |
| Greater fusion of coating into substrate, which improves coating-substrate adhesion during and after hot stamping. | Greater surface decarburisation of uncoated steel. | |
| | Greater energy, time and cost consumption. | |

The austenisation time should be tailored to the austenisation temperature and blank thickness so to optimise the listed effects such as carbon homogeneity, boron segregation to grain boundaries, microstructural refinement etc.

It has been shown [60] for 22MnB5 with blank thickness of 3 mm and austenisation temperatures of 850 and 900 °C that maximum as-quenched tensile strength is gained with austenisation times of 3.5 minutes and 1 minute respectively. Moreover, between 3.5 and 7 minutes for both temperatures, relative consistency is gained in as-quenched tensile strength and it is interpreted that as-quenched tensile strength is dramatically lost beyond 7 minutes austenisation

time. For the lower austenisation temperature (850 °C) and below 3.5 minutes austenisation time, inferior as-quenched tensile strength is found, which suggests incomplete martensite formation and/or incomplete dissolution of inter-metallic compounds. Between 3.5 and 7 minutes austenisation time, as-quenched tensile strength slowly decreases and then dramatically decreases beyond 7 minutes austenisation time, which coincides with the grain growth and/or auto-tempering concepts [31]. For the higher austenisation temperature (900 °C) and below 1 minute austenisation time, a dramatic decrease in as-quenched tensile strength is found, which again suggests incomplete martensite formation and/or incomplete dissolution of inter-metallic compounds. Between 1 and 3.5 minutes austenisation time, as-quenched tensile strength quite dramatically decreases, which coincides with the grain growth and/or auto-tempering concepts, although as-quenched tensile strength stabilises beyond 3.5 minutes austenisation time, before dramatically decreasing once more beyond 7 minutes austenisation time.

In agreement with the above [60] is that maximum hardness following hot stamping of 22MnB5 austenised at 950 °C with blank thicknesses of 1, 1.5, 1.75 and 2.5 mm, has been shown [49] to result from austenisation times of 2.25, 2.75, 3 and 4 minutes respectively. Moreover, the greatest martensitic microstructural homogeneity in quenched 22MnB5 with blank thickness of 1.5 mm has been shown [35] to result from austenisation at 900 °C as opposed to 1100 or 1200 °C.

It has been suggested [94] to employ the austenisation time-temperature combination that yields complete austenisation without the onset of γ-austenite grain growth. By this suggestion, for 1.5 mm thick 22MnB5 austenised over 2, 3, 5 or 10 minutes at 850, 900 or 950 °C; 5 minutes at 950 °C was deemed to be optimal (Figure 2.26) [94].

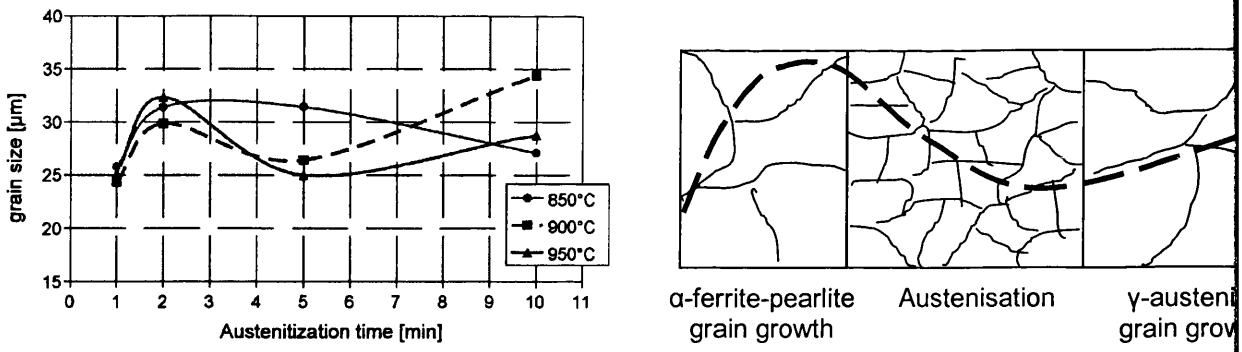


Figure 2.26: Optimal austenisation time-temperature as a function of γ-austenite grain growth [94]

In summary, it has been suggested by multiple sources [15] to employ the austenisation temperature of 20-50 °C above the $Ac_3$ (taking the 22MnB5 $Ac_3$ to be ~ 850 °C with the typical hot stamping heating rate of 10 °C/s). This minimises γ-austenite grain growth, surface decarburisation, surface oxidation, intra-granular boron dissolution, energy consumption and process time; but without excessive compromise to carbon homogeneity, defect homogeneity, inter-metallic compound dissolution and coating diffusion (for coated steel). It also provides a standardised parameter to simplify the situation (temperature is standardised to a constant that depends on the $Ac_3$). Austenisation time then remains as the austenisation variable and can be modified accordingly depending on blank thickness (increased for thicker blanks) or the desire to initiate γ-austenite grain growth and in turn to raise quench hardenability and the Ms temperature for the occurrence of auto-tempering and enhanced elongation and impact toughness.

*Dual Phase*

To achieve a complete transformation to martensite and in turn, maximum tensile strength following hot stamping, the blank must be completely austenised by transforming the entirety of the microstructure to γ-austenite. This is achieved by maintaining the $\geq Ac_3$ temperature for the necessary time, before hot stamping and rapid quenching, with the latter stage transforming (essentially) the entirety of the austenitic microstructure to martensite. However, martensite is inherently susceptible to limited ductility, with a typical total elongation of just 4-8 % in 22MnB5. Improvement to elongation in purely martensitic microstructures without notable chemical composition alterations, is limited. Moreover, such chemical composition alterations have to be pursued with experiment and analysis; and

likely alloying additions; all of which adds expense. Subsequent heat treatments to hot stamping such as post-quench tempering can improve elongation [89], but involve further energy, equipment, floor space and time demands, also adding to expense. Moreover, unconstrained heat treatment may alter the geometry of the hot stamped component, annihilating one of the virtues of hot stamping.

The concept of dual phase can provide a means of achieving improved elongation in the hot stamped component [93], but without costly alloying additions or additional heat treatment stages. Indeed, chemical compositions may even be altered towards economy (fewer alloying additions), as quench hardenability is less desirable.

The 'dual phase' terminology refers to the microstructure of proeutectoid α-ferrite and martensite and moreover, only these two phases (a microstructure of any two other phases is strictly not to be termed 'dual phase') [1]. The proeutectoid α-ferrite volume fraction is typically 70-80 vol. % and forms a continuous matrix that encompasses a uniform dispersion of martensite. When the proeutectoid α-ferrite volume fraction exceeds 80 vol. %, the microstructure is sometimes termed 'partially martensitic' [1].

The dual phase microstructure (although not termed 'dual phase' at the time) was first recognised in 1937 when the patent [95] for a new 'bearing' steel exhibiting the ferritic-martensitic microstructure was filed.

The 1960s saw further development of ferritic-martensitic steels. Two reports [96] [97] detailed the advantages of combining proeutectoid α-ferrite with martensite. During the beginning of deformation, the martensite does not plastically deform, since the stress is below the yield strength of this 'hard' phase. Stress is accommodated by the 'softer' proeutectoid α-ferrite. As stress is accommodated by the proeutectoid α-ferrite, it work hardens. It is only after the proeutectoid α-ferrite has work hardened to a great degree that stress is transferred to the harder martensite. This is beneficial since the harder martensite has limited ductility. Thus, if the harder martensite begins to plastically deform late in the deformation

process, its high strength can be exploited without the compromise of low ductility. Essentially, the high strength of the harder phase is reserved for late in the deformation process. This phenomenon has been termed 'composite deformation behaviour' [98]. The ferritic-martensitic microstructure was analogised to a fibre reinforced plastic composite material, with martensite analogous to the fibres and proeutectoid α-ferrite analogous to the polymeric matrix.

The 1970s saw much interest from the United States in low alloy steels that could be heat treated to present the ferritic-martensitic microstructure. It was in this period that the 'dual phase' term was established [99].

The 1990s saw the introduction of AHSS; including dual phase (DP) AHSS [1]. Owing to mass development associated with AHSS, DP steels became established with the arrival of several different DP grades exhibiting different mechanical properties (e.g. DP 600, DP 800 and DP 1000). Moreover, development of DP steels continues in 2014.

The dual phase microstructure may be achieved via two methods [3]: 1) controlled cooling; or 2) inter-critical annealing.

Controlled cooling (Figure 2.27a) involves complete austenisation (i.e. at a temperature $\geq Ac_3$ so to transform the entirety of the microstructure to γ-austenite) followed by controlled cooling to a temperature in the $Ar_3$-$Ar_1$ range so to yield a precise volume fraction of proeutectoid α-ferrite. The controlled cooling may be continuous, or a 'gap' temperature in the $Ar_3$-$Ar_1$ range may be maintained for a precise duration (typically 4-6 seconds) in the fashion of isothermal heat treatment. Quenching to below Mf then follows controlled cooling so to transform the remaining γ-austenite (that which did not transform to proeutectoid α-ferrite) to martensite. The controlled cooling method of producing the dual phase microstructure is typically employed on the run out table following hot rolling to produce hot rolled DP steels [3].

Inter-critical annealing (Figure 2.27b) involves partial austenisation of typically a ferritic-pearlitic microstructure, at a temperature between the $Ac_1$ and $Ac_3$. Here, only carbon rich microconstituents (carbide) readily transform to γ-austenite, while the low carbon microconstituent (proeutectoid α-ferrite) is more easily retained and does not transform to γ-austenite as abruptly. The concentration of proeutectoid α-ferrite that is retained during inter-critical annealing depends on the absolute temperature: temperatures closer to the $Ac_1$ give rise to greater proeutectoid α-ferrite retention, while temperatures closer to the $Ac_3$ give rise to greater proeutectoid α-ferrite transformation to γ-austenite. Quenching to below Mf then follows inter-critical annealing, but only the γ-austenite hardens to martensite, while the retained proeutectoid α-ferrite persists. The inter-critical annealing method of producing the dual phase microstructure is typically employed during the annealing cycle following cold rolling to produce cold rolled DP steels [3].

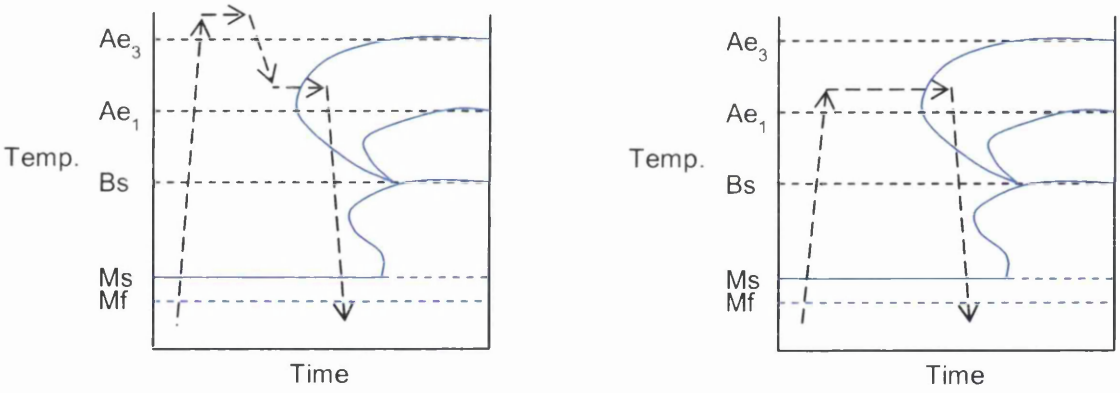


(a) Controlled cooling (b) Inter-critical annealing

Figure 2.27: Heat treatment cycles for producing DP steels

Depending on the ratio between the two phases, total elongation can be improved by up to 100 % (although with reduced tensile strength) compared to completely martensitic microstructures [31].

It has been stated [15] that a finer and more uniform dual phase microstructure with improved tensile strength, elongation and impact toughness is obtained from the inter-critical annealing method. However, the controlled cooling method also offers advantages, particularly to hot stamping: 1) the soak (austenisation)

temperature can be maintained constant on the hot stamping line, for both completely martensitic components and dual phase components; 2) steels exhibiting chemical compositions of greater economy (fewer alloying additions) can be exploited as quench hardenability is less desirable; and 3) the tailor welded blank concept can be exploited – this is indeed the case with ArcelorMittal's Usibor 1500 and Ductibor 500 grades [14]; sheets of the two grades are welded to form the tailor welded blank which is then austenised at 900-950 °C and hot stamped with a uniform quench rate. However, the higher quench hardenability of Usibor 1500 gives rise to complete martensite formation, while the lower quench hardenability of Ductibor 500 gives rise to a ferritic-martensitic microstructure.

The effect of inter-critical annealing on 22MnB5 (ThyssenKrupp MBW) with blank thickness of 1.5 mm, has been shown [32]. The soak time was a constant at 6 minutes as the soak temperature was varied over 780, 810 and 950 °C ($Ac_1$ ~ 720 °C and $Ac_3$ ~ 880 °C); transfer time was 9 seconds and press closing time was 15 seconds with a force of 3.8 MPa. The cooling rate was not mentioned, but assumed consistent between specimens. Tensile properties following quenching are shown in Table 2.10. Inter-critical annealing gave rise to lower tensile strength, but higher elongation. Further, reduced inter-critical annealing temperature (780 rather than 810 °C) gave rise to yet lower tensile strength, but yet higher elongation.

The increase to uniform elongation from inter-critical annealing was particularly significant – from the complete austenisation temperature of 950 °C to the inter-critical temperature of 780 °C, total elongation increased from 6.0 to 10.0 %, while uniform elongation increased from 4.5 to 9.0 % and with uniform elongation becoming closer to total elongation. By reviewing the $R_m \times A_{80}$ index, the optimal combination of tensile strength and elongation can be found from the 780 °C inter-critical temperature.

Table 2.10: Influence of inter-critical annealing on hot stamped 22MnB5 tensile properties (adapted from [32])

| *Soak temp. (°C)* | *$R_e$ (MPa)* | *$R_m$ (MPa)* | *$A_u$ (%)* | *$A_{80}$ (%)* | *$R_m \times A_{80}$* |
|---|---|---|---|---|---|
| 780 (inter-critical) | 500 | 1050 | 9.0 | 10.0 | 10500 |
| 810 (inter-critical) | 850 | 1110 | 6.5 | 8.0 | 8880 |
| 950 | 1050 | 1550 | 4.5 | 6.0 | 9300 |

*Alternative Austenisation Techniques*

Austenisation is traditionally conducted by an electric or gas fired roller hearth furnace of 30-40 m in length, with a combined heating and soaking time of ~ 10 minutes [1] [15] [20]. Alternative austenisation techniques are under development [23] [100] [101] [102], including resistance [103] [104] [105] [106], induction [107] [108], mixed furnace-induction [109], localised ('tailored heating') [110] and in-press [105] variants. The alternative austenisation techniques endeavour to reduce austenisation time, reduce energy consumption, reduce floor space, improve environmental sustainability, improve economy, improve microstructural homogeneity and/or tailor austenisation to specific regions of the blank.

***Hot Stamping***

*Deformation Force*

Increasing deformation force from 20 to 40 MPa in hot stamping 22MnB5 (with austenisation time of 3 minutes at 950 °C and blank thickness of 3 mm) has been shown [111] to increase proof strength of the hot stamped component by 10-20 % and ultimate tensile strength by 1-2 %, but with no consistent loss to elongation.

*Deformation Rate*

Deformation rate can be measured by two parameters: 1) punch descent rate; and 2) blank strain rate.

The influence of punch decent rate has been considered [94] with 22MnB5; blank thickness 1.5 mm, austenised at 900 °C for 5 minutes and hot stamped with a 60 mm punch stroke. The die, punch and blank holder were maintained at ambient temperature at the commencement of hot stamping while the punch decent rate was varied across 1, 5 and 10 mm/s. Six thermocouples were located on an extended flange of the blank (Figure 2.28a) [94] in order to record temperatures and in turn, to estimate the volume fraction of γ-austenite remaining at different

stages during the punch decent. Since the thermocouples were positioned on the blank flange and not actually in the deformed region (where heat transfer from blank to tooling takes place directly), these temperatures were exaggerated with respect to the probable temperatures within the deformed region. Consequently, the volume fraction of γ-austenite remaining in the deformed region was likely to have been lower than that in the flange at any given time during deformation. Thus, the results need to be extrapolated to the deformed region and provide only an estimate of the phenomena occurring in the deformed region.

The results from thermocouple three are shown in Figure 2.28b [94] and reveal that the minimum punch decent rate that ensures all deformation (to the 60 mm maximum punch stroke) takes place with a significant volume fraction of γ-austenite present is 20 mm/s. With a punch decent rate of 10 mm/s, the γ-austenite volume fraction is close to zero during the final 20 mm of the punch stroke. Thus, by maximising the punch descent rate, the volume fraction of γ-austenite remaining during the hot stamping stage is increased. Most notably, this aids formability since the FCC structured γ-austenite is more formable than all potential transformation products. Moreover, it was suggested that this also increases quench hardenability for a given chemical composition. This is discussed further in section: Quench Hardening.

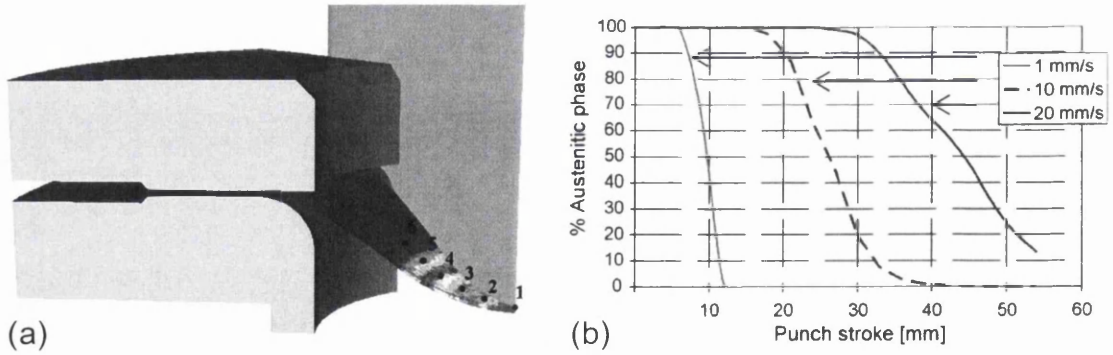


Figure 2.28: Influence of punch decent rate (a) location of thermocouples on blank (b) punch stroke-γ-austenite volume fraction for thermocouple three [94]

While punch decent rate is simply proportional to the rate at which force is applied to the punch and is therefore a directly controllable variable, blank strain rate is dependent on several factors and is not a directly controllable variable. Strain rate

is dependent on [35]: 1) material specific true stress-true strain (flow) behaviour and therefore, can vary from one steel grade to another; 2) absolute strain as strain rate can vary at different strains within a single deformation process; 3) specimen thickness; and 4) temperature. Thus, blank strain rate can vary even if the punch decent rate is maintained constant. The further complication is that strain rate can vary across a single blank, giving rise to numerous local strain rates rather than one universal strain rate across the entire blank [35].

It has been suggested [35] that increasing strain rate results in more transformation nuclei and thus finer martensite on quenching, where microstructural refinement of lath martensite increases strength without decreasing impact toughness [31].

Under isothermal deformation, increased strain rate increases true strength and (generally) decreases true strain [35] and therefore can be said to reduce formability. However, under anisothermal deformation (as in hot stamping) the relationship between strain rate and formability is more arbitrary. This is demonstrated by Figure 2.29 [94] which plots true stress-true strain curves for 22MnB5 with several strain rates, an initial (pre-deformation) temperature of 800 °C, a final (post-deformation) temperature of 600 °C and a cooling rate of -40 °C/s (typical hot stamping temperature range and cooling rate).

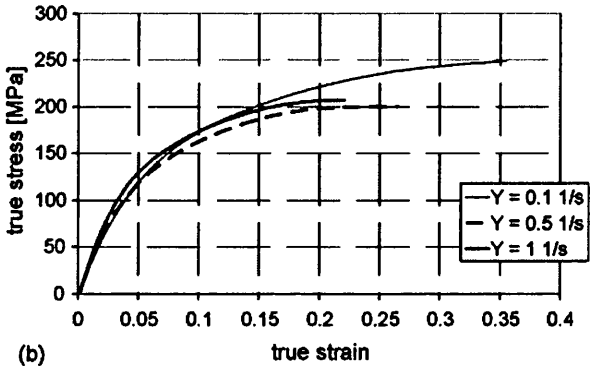


Figure 2.29: True stress-true strain 22MnB5 with different strain rates and continuous cooling (-40 °C/s) from 800 to 600 °C [94]

In conclusion, the deformation rate should be maximised so to establish: 1) maximum γ-austenite volume fraction during hot stamping and in turn, maximum formability and subsequent martensite formation [94]; 2) maximum transformation nuclei and in turn, fine lath martensite of high strength and impact toughness [31]; and 3) no impairment on flow behaviour (formability) under anisothermal deformation [94].

*Deformation Temperature*

Deformation temperature can be controlled by the austenisation temperature, the transfer time from austenisation to hot stamping, the residual press temperature and the deformation rate. Increasing austenisation temperature, decreasing transfer time, increasing residual press temperature and/or increasing deformation rate, raises the deformation temperature.

Generally, as temperature increases, true strength decreases and true strain increases, giving rise to enhanced formability. This is true under isothermal and anisothermal deformation [35]. Thus, higher deformation temperature during hot stamping is advantageous for greater formability.

Traditionally, the press is maintained at ambient temperature. However, the press temperature can be raised by heating the punch and/or die prior to inserting the blank.

The influence of punch temperature has been considered [94] with 22MnB5, blank thickness 1.5 mm, austenised at 900 °C for 5 minutes and hot stamped with a 60 mm punch stroke. The die and blank holder were maintained at ambient temperature at the commencement of hot stamping, the punch descent rate was maintained at 20 mm/s, while the punch temperature at the commencement of hot stamping was set at ambient (~ 20 °C) or 300 °C. Six thermocouples were located on an extended flange of the blank (Figure 2.30a) [94] in order to record temperatures and in turn, to estimate the volume fraction of γ-austenite remaining at different stages during the punch decent. It should be remembered that lower temperatures and in turn, lower γ-austenite volume fractions would have been

present in the deformed region where faster cooling through direct conductive heat transfer to the tooling would have commenced. Thus, the flange region in which measurements were recorded serves only as an estimate of the deformed region.

The results from thermocouples 1, 3 and 5 are shown in Figure 2.30b [94] and reveal that for all three thermocouple locations, the volume fraction of γ-austenite remaining at most stages of the punch descent was greater with the raised punch temperature. In other words, with the punch maintained at ambient temperature at the commencement of hot stamping, the volume fraction of γ-austenite decreased rapidly during the punch descent. In contrast, with the punch maintained at 300 °C at the commencement of hot stamping, the volume fraction of γ-austenite decreased more slowly during the punch descent so that at later stages of the punch descent there was a greater volume fraction of γ-austenite remaining. Thus, by raising the punch temperature, the volume fraction of γ-austenite remaining throughout the hot stamping stage is increased. Most notably, this aids formability since the FCC structured γ-austenite is more formable than all potential transformation products. Moreover, it was suggested that this also increases quench hardenability for a given chemical composition. This is discussed further in section: Quench Hardening.

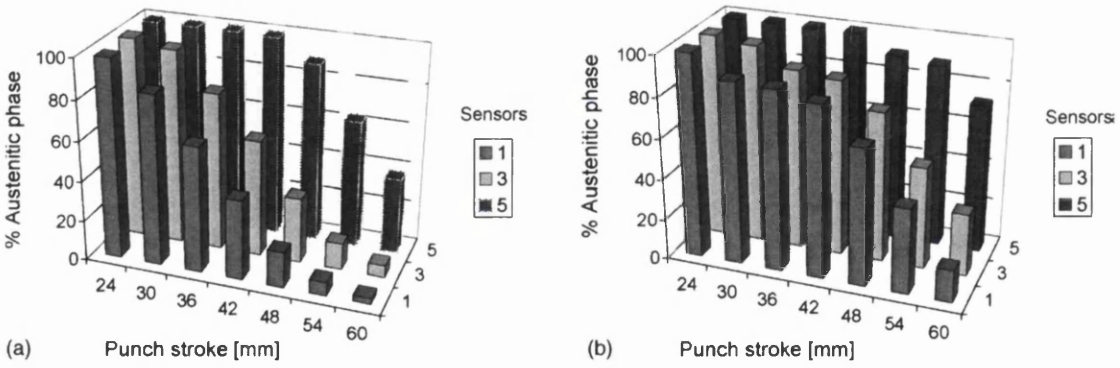


Figure 2.30: γ-austenite decomposition during hot stamping with punch at (a) ambient temperature (~ 20 °C) and (b) 300 °C at commencement of hot stamping [94]

*Pre-Strain*

Deformation of γ-austenite at high temperature during hot stamping can have considerable consequences to the kinetics of subsequent phase transformations. This is an important consideration when assessing CCT diagrams as such diagrams (used to anticipate the kinetics of phase transformations) are generally obtained under pure thermal treatment, by heating and cooling a static (non-deformed) specimen.

The influence of pre-strain in the γ-austenite phase, on dilatation (which can be used to measure martensite formation) during quenching of 22MnB5 has been investigated [112]. The results demonstrated that pre-strain of up to 80 % at temperatures between $Ar_3$ and $Ar_1$ followed by quenching at -280 °C/s, enhances γ-austenite retention and proeutectoid α-ferrite formation; and reduces martensite formation significantly. Microstructural analysis revealed that the pre-strained specimen exhibited 20-40 vol. % proeutectoid α-ferrite, while the non-strained specimen (simply quenched without pre-strain) exhibited essentially 100 vol. % martensite.

In a second investigation [112], it was revealed that the Ms temperature was lowered by 25-70 °C with increased pre-strain from 16 to 39 % (assuming all other parameters equal).

In a third investigation [112], it was found that with severe pre-strain (80-100 %) between $Ar_3$ and $Ar_1$, followed by continuous cooling at -50 °C/s, much lower final flow stress (800-950 MPa) was obtained compared to that obtained from a non-strained isothermal transformation (1650-1900 MPa). It was also observed that strain induced proeutectoid α-ferrite with an ultrafine grain size can be formed by severe γ-austenite pre-straining (> 80 %) slightly above the $Ar_3$.

In evaluation of the three investigations, it was suggested [112] that the reason for the drastic decrease in martensite formation and corresponding increase in proeutectoid α-ferrite formation with γ-austenite pre-strain, could be that as the deformation energy of the γ-austenite increases (particularly at lower

temperatures close to the $Ar_3$), the kinetic driving force for transformation to proeutectoid α-ferrite is increased. Then, as proeutectoid α-ferrite forms and rejects carbon into the remaining γ-austenite, the Ms of the remaining γ-austenite is lowered, leading to probable γ-austenite retention. Thus, the result is strain induced proeutectoid α-ferrite and retained γ-austenite, rather than martensite. Another theory for γ-austenite retention is mechanical stabilisation by pinning of the austenitic microstructure with dislocations.

Another investigation [67] considered the influence of γ-austenite pre-strain (8 or 17 % at 800, 700 or 600 °C) on the transformation kinetics, resulting microstructure and hardness of quenched 22MnB5. Tests were performed with standard tensile specimens of 50 mm gauge length, 1.75 mm thickness and with a constant strain rate of 0.08 $s^{-1}$. All specimens were austenised for 4 minutes at 950 °C. Quenching was performed with compressed air and the quench rate was varied by changing the air pressure from 1 to 7 bar with 1 bar increments. The range of experimental conditions is summarised in Table 2.11 [67].

Table 2.11: Range of experimental conditions to establish the influence of γ-austenite pre-strain on the transformation kinetics of quenched 22MnB5 [67]

| *Temperature at beginning of quench (°C)* | *Pre-strain (%)* | *Air pressure for quenching (bar) [Quench rate (- °C/s)]* | | | | | | | |
|---|---|---|---|---|---|---|---|---|---|
| | | 1 | 2 | 3 | 4 | 5 | 6 | 7 | 8 |
| 950 | 0 | [22] | [32] | [49] | [57] | [63] | [68] | [73] | [101] |
| 800 | 8 | [21] | [30] | [45] | [52] | [59] | [67] | [72] | [100] |
| | 17 | | | | | | | | |
| 700 | 8 | [9] | [23] | [39] | [45] | [50] | [58] | [66] | [77] |
| | 17 | | | | | | | | |
| 600 | 8 | [3] | [8] | [15] | [26] | [32] | [39] | [45] | [51] |
| | 17 | [6] | [15] | [28] | [6] | [40] | [48] | [54] | [63] |

It was found that pre-strain increased the potential for reconstructive proeutectoid α-ferrite formation, while the displacive transformation to martensite was suppressed to lower temperatures. This supposed strain induced proeutectoid α-ferrite formation and resulting enrichment of the remaining γ-austenite with carbon, which then lowers the residual Ms, is in agreement with the dilatation investigation [112] mentioned previously.

The pre-strain investigations [67] [112] demonstrate that γ-austenite deformation that takes place during hot stamping before quench hardening, modifies the transformation kinetics from the non-strained condition. Chiefly, the modifications include: 1) accelerating proeutectoid α-ferrite formation to shorter times; and 2) lowering the Bs and Ms temperatures. Figure 2.31 [67] summarises the modifications in the context of the CCT diagram, where the solid transformation curves represent pure thermal treatment without mechanical deformation and where the dashed transformation curves represent thermal treatment with mechanical deformation.

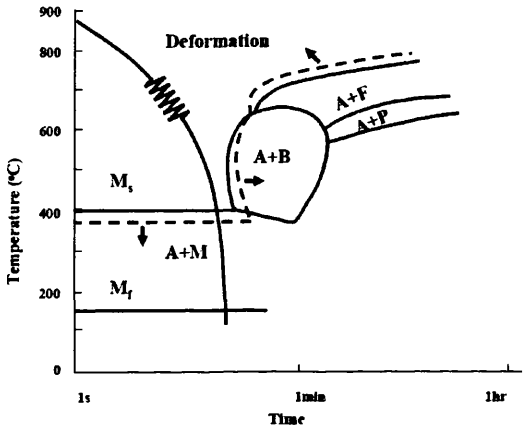


Figure 2.31: Effect of γ-austenite deformation on the CCT diagram [67]

The extent of the modifications to the CCT diagram is dependent on the degree of deformation and the temperature at which the deformation takes place, being most pronounced with a greater degree of deformation and with deformation taking place in the region of $Ar_3$-$Ar_1$. The modifications must be considered when evaluating CCT diagrams generated under pure thermal treatment without the inclusion of mechanical deformation; and also when defining hot stamping process parameters. The CCT diagram generated under pure thermal treatment may depict adequate quench hardenability for hot stamping. However, when the mechanical deformation intrinsic to hot stamping is introduced, quench hardenability may no longer be adequate. When complex component geometries with deep stamping depths are desired (which demand the most severe degree of deformation), the modifications become even more significant.

In conclusion, to avoid γ-austenite retention and/or strain induced proeutectoid α-ferrite formation and thus, to achieve maximum martensite formation, it has been suggested [15] that the consequences of γ-austenite deformation (mechanical stabilisation of γ-austenite and/or strain induced proeutectoid α-ferrite or granular bainite formation) should be insignificant or annihilated before the temperature reaches the $Ar_3$. This means that hot stamping should take place at a high temperature comfortably above the $Ar_3$ where recrystallisation and elimination of dislocations is profuse and where the thermodynamic driving force for γ-austenite decomposition to proeutectoid α-ferrite is low. An alternative and perhaps more industrially practicable concept is that hot stamping takes place below the $Ar_1$. In other words, rapid quenching from the austenisation temperature to below the $Ar_1$ before hot stamping commences. With Ms and Mf at ~ 410 and ~ 200 °C respectively (22MnB5) and the necessity to complete all hot stamping before reaching Mf (and ideally Ms), this would leave a very narrow temperature range in which to complete all hot stamping. However, the lower deformation temperature, close to Ms, would coincide with the theory [31] that states that this condition results in greater transformation nuclei and in turn, finer martensite. Conversely, for the purpose of producing ultrafine proeutectoid α-ferrite in the final microstructure and in turn, for a lower tensile strength-higher elongation dual phase hot stamped component, γ-austenite deformation slightly above the $Ar_3$ would be desired. By refining the deformation temperature, perhaps into the $Ar_3$-$Ar_1$ range, γ-austenite retention might be possible, leading to yet further mechanical property combinations in the hot stamped component.

***Quench Hardening***

The quench rate is probably the most important parameter throughout the hot stamping process [31] since a higher quench rate permits: 1) complete martensite formation for a chemical composition of lower quench hardenability, which may aid economy, formability, coatability and weldability while obtaining equivalent mechanical properties; 2) a finer microstructure; and 3) reduced process time.

Besides component geometry, the quench rate is determined by quench type, quench medium, press thermal conductively, press temperature and deformation rate [31].

*Quench Type*

Traditionally, the quench type is indirect: the quench medium and hot stamped component do not make direct contact with each other. Rather, the quench medium is circulated through the punch and/or die and it is the conductive heat transfer from the hot stamped component to the cooled tooling that has the quench effect.

By the direct type of quenching (which has long been employed in other hot forming and heat treatment processes such as quenching of hot rolled sheet on the run out table), the quench medium and component do make direct contact with each other. This is achieved by the 'still bath' method in which the component is submersed in a bath of the liquid quench medium, or by the 'flash' method in which the component is sprayed with jets of the gaseous or liquid quench medium (as on the run out table) [113].

It has been demonstrated [15] that direct quenching generally gives rise to higher tensile strength-lower elongation compared to indirect quenching, which is believed to result from the greater quench rate of the direct type, leading to greater martensite formation and/or a finer microstructure. Further, for the majority of investigated steels [15], the optimal tensile strength-elongation combination (characterised by the $R_m \times A$ index) was achieved with direct quenching. Thus, it is desired to incorporate direct quenching into hot stamping. However, by virtue of press geometry, maintaining forming forces and ensuring homogeneous quenching, incorporating direct quenching into hot stamping is a difficult task.

The solution has been trialled [114] wherein a so called 'quench press' was developed containing an intrinsic direct oil quenching system. The quench press (Figure 2.32a) [114] was used for hot stamping a high carbon flex plate engine component with blank thickness of 6.7 mm and with a critical cooling rate of -100

°C/s. Oil (which may be at ambient temperature, although theoretically any quench medium at any suitable temperature could be employed) is injected from a centre hole in the die and circulates with direct contact with the tooling and the hot stamped component. To enable the oil to achieve this circulation and contact, the punch and die exhibit 5 mm deep, concave-shaped dimples which collect with oil (Figure 2.32b) [114]. Since oil inflows from a centre hole and outflows to the circumference of the hot stamped component, the quench rate may be controlled by injection pressure of the oil (with greater injection pressure, the quench rate increases) in addition to the initial temperature of the oil. An outer guide plate may also be installed to introduce backflow of the oil to the outer region of the hot stamped component.

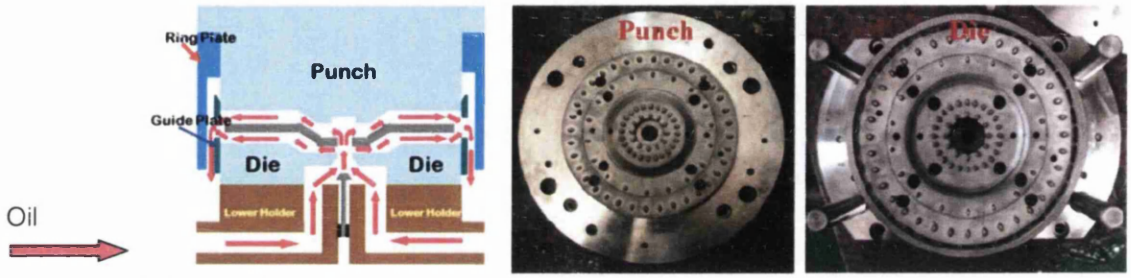


(a) Quench press (b) Punch and die faces

Figure 2.32: Hot stamping with direct quenching [114]

*Direct Quench Media*

There are four common direct quench media [11]: air, oil, water and brine; with the severity of quench (quench rate) increasing from air to brine. However, in addition to producing the desired quench rate, the quench must avoid heterogeneity, cracking and warping.

Water can be used to quench low-mild carbon, low alloy steels; but does not produce optimal results with higher carbon or high alloy steels [113]. It has been shown [60] that direct water quenching of 22MnB5 with blank thickness of 3 mm produces a quench rate of more than -80 °C/s in the range of 800-500 °C. However, water absorbs large quantities of atmospheric gases and when a hot component is quenched, these gases have a tendency to form bubbles on the component surface and in turn, reduce the quench rate [113]. Moreover, bubbles

can collect in holes or recesses and locally reduce the quench rate, leading to 'soft spots' and in turn, cracking or warping as adjacent regions quench, harden and dilate more severely [113].

Brine (salt water) exhibits lower absorption of atmospheric gases compared to water, so that the evolution of bubbles on quenching is minimised. As a result, brine wets the surface more homogeneously and generates a greater and more homogenous quench rate [113]. In addition, brine removes a large percentage of any oxide scale that may be present [113]. The brine solution should contain 7-10 % salt [113]. Low-mild carbon, low alloy steels can be quenched in brine solution without cracking or warping [113].

Of the liquid quench media, oil is the least severe [113]. Oil is used for high carbon and high alloy steels where brine or even water is too severe, leading to cracking or warping [113]. In fact, provided that the desired martensite volume fraction can be obtained (the critical cooling rate can be achieved), oil is the preferred quench medium for all steels [113]. It has been shown [60] that direct oil quenching of 22MnB5 with blank thickness of 3 mm produces a quench rate of more than -40 °C/s in the range of 800-500 °C.

Natural air is the least severe quench medium, although compressed air may be used to increase the quench rate closer to that of oil or to concentrate quenching on specific areas of the component [113]. It has been shown [60] that direct compressed air quenching of 22MnB5 with blank thickness of 3 mm produces a quench rate of more than -25 °C/s in the range of 800-500 °C.

In addition to chemistry of the quench medium, agitation of the quench medium (e.g. by pumps in the still bath method or by increased pressure in the flash method) or movement (oscillation) of the component, increase the quench rate and quench homogeneity by breaking up the gas layer that forms an insulating blanket between the quench medium and the component [113].

*Indirect Quench Media*

There are two common indirect quench media: water and liquid nitrogen. It has been demonstrated [15] that liquid nitrogen generally gives rise to higher tensile strength-lower elongation compared to water, which is believed to result from the higher quench rate of the former, leading to greater martensite formation and/or a finer microstructure. Further, for the majority of investigated steels [15], liquid nitrogen gave rise to the superior tensile strength-elongation combination (characterised by the $R_m \times A$ index).

*Press Thermal Conductivity*

By maximising thermal conductivity of the tool material, the quench rate can be increased [31] [115]. Moreover, different tool materials that exhibit different thermal conductivities can be exploited to produce tailed properties in the single component. This has been investigated [116] where the 'modular tool system' consisted of multiple tool sequences fabricated from different tool steels exhibiting thermal conductivities from 7 W/mK up to 66 W/mK. In this fashion, the quench rate can be raised in the regions of the component corresponding to the tool sequences fabricated from tool steels exhibiting higher thermal conductivities (so to maximise martensite formation), while the quench rate can be lowered in the regions of the component corresponding to the tool sequences fabricated from tool steels exhibiting lower thermal conductivities (so to encourage proeutectoid α-ferrite or bainite formation).

*Press Temperature*

The influence of press temperature was introduced with respect to deformation temperature (section: Deformation Temperature), where increased press temperature was seen to result in greater deformation in the γ-austenite phase and a greater volume fraction of γ-austenite remaining at the end of the hot stamping stage, before going into the quench hardening stage (Figure 2.30). Here, the influence of press temperature with respect to quench rate shall be considered further.

Increasing press temperature may increase quench hardenability for a given chemical composition since more γ-austenite is present to rapidly quench harden when the punch has fully descended its stroke [94]. In other words, a greater volume fraction of γ-austenite is retained at the end of the hot stamping stage and is then quenched to martensite during the quench hardening stage.

Contrary to the above suggestion is that any residual heat from raised press (deformation) temperature during the hot stamping stage would raise the press temperature during the quench hardening stage and thereby, decrease the quench rate. Indeed, this has been considered [31] with 22MnB5, in which the press temperature was raised from ambient to 200 °C prior to hot stamping. The results revealed that increased press temperature decreased ultimate tensile strength (approximately 1550 down to 1475 MPa) and increased total elongation (approximately 5 up to 6 %) in the hot stamped component. This was considered to result from reduced quench rate owing to residual heat from raised press temperature, which did not prevent complete martensite formation (the critical cooling rate was still achieved), but rather enabled auto-tempering of martensite.

Following the above finding, tooling with both heating and cooling channels, which enables localised temperature control of the hot stamped component (Figure 2.33) has been considered [117]. This concept is also known as 'tailor quenching' [118]. In the simplified example shown by the figure, the central region of the hot stamped component that requires maximum tensile strength for anti-intrusive crash performance, can be maintained at relatively low temperature during the hot stamping stage, maximising the quench rate during the quench hardening stage and giving rise to higher tensile strength-lower elongation in the final component. Simultaneously, the peripheral regions of the hot stamped component that require maximum formability due to greater geometric complexion; and possibly higher elongation for impact energy absorptive crash performance, can be maintained at relatively high temperature during the hot stamping stage, reducing the quench rate during the quench hardening stage and giving rise to lower tensile strength-higher elongation in the final component.

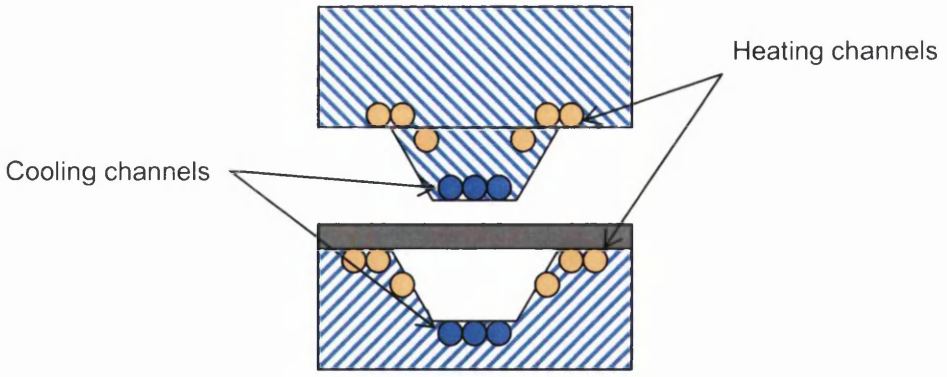


Figure 2.33: Tailor quenching with heating and cooling channels (adapted from [117])

Traditionally, the cooling channels in the tooling are linear (Figure 2.34a) [119]. Thus, for geometrically complex components, there are areas that are directly in-line with the linear cooling channels (which receive the greatest quench rate) and other areas that are not directly in-line with the linear cooling channels (which receive a lower quench rate). Thus, heterogeneous quenching can result. However, tooling with curved cooling channels that follow the contours of the punch and die has been developed (Figure 2.34b) [119]. The curved cooling channels are claimed to result in more homogeneous quenching since the indirect quench medium is distributed across a greater area of the hot stamped component (including the geometrically intricate areas) rather than concentrated in localised regions.

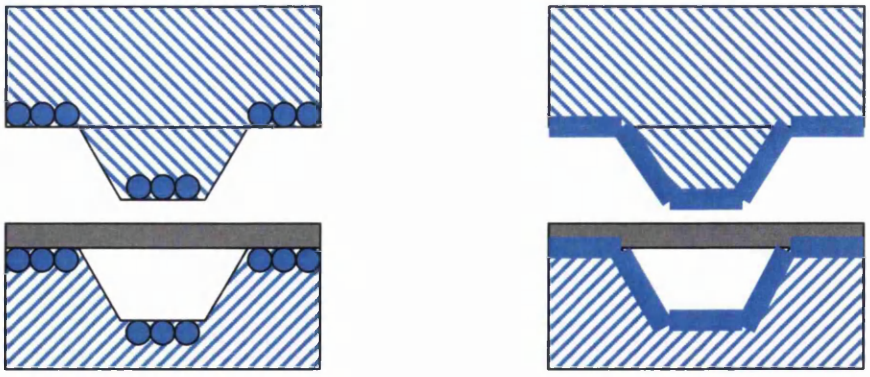

(a) Linear cooling channels (b) Curved cooling channels

Figure 2.34: Hot stamping with (a) linear cooling channels and (b) curved cooling channels (adapted from [119])

Heterogeneous quenching can also result from dissimilar boundary conditions between the hot stamped component and the tooling in different regions (which causes different heat transfer rates). Micrographs illustrating microstructural heterogeneity resulting from dissimilar boundary conditions and in turn, heterogeneous quenching, are illustrated in Figure 2.35 [15]. The microstructure in the linear regions of the hot stamped component (the base, mid-section and upper section) where contact between the hot stamped component and tooling was greater, is fully martensitic. In contrast, in the corner of the hot stamped component where contact between the hot stamped component and tooling was lesser, a significant volume fraction of bainite has developed. Hence, any efforts that can be made to homogenise quenching through press temperature control are desirable.

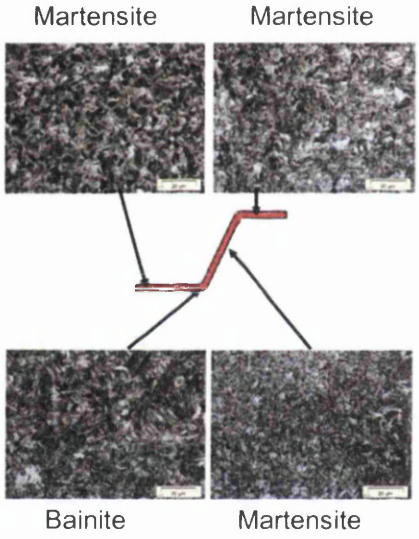


Figure 2.35: Microstructural heterogeneity due to heterogeneous quenching [15]

The further consideration relating to press temperature and consequential quench rate is the accumulation of residual heat over multiple hot stamping cycles. This has been investigated [32] in which the ejection temperatures (the temperature at the end of the quench hardening stage at which point the hot stamped component is ejected from the press) of the punch and B-pillar component were analysed by thermal imaging over 20 hot stamping cycles; that is, 20 B-pillars were consecutively hot stamped and the temperature evolution in the punch and each of the 20 B-pillars at the point of component ejection from the press, was measured. The steel was 22MnB5 (ThyssenKrupp MBW) with blank thickness of

1.5 mm, austenised at 925 °C for 6 minutes before transfer to the press in 8 seconds. The press did not include an active cooling system (it was a conventional press) and remained closed during the quench hardening stage for 9 seconds. The B-pillar component was subsequently ejected and the punch and component (ejection) temperatures were measured by thermal imaging at three selected points corresponding to the centre and each end of the B-pillar geometry (Figure 2.35) [32]. Due to the time required for temperature measurements, hot stamping cycles were carried out every 8 minutes (it is worth considering that this is considerably longer than in industrial practice in which hot stamping cycles are carried out continuously. Thus, the evolution of temperature is likely to be underestimated by this investigation). The evolution of temperature in the punch and components over the 20 hot stamping cycles is illustrated by Figure 2.36 [32].

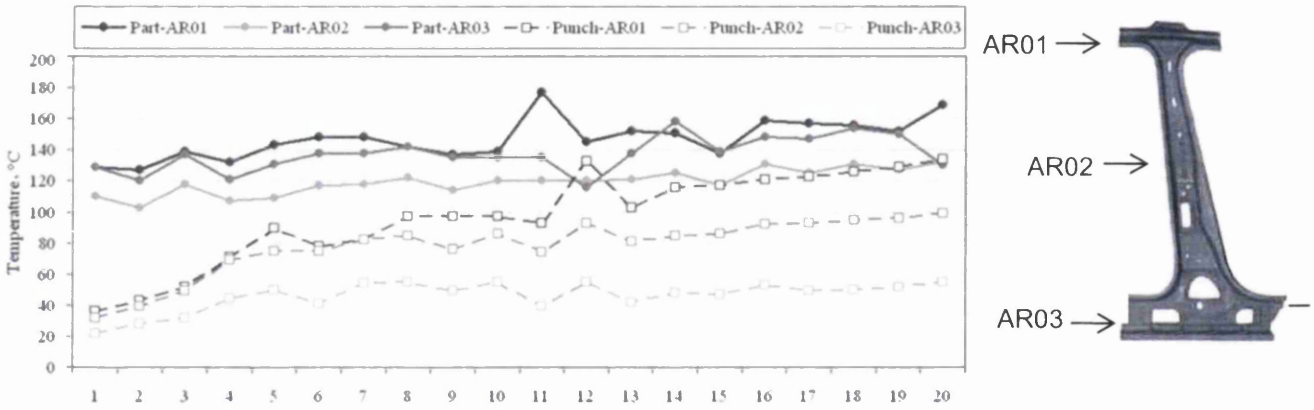


Figure 2.36: Hot stamping cycle-temperature evolution of punch and component [32]

The component temperature increased locally by a maximum of 50 °C (AR01 cycle 1: 130 °C to cycle 11: 180 °C) between the first and twentieth cycles, with the maximum local temperature reaching 180 °C (AR01 cycle 11). In contrast to the relatively small temperature increase in the components over the 20 hot stamping cycles, the punch temperature increased by a greater degree, with a maximum local temperature increase of 100 °C (AR01 cycle 1: 35 °C to cycle 20: 135 °C) and with the maximum local temperature reaching 135 °C (AR01 cycle 20). The clear temperature increase in the punch and each successive component was due to residual heat accumulating from one hot stamping cycle to the next.

For the component and the punch, temperature increase over the 20 hot stamping cycles was highest in the region corresponding to the upper section of the B-pillar geometry (AR01) and lowest in the region corresponding to the lower section of the B-pillar geometry (AR03). This was due to different local geometry, different mass conditions and in turn, different heat transfer rates in different sections of the B-pillar. The upper section of the B-pillar exhibits a narrow geometry and thus, relatively low mass. Heat is then transferred from this section of the B-pillar to the press more rapidly compared to the lower section which exhibits a wider geometry and greater mass. Hence, over successive hot stamping cycles, the punch temperature in the region corresponding to the narrow upper section of the B-pillar increases more rapidly compared to the region corresponding to the wider lower section of the B-pillar. The faster temperature increase in this region of the punch then results in a lower cooling rate in the corresponding upper section of the B-pillar over successive hot stamping cycles.

Tensile properties were measured in the B-pillars produced from the first, tenth and twentieth hot stamping cycles (Table 2.12). Tensile specimens were taken from the centre section (AR02) and upper section (AR01) of each B-pillar. For the first, tenth and twentieth hot stamping cycles, higher tensile strength can be seen in the centre section (AR02) compared to the upper section (AR01). For the tenth and twentieth hot stamping cycles, higher elongations can also be seen in the centre section (AR02) compared to the upper section (AR01). For both the centre section (AR02) and upper section (AR01), tensile strength generally decreases while elongation remains similar from the first hot stamping cycle to the tenth hot stamping cycle and to the twentieth hot stamping cycle. These effects can be attributed to the rising punch temperature from one cycle to the next (more pronounced in the region corresponding to the upper section of the B-pillar), lowering the quench rate and/or increasing the Ms temperature; leading to a coarser martensite of lower tensile strength.

Table 2.12: Tensile properties as a function of hot stamping cycle [32]

| Section | Cycle 1 | | | Cycle 10 | | | Cycle 20 | | |
|---|---|---|---|---|---|---|---|---|---|
| | $R_{p0.2}$ (MPa) | $R_m$ (MPa) | $A_{50}$ (%) | $R_{p0.2}$ (MPa) | $R_m$ (MPa) | $A_{50}$ (%) | $R_{p0.2}$ (MPa) | $R_m$ (MPa) | $A_{50}$ (%) |
| AR01 | 1005 | 1460 | 6.6 | 1001 | 1450 | 4.9 | 980 | 1420 | 5.3 |
| AR02 | 1035 | 1480 | 5.2 | 1019 | 1493 | 6.0 | 992 | 1477 | 5.8 |

*Deformation Rate*

The influence of deformation rate was introduced with respect to punch descent rate, where increased punch descent rate was seen to result in greater deformation in the γ-austenite phase and a greater volume fraction of γ-austenite remaining at the end of the hot stamping stage, before going into the quench hardening stage (Figure 2.28). Here, the influence of punch descent rate with respect to quench rate shall be considered further.

By increasing the punch descent rate, the overall quench rate from the beginning of the hot stamping stage to the end of the quench hardening stage is raised – the sooner the hot stamping stage is complete, the sooner the quench hardening stage can begin and the greater the overall quench rate. An alternative view is that more γ-austenite is present to rapidly quench harden to martensite once the punch has fully descended its stroke, rather than gradually transforming to 'softer' phases during a leisurely punch descent. This could potentially enable more economical chemical compositions (of lower quench hardenability) for the same degree of martensite formation [94], or finer martensite for the same chemical composition [31]. Further, increasing punch descent rate reduces process time and thereby aids efficiency.

***Post-Quench Heat Treatment***

It must be stated from the outset that post-quench heat treatment involves further energy, equipment, floor space and time demands; and thus, adds to expense. Further, unconstrained post-quench heat treatment may alter the geometry of the hot stamped component, annihilating one of the virtues of hot stamping. Thus, the added expense must be justified by the metallurgical advantages, while geometric modification must be avoided, either by the post-quench heat treatment temperature being suitably low or by introducing the post-quench heat treatment while the component remains constrained in the press.

*Tempering*

Tempering is the post-quench heat treatment process in which a martensitic microstructure is heated to and maintained at an elevated temperature (typically in the range of 250-650 °C) for a given duration [11]. This gives rise to the tempered martensite microconstituent, which can exhibit significantly higher ductility and impact toughness than as-quenched martensite, yet with minor strength sacrifice [11].

Tempering broadly includes the following stages [11] [31] [120] [121] [122]. However, it should be remembered that the chemical composition of the given steel alloy can dramatically influence the precise temperature at which each stage occurs. Moreover, it is worth noting that the numerous stages may overlap.

*Stage 1 – 50-120 °C:* Interstitial carbon atoms begin to diffuse through martensitic supersaturated solid solution and segregate at defects where they form carbon clusters.

*Stage 2 – 120-200 °C:* Transition carbides are precipitated from the carbon clusters. Transition carbides represent metastable precursors to the equilibrium carbide, cementite/θ-carbide ($Fe_3C$). The transition carbides include ε-carbide ($Fe_{2.4}C$) and various double carbides [$(MFe)_XC$]. The associated partial relief of supersaturating carbon atoms also results in 'decomposed martensite'.

In common with as-quenched martensite, decomposed martensite is supersaturated with carbon and exhibits the BCT crystal structure. However, due to the partial carbon relief, decomposed martensite is less supersaturated and closer in crystallography to BCC α-ferrite. Thus, decomposed martensite is sometimes termed 'weakly tetragonal α-solid solution'.

The precipitation of transition carbides usually requires little carbon. Thus, the majority of carbon atoms remain in supersaturated solid solution.

In high carbon steels, precipitation of the first transition carbides can occur during stage 1, even at such low temperatures that are not usually associated with diffusion and precipitation of inter-metallic compounds. This is possible since the precipitation of transition carbides during stage 1 occurs by a semi-displacive mechanism that does not require the diffusion of substitutional atoms (including iron), but rather, relies on the diffusion of carbon atoms only, which as highly mobile interstitial solutes, is possible at such low temperatures. The semi-displacive precipitation of transition carbides corresponds to paraequilibrium in which the iron/substitutional solute ratio is maintained constant (substitutional atoms do not redistribute), but carbon atoms are able to redistribute. This is a similar process to that which occurs during the precipitation of carbides in bainite formation.

Conversely to the above, in low carbon steels or indeed any steel containing a very high defect density, stage 2 and the precipitation of transition carbides may be bypassed with the direct precipitation of cementite in stage 4.

*Stage 3 – 100-500 °C:* Retained γ-austenite decomposes into an aggregate arrangement of α-ferrite and carbide. The α-ferrite-carbide aggregate is comparable to bainite. However, the carbide component may be represented by numerous transition carbides prior to cementite (similar to stage 2): ε-carbide[26] (200-400 °C) and η-carbide[27] (400-500 °C) have been recognised. The transition carbides eventually transform to cementite at ~ 500 °C.

*Stage 4 – 260-700 °C:* Precipitation of cementite occurs from the residual martensite (that did not decompose during stage 2) and from the decomposed martensite (resulting from stage 2). Transition carbides (resulting from stage 2) transform to cementite, while the decomposed martensite loses tetragonality to assume the equilibrium BCC crystal structure. Moreover, the α-ferrite-carbide

---

[26] ε-carbide resulting from retained γ-austenite decomposition exhibits the variable chemical composition $Fe_{2\text{-}2.4}C$ and the HCP crystal structure.

[27] η-carbide resulting from retained γ-austenite decomposition also exhibits the variable chemical composition $Fe_{2\text{-}2.4}C$, but with the orthorhombic crystal structure (in common with cementite).

(cementite) aggregate resulting from retained γ-austenite decomposition (stage 3) homogenises. This combination of events gives rise to a stable microstructure of a (generally) continuous α-ferrite matrix embedded with a fine uniform dispersion of cementite crystals and is termed 'tempered martensite'.

At first, the cementite crystals may exhibit a Widmanstätten needle-like morphology, with length and diameter of up to 200 and 15 nm respectively; and have a defined crystallographic orientation relationship with the α-ferrite matrix. With continued tempering, changes to the cementite crystals' morphology occur by an Ostwald ripening process, where the smaller crystals dissolve into the α-ferrite matrix and liberate carbon for the selective growth of larger crystals. As cementite crystals grow, the needle-like morphology is replaced with a spherical morphology. Simultaneously, dislocation structures undergo recovery and the α-ferrite matrix can recrystallise, giving rise to an equiaxed grain structure.

The strength and hardness of tempered martensite arise from the large phase boundary area per unit volume that exists for the very fine cementite dispersion. The hard cementite crystals reinforce the soft α-ferrite matrix in the vicinities of the phase boundaries and prevent or reduce localised plastic deformation in these regions. Moreover, the phase boundaries act as barriers to dislocation movement. The ductility and impact toughness arise from the α-ferrite matrix. Furthermore, impact toughness is enhanced by the impediment to crack propagation by the fine cementite dispersion. Graphitising agents such as aluminium and silicon inhibit stage 4.

*Stage 5 – 480-700 °C:* The fifth stage is arguably beyond the tempering process, but rather, encroaches on separate processes of precipitation hardening and/or spheroidisation [11]. Nevertheless, these phenomena are worthy of consideration in relation to tempering.

Precipitation hardening may arise from alloy compounds (carbides, nitrides and carbonitrides) of vanadium, titanium, molybdenum and chromium etc. Suitable alloy additions are therefore necessary for precipitation hardening to occur [11].

Precipitation hardening following tempering gives rise to a hardness increase following the initial hardness decrease of tempering and is thus sometimes termed 'secondary hardening' [11]. In other words, primary hardening corresponds to martensite formation on quenching. During the earlier stages of tempering in which transition carbides and cementite are precipitated from supersaturated solid solution, hardness decreases, since carbon provides a greater hardening effect when in martensitic supersaturated solid solution than it does when in transition carbides or cementite. However, alloy compounds yielded during precipitation hardening can see hardness increase back towards that of the as-quenched condition.

In contrast to the hardening effect of precipitation hardening, a softening effect may be encountered from spheroidisation, where the cementite crystals coarsen to such a degree that the microstructure is no longer of tempered martensite, but rather of a new microconstituent termed 'spheroidite'.

Spheroidite is the microconstituent characterised by a continuous α-ferrite matrix containing sphere-like cementite crystals [11]. Spheroidite is usually obtained by isothermal heat treatment of a pearlitic or bainitic microstructure at a temperature just below the $Ac_1$, but can also supersede tempering. Maintained at this elevated temperature, atomic diffusion rates become appreciable so that the α-ferrite and cementite crystals of the precursor pearlitic or bainitic microstructure decompose and then reform in the spheroidal microstructure as atoms move via diffusion into their new positions. Superseding tempering, the spheroidal microstructure is achieved by over coarsening of the cementite crystals. The thermodynamic driving force behind spheroidisation is the reduction in phase boundary area between the α-ferrite and cementite phases and thus, the reduction in interfacial free energy [11].

As with all heat treatments, the variables of tempering are temperature and time. Once the martensite has completely transformed to tempered martensite (α-ferrite and cementite), an increase to either tempering temperature or tempering time increases the size of the cementite crystals, since the growth rate or growth

duration respectively, is increased. With greater cementite crystal growth, strength hardness and impact toughness decrease; while elongation increases as the α-ferrite-cementite phase boundary area is reduced. Spheroidisation represents the marked reduction in strength and hardness [11].

The benefits of post-quench tempering 37MnB4 were reported in section: Naderi et al (Table 2.5b) [89]. Further investigations [31] [123] have also presented such benefits. This highlights the desire to include a post-quench tempering stage in hot stamping.

*Precipitation Hardening*

As far as it is known, the introduction of post-quench precipitation hardening to hot stamped boron steels has not been investigated. However, precipitation hardening is an established strengthening mechanism in other steels (e.g. austenitic stainless steels and maraging steels) and other alloys (e.g. aluminium-copper alloys) [11].

Precipitation hardening is the process by which sufficiently alloyed steels are strengthened and hardened by a fine uniform dispersion of second phase, alloy, precipitated particles within the original, solid solution matrix phase [11].

Although precipitation hardening shares similarities with tempering, there are subtle yet distinct differences between the two. Most notably, tempering is a 'softening' mechanism to achieve increased ductility and impact toughness, although at the expense of decreased strength and hardness relative to the pre-tempered state. Conversely, precipitation hardening is a 'hardening' mechanism to achieve increased strength and hardness, although at the expense of decreased ductility relative to the pre-precipitation hardened state.

The generic precipitation hardening process is accomplished by three separate heat treatment stages [11]:

*Stage 1 – solution heat treatment:* In the solution heat treatment stage, all alloying elements are dissolved to form a single phase, homogeneous solid solution. In hot stamping, this corresponds to the austenisation stage.

*Stage 2 – quenching:* Solution heat treatment is followed by a rapid quench to a relatively low temperature, where the quench rate is rapid enough and the quench temperature is low enough so that any atomic diffusion and the accompanying formation of stable phases such as proeutectoid α-ferrite, pearlite and alloy compounds by time dependent diffusional nucleation and growth processes, are for all intents and purposes, prevented. Thus, a metastable situation exists in which the microstructure consists of supersaturated martensite and/or retained γ-austenite. In hot stamping, this corresponds to the quench hardening stage.

*Stage 3 – precipitation heat treatment:* During precipitation heat treatment (also termed 'aging') the metastable microstructure is heated to and held at an intermediate temperature between the solution heat treatment temperature and the quench temperature. At this intermediate temperature, atomic diffusion rates become appreciable and through a sequence of atomic rearrangement, segregation, clustering and precipitate transition, alloy compounds begin to form as finely dispersed precipitated particles. After the appropriate 'aging time' at this constant 'aging temperature', the specimen is cooled to ambient. Normally, this cooling rate is not an important factor for direct precipitation characteristics, although may alter other microstructural characteristics such as grain size (a very slow cooling rate may permit greater grain growth). In hot stamping, the precipitation heat treatment stage corresponds to the post-quench heat treatment.

# RESEARCH OBJECTIVES

The demands from the automotive industry for materials exhibiting greater sophistication were demonstrated in chapter: Introduction. These demands primarily include greater formability in the as-delivered condition, yet greater strength and/or impact toughness in the final component; to enable manufacturing of down gauged and thus lighter automotive structural body components so to improve fuel efficiency, yet with improved crash performance.

How hot stamped boron steels (22MnB5) have met the demands from the automotive industry was demonstrated in chapter: Literature Review. The highly formable, high temperature austenitic microstructure that is maintained throughout the forming stage of the hot stamping process permits down gauging while not compromising forming limits. Moreover, the high formability permits component consolidation, where welded assemblies consisting of multiple, individually cold formed components, can be consolidated in one single, geometrically complex hot forming operation. Component consolidation reduces process time (cost), reduces weight and increases structural strength. The ultrahigh strength martensitic microstructure resulting in the final component permits down gauging while not compromising anti-intrusive crash performance. Forming above the proeutectoid α-ferrite recrystallisation temperature of ~ 750 K (477 °C) where high temperature transient creep deformation is permitted; the martensitic transformation which releases the stress imposed during forming; and geometric constraint on the component throughout quenching, all contribute to the elimination of springback. Further, the above can be achieved with mild carbon low alloy steels, thereby aiding economy, formability, weldability and coatability.

However, it is reported by experts within the automotive steel industry that hot stamped 22MnB5 is now widely regarded as a commodity product. Moreover, it is reported that demand exists for steels that exhibit higher tensile strength and/or higher elongation values following hot stamping compared to 22MnB5, where higher tensile strength can provide improved anti-intrusive crash performance and thus enable down gauging of anti-intrusive structural body components; and

where higher tensile strength and/or higher elongation can provide higher impact toughness, improved impact energy absorptive crash performance and thus, enable down gauging of impact energy absorptive structural body components. For these reasons, novel grades for automotive hot stamping technologies must be developed. The worldwide interest in developing novel grades for hot stamping was also demonstrated in chapter: Literature Review.

The overall objective of the research reported in this thesis was to develop novel grades for automotive hot stamping technologies that demonstrated novel mechanical properties following hot stamping. Broadly, these properties were divided into three categories: 1) higher tensile strength; 2) higher elongation; and 3) higher tensile strength-higher elongation, compared to 22MnB5. These properties would fill the ultimate tensile strength-total elongation range targeted by the steel and automotive industries (Figure 1.1).

By achieving the above objective it was hoped to: 1) meet the escalating demands from the automotive industry for materials that exhibit greater strength and/or impact toughness in the final component; 2) expand application of hot stamped steels to the entire range of automotive structural body components that require different crash performance characteristics; 3) maintain steel as the material of choice of the automotive industry; and 4) establish Tata Steel as the leading manufacturer of steels for hot stamping.

The objective was to be achieved through evaluating steel parameters and hot stamping process parameters. In this context, steel parameters primarily included chemical composition, while hot stamping process parameters primarily included those of the austenisation stage. The parameters of the transfer, hot stamping and quench hardening stages were of lesser interest, since these parameters are mostly dictated by the hot stamping line design or press design and therefore, are beyond control of the Materials Engineer.

Following literature review, experimental grades and hot stamping process parameters could be specified. The experimental grades and hot stamping

process parameters were then subjected to laboratory investigation. Details of the above are presented in chapter: Experimental.

The overall research objective was divided into the following sub-objectives:

- Evaluate existing Tata Steel laboratory hot stamping facilities and identify potential enhancements through literature review.
- Determine hot stamping potential of Tata Steel commercial dual phase steels through literature review and laboratory investigation.
- Determine chemical compositions and hot stamping process parameters for higher elongation variants compared to 22MnB5, through literature review and laboratory investigation.
- Determine chemical compositions and hot stamping process parameters for higher tensile strength variants compared to 22MnB5, through literature review and laboratory investigation.
- Further laboratory investigation, including dynamic tensile testing, three-point bend testing and FEM crash simulation on the most successful outcomes from preliminary laboratory investigation.

# EXPERIMENTAL

## Investigated Grades

The series of investigated grades is presented in Table 4.1. Included in the series is the commercial Tata Steel 22MnB5, which was considered as the control grade since it is the conventional grade for hot stamping and for which a collection of published data and expected results exist (e.g. critical phase transformation temperatures, critical cooling rate and mechanical properties). Thus, 22MnB5 was used to validate: 1) the experimental procedures employed by comparing yielded results to expected results; and 2) the hot stamping potential of the experimental grades.

Experimental grades included three existing commercial grades and seven bespoke trial grades. Commercial grades are those that were industrially produced by Tata Steel Europe. Trial grades are those that were tailor-designed and laboratory produced by Tata Steel Research Development & Technology UK specifically for the research programme. The laboratory production process involved vacuum batch casting of ingots weighing approximately 30 kg with approximate geometry of 550×110×38 mm. The cast ingots were subsequently cut into blocks with approximate geometry of 55×110×38 mm. The blocks were reheated to 1250 °C and soaked for 3 hours. Following the soak time, the blocks were hot rolled to sheet with thickness of 2 mm via seven passes through a single stand, two high reversing mill. Target finishing temperature was 850 °C. The hot rolled sheet was cooled to a simulated 'coiling' temperature with target of 630 °C on the run out table and with line speed of 160 mm/s. The sheet at ~ 630 °C was placed in the furnace set at 630 °C, the furnace was switched off and both furnace and sheet steel were permitted to naturally cool to ambient temperature. This final stage was to simulate the slow cooling of a coil in industrial production.

The hot band with thickness of 2 mm was then cold reduced by 25 % to exhibit cold rolled thickness of 1.5 mm. Cold rolling was achieved via several passes through a single stand, two high reversing mill.

All investigated grades exhibited cold rolled thickness of 1.5 mm (except for one commercial grade that exhibited cold rolled thickness of 2 mm). Employing grades of equal cold rolled thickness was desirable for consistency. Moreover, 1.5 mm is typical cold rolled thickness of as-delivered sheet steel for hot stamping.

Significant differences with respect to chemical composition between the 22MnB5 control grade and each experimental grade are highlighted in Table 4.1.

Carbon equivalent (CEN) of each investigated grade was calculated according to Equation 2.13. Carbon equivalent is illustrated by Figure 4.1.

The experimental grades can be divided into three categories:

1) XMnB5 (where 'X' represents carbon content in tenths of percent).
2) 25MnB5 (X) (where 'X' represents molybdenum, vanadium or nickel).
3) Dual Phase.

***XMnB5***

The XMnB5 category consisted of 15MnB5, 25MnB5, 29MnB5 and 38MnB5. These four experimental grades shared the same base chemical composition as the 22MnB5 control grade, except for lower carbon content (15MnB5) or higher carbon content (25MnB5, 29MnB5 and 38MnB5). Thus, the primary objective of the XMnB5 category was to determine the influence of carbon content on the base MnB5 chemical composition.

It is widely known that carbon increases the strength/hardness of martensite more dramatically than any other alloying element on a weight-for-weight basis [39]. Carbon introduces precipitation hardening potential as carbides may be precipitated [39], where carbides may also serve to restrict austenitic grain growth and thereby, refine the quenched microstructure, where microstructural refinement of lath martensite has been reported to increase strength without decreasing impact toughness [31]. Carbon increases quench hardenability [39], where it has been suggested that quench hardening with a cooling rate somewhat greater than the critical achieves a finer martensitic microstructure [31]. Moreover,

greater quench hardenability intrinsic to the chemistry may allow for a complete transformation to martensite without such a great requirement for austenitic grain growth, also giving rise to a finer martensitic microstructure. Carbon lowers the Ms temperature while the $Ar_1$ temperature remains unchanged [39], which can provide a greater (metastable) austenitic hot stamping window. Furthermore, it has been reported that with more than 0.2 wt % carbon, auto-tempering of martensite becomes significantly more probable during quenching (owing to increased carbon saturation and the lower Mf temperature), which can provide enhanced elongation and impact toughness while maintaining strength [31].

Since carbon content was significantly below 0.6 wt % for each of the XMnB5 grades, martensite was expected to be predominantly of the lath character rather than the plate character [39]. Lath martensite is preferential since the sub-structures constituted by packets, blocks and laths provide strength and impact toughness in a microstructural refinement mode. Additionally, since carbon content was below 0.35 wt % (or close to in the case of 38MnB5), the substitutional alloying elements dissolved in martensitic supersaturated solid solution were expected to contribute significantly to martensitic hardness, where it has been reported that with more than ~ 0.35 wt % carbon, the contribution to martensitic hardness by the dissolved substitutional alloying elements is deteriorated [39].

It is also worthy to note that carbon represents one of the most economical alloying elements. Further, maintaining the base chemical composition approximately equal to that of the 22MnB5 control grade, except for modification to the content of just one alloying element (carbon), is attractive from the perspective of industrial logistics should the experimental grades reach commercialisation.

The above factors formed the basis for the inclusion of grades 25MnB5, 29MnB5 and 38MnB5. These grades were targeted to meet the higher tensile strength objective.

However, it is also widely known that increased carbon content degrades weldability and elongation. These negative attributes of carbon content formed the basis for the inclusion of grade 15MnB5. It was anticipated that limited quench hardenability intrinsic to the 15MnB5 chemistry would give rise to a partially martensitic or dual phase ferritic-martensitic microstructure following hot stamping, exhibiting higher elongation compared to martensitic 22MnB5. Moreover, since carbon content was below 0.15 wt %, it was expected that the martensite would be entirely of the lath character [39]. These factors, combined with the fundamental higher elongation that is known to arise from decreased carbon content (owing to reduced interstitial solid solution strengthening), were targeted to meet the higher elongation objective. Moreover, a ferritic-martensitic microstructure and relatively low carbon equivalent would provide improved weldability over 22MnB5. This might be exploited in the tailor welded blank concept to assist joining of the hot stamped component to adjacent components of the automotive body structure.

***25MnB5 (X)***

The 25MnB5 (X) category consisted of 25MnB5 (Mo), 25MnB5 (V) and 25MnB5 (Ni). These three experimental grades shared the same base chemical composition as the 25MnB5 experimental grade, except for the independent additions of molybdenum, vanadium and nickel, respectively. Thus, the primary objective of the 25MnB5 (X) category was to determine the influence of independent molybdenum, vanadium and nickel additions to the base 25MnB5 chemical composition.

Molybdenum is known to exhibit a strong carbide forming affinity [39], which can be exploited to limit austenitic grain growth (leading to a finer quenched microstructure) and to maintain boron in solid solution (thereby maximising the boron quench hardenability effect). The carbide forming affinity of molybdenum can also contribute towards precipitation hardening. Molybdenum increases quench hardenability strongly when dissolved in γ-austenite solid solution [39]. Moreover, German steel and automotive component manufacturer Benteler has reported [68] that molybdenum addition to boron steel increases fatigue strength.

Vanadium addition was investigated for its similar chemical characteristics to molybdenum. Moreover, vanadium is known to exhibit a stronger carbide forming affinity than molybdenum [39] and is also known to increase quench hardenability more strongly than molybdenum when dissolved in γ-austenite solid solution [39].

Nickel does not form carbides [39]. However, nickel is reported to increase impact toughness, especially in martensitic steels [39]. Moreover, nickel is known to introduce substitutional solid solution strengthening and quench hardenability [39].

Grades 25MnB5 (Mo), 25MnB5 (V) and 25MnB5 (Ni) were targeted to meet the higher tensile strength-higher elongation objective.

***Dual Phase***

The Dual Phase category consisted of DP 600, DP 800 and DP 1000. The three DP steels were commercial grades and thus, exhibited pre-defined chemical compositions and cold rolled thicknesses. The primary objective of the Dual Phase category was to determine the hot stamping potential of commercial DP steels.

There is much interest in extending the application of DP steels to hot stamping. This is due to the following reasons:

- DP steels represented the first generation AHSS introduced to the mainstream steel and automotive industries in the late 1990s and development of these steels continues in 2014. Thus, these steels are established and understood.
- Extending the application of existing commercial DP steels to hot stamping, rather than producing new grades, is attractive from the production, logistical and ultimately, financial viewpoints of the steel manufacturer.
- The tensile properties of the highest strength DP grades (e.g. DP 1400) have proven to be similar to those tensile properties of 22MnB5.
- The collection of DP grades has proven to offer a wide range of tensile properties, from lower tensile strength-higher elongation, to higher tensile strength-lower elongation.

- While it may be argued that ultrahigh strength 'higher elongation' alternatives to hot stamped boron steels already exist, such as TRIP steels, it should be noted that these steels exhibit rich chemical compositions (approximately 1.5 wt % silicon and aluminium combined, which is typically 5 to 8 times the combined silicon and aluminium content of boron and DP steels), which degrade economy and severely degrade weldability. TRIP steels require the steel manufacturer to undertake complex and lengthy heat treatment regimens in order to obtain the desired microstructures in the as-delivered sheet steels, degrading economy further. For these reasons combined, TRIP steels have experienced limited uptake by the automotive industry compared to boron and DP steels, which are used extensively throughout the automotive body structure. Moreover, conventionally cold formed steels such as TRIP steels suffer from springback and limited formability compared to hot stamped steels.
- The ferritic-martensitic microstructures and/or lower carbon equivalents of DP steels compared to martensitic boron steels (giving rise to superior weldability) might be exploited in the tailor welded blank concept to assist joining of the hot stamped component to adjacent components of the automotive body structure.

Moreover, literature [15] has suggested that DP 800 may exhibit hot stamping potential as a lower tensile strength-higher elongation alternative to 22MnB5. It has also been suggested that if quench hardenability of DP 800 could be increased, similar tensile strength-higher elongation may be obtained compared to 22MnB5. Thus, the DP steels were targeted to meet the higher elongation objective.

However, it must be acknowledged that the DP steels exhibit expensive chemical compositions compared to boron steels. Investigating the hot stamping potential of the DP steels was of interest for the listed reasons, in addition to academic reasons. However, it was anticipated that the mechanical properties to be obtained from the DP steels could be obtained from a low-mild carbon boron steel (15MnB5), where the latter exhibits a more economical chemical composition.

Thus, the proposal with respect to the DP steels was as follows: 1) determine the mechanical properties of the hot stamped DP steels; 2) determine the market demand for such mechanical properties; and 3) endeavour to replicate such mechanical properties with a low-mild carbon boron steel (if market demand for such mechanical properties warrants production of a new 'stand-alone' grade).

Table 4.1: Chemical compositions (wt %) of investigated grades (Fe balanced) – blue = control grade, yellow = experimental trial grades, pink = experimental commercial grades; significant differences between the control grade and each experimental grade are highlighted

| *Grade* | *Thickness (mm)* | *C* | *Mn* | *Si* | *P* | *S* | *Cr* | *V* | *Nb* | *Mo* | *Ni* | *Ti* | *B* | *N* | *CEN* |
|---|---|---|---|---|---|---|---|---|---|---|---|---|---|---|---|
| 22MnB5 | 1.5 | 0.225 | 1.229 | 0.211 | 0.018 | 0.008 | 0.289 | 0.000 | 0.000 | 0.001 | 0.000 | 0.037 | 0.0041 | 0.0049 | 0.515 |
| 15MnB5 | 1.5 | **0.145** | 1.200 | 0.190 | 0.015 | 0.004 | 0.280 | 0.000 | 0.000 | 0.005 | 0.005 | 0.023 | 0.0030 | 0.0044 | 0.387 |
| 25MnB5 | 1.5 | **0.245** | 1.195 | 0.178 | 0.021 | 0.009 | 0.251 | 0.000 | 0.000 | 0.001 | 0.000 | 0.033 | 0.0032 | 0.0040 | 0.517 |
| 25MnB5 (Mo) | 1.5 | **0.257** | 1.180 | 0.202 | 0.016 | 0.005 | 0.280 | 0.000 | 0.000 | **0.218** | 0.000 | 0.029 | 0.0041 | 0.0072 | 0.581 |
| 25MnB5 (V) | 1.5 | **0.255** | 1.200 | 0.190 | 0.016 | 0.004 | 0.280 | **0.097** | 0.000 | 0.005 | 0.005 | 0.024 | 0.0030 | 0.0047 | 0.553 |
| 25MnB5 (Ni) | 1.5 | **0.255** | 1.310 | 0.190 | 0.014 | 0.004 | 0.280 | 0.000 | 0.000 | 0.005 | **0.500** | 0.024 | 0.0030 | 0.0050 | 0.561 |
| 29MnB5 | 1.5 | **0.291** | 1.260 | 0.179 | 0.017 | 0.007 | 0.195 | 0.000 | 0.000 | 0.001 | 0.000 | 0.030 | 0.0036 | 0.0061 | 0.565 |
| 38MnB5 | 1.5 | **0.380** | 1.200 | 0.190 | 0.015 | 0.004 | 0.280 | 0.000 | 0.000 | 0.005 | 0.005 | 0.024 | 0.0030 | 0.0047 | 0.660 |
| DP 600 | 1.5 | **0.093** | **1.850** | 0.233 | 0.011 | 0.002 | **0.575** | **0.004** | **0.002** | 0.002 | **0.024** | 0.003 | **0.0000** | 0.0038 | 0.365 |
| DP 800 | 1.5 | **0.130** | **1.700** | 0.250 | 0.010 | 0.005 | **0.550** | 0.000 | **0.025** | 0.000 | 0.000 | 0.020 | **0.0000** | 0.0080 | 0.456 |
| DP 1000 | 2.0 | **0.135** | **2.100** | 0.290 | 0.014 | 0.001 | **0.620** | 0.000 | **0.018** | 0.015 | 0.000 | 0.000 | **0.0000** | 0.0065 | 0.540 |

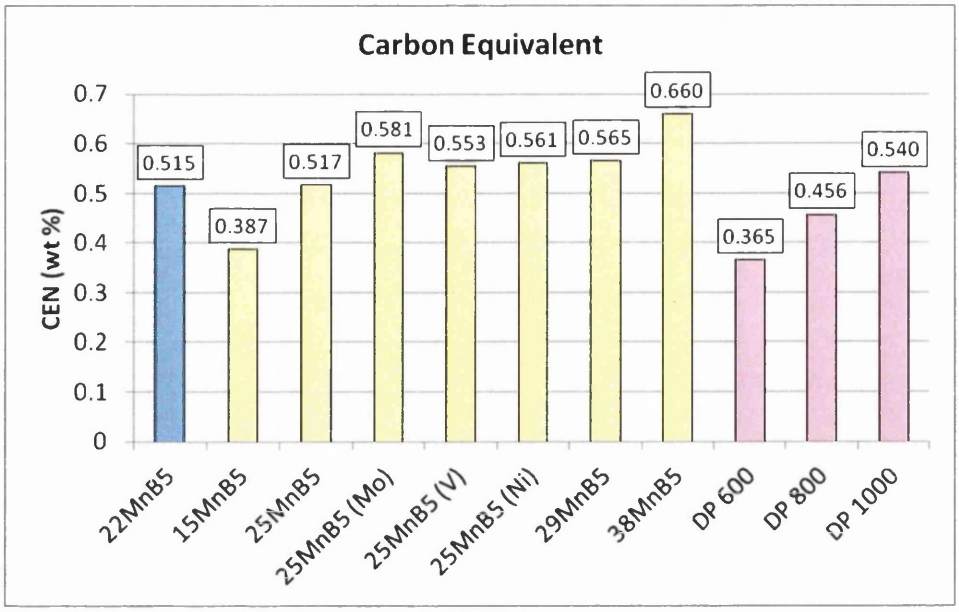


Figure 4.1: Carbon equivalent of investigated grades

***Critical Phase Transformation Temperature Predictions***

Equations 2.1 to 2.9 were used to predict the critical phase transformation temperatures of the investigated grades, as presented in Table 4.2.

Table 4.2: Critical phase transformation temperature (°C) predictions

| *Grade* | *$Ae_3$* | *$Ae_1$* | *Bs* | *Ms (1)* | *Ms (2)* | *Ms (3)* | *Ms (4)* | *Ms (5)* | *Ms (6)* |
|---|---|---|---|---|---|---|---|---|---|
| 22MnB5 | 819 | 721 | 574 | 380 | 389 | 403 | 405 | 404 | 406 |
| 15MnB5 | 846 | 720 | 582 | 406 | 414 | 438 | 440 | 439 | 445 |
| 25MnB5 | 814 | 720 | 578 | 376 | 385 | 396 | 398 | 397 | 399 |
| 25MnB5 (Mo) | 809 | 721 | 566 | 370 | 384 | 389 | 393 | 392 | 389 |
| 25MnB5 (V) | 829 | 720 | 575 | 372 | 382 | 391 | 393 | 392 | 393 |
| 25MnB5 (Ni) | 831 | 711 | 564 | 360 | 370 | 379 | 390 | 389 | 381 |
| 29MnB5 | 811 | 718 | 575 | 361 | 371 | 375 | 376 | 375 | 376 |
| 38MnB5 | 797 | 720 | 568 | 333 | 345 | 338 | 340 | 340 | 334 |
| DP 600 | 893 | 719 | 548 | 392 | 401 | 436 | 442 | 441 | 442 |
| DP 800 | 870 | 721 | 552 | 386 | 397 | 426 | 430 | 430 | 431 |
| DP 1000 | 884 | 719 | 531 | 369 | 381 | 410 | 416 | 415 | 413 |

### *Continuous Annealing Resistance Heating Simulator*

The continuous annealing resistance heating simulator (CASIM) is a bespoke 'in-house' apparatus designed for simulating industrial heat treatment cycles on sheet specimens with length and width of 400×100 mm and with the longitudinal axis parallel to the rolling direction.

The CASIM (Figure 4.2) consists of two sets of opposite facing jaws that serve to hold the specimen under minor tension at each end of its longitudinal axis. The jaws are imbedded with copper electrodes that transmit high voltage electric current through the specimen and thereby, create electrical resistance heating.

The compressed air system is located directly above the specimen. The cooling rate achieved by the CASIM can be finely adjusted from that of natural air cooling, to that of rapid compressed air quenching by tailoring the position of the valve that feeds the compressed air system.

The CASIM is linked to management software by the control (type-K) thermocouple that is spot welded to the specimen surface. The parameters of the desired heat treatment cycle are imputed into the management software. Temperature is constantly measured via the control thermocouple and in a closed-loop process, the applied voltage/compressed air is automatically adjusted as necessary in order to achieve the imputed heat treatment cycle.

Five additional (type-K) thermocouples are spot welded to the specimen surface in the configuration shown by Figure 4.2, covering an area of 2000 $mm^2$. The five thermocouples are linked to data logging software, which records temperature evolution as a function of time. Moreover, uniformity of heating and cooling across the area of 2000 $mm^2$ can be determined.

It must be stressed that the CASIM employs pure thermal treatment in the absence of mechanical treatment (deformation). Meanwhile, in hot stamping, the treatment is not purely thermal, but rather thermo-mechanical as major

temperature variation and complex stress-strain states are experienced simultaneously by the blank as it is hot stamped and quenched into the final component. The significance of this combination of thermal and mechanical treatments is that the kinetics of phase transformations can be modified when mechanical treatment is added to the thermal treatment (e.g. mechanical stabilisation of γ-austenite, strain induced proeutectoid α-ferrite formation and lowering of the Ms temperature – Figure 2.31). Consequently, the microstructure and mechanical properties of the thermo-mechanically treated specimen can be different from the purely thermally treated specimen.

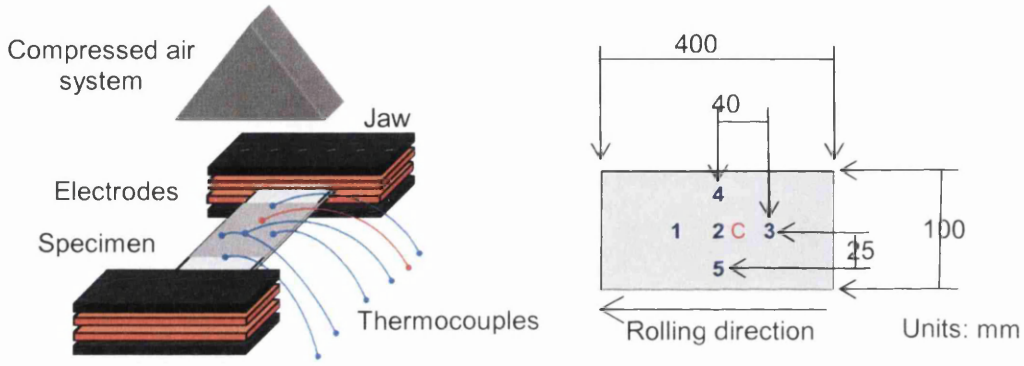


Figure 4.2: Continuous annealing resistance heating simulator

The CASIM provided a convenient, economical and most importantly, accessible means of simulating hot stamping heat treatment cycles, while experimental trial grades were prepared and while laboratory hot stamping facilities were reviewed. Moreover, the procedure was comparable to that employed by other researchers [124]. Thus, the CASIM was used as a preliminary tool ahead of laboratory hot stamping. The preliminary investigation with the CASIM provided fundamental knowledge and experience of heat treatment and its influences on the resulting microstructure and mechanical properties. It also enabled the hot stamping potential of the commercial DP steels to be evaluated at an early stage of the research programme. Knowledge gained from the preliminary investigation using the CASIM then influenced later laboratory hot stamping investigations.

*CASIM Simulation of Hot Stamping Heat Treatment Cycles with Dual Phase Steels*

The objective was to produce ultrahigh strength ferritic-martensitic microstructures from hot stamping heat treatment, exhibiting superior tensile properties for impact energy absorptive crash performance compared to 22MnB5. Specifically, the targeted tensile properties included lower proof strength, higher uniform elongation and higher total elongation, with minimal loss to ultimate tensile strength.

The simulated hot stamping heat treatment cycles are illustrated by Figure 4.3. The heating rate from ambient temperature to the soak temperature was 10 °C/s. The 5 second natural air cool immediately following the soak time simulated the transfer stage of hot stamping. The compressed air quench from the conclusion of the 5 second natural air cool, to 150 °C, simulated the stamping (forming) and quenching stages of hot stamping. The mean quench rate to 150 °C was approximately -35 °C/s. The aforementioned parameters were constants and were selected in order to replicate a typical, standardised hot stamping heat treatment cycle [15] [20] [23]. The variable parameters concerned soak time and soak temperature.

For the experimental DP grades, soak temperatures included 800, 850 and 900 °C. These soak temperatures were selected in order to provide a range of temperatures above the theoretical $Ae_1$ temperatures (Table 4.2).

Soak time at all soak temperatures was 1 minute. This limited soak time was selected in order to minimise austenitic grain growth and thereby, yield a fine as-quenched microstructure; where it has been reported [31] that microstructural refinement of lath martensite (as opposed to plate martensite) increases strength without decreasing impact toughness; and where lath martensite (as opposed to plate martensite) is exclusive in low carbon steels (such as the DP steels) with less than ~ 0.15 wt % C [39].

Additionally, at the highest soak temperature of 900 °C, the extended soak time of 3 minutes was investigated. The extended soak time was selected in order to increase austenitic grain growth, decrease austenitic gain boundary surface area where the heterogeneous nucleation of reconstructive phase transformations is dominant and thereby, increase quench hardenability [62] [63] [64] for a higher strength product.

For the 22MnB5 control grade, soak time-temperature was 3 min-900 °C. This soak condition is typically employed on industrial hot stamping lines [15] [20] [23].

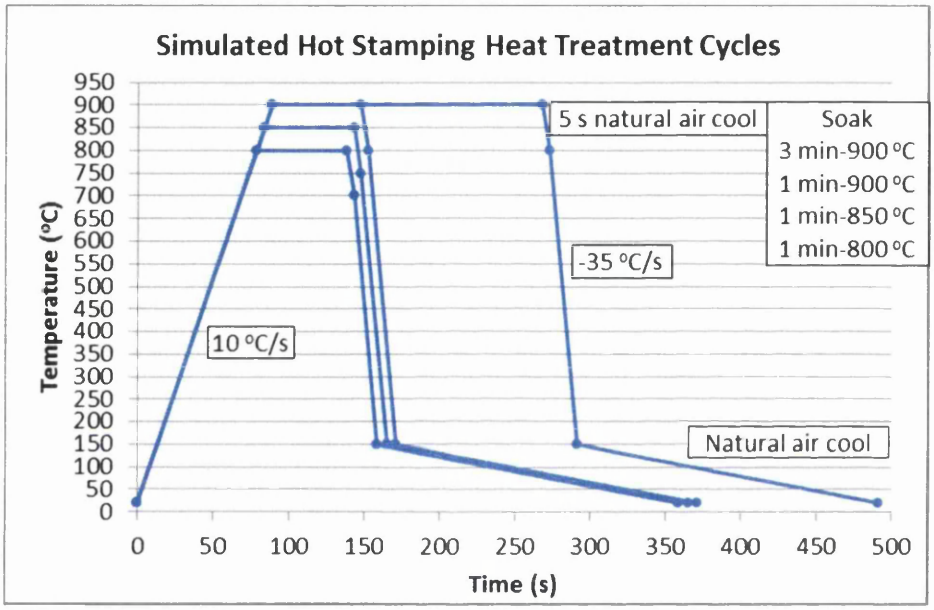


Figure 4.3: Simulated hot stamping heat treatment cycles

***Heating Curves & Water Quenching***

With the full series of investigated grades available and with laboratory hot stamping facilities in place; investigation could progress from the preliminary measure that was the CASIM, to laboratory hot stamping.

However, prior to laboratory hot stamping, the Heating Curves & Water Quenching experimental was conducted. This was necessary in order to obtain the following data (note that thermocouple data logging was not possible during laboratory hot stamping):

- Furnace heating time to soak temperature for each grade-thickness-soak temperature combination.
- Critical phase transformation temperatures on heating[28].
- Probability of phase transformations during the transfer stage of laboratory hot stamping.
- Water quenched properties[29].

Critical phase transformation temperatures were estimated by identifying inflections in the time-temperature 'heating/cooling curves' that were associated with extraction/release of latent heat. During phase transformations on heating, latent heat is extracted by the specimen from the external atmosphere (and from the specimen surface where the thermocouple is positioned), which manifests itself in a temporary decrease to the recorded heating rate [125]. During phase transformations on cooling, latent heat is released by the specimen to the external atmosphere (and to the specimen surface where the thermocouple is positioned), which manifests itself in a temporary decrease to the recorded cooling rate [125].

Inflections in the time-temperature heating/cooling curves were more easily identified by converting the raw time-temperature data to mean temperature-mean heating/cooling rate data. Here, the mean data were calculated over a defined time interval. Time intervals were typically one, two or three seconds. By selecting a shorter time interval for the mean data, accuracy is improved. However, the data can become noisy, which makes identifying genuine inflections from the natural heating/cooling curve difficult. By selecting a longer time interval for the mean data, the data become smoother and it is thus easier to identify genuine inflections. However, the temperature at which the inflection occurs loses accuracy with respect to the original time-temperature data. Thus, the time

---

[28] Critical phase transformation temperatures would have been more accurately estimated from dilatometry with the Gleeble 3500. However, the Gleeble 3500 did not become available until late in the research project.

[29] Water quenched properties, including tensile properties, Vickers hardness properties, microconstituent volume fractions and proeutectoid α-ferrite grain sizes, are not presented in this thesis. However, these data are available on request.

interval was selected from one, two or three seconds in order to provide the optimal balance between these two factors.

Figure 4.4 illustrates the conversion of raw time-temperature data to mean temperature-mean heating/cooling rate data; and how critical phase transformation temperatures were estimated (note that no phase transformations were identified on cooling, thus an example cannot be given).

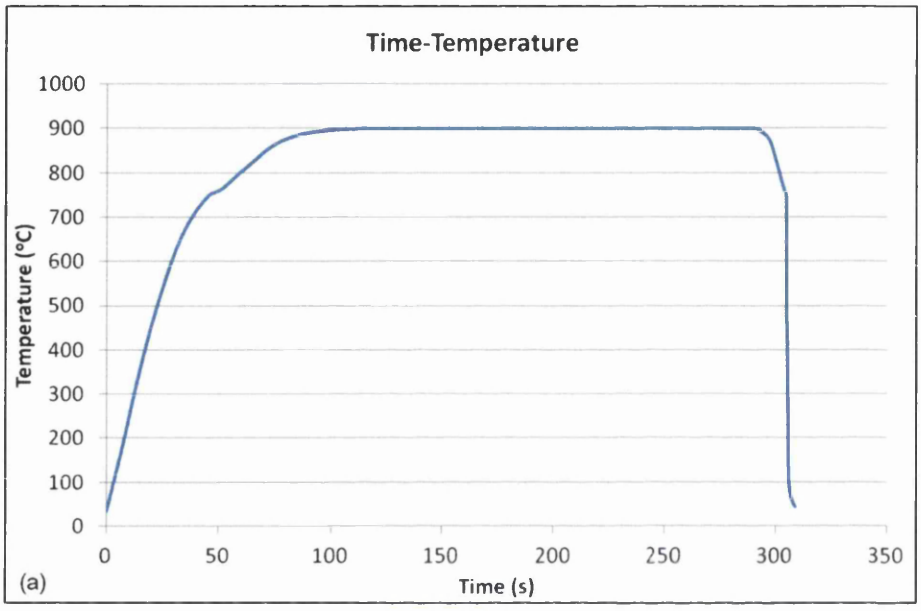


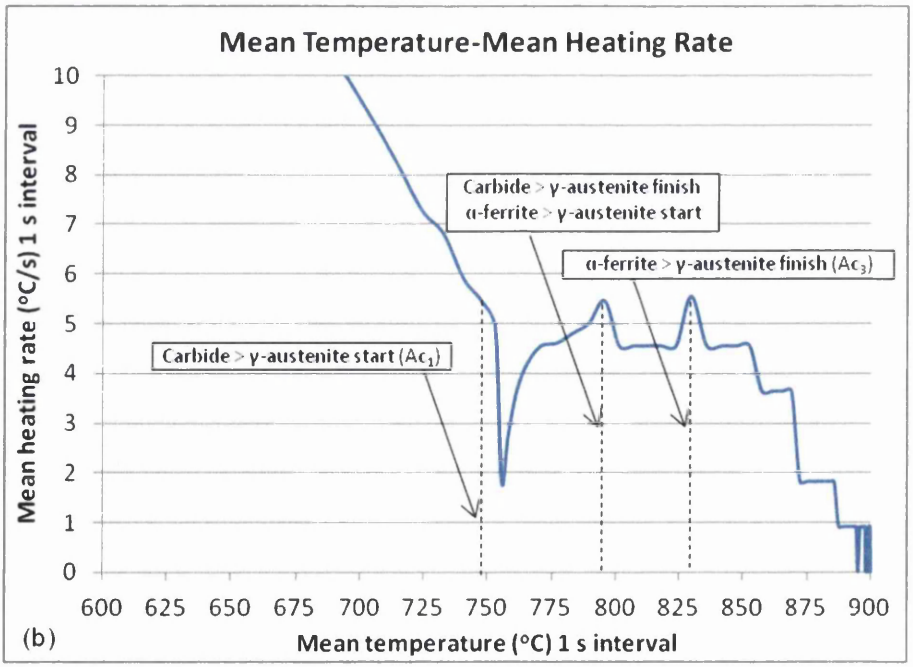

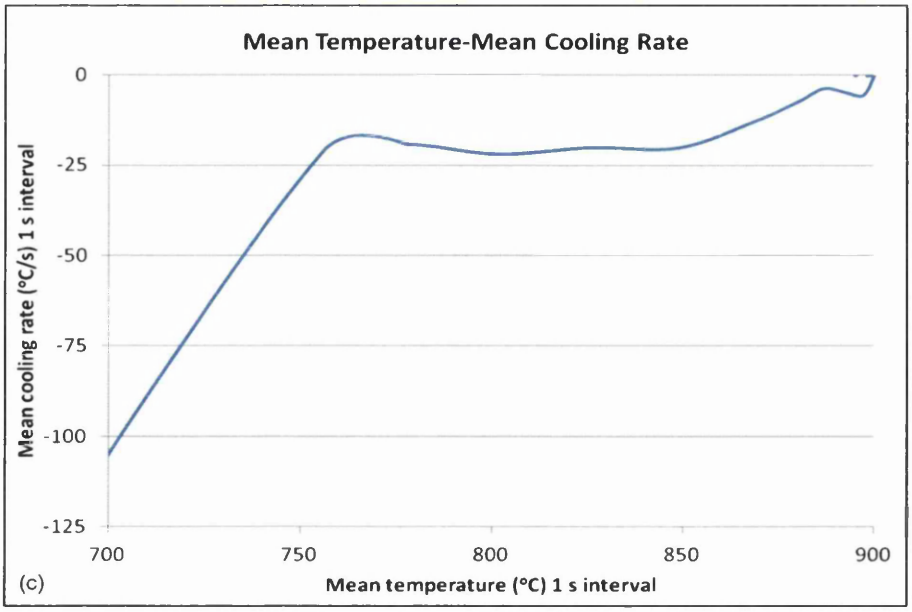


Figure 4.4: Conversion of (a) raw time-temperature data to (b) mean temperature-mean heating rate data and (c) mean temperature-mean cooling rate data

Blanks with length and width of 225×25 mm and with the longitudinal axis parallel to the rolling direction (as used in laboratory hot stamping) were taken from the cold rolled sheet.

The (type-K) thermocouple was spot welded to the blank surface centre point. The blank was furnace heated in un-protected atmosphere to the desired soak temperature. Soak temperatures included 800, 850 and 900 °C (as used in laboratory hot stamping). Soak time was 3 minutes (the median soak time used in laboratory hot stamping). Following the soak time, the blank was removed from the furnace, naturally air cooled for ~ 10 seconds (to simulate the transfer stage of laboratory hot stamping) and water quenched to ambient temperature. The heat treatment cycles are illustrated by Figure 4.5.

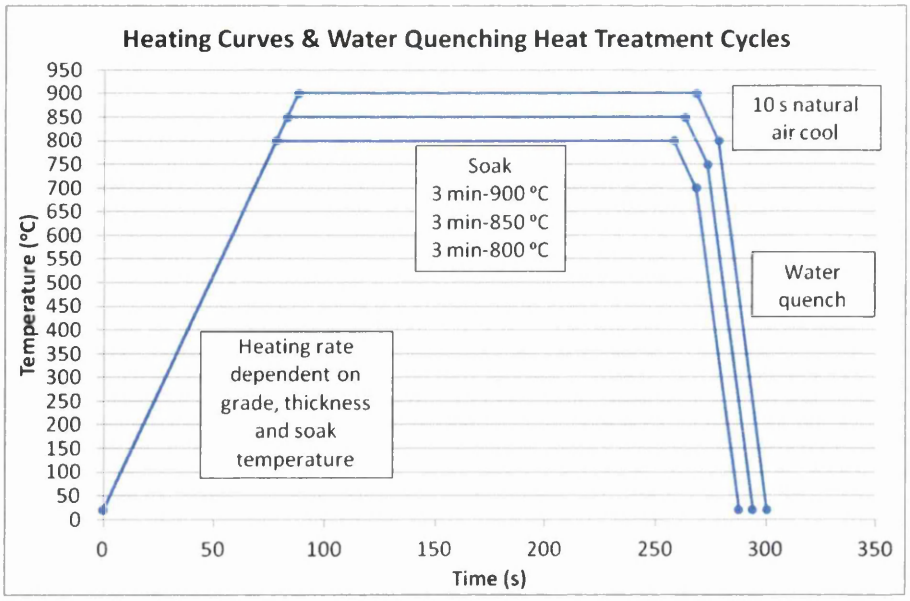


Figure 4.5: Heating curves & water quenching heat treatment cycles

***Laboratory Hot Stamping***

Following literature review, in addition to review of existing laboratory hot stamping facilities, the proposal was made for investment into an advanced laboratory hot stamping line, including furnace with protected atmosphere, automated transfer system, press with active cooling system and integrated thermo-mechanical data logging; and tooling to replicate automotive structural body components. However, due to financial constraints, the proposal was not approved.

Thus, laboratory hot stamping depended on the existing facilities. These facilities consisted of an electric fired furnace with maximum temperature capacity of 1200 °C (and un-protected atmosphere), manual transfer from furnace to press in ~ 8 seconds and conventional (non-cooled) press with a maximum force capacity of 30 tonnes.

Tool and blank geometry is illustrated by Figure 4.6. No 'forming' took place. Rather, the blank was simply die quenched. This was principally due to geometric constraints of the tooling, as illustrated. However, with the intention of taking a tensile specimen from the base of the hot stamped blank, the employed procedure was considered to be sufficient. Moreover, the procedure was comparable to that employed by other researchers [15] [115].

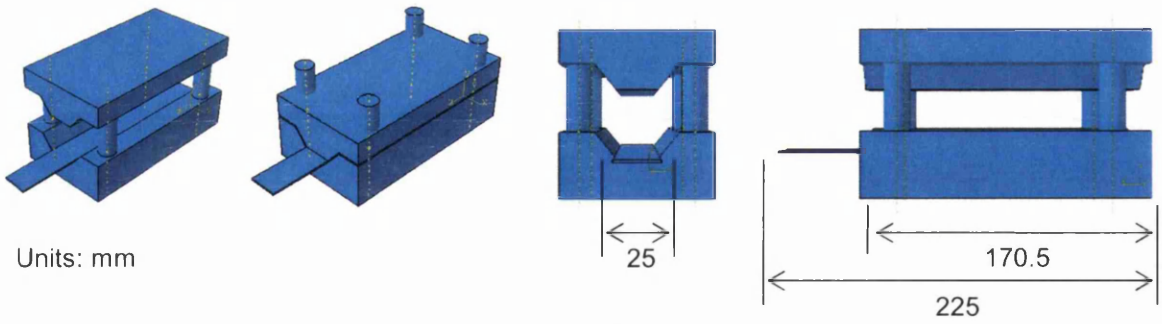


Figure 4.6: Laboratory hot stamping tool and blank geometry

Cooling rates were determined by a preliminary investigation wherein thermocouple data logging was performed on the die/blank interface. Figure 4.7 presents the time-temperature cooling curve for 22MnB5 soaked at 900 °C. Note that accurate temperature measurement was possible from only ~ 500 °C downwards, due to the time required to establish full thermal contact between the thermocouple (positioned in the die) and the blank. During this time, the blank was already cooling at a rapid rate. Nevertheless, the mean cooling rate above 500 °C was in excess of -100 °C/s. The mean cooling rate between 500 and 200 °C was in excess of -60 °C/s.

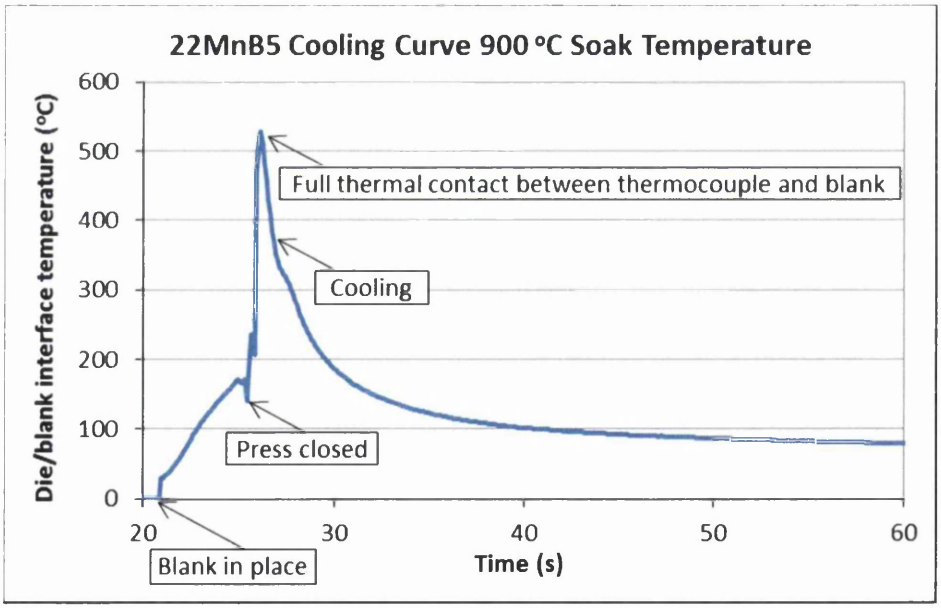


Figure 4.7: 22MnB5 time-temperature cooling curve from 900 °C soak temperature

The blank with length and width of 225×25 mm (and with the longitudinal axis parallel to the rolling direction) was furnace heated to the desired soak temperature with the heating time derived from the preliminary Heating Curves & Water Quenching experimental. Soak temperatures included 800, 850 and 900 °C. Soak times included 1, 3 and 5 minutes. Thus, nine soak time-temperature conditions were investigated.

Following the soak time, the blank was manually transferred from furnace to press in ~ 8 seconds. In the press, the blank was hot stamped and simultaneously die quenched to ~ 150 °C. Following hot stamping/die quenching, the hot stamped blank was removed from the press and naturally air cooled to ambient temperature.

The laboratory hot stamping heat treatment cycles are illustrated by Figure 4.8. The laboratory hot stamping programme is summarised by Table 4.3.

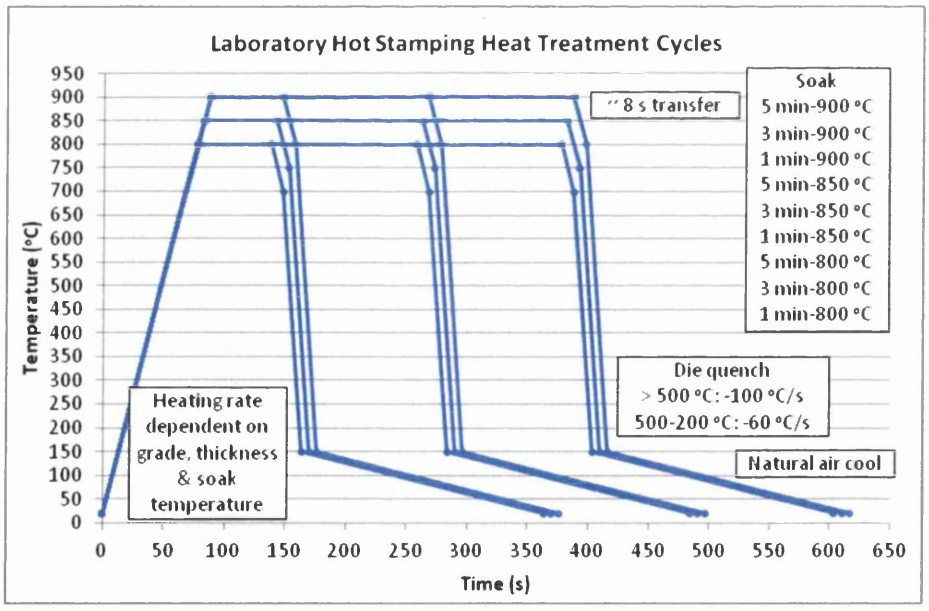


Figure 4.8: Laboratory hot stamping heat treatment cycles

Table 4.3: Laboratory hot stamping programme

| Grade | Soak time-temperature | | | | | | | | |
|---|---|---|---|---|---|---|---|---|---|
| | 800 °C | | | 850 °C | | | 900 °C | | |
| | 1 min | 3 min | 5 min | 1 min | 3 min | 5 min | 1 min | 3 min | 5 min |
| DP 1000 | Group 1 (January-June 2012) | | | | | | | | |
| 22MnB5 | | | | | | | | | |
| 25MnB5 | | | | | | | | | |
| 25MnB5 (Mo) | | | | | | | | | |
| 29MnB5 | | | | | | | | | |
| 15MnB5 | Group 2 (July-December 2012) | | | | | | | | |
| 25MnB5 (Ni) | | | | | | | | | |
| 25MnB5 (V) | | | | | | | | | |
| 38MnB5 | | | | | | | | | |
| DP 600 | | | | | | | | | |
| DP 800 | | | | | | | | | |
| Time-temperature cycles | 9 | | | | | | | | |
| Grades | 11 | | | | | | | | |
| Duplicates | 3 | | | | | | | | |
| Total cycles | 297 | | | | | | | | |

### *Quasi-Static Tensile Testing*

Quasi-static tensile testing was performed with the Zwick 1474 100 kN Electro-Mechanical tensile testing machine according to standard procedures [126]. Throughout the research project, standard tensile specimens with the standard 50 mm gauge length were used (Figure 4.9). All tensile specimens were thoroughly descaled with hydrochloric acid pickling and manual grinding before tensile testing commenced.

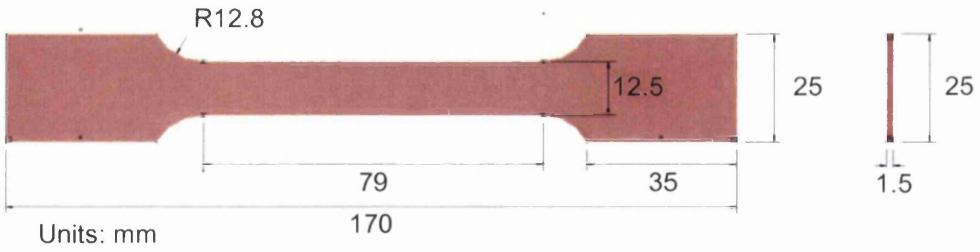


Figure 4.9: Quasi-static tensile specimen

In the case of the CASIM experimental, two tensile blanks each with length of 170 mm were cut from the heat treated CASIM specimen. The tensile blanks were subsequently machined to standard tensile specimens. The configuration is illustrated by Figure 4.10.

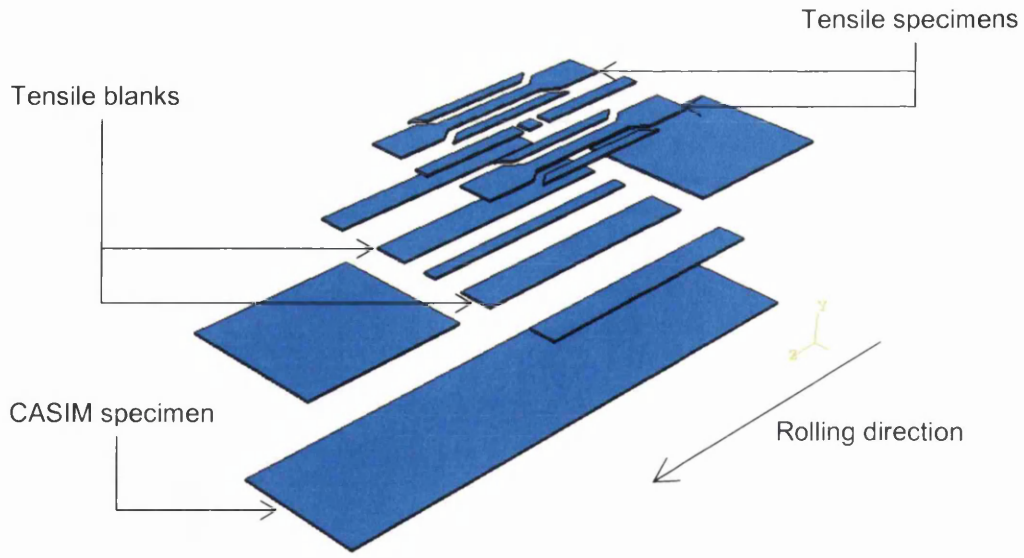


Figure 4.10: Configuration of tensile specimens from heat treated CASIM specimen

In the case of the Heating Curves & Water Quenching experimental and the Laboratory Hot Stamping experimental, the heat treated blank was cut to a 170 mm tensile blank by removing 55 mm from the end that was handled during heat treatment. This meant that the entirety of the tensile blank received 'homogeneous' heat treatment. Finally, the tensile blank was machined to a standard tensile specimen. The configuration is illustrated by Figure 4.11.

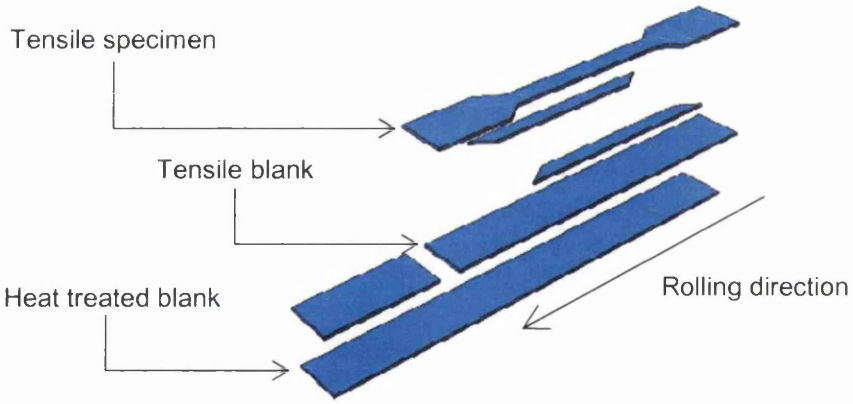


Figure 4.11: Configuration of tensile specimen from heat treated blank

The raw data output from the tensile test was force-displacement. This was converted to engineering stress-engineering strain with Equations 4.1 and 4.2 [11].

$$\sigma_e = \frac{F}{A_0}$$

(Eq. 4.1)

Where: $\sigma_e$ = engineering stress (MPa)

F = force (N)

$A_0$ = original cross-sectional area ($mm^2$)

$$\varepsilon_e = \frac{l - l_0}{l_0}$$

(Eq. 4.2)

Where: $\varepsilon_e$ = engineering strain (unit-less)

l = final gauge length (mm)

$l_0$ = original gauge length (mm)

It is often desirable to covert engineering stress-engineering strain to true stress-true strain. This can be achieved with Equations 4.3 and 4.4 [11].

$$\sigma_t = \sigma_e \times (1 + \varepsilon_e)$$

(Eq. 4.3)

Where: $\sigma_t$ = true stress (MPa)

$\sigma_e$ = engineering stress (MPa)

$\varepsilon_e$ = engineering strain (unit-less)

$$\varepsilon_t = LN(1 + \varepsilon_e)$$

(Eq. 4.4)

Where: $\varepsilon_t$ = true strain (unit-less)

$\varepsilon_e$ = engineering strain (unit-less)

Equations 4.3 and 4.4 remain valid only under the condition of constant volume in the specimen gauge length [127]. It can be assumed that this condition is met during uniform elongation and to the commencement of 'necking'. However, beyond uniform elongation, where the specimen begins to 'neck', Equations 4.3 and 4.4 become invalid and as a consequence, the true stress-true strain data become invalid. This is demonstrated by an apparent decline of true stress from

the point corresponding to the commencement of necking, to the failure strength. In actuality, true stress should continue to increase to the failure strength. Hence, although the 'true strength' value that can be calculated with Equation 4.3 is closer to the actual true strength than the engineering ultimate tensile strength, it is still an underestimate of the actual true strength. These features are illustrated by Figure 4.12.

Moreover, true strain to failure cannot be calculated accurately; the steel and automotive industries often quote engineering data rather than true data [68]; and finally, the automotive industry often focuses on yield strength/proof strength rather than ultimate tensile strength [8]. With these considerations, engineering data are presented.

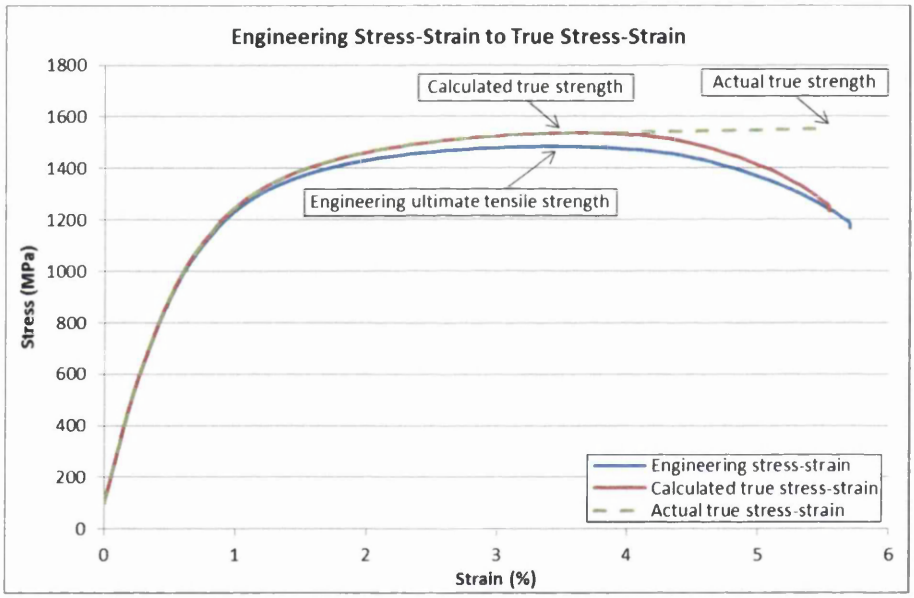


Figure 4.12: Engineering stress-strain to true stress-strain

Elongation to failure was measured manually, rather than depending on the extensometers of the testing machine. Prior to the tensile test, two parallel lines were scribed onto the reduced section of the tensile specimen, with the distance between the two parallel lines of known length. Further, this procedure was performed twice: 1) with 50 mm distance between the two parallel lines; and 2) with 80 mm distance between the two parallel lines. These distances thus represented gauge lengths for the manual measurement of elongation. Following the tensile test, the distance between the two parallel lines was re-measured. On

the condition that the specimen fractured inside the 50 mm gauge length, the 50 mm gauge length was used. On the condition that the specimen fractured outside the 50 mm gauge length, the 80 mm gauge length was used.

The advantage of manually measuring elongation in the above manner was that the testing machine only provides an accurate measurement of elongation provided that the specimen fractures exactly centre of the gauge length and thus, exactly centre of the extensometers. The further the fracture point from the extensometers, the lesser elongation to failure occurs where the testing machine is measuring and thus, the more underestimated is the testing machine's measurement.

The manually measured elongation to failure often diverged significantly from that elongation measured by the testing machine. This gave rise to unsightly stress-strain curves. For this reason, combined with the very large number of stress-strain curves produced; stress-strain curves are not presented.

Elastic modulus is not presented as the accuracy of the testing machine at low strains was insufficient.

Figure 4.13 illustrates critical quasi-static tensile properties that are presented and how they were derived from the engineering stress-engineering strain curve.

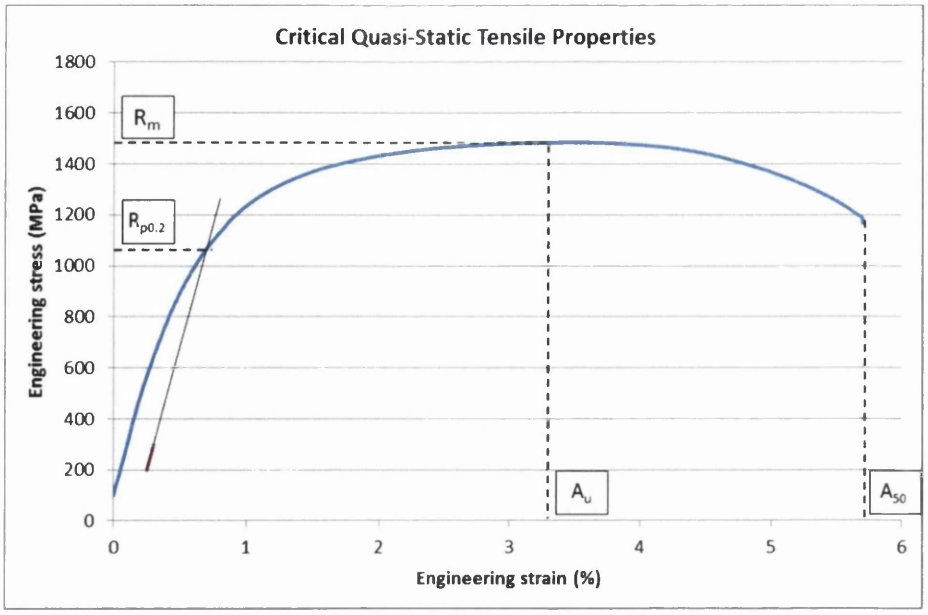


Figure 4.13: Critical quasi-static tensile properties

### *Dynamic Tensile Testing*

Following laboratory hot stamping and evaluation (including quasi-static tensile testing described above), the three most successful outcomes were selected. The three most successful outcomes included three experimental grades with each treated to its as-determined optimal hot stamping soak condition (Table 4.4). Collectively, these three experimental grades treated to their optimal hot stamping soak conditions met the three objectives of: 1) higher tensile strength; 2) higher elongation; and 3) higher tensile strength-higher elongation, compared to the 22MnB5 control grade. The three selected experimental grades, in addition to the 22MnB5 control grade (with each grade treated to its optimal hot stamping soak condition) were further evaluated with dynamic tensile testing, three-point bend testing and FEM crash simulation.

Table 4.4: Grades & soak conditions selected for dynamic tensile testing, three-point bend testing and FEM crash simulation

| *Objective relative to control grade* | *Grade* | *Soak condition* |
|---|---|---|
| Control | 22MnB5 | 1 min-850 °C |
| Higher tensile strength | 38MnB5 | 5 min-850 °C |
| Higher elongation | DP 1000 | 5 min-850 °C |
| Higher tensile strength-higher elongation | 25MnB5 (V) | 3 min-850 °C |

Quasi-static tensile testing is defined by a strain rate of $\leq 0.008\ s^{-1}$ [128]. In the current research project, the quasi-static strain rate of $0.001\ s^{-1}$ was used. While tensile data produced under quasi-static loading are certainly of value (and significantly more economical to obtain), higher strain rates, particularly in the region of 100-200 $s^{-1}$ are considered [3] to be more realistic and thus of greater relevance when evaluating automotive crash performance. For this reason, plentiful research has been conducted into the response of automotive steels to dynamic tensile testing [3] [129] [130] [131] [132] [133] [134] [135] [136]. However, there is seldom or even no published research available concerning the response of hot stamped steels to dynamic tensile testing.

The impetus for dynamic tensile testing when evaluating the automotive crash performance of steels is that certain steel grades exhibit 'strain rate sensitivity', where the tensile properties obtained under dynamic loading conditions deviate from the tensile properties obtained under quasi-static loading conditions [3] [133] [134].

Dynamic tensile testing is defined by a strain rate of $> 0.008\ s^{-1}$ [128]. While it is possible to conduct dynamic tensile testing up to a strain rate of $10^3\ s^{-1}$ (i.e. equipment and published standards exist for dynamic tensile testing up to this strain rate), it is reported [137] that the strain rate range of interest to automotive crash performance includes 1 to 200 $s^{-1}$. Thus, in the current research, the three dynamic strain rates were investigated: 1, 100 and 200 $s^{-1}$.

The strain rate of 1 $s^{-1}$ was performed with the 100 kN Electro-Servo-Hydraulic Universal test machine, while the strain rates of 100 and 200 $s^{-1}$ were performed with the 100 kN Servo-Hydraulic High Rate Impact test machine. The principal difference between the two machines relates to specimen orientation and test set-up. More information regarding the two machines is given in the reference [3].

The geometry of the standard dynamic tensile specimen (Figure 4.14) differs from the standard quasi-static tensile specimen. Most notably, the reduced section is smaller so to facilitate higher strain rates.

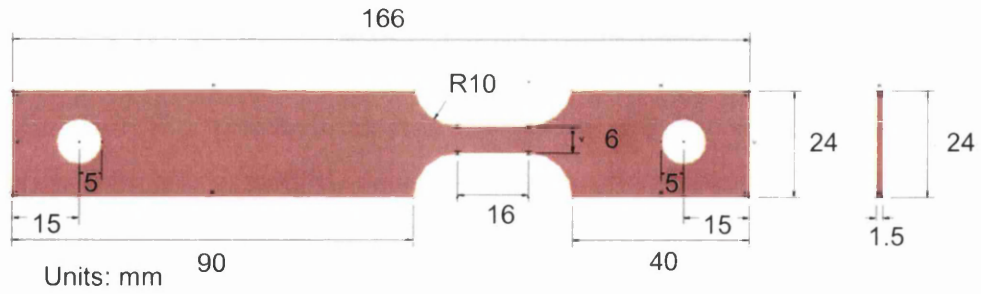


Figure 4.14: Dynamic tensile specimen

Specimens for dynamic tensile testing were prepared in a similar fashion to those specimens for quasi-static tensile testing describe above. The hot stamped blank was cut to a 166 mm dynamic tensile blank by removing 59 mm from the end that was handled during hot stamping. Finally, the dynamic tensile blank was machined to a standard dynamic tensile specimen. The configuration is illustrated by Figure 4.15.

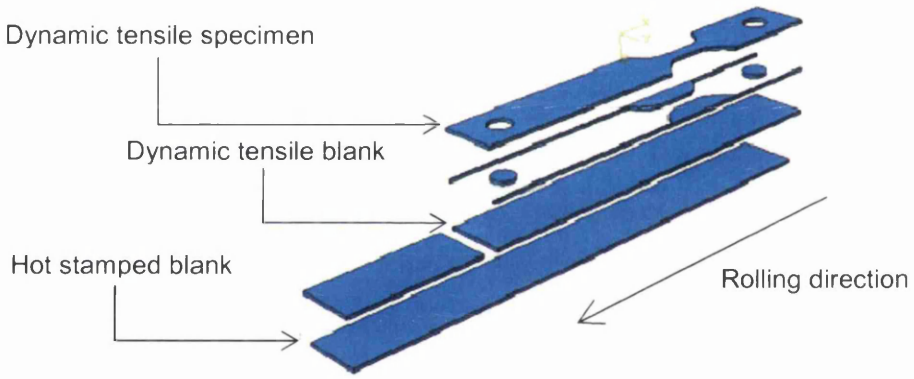


Figure 4.15: Configuration of dynamic tensile specimen from hot stamped blank

Until September 2011, there was no published standard procedure available for dynamic tensile testing of metallic materials. However, Tata Steel has employed its own internal standard procedure [138] [139] for nearly 20 years, which has been accepted by its automotive customers. Moreover, the internal standard procedure conformed to a draft copy [140] of a published standard procedure. Since September 2011, the internal standard procedure has been updated in order to conform to the published standard procedure [128]. The published standard procedure was followed at all times.

In common with the quasi-static tensile test, the raw data output from the dynamic tensile test was force-displacement, which was converted to engineering stress-engineering strain. However, while engineering stress-engineering strain data were sufficient from the quasi-static tensile test, data from the dynamic tensile test required further processing.

While a smooth engineering stress-engineering strain curve can be derived immediately from the quasi-static tensile test (Figure 4.13), the engineering stress-engineering strain curve derived immediately from the dynamic tensile test is susceptible to noise (Figure 4.16), with increasing noise resulting from increasing strain rate. This is due to shockwaves that are transmitted from the testing machine to the specimen under high strain rate conditions [128].

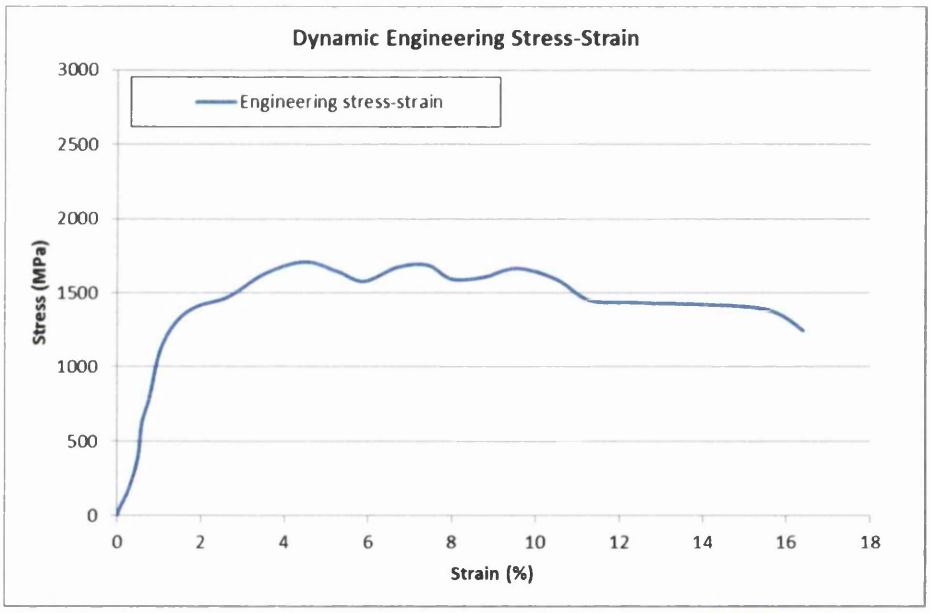


Figure 4.16: Dynamic engineering stress-strain

The noise associated with the raw dynamic engineering stress-engineering strain curve was eliminated by fitting a polynomial trendline (Figure 4.17). Although it is acknowledged that fitting a trendline introduces error, any associated error was considered to be smaller than that error introduced by noise. Moreover, fitting a polynomial trendline is recommended in the published standard procedure [128].

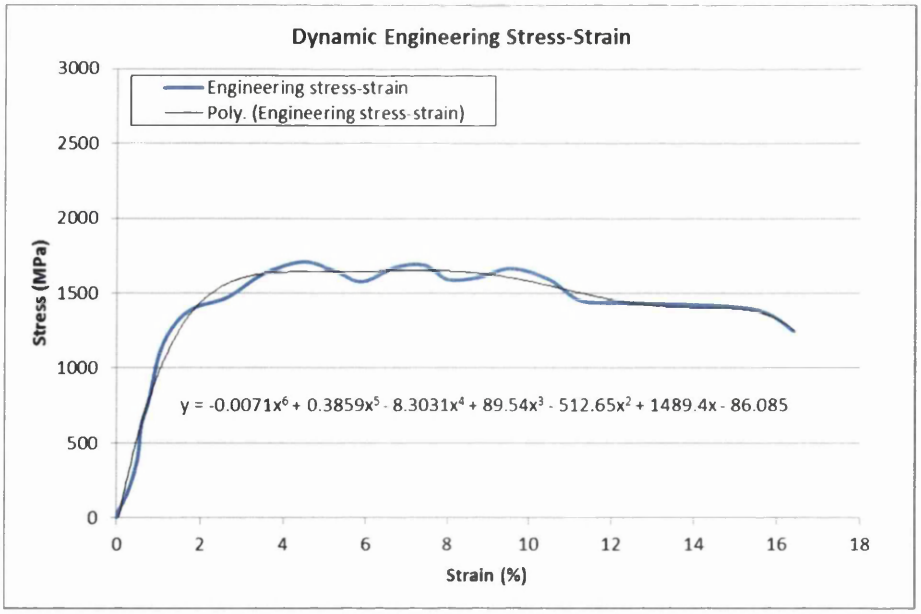


Figure 4.17: Polynomial fitted to dynamic engineering stress-strain

The dynamic tensile data were intended for FEM crash simulation, which requires data to be prepared in the format of true stress-true plastic strain [127]. Moreover, this is a common format of presenting dynamic tensile data, where the elastic region is eliminated due to increasing inclusion of the elastic response of the testing machine with increasing strain rate [3]. Thus, the polynomial engineering stress-engineering strain curve was converted to a true stress-true strain curve (Figure 4.18) with Equations 4.3 and 4.4 (see page 162).

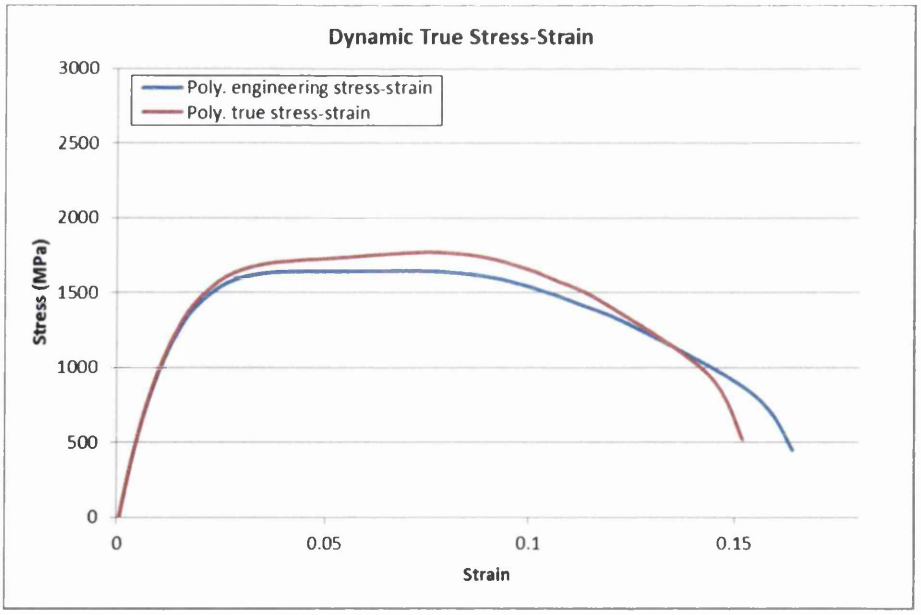


Figure 4.18: Polynomial engineering stress-strain to true stress-strain

However, as discussed in relation to quasi-static tensile testing, the conversion of engineering stress-engineering strain to true stress-true strain with Equations 4.3 and 4.4 is only valid during uniform elongation and to the commencement of necking. Thus, the true stress-true strain curve had to be truncated at the commencement of necking.

The exact true stress-true strain data point at which necking commenced was established by evaluating the work hardening rate (k) and work hardening exponent (n) values, where the work hardening rate is equal to the gradient of the true stress-true strain curve and where the work hardening exponent is equal to the gradient of the log true stress-log true strain curve [127]. True stress-true strain, work hardening rate-true strain, work hardening exponent-true strain and true strain-true strain were plotted on the same graph (Figure 4.19).

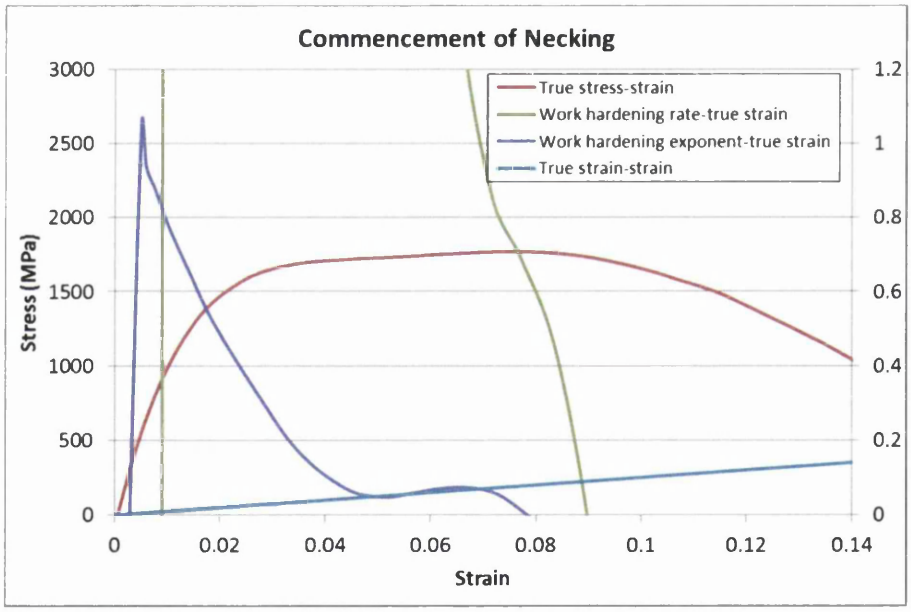


Figure 4.19: Commencement of necking

The true strain value at which the work hardening rate-true strain curve traversed the true stress-true strain curve was noted: this formed the 'major strain'. The true strain value at which the work hardening exponent-true strain curve traversed the true strain-true strain curve was noted: this formed the 'minor strain' (Figure 4.20).

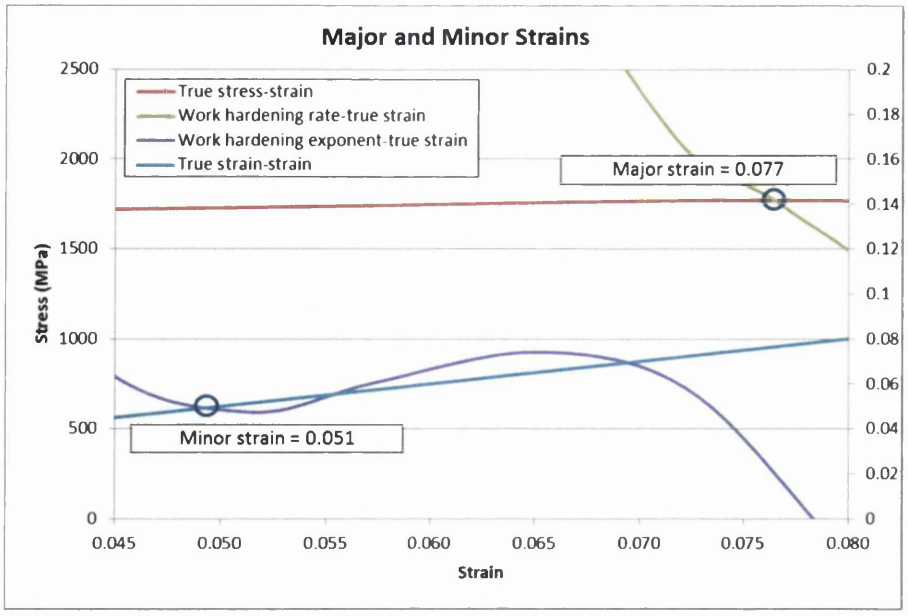


Figure 4.20: Major and minor strains

The true stress-true strain data points between the major and minor strains were evaluated. The true stress-true strain data point with the true stress value closest to the corresponding work hardening rate value was established as the data point where necking commenced (Figure 4.21).

| True Strain | True Plastic Strain | True Stress MPa | k MPa |
|---|---|---|---|
| 0.000 | 0.001 | -86 | |
| 0.001 | 0.001 | -1 | |
| 0.003 | 0.000 | 307 | |
| 0.005 | 0.000 | 547 | |
| 0.006 | 0.000 | 633 | |
| 0.008 | 0.001 | 805 | -734564 |
| 0.010 | 0.001 | 998 | 396492 |
| 0.014 | 0.003 | 1224 | 266178 |
| 0.019 | 0.006 | 1428 | 142855 |
| 0.026 | 0.012 | 1606 | 76038 |
| 0.035 | 0.020 | 1687 | 41936 |
| 0.044 | 0.028 | 1716 | 23425 |
| 0.051 | 0.036 | 1729 | 13408 |
| 0.057 | 0.042 | 1741 | 7435 |
| 0.065 | 0.049 | 1757 | 3599 |
| 0.071 | 0.056 | 1767 | 2159 |
| 0.077 | 0.061 | 1770 | 1739 |
| 0.084 | 0.068 | 1758 | 1088 |
| 0.091 | 0.076 | 1725 | -332 |
| 0.100 | 0.085 | 1658 | -2717 |
| 0.107 | 0.093 | 1581 | -5041 |
| 0.117 | 0.105 | 1447 | -7488 |
| 0.143 | 0.135 | 961 | -12170 |
| 0.152 | 0.147 | 521 | -16317 |

Minor strain

Major strain

True stress closest to k

Figure 4.21: Evaluation of true stress-strain between major and minor strains

Figure 4.22 illustrates the truncated true stress-true strain curve, presenting only the valid data.

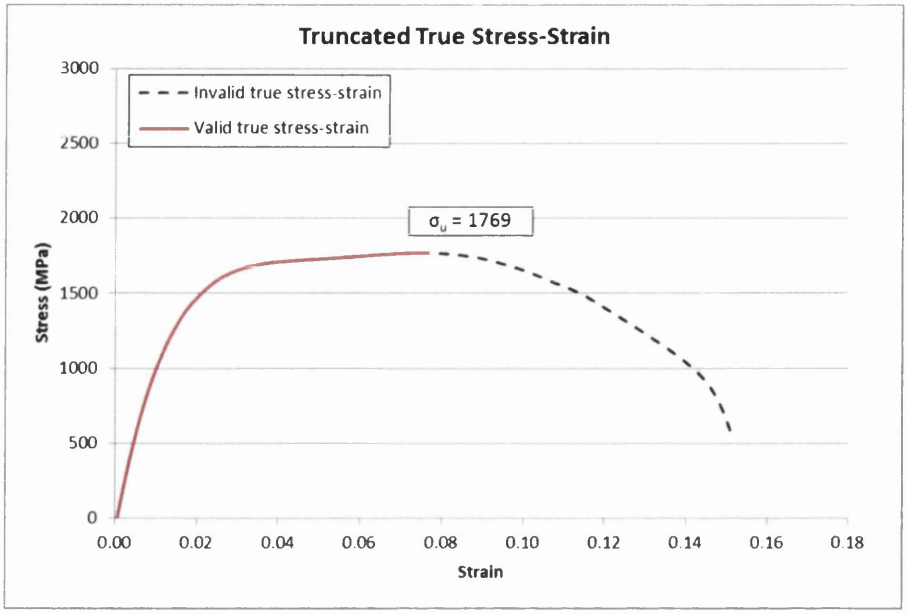


Figure 4.22: Truncated true stress-strain

True plastic strain was calculated with Equation 4.5. The transition from elastic to plastic deformation was evaluated as the true plastic strain value of zero resulting from Equation 4.5.

$$\varepsilon_{tp} = \varepsilon_t - \frac{\sigma_t}{E}$$

(Eq. 4.5)

Where: $\varepsilon_{tp}$ = true plastic strain (unit-less)

$\varepsilon_t$ = true (total) strain (unit-less)

$\sigma_t$ = true stress (MPa)

E = elastic modulus (MPa)

Data were now in the format of truncated true stress-true plastic strain (Figure 4.23).

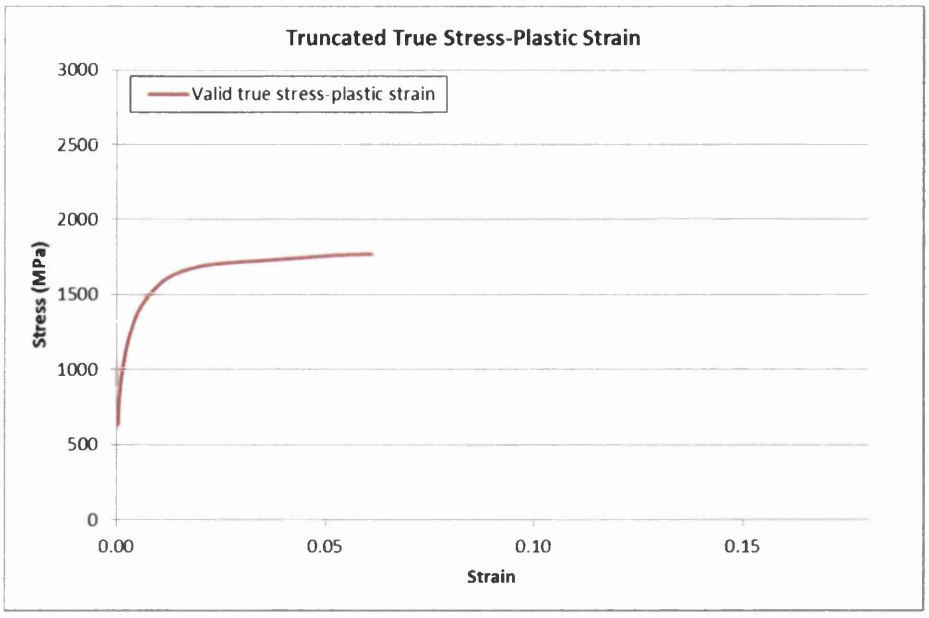


Figure 4.23: Truncated true stress-plastic strain

The truncated true stress-true plastic strain data next had to be extrapolated over the full true plastic strain range. This can be achieved with a number of empirical equations, as presented in Equations 4.6 to 4.9 [127] and illustrated by Figure 4.24.

Linear: $$\sigma = \sigma_u + k(\varepsilon - \varepsilon_g) \quad \text{(Eq. 4.6)}$$

Constant: $$\sigma = \sigma_u \quad \text{(Eq. 4.7)}$$

Log linear: $$\sigma = \sigma_u \left(\frac{\varepsilon}{\varepsilon_g}\right)^n \quad \text{(Eq. 4.8)}$$

Half linear-log linear $$\sigma = 0.5\left\{\left[\sigma_u + k(\varepsilon - \varepsilon_g)\right] + \left[\sigma_u \left(\frac{\varepsilon}{\varepsilon_g}\right)^n\right]\right\} \quad \text{(Eq. 4.9)}$$

Where: σ = stress (MPa)

$\sigma_u$ = stress at necking (MPa)

k = work hardening rate (MPa)

ε = strain (unit-less)

$\varepsilon_g$ = strain at necking (unit-less)

n = work hardening exponent (unit-less)

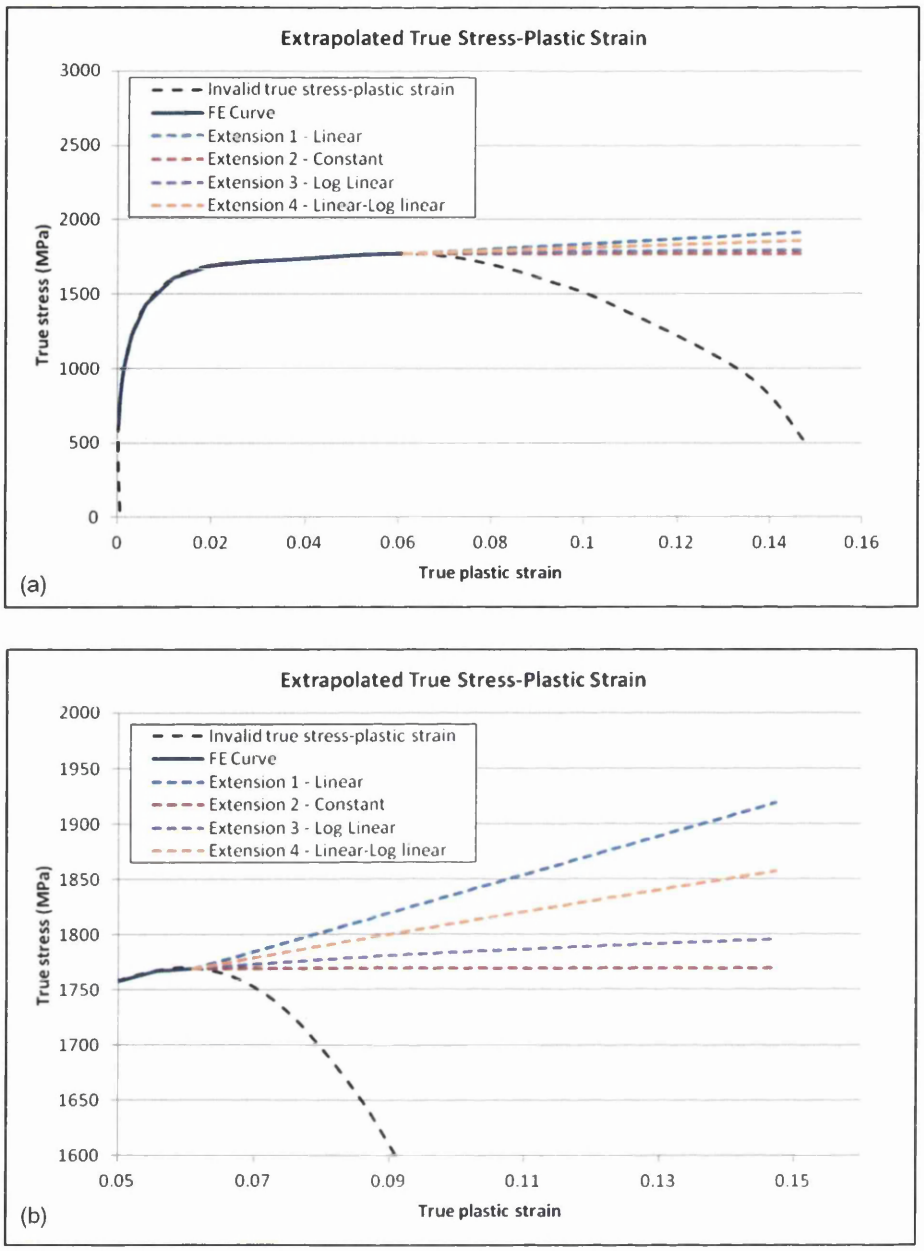


Figure 4.24: Truncated true stress-plastic strain extrapolation methods

It has been found [127] that the 'half linear-log linear' extrapolation method (Equation 4.9) provides the closest match with physical measurement. The half linear-log linear extrapolation method is accepted throughout Tata Steel and is routinely employed to produce the 'FE Curve' for FEM. Thus, the half linear-log linear extrapolation method was used in the current research project to produce the final true stress-true plastic strain curve (Figure 4.25).

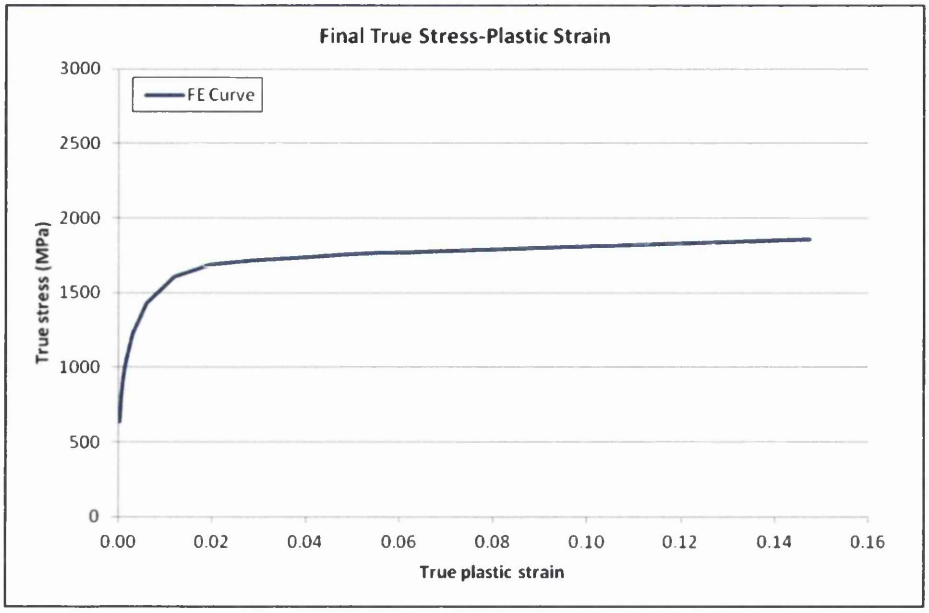


Figure 4.25: Final true stress-plastic strain curve

Critical tensile properties were derived from the final true stress-true plastic strain curve (Figure 4.26). In addition to the common tensile properties, including (true) proof strength, (true) ultimate tensile strength, uniform (plastic) elongation and total (plastic) elongation; work hardening exponent and modulus of toughness (from here on referred to as just 'toughness') were also derived. Toughness is a measure of energy absorption per unit volume and can be derived from the area under the stress-strain curve [11]. Two toughness values were determined: 1) toughness (2 % plastic strain); and 2) toughness (total plastic strain). Toughness (total plastic strain) was derived from the area under the entire true stress-true plastic strain curve. Toughness (2 % plastic strain) was derived from the area under the true stress-true plastic strain curve up to a fixed true plastic strain value of 2 %. It is beneficial to evaluate toughness up to a limited and fixed strain value in this manner since automotive structural body components are rarely strained to fracture in a crash event. Therefore, applying a limited strain value to the toughness evaluation is perhaps more realistic [3] [133].

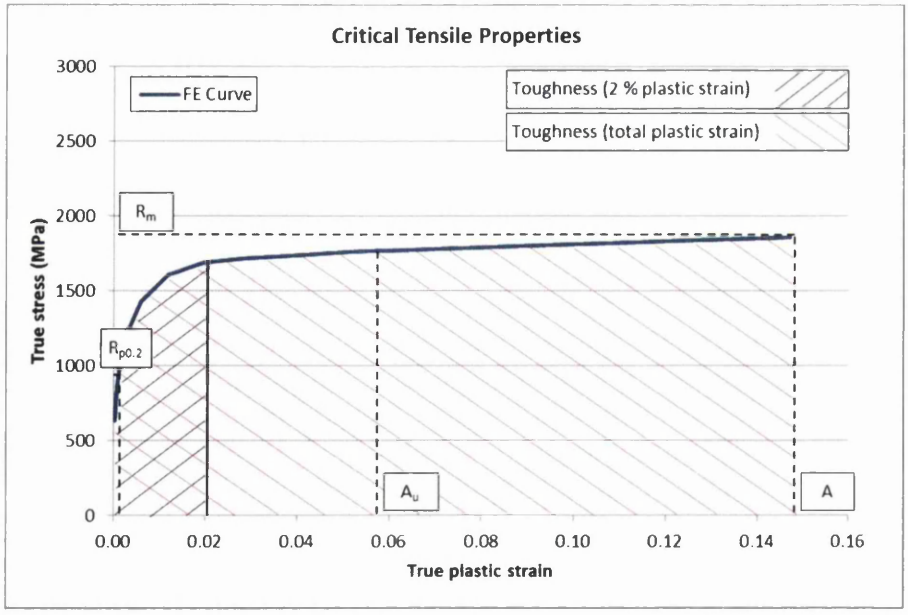


Figure 4.26: Critical tensile properties

The above data processing procedure for converting engineering stress-engineering strain to true stress-true plastic strain was performed on not only the dynamic tensile data, but also on the quasi-static tensile data for the grades and soak conditions selected for dynamic tensile testing. This gave rise to true stress-true plastic strain data for each of the grades and soak conditions selected for dynamic tensile testing, across strain rates of 0.001 (quasi-static), 1, 100 and 200 $s^{-1}$ (dynamic). Thus, direct comparisons could be made across all four strain rates.

Strain rate sensitivity (m-value) is defined as the gradient of the log strain rate-log proof strength plot [3]. Given that four strain rates were investigated, three m-values could be derived, namely:

- m-value from 0.001 to 1 $s^{-1}$ ($m_{0.001\text{-}1}$).
- m-value from 1 to 100 $s^{-1}$ ($m_{1\text{-}100}$).
- m-value from 100 to 200 $s^{-1}$ ($m_{100\text{-}200}$).

Additionally, the mean m-value ($m_{mean}$) across all four strain rates was derived. Figure 4.27 illustrates derivation of the m-values.

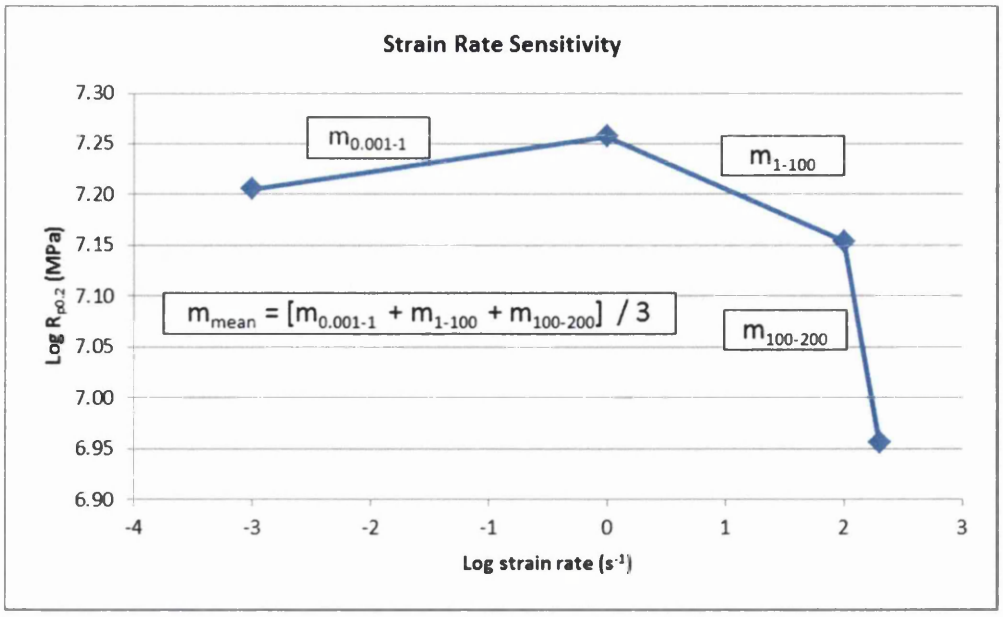


Figure 4.27: Strain rate sensitivity

*Temperature Evolution with Increasing Strain Rate*

During dynamic tensile testing, the 'adiabatic heating' theory was suspected with increasing strain rate (see chapter: Results & Discussion). Moreover, increasing adiabatic heating with increasing strain rate was suspected to be more significant for 38MnB5 than for the other grades, owing to the higher carbon content. In order to demonstrate the adiabatic heating suspicion, quasi-static and dynamic tensile testing across all four strain rates of 0.001, 1, 100 and 200 $s^{-1}$ was repeated for 22MnB5 and 38MnB5 with the addition of thermocouple data logging. Note that only two grades could be selected for repeat dynamic tensile testing due to limited availability of the dynamic tensile testing facility.

For the quasi-static tensile specimen, eight thermocouples were welded to the 79 mm reduced section at approximately 11 mm intervals. For the dynamic tensile specimen, three thermocouples were welded to the 16 mm reduced section at 8 mm intervals. Multiple thermocouples were welded to the reduced section in the described manner in order to maximise the probability of fracture occurring in the vicinity of a thermocouple and thereby, in order to accurately measure the maximum temperature rise during the tensile test.

***Microscopy***

The preliminary stages to microscopy included hot mounting, grinding, polishing and chemical etching. Standard metallographic preparation procedures [141] were followed as far as was practicable. Microscopy included both light optical microscopy (LOM) and scanning electron microscopy (SEM). LOM was performed with both the Reichert Polyvar 2 Light Optical Microscope and the Reichert Jung MeF3 Light Optical Microscope. SEM was performed with the JEOL JSM 6100 Scanning Electron Microscope.

In the case of the CASIM experimental, the metallographic specimen (~ 11 mm in length) was taken from the longitudinal centreline of the heat treated CASIM specimen and thus, from the region between the two tensile specimens. The cross-section directly adjacent to each tensile specimen was examined. The configuration is illustrated by Figure 4.28.

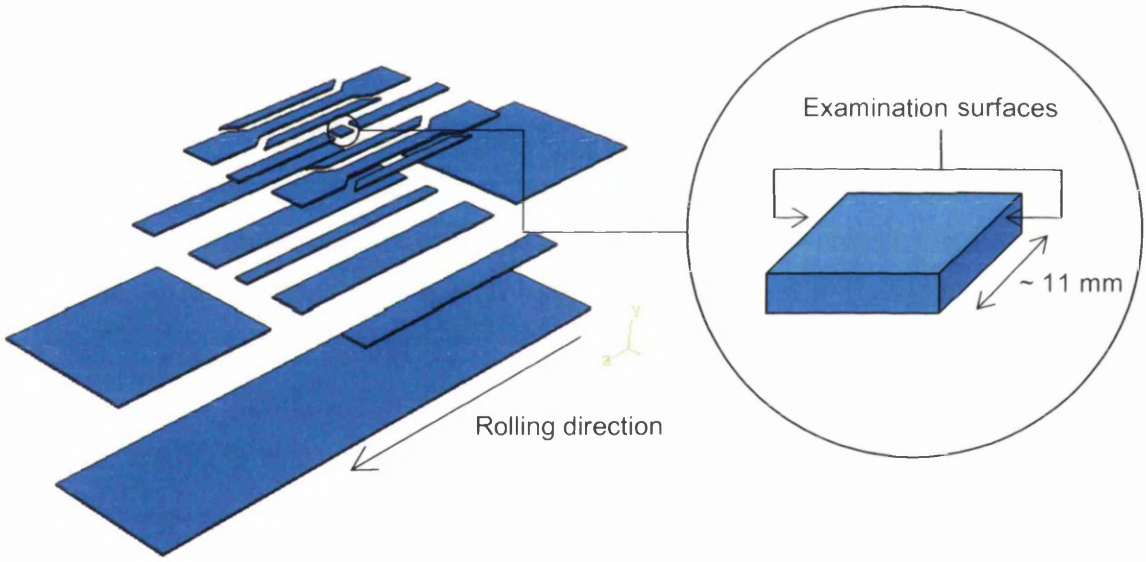


Figure 4.28: Configuration of metallographic specimen from heat treated CASIM specimen

In the case of the Heating Curves & Water Quenching experimental and the Laboratory Hot Stamping experimental, the metallographic specimen (~ 11 mm in length) was taken from the widest region of the fractured tensile specimen that was gripped by the tensile machine during the tensile test. The end of the tensile specimen selected was that furthest from the fracture point, so to ensure that the microstructure represented the as-heat treated condition, without any modification from the tensile test. The cross-section corresponding to the longitudinal

centreline of the tensile specimen was examined. The configuration is illustrated by Figure 4.29.

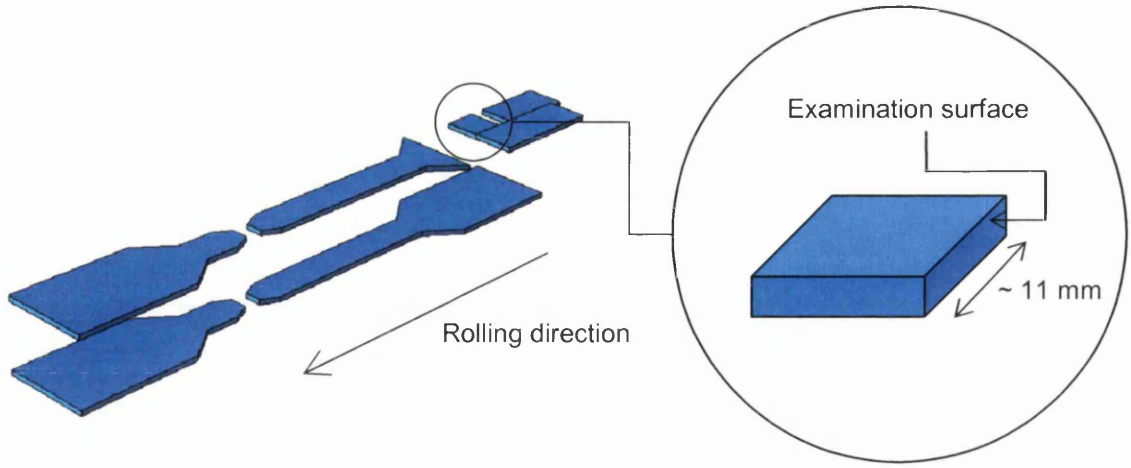


Figure 4.29: Configuration of metallographic specimen from heat treated tensile specimen

For the specimens subjected to dynamic tensile testing, two metallographic specimens were taken from each fractured dynamic tensile specimen. The first metallographic specimen (~ 11 mm in length) was taken from the end of the dynamic tensile specimen furthest from the fracture point so to ensure that the microstructure represented the as-heat treated condition, without any modification from the dynamic tensile test; in a similar fashion to that described above. The second metallographic specimen was taken from the reduced section. Here, the metallographic specimen began at the 'shoulders' of the dynamic tensile specimen and extended along the reduced section to the fracture point. For both metallographic specimens, the cross-section corresponding to the longitudinal centreline of the dynamic tensile specimen was examined. From the second metallographic specimen, modification to the microstructure resulting from increasing deformation along the reduced section to the fracture point could be determined. The configuration is illustrated by Figure 4.30.

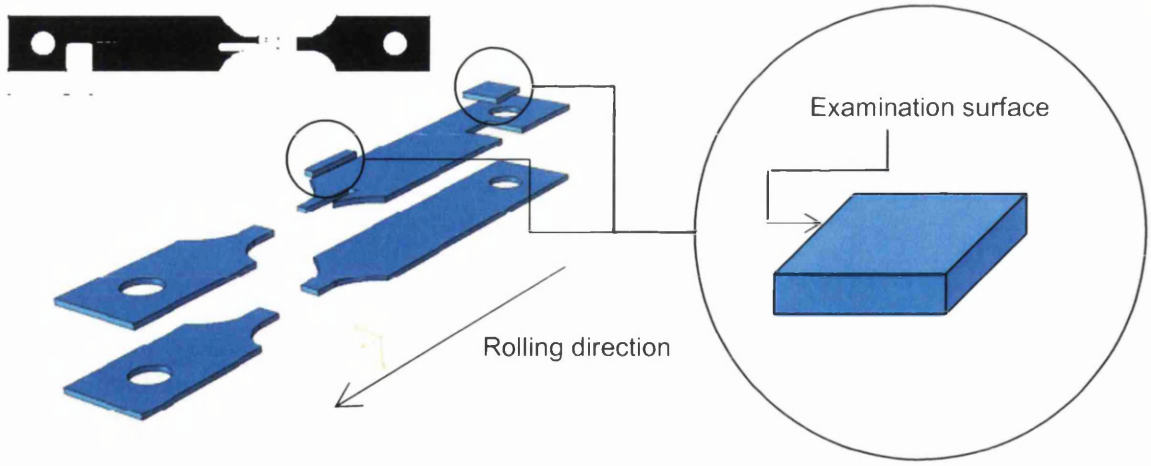


Figure 4.30: Configuration of metallographic specimens from heat treated dynamic tensile specimen

In addition to the generic etchant Nital; Marshall's, Klemm's and Vilella's etchants were used. The content of each etchant and a brief summary of its application are given in Table 4.5 [3] [142] [143].

Metallographic preparation has been described [144] as *'an art, the theory of which is unknown; and because success depends on numerous causes and on apparently trivial differences in the quality of the materials and in the manner of using them; each person has therefore to serve his own apprenticeship, which the experience of others may shorten, but cannot entirely supercede'*. Indeed, this statement was found to be correct, especially with regard to chemical etching. The most successful etchant, etchant strength, etching technique (face-down submersion, face-up submersion, perpendicular submersion, pipette dispersion or swabbing) and etching time; depended greatly on the specimen under examination.

Table 4.5: Etchants (adapted from [3] [142] [143])

| *Etchant* | *Content* | *Comments* |
|---|---|---|
| Nital | Ethanol 100 ml<br>Nitric acid 1-10 ml | General etchant<br>Proeutectoid α-ferrite white, pearlite black, bainite grey, martensite dark brown, retained γ-austenite light brown<br>Submerse specimen face-down<br>Etching time 5-20 s |
| Marshall's | Oxalic acid 8 g<br>Sulphuric acid 5 ml<br>Water 100 ml<br>Hydrogen peroxide 30-40 ml | Proeutectoid α-ferrite grain boundaries<br>Submerse specimen perpendicular to the etchant<br>Etching time 10-60 s<br>Pre- and post-etch with Nital often beneficial |
| Klemm's | Sodium thiosulfate 50 ml<br>Potassium metabisulfite 1 g | Distinct colour contrast between proeutectoid α-ferrite (blue/brown), bainite (grey/black) and martensite (white/yellow)<br>Submerse specimen face-up and gently agitate<br>Etching time 10-90 s |
| Vilella's | Picric acid 1 g<br>Hydrochloric acid 5 ml<br>Ethanol 100 ml | Ferrite-carbide structures, particularly tempered martensite<br>Gently swab specimen<br>Etching time 30-120 s |

Nital was sufficient in nearly all cases for revealing the final, heat treated microstructure. Marshall's, Klemm's and Vilella's etchants merely provided additional information or confirmation of what was discovered by Nital etching.

As a general rule, it was found that higher carbon equivalent responded better to more subdued etchant strength and etching technique; in addition to shorter etching time. However, the most successful etchant strength, etching technique and etching time varied considerably, even between two specimens from the same grade and exposed to the same heat treatment. This demonstrates the sensitivity of chemical etching to many factors, such as ambient temperature, age/freshness of etchant and minor chemical heterogeneity within the specimen. Thus, there was not a defined method to follow during metallographic preparation. Guidelines (such as listed in Table 4.5) were followed as far as was practicable. However, experimentation and adaptability was vital. Moreover, the appearance under microscopy varied, even between two specimens from the same grade, exposed to the same heat treatment and etched with the same treatment. For example, in certain cases, martensite appeared very dark brown; while in other cases, martensite appeared much lighter or even grey rather than brown.

As far as was appropriate, consistent magnifications were used throughout the research project, namely ×500 for LOM and ×2500 for SEM. This was desired so to aid direct comparison between micrographs. Ultimately however, magnifications were selected according to the individual specimen so to best represent the microstructural features.

In the case of the CASIM, Heating Curves & Water Quenching and Laboratory Hot Stamping experimentals, nine LOM micrographs and three SEM micrographs were taken per examination surface. The configuration is illustrated by Figure 4.31

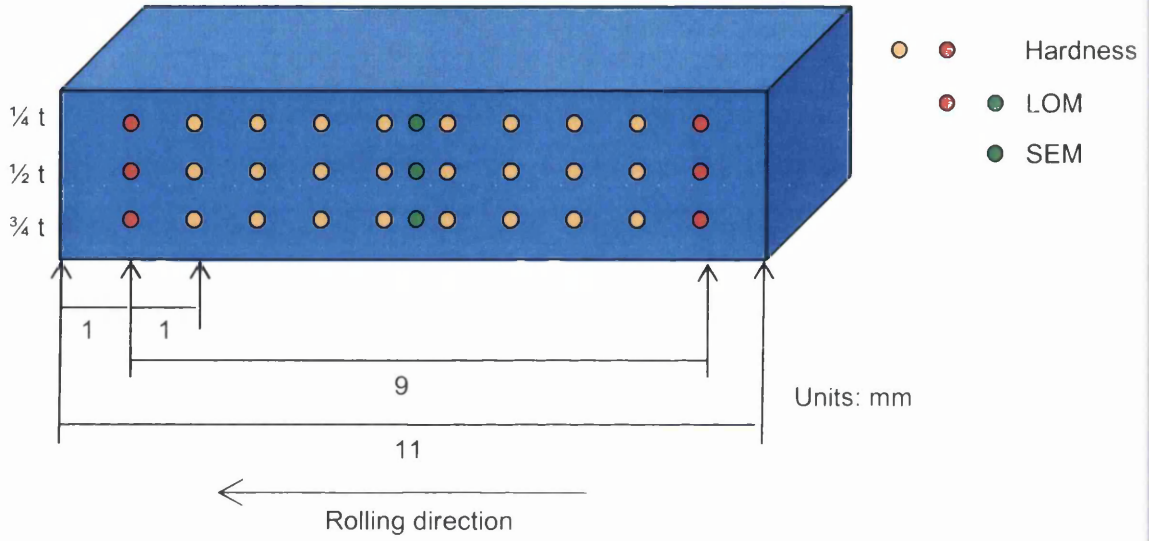


Figure 4.31: Configuration of microscopy and hardness testing points

For the metallographic specimen taken from the un-deformed region of the fractured dynamic tensile specimen, nine LOM micrographs and three SEM micrographs were taken per examination surface, in the same fashion as illustrated by Figure 4.31. However, for the metallographic specimen taken from the reduced section of the fractured dynamic tensile specimen, the three SEM micrographs were taken at the fracture point, as illustrated by Figure 4.32.

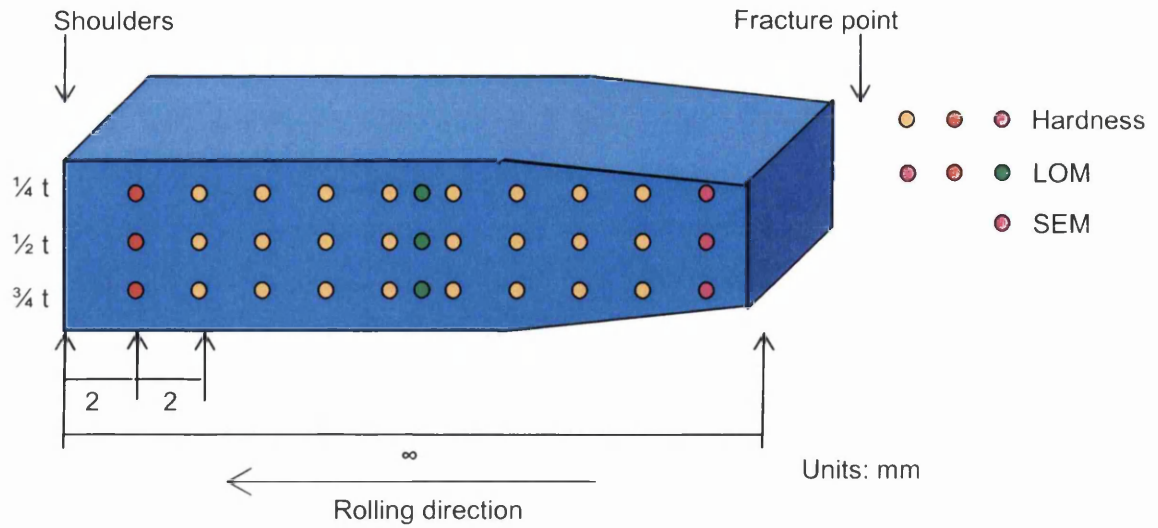


Figure 4.32: Configuration of microscopy and hardness testing points (reduced section of fractured dynamic tensile specimen)

***Image Analysis***

Image analysis included microconstituent volume fraction measurement and proeutectoid α-ferrite grain size measurement.

Throughout microscopy, the only microconstituents to be observed were proeutectoid α-ferrite, martensite and intermetallic compounds/inclusions (e.g. carbides, nitrides and sulphides). Retained γ-austenite, pearlite and bainite were not observed, which reflects the chemistries of the investigated grades and also the nature of heat treatment. Moreover, measuring the crystal (packet, block, lath or plate) size of martensite is notoriously difficult and even, impossible [145]. Hence, only proeutectoid α-ferrite grain size was measured.

The preferred method of image analysis used Adobe Photoshop software. The method involved rendering a 'map' of the micrograph by manually tracing around each individual proeutectoid α-ferrite grain and intermetallic compound/inclusion. Proeutectoid α-ferrite grains were coloured pink, intermetallic compounds/inclusions were coloured orange, while the remaining microstructure constituted by martensite was coloured black. Figure 4.33 presents an example. Microconstituent volume fractions (expressed as percentages) and mean proeutectoid α-ferrite grain size (expressed as grain area) could then be calculated from the pixel count.

Although it is acknowledged that a published standard procedure does not exist for the above analyses using Adobe Photoshop, the method represents an 'in-house' standard procedure that is accepted throughout Tata Steel since it is considered [68] to be more accurate and precise than published standard procedures that are available, such as the Manual Point Counting method for estimating microconstituent volume fractions [146] and the Lineal Intercept method for estimating grain size [147]. However, the Photoshop method required considerable development before it was fit for use. Thus, during the preliminary CASIM experimental, at which time the Photoshop method was still under development, the Manual Point Counting and Lineal Intercept methods were used.

In the case of the CASIM experimental, LOM micrographs were used for image analysis (while SEM micrographs were used for closer observation of microconstituent morphology). In the case of the Heating Curves & Water Quenching and Laboratory Hot Stamping experimentals, SEM micrographs were used for image analysis (while LOM micrographs were used for preliminary detection of microconstituents).

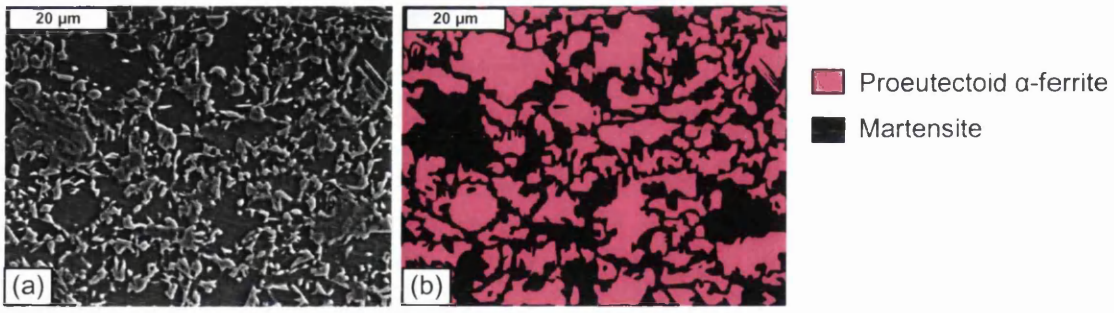


Figure 4.33: Image analysis using Adobe Photoshop (a) SEM micrograph (b) rendered map

***Energy Dispersive X-Ray Spectroscopy***

During microscopy, intermetallic compounds/inclusions were observed in the microstructure of grade 25MnB5 (Mo). In order to chemically characterise these intermetallic compounds/inclusions, energy dispersive X-ray spectroscopy (EDX) was conducted.

EDX was performed with the JEOL JSM 35C Scanning Electron Microscope and Oxford Instruments AZTec analysis system with a SiLi SATW (high resolution cryo cooled) detector. Standard procedures [148] were followed at all times.

When irradiated by electrons, different chemical elements emit characteristic X-rays dependent on the atomic structure. Determination of the chemical character of different elements can then be made from assessment of such X-ray emission, since the X-ray energy emitted from each element is unique to the atomic structure of that element [149].

Specimens subjected to EDX were equivalent to the metallographic specimens subjected to microscopy.

***X-Ray Diffraction***

It is widely reported that quench hardened martensitic grades exhibit a volume fraction of retained γ-austenite. Moreover, the probability of retained γ-austenite is raised with increased carbon content or carbon equivalent, since the Mf temperature is depressed. However, the retained γ-austenite usually presents itself with such a low volume fraction and with such a thin 'film-like' or 'inter-lath' [150] [151] morphology, that it is seldom observable from LOM or even SEM. Thus, to assess the presence of retained γ-austenite, X-ray diffraction (XRD) was performed on the 22MnB5 control grade and the 38MnB5 experimental trial grade following laboratory hot stamping. Note that only two grades could be selected for XRD due to limited availability of the XRD facility. 22MnB5 was selected as the control grade. 38MnB5 was selected as the experimental grade with the highest probability of exhibiting retained γ-austenite due to the highest carbon content and carbon equivalent.

XRD was performed with the Philips PW1830 generator and PW1710 diffractometer controller operating at 50 kV and 40 mA using molybdenum irradiation, according to standard procedures [152].

When irradiated by X-rays, crystalline materials produce characteristic diffraction patterns dependent on the crystal structure. Quantitative determination of the relative volume fraction of different phases, including γ-austenite, can then be made from assessment of such X-ray diffraction patterns, since the X-ray intensity diffracted from each phase is proportional to the volume fraction of that phase present [153].

Specimens subjected to XRD were equivalent to the metallographic specimens subjected to microscopy. However, whereas for microscopy the cross-section was examined, for XRD, the upper surface with approximate area of 11×12.5 mm was examined.

***Hardness Testing***

Vickers hardness testing was performed with the Leco Micro-Hardness testing machine according to standard procedures [154]. The hardness specimen was equivalent to the metallographic specimen subjected to microscopy. Loads of 0.5 or 1 kg were used depending on the specimen.

In the case of the CASIM, Heating Curves & Water Quenching and Laboratory Hot Stamping experimentals, ten hardness measurements were taken at 1 mm intervals along the examination surface length. This was performed at ¼, ½ and ¾ the specimen thickness, giving rise to thirty hardness measurements in total. The configuration is illustrated by Figure 4.31. Hardness testing in this fashion gave rise to the 'hardness profile' (Figure 4.34). The standard deviation of the hardness profile was used to express the degree of microstructural heterogeneity/homogeneity.

For the hardness specimen taken from the un-deformed region of the fractured dynamic tensile specimen, thirty hardness measurements were taken in the same

fashion as described above and illustrated by Figure 4.31. However, for the hardness specimen taken from the reduced section of the fractured dynamic tensile specimen, hardness measurements were taken at 2 mm intervals along the examination surface length, from the shoulders to the fracture point. Moreover, the total number of hardness measurements taken was variable, depending on the length of the fractured reduced section. The configuration is illustrated by Figure 4.32. Hardness testing in this fashion demonstrated increasing work hardening along the reduced section to the fracture point and thus gave an approximation of the degree of deformation sustained. Figure 4.35 presents an example.

Hardness testing was also used to estimate the microconstituents present. It has been suggested [15] that each microconstituent is associated with a unique hardness range, namely:

- Proeutectoid α-ferrite < 200 Hv
- Bainite 200-400 Hv
- Martensite > 400 Hv

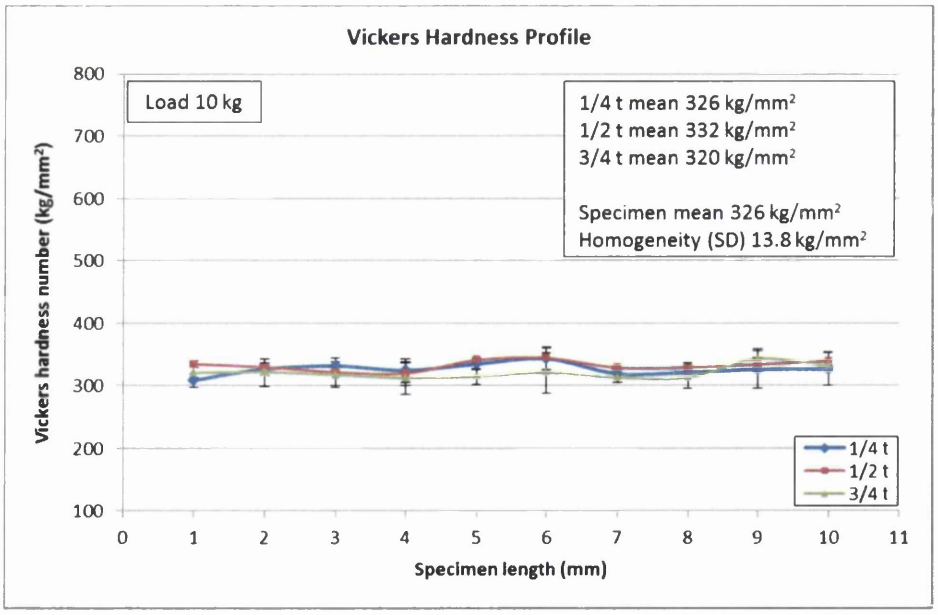


Figure 4.34: Hardness profile (un-deformed region)

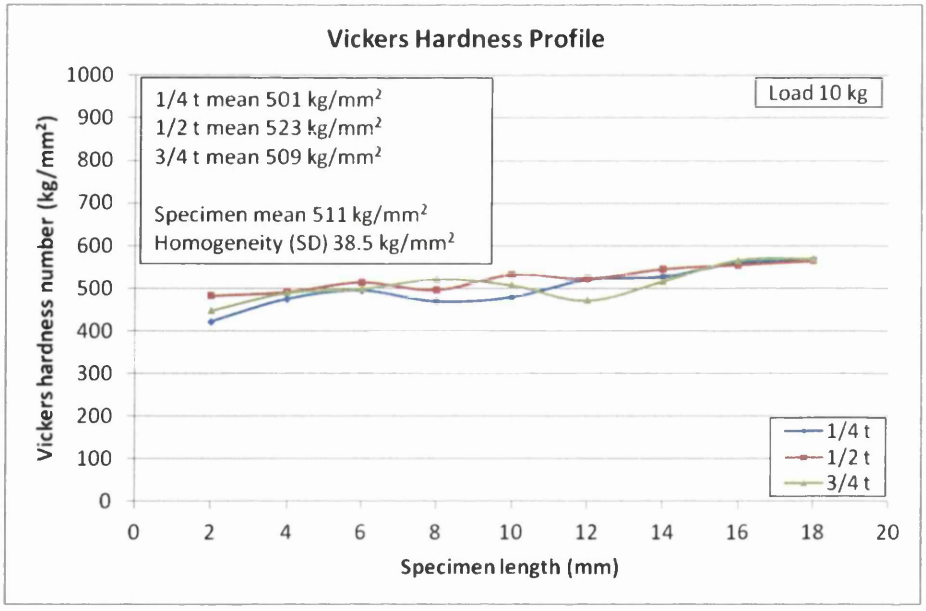


Figure 4.35: Hardness profile (deformed reduced section)

***Dilatometry***

Volume fraction of γ-austenite formed as a function of continuous temperature increase was determined via dilatometry performed with the Gleeble 3500 thermal-mechanical testing machine[30].

The dilatometry specimen with length and width of 130×10 mm and with the longitudinal axis parallel to the rolling direction was taken from the cold rolled sheet.

The continuous heating rate of 2 °C/s from ambient temperature to 1000 °C was maintained. The heating rate of 2 °C/s was selected in order to approximate the typical mean heating rate achieved during laboratory hot stamping.

The conventional method of calculating phase volume fractions from dilatometry is the 'lever rule', as performed according to standard procedures [155].

[30] Note that it would have been desirable to conduct all heat treatment, most notably laboratory hot stamping, with the Gleeble 3500 thermal-mechanical testing machine. However, the Gleeble 3500 did not become available until late in the research project, by which time, the research project had already committed to laboratory hot stamping.

The raw data output from dilatometry was time-transversal dilatation-temperature. Transversal dilatation was converted to dilatation strain with Equation 4.10.

$$\varepsilon_d = \frac{d}{w_0}$$

(Eq. 4.10)

Where: $\varepsilon_d$ = dilatation strain (unit-less)

d = transversal dilatation (mm)

$w_0$ = original specimen width (mm)

Time was plotted against dilatation strain to give the 'dilatometric curve' (Figure 4.36). The dilatometric curve demonstrates linear thermal expansion in the temperature ranges where no phase transformations occur. The 'S-curve' presented in the centre of the dilatometric curve corresponds to the BCC α-ferrite to FCC γ-austenite phase transformation. The greater density (atomic packing factor) of the FCC crystal structure gives rise to shrinkage (negative dilatation) during the course of the phase transformation [125], which is significant enough to overcome the 'natural' thermal expansion and thus, cause the dilatometric curve to deviate from linearity.

In the lever rule method, two linear segments of the dilatometric curve (one pre-transformation, coloured red in Figure 4.36; and one post-transformation, coloured green in Figure 4.36) are extrapolated through the S-curve. The volume fraction of the product phase at a given temperature during the course of the phase transformation is evaluated as the relative position of the measured dilatometric curve between the extrapolated linear segments [156], as illustrated by Figure 4.37.

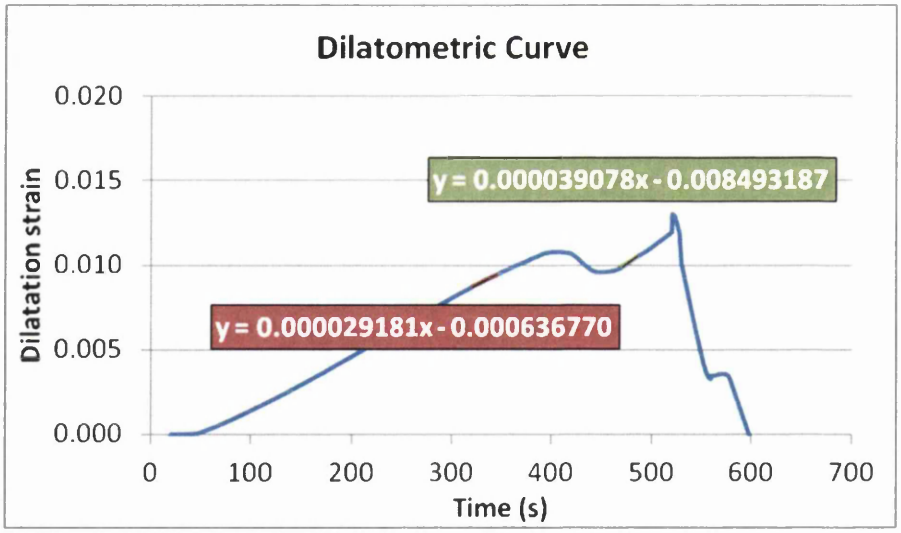


Figure 4.36: Dilatometric curve

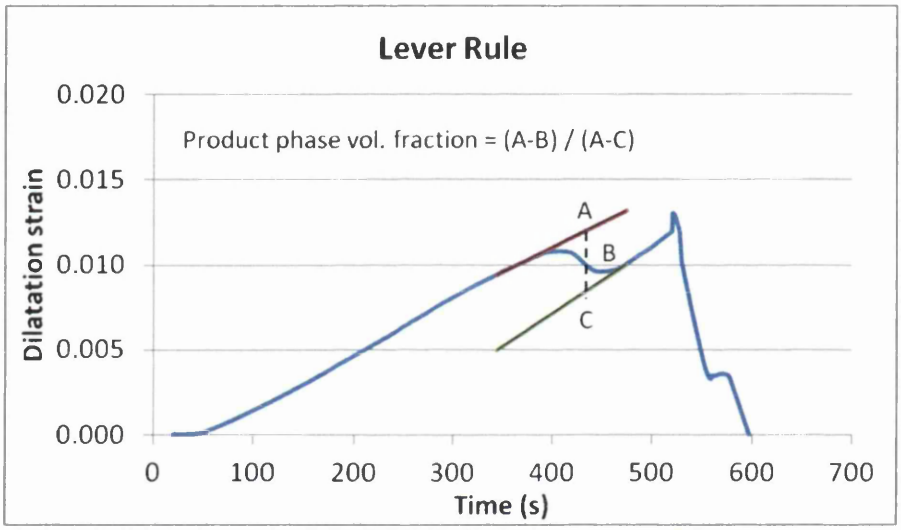


Figure 4.37: Lever rule

Finally, temperature was plotted against volume fraction of γ-austenite formed (expressed as a percentage) to give the 'austenisation curve' (Figure 4.38).

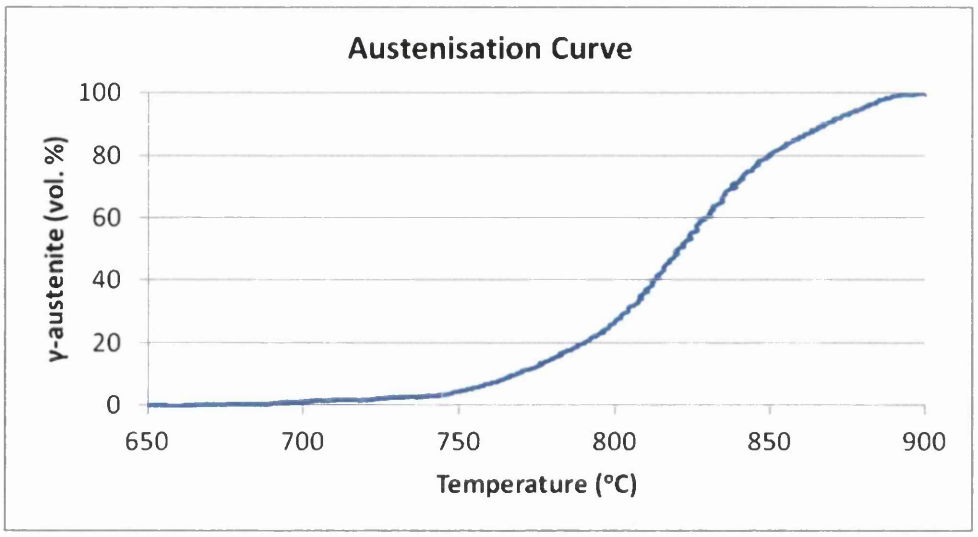


Figure 4.38: Austenisation curve

***Three-Point Bend Testing***

Three-point bend testing was performed according to standard procedures [157], using the Dartec Universal Hydraulic Press test machine and the 'two supports and former' method.

Specimens for three-point bend testing were prepared by cutting the hot stamped blank to 180 mm, in turn by removing 45 mm from the end that was handled during hot stamping. Thus, the three-point bend test specimen exhibited length and width of 180×25 mm.

In order to eliminate surface oxide, surface defects and most significantly, decarburisation from influencing the test and complicating fair comparison between the different grades, the three-point bend test specimens were thoroughly prepared prior to testing. The specimens were pickled in hydrochloric acid and manually ground so to remove surface oxide and the outer surface of the specimen, which is highly susceptible to decarburisation. It has been reported [158] that uncontrolled decarburisation can lead to a 30 $^{\circ}$ increase in bend angle, since decarburisation 'softens' the outer surface where bending stresses are most pronounced. The specimens were finally polished so to remove surface defects (e.g. scratches that might act as stress raisers). Thus, the thorough pickling, grinding and polishing meant that all specimens were in an equivalent condition,

with different degrees of surface oxide, surface defects and decarburisation prevented from influencing the test.

The configuration of the three-point bend test is illustrated by Figure 4.39. Force was applied so to achieve a constant displacement rate of 1 mm/s, to a maximum displacement of 30 mm, or until specimen fracture.

The raw data output from three-point bend testing was force-displacement. Note that both force and displacement are presented as negative values due to the compressive nature of the test.

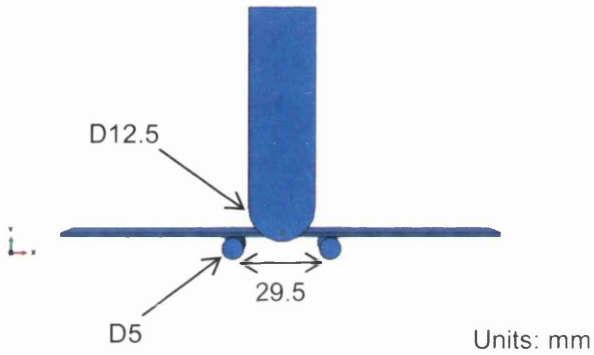


Figure 4.39: Three-point bend testing

***Finite Element Modelling Crash Simulation***

FEM crash simulation, conducted with LS-DYNA commercial software, involved full vehicle side impact with the experimental material data applied to the B-pillar reinforcement.

According to EURO NCAP, the second most important crash type is car to car side impact [159]. EURO NCAP simulates this type of crash by projecting a mobile deformable barrier of 1.5 m width into the driver's door at 50 km/h (~ 30 mph) (Figure 4.40) [159]. The FEM side impact simulation (Figure 4.41) conformed to the specification of the EURO NCAP side impact test.

The B-pillar is the second vertical roof pillar, supporting the central area of the roof (Figure 2.5). The B-pillar is imperative for anti-intrusive crash performance,

particularly in rollover incidents and side impact. The level of vehicle occupant protection provided in side impact is highly dependent on intrusion (displacement) of the B-pillar.

In the FEM crash simulation, the B-pillar reinforcement exhibited thickness of 1.6 mm. Following analysis of preliminary results, opportunities for down gauging with 38MnB5 were investigated with additional thicknesses of 1.4 and 1.2 mm.

The vehicle selected for FEM crash simulation was a generic, small, five-door hatchback. The implicit model comprised over ½ million elements, including the full vehicle (composed of tyres, wheels, steering column, engine (rigid mass), drive train, radiator and closures), in addition to the mobile deformable barrier. Mass was balanced over the vehicle to obtain a realistic centre of gravity.

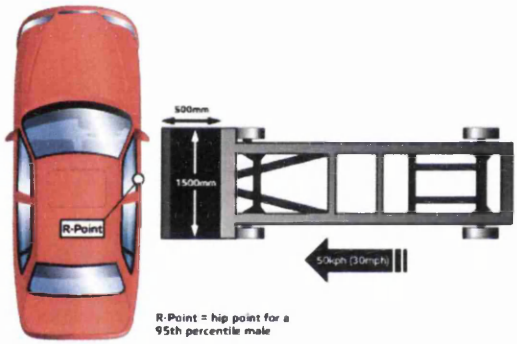


Figure 4.40: EURO NCAP side impact test [159]

Figure 4.41: FEM side impact simulation

Material data modelled into FEM crash simulation were based on tabulated quasi-static tensile data derived from mechanical testing. As mentioned in section: Dynamic Tensile Testing, it was originally planned to model the dynamic tensile

data into FEM crash simulation. However, due to a relatively insignificant difference between the quasi-static and dynamic tensile data, in addition to limited availability of FEM (and with 16 hrs required to run a single simulation), it was decided to base FEM on quasi-static data. The experimental material data were modelled into the B-pillar reinforcement, while the remaining components of the vehicle were modelled with conventional automotive steel data.

Using the procedure explained in section: Dynamic Tensile Testing, tensile data had to be prepared prior to fitting into the model. The raw force-displacement data resulting from quasi-static tensile testing were converted to true stress-true plastic strain (Equations 4.3 and 4.4). However, the true stress-true plastic strain data resulting from the conversion process are only valid during uniform elongation and to the commencement of necking. Thus, the true stress-true plastic strain data had to be extrapolated over the full true plastic strain range (Equation 4.9). Figure 4.42 presents the extrapolated true stress-true plastic strain 'FE Curves' that were fitted into the model.

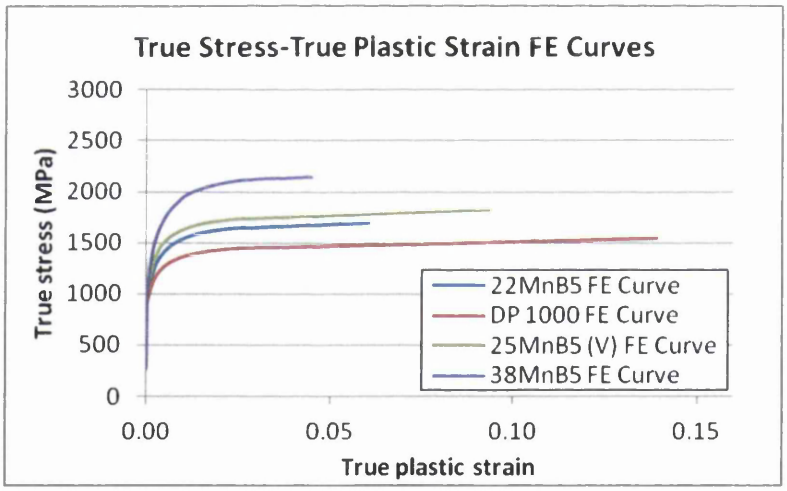


Figure 4.42: True stress-true plastic strain 'FE Curves'

The output from FEM crash simulation included plastic strain, displacement and internal energy. Note that displacement is presented as negative values due to the orientation of the simulation.

## CASIM Simulation of Hot Stamping Heat Treatment Cycles with Dual Phase Steels

### *Microstructural Analysis – Microconstituent Volume Fractions*

Figures 5.1a-p present LOM micrographs using the range of etchants, as indicated. Figures 5.2a-m present SEM micrographs. Figures 5.3a-c present microconstituent volume fractions for the DP steels. Figure 5.4 presents proeutectoid α-ferrite grain size for the DP steels.

For 22MnB5, the soak condition of 1 min-900 °C is believed to have achieved complete austenisation. On cooling, the austenitic microstructure is considered to have transformed to a completely martensitic microstructure (Figure 5.1a and 5.2a).

For DP 600 and DP 800, the soak conditions of 1 min-800 °C and 1 min-850 °C are believed to have been inter-critical annealing conditions, while the soak conditions of 1 min-900 °C and 3 min-900 °C achieved complete austenisation. On cooling from each soak condition, the γ-austenite is considered to have transformed to proeutectoid α-ferrite and/or martensite, with the transformation product(s) joining retained proeutectoid α-ferrite that was not austenised during inter-critical annealing, giving rise to a dual phase ferritic-martensitic microstructure (Figures 5.1c-f, 5.1h-k and 5.2b-i). With increased soak temperature from 800 to 850 and to 900 °C, or increased soak time from 1 to 3 minutes at the soak temperature of 900 °C, the volume fraction of martensite increased. This can be related to greater austenisation (thus providing a higher volume fraction of γ-austenite to potentially quench harden to martensite on cooling) and greater austenitic grain growth reducing the austenitic grain boundary surface area where the heterogeneous nucleation of reconstructive phase transformations is dominant and thereby, increasing quench hardenability.

For DP 1000, all soak conditions are believed to have achieved complete austenisation. On cooling, the austenitic microstructure is considered to have

transformed to a dual phase ferritic-martensitic microstructure (Figures 5.1m-p and 5.2j-m). With increased soak temperature from 800 to 850 and to 900 °C, or increased soak time from 1 to 3 minutes at the soak temperature of 900 °C, the martensite volume fraction increased, however only very marginally. From these observations it can be inferred that select precipitates (most likely high-temperature resistant niobium carbides/nitrides [39]) remained stable and restricted austenitic grain growth (so to restrict quench hardenability) up to 900 °C. The above suggestion is supported by the relatively small increase to proeutectoid α-ferrite grain size with increasing soak time-temperature. Dissolution of precipitates can increase quench hardenability two-fold [39]: 1) by enriching the γ-austenite solid solution with quench hardenability-raising alloying elements; and 2) by alleviating the restriction on austenitic grain growth that is posed by precipitates.

***Microstructural Analysis – Microconstituent Morphology***

With increasing soak time-temperature, the proeutectoid α-ferrite gain size increased for all three DP steels. Moreover, the microstructures of DP 600 were consistently coarser than the equivalent microstructures (equivalent soak conditions) of DP 800 and DP 1000. This may be attributed to the richer niobium contents of DP 800 and DP 1000, where niobium precipitates are potent grain size refiners during austenisation [39].

From the SEM micrographs (Figures 5.2a-m), it can be seen that for DP 800 and particularly DP 1000, the 1 min-900 °C microstructures exhibited impingement amongst martensitic packets (or 'islands'), with the proeutectoid α-ferrite matrix becoming less continuous. The 3 min-900 °C microstructures exhibited further impingement amongst martensitic packets. Impingement amongst martensitic packets can be related to martensitic coarsening and γ-austenite to martensite transformation kinetics [58]. Martensitic coarsening is the product of greater austenitic grain growth resulting from increasing soak time-temperature.

With increasing soak time-temperature, the martensitic morphology became progressively less 'globular' and more irregular. Indeed, the 1 min-900 °C

microstructures (Figures 5.2h and 5.2l) exhibited martensite with a fine 'needle-like' morphology in regions (although relative coarseness mentioned above was apparent in other regions). The 3 min-900 °C microstructures (Figures 5.2i and 5.2m) exhibited further martensitic morphological irregularity.

Similar morphological change resulting from increasing soak time-temperature was also observed in proeutectoid α-ferrite. Morphology is the leading characteristic distinguishing the form of proeutectoid α-ferrite, where several forms have been identified in the 'Dubé morphological classification scheme' (Figure 2.12) [55]. The allotriomorphic inter-granular form was apparent in the 1 min-800 °C and 1 min-850 °C microstructures. However, the 1 min-900 °C (Figure 5.1e) and 3 min-900 °C (Figure 5.2i) microstructures exhibited additional regions of the Widmanstätten form.

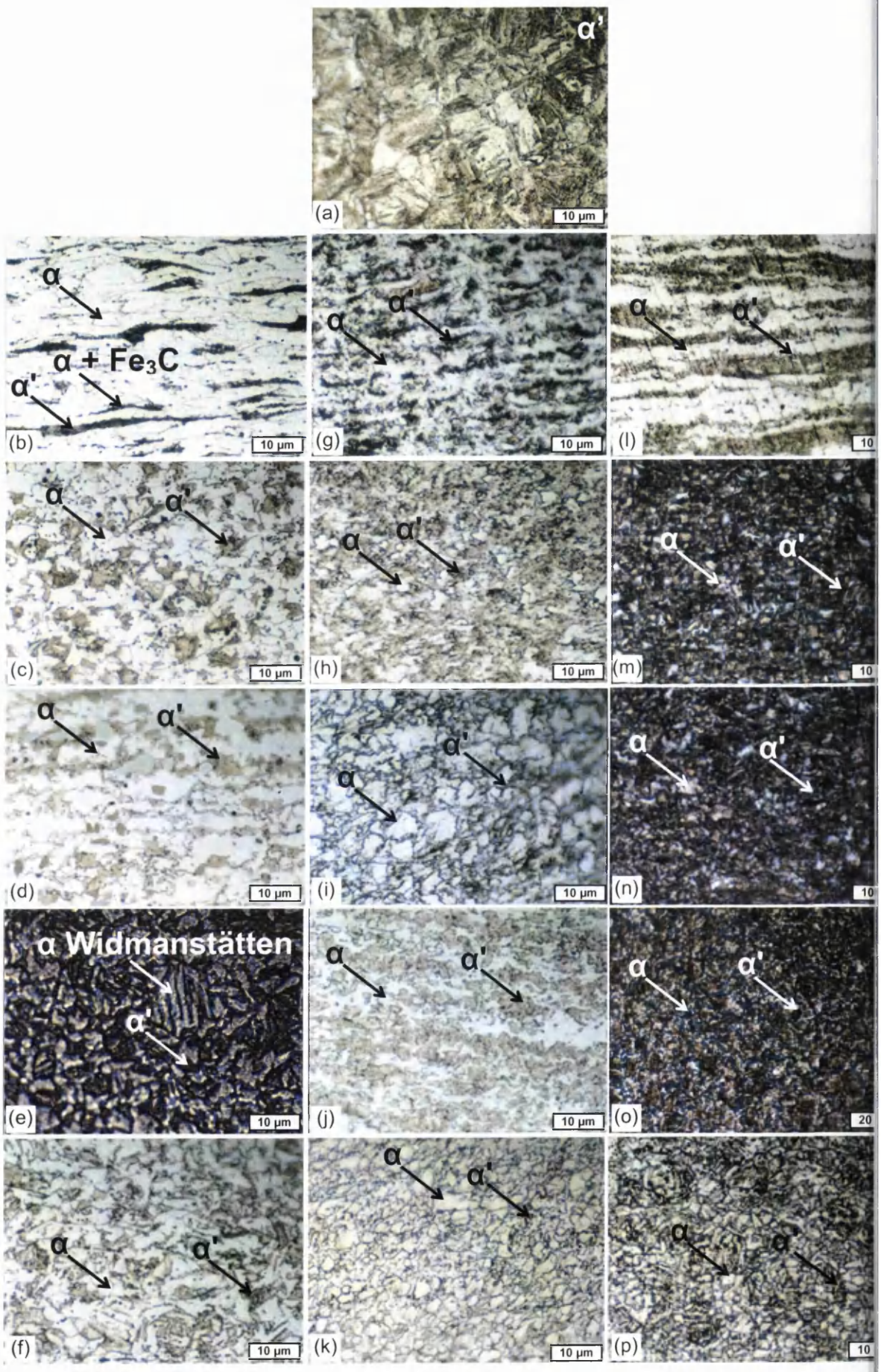
α'
(a)
10 μm
α
α + Fe3C
α'
(b)
10 μm
α
α'
(g)
10 μm
α
α'
(l)
10
α
α'
(c)
10 μm
α
α'
(h)
10 μm
α
α'
(m)
10
α
α'
(d)
10 μm
α
α'
(i)
10 μm
α
α'
(n)
10
α Widmanstätten
α'
(e)
10 μm
α
α'
(j)
10 μm
α
α'
(o)
20
α
α'
(f)
10 μm
α
α'
(k)
10 μm
α
α'
(p)
10

Figure 5.1: LOM micrographs (a) 22MnB5 3 min-900 °C Nital (b) DP 600 as-delivered Nital (c) DP 600 1 min-800 °C Nital (d) DP 600 1 min-850 °C Nital (e) DP 600 1 min-900 °C Nital/blue lens (f) DP 600 3 min-900 °C Nital (g) DP 800 as-delivered Nital (h) DP 800 1 min-800 °C Nital (i) DP 800 1 min-850 °C Nital (j) DP 800 1 min-900 °C Nital (k) DP 800 3 min-900 °C Nital (l) DP 1000 as-delivered Nital (m) DP 1000 1 min-800 °C Nital (n) DP 1000 1 min-850 °C Nital (o) DP 1000 1 min-900 °C Klemm's (p) DP 1000 3 min-900 °C Marshall's

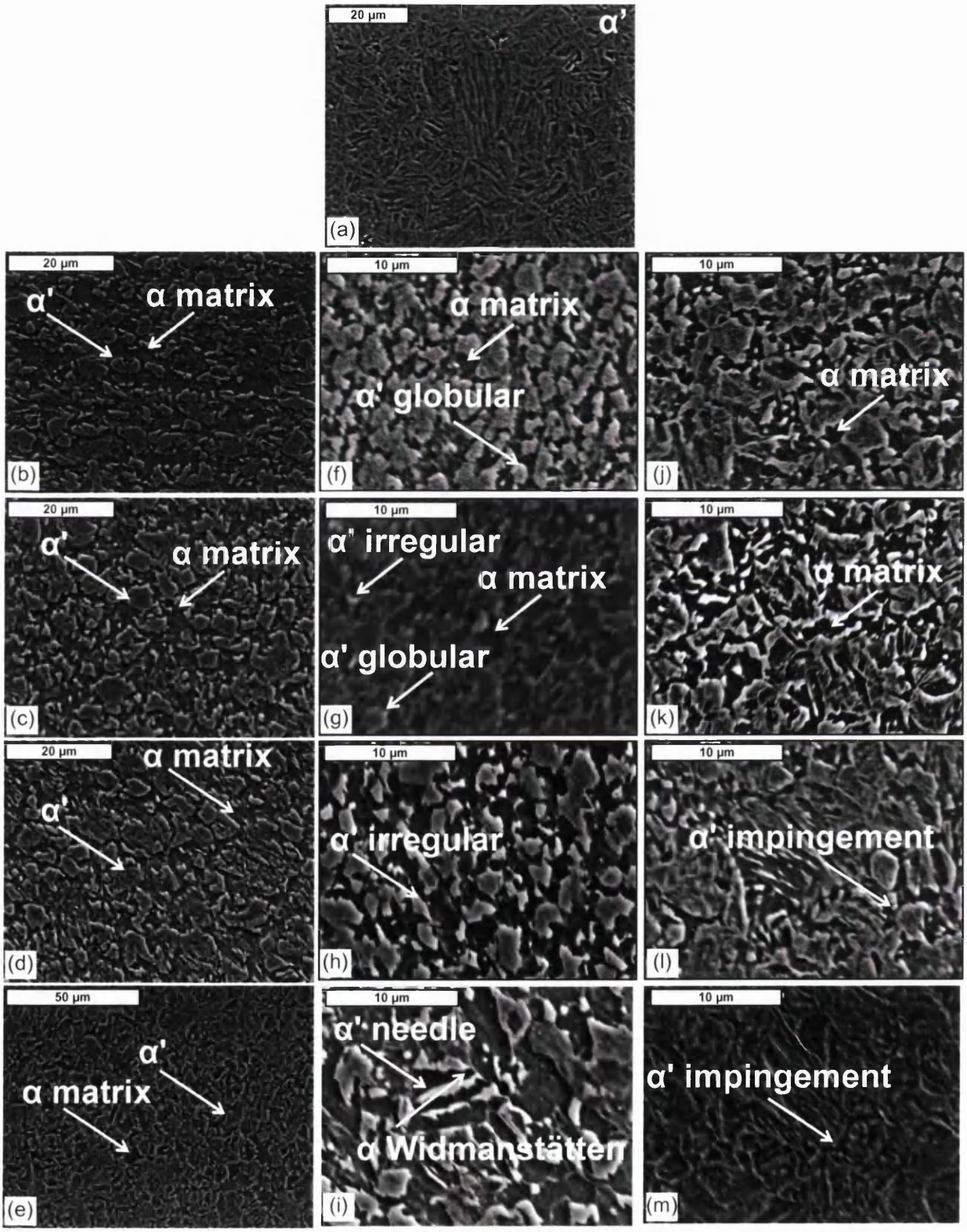

Figure 5.2: SEM micrographs (a) 22MnB5 3 min-900 °C (b) DP 600 1 min-800 °C (c) DP 600 1 min-850 °C (d) DP 600 1 min-900 °C (e) DP 600 3 min-900 °C (f) DP 800 1 min-800 °C (g) DP 800 1 min-850 °C (h) DP 800 1 min-900 °C (i) DP 800 3 min-900 °C (j) DP 1000 1 min-800 °C (k) DP 1000 1 min-850 °C (l) DP 1000 1 min-900 °C (m) DP 1000 3 min-900 °C

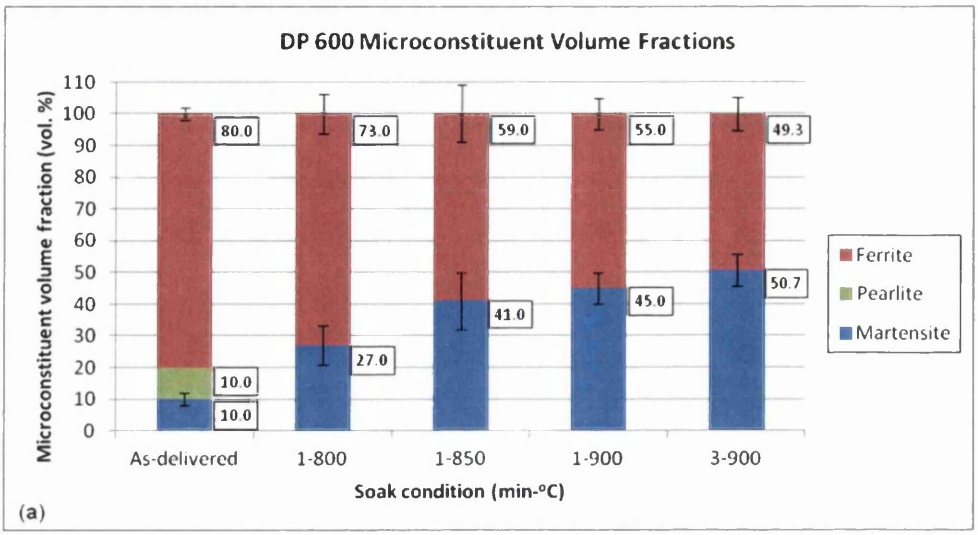


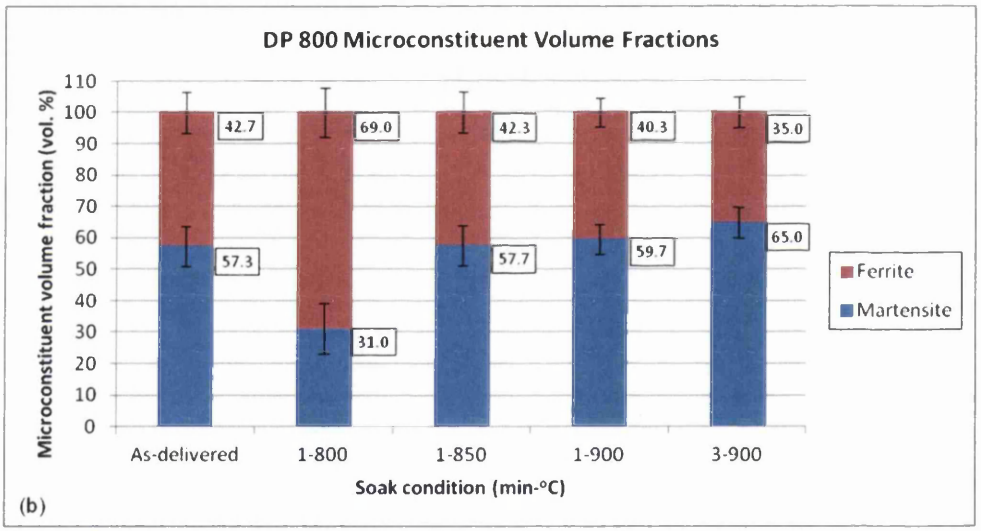

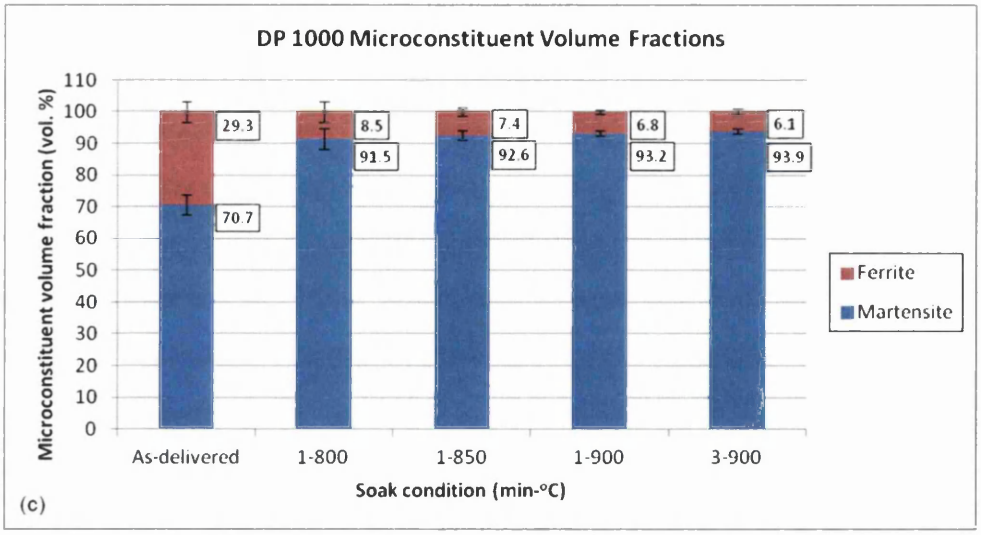


Figure 5.3: Microconstituent volume fractions (a) DP 600 (b) DP 800 (c) DP 1000

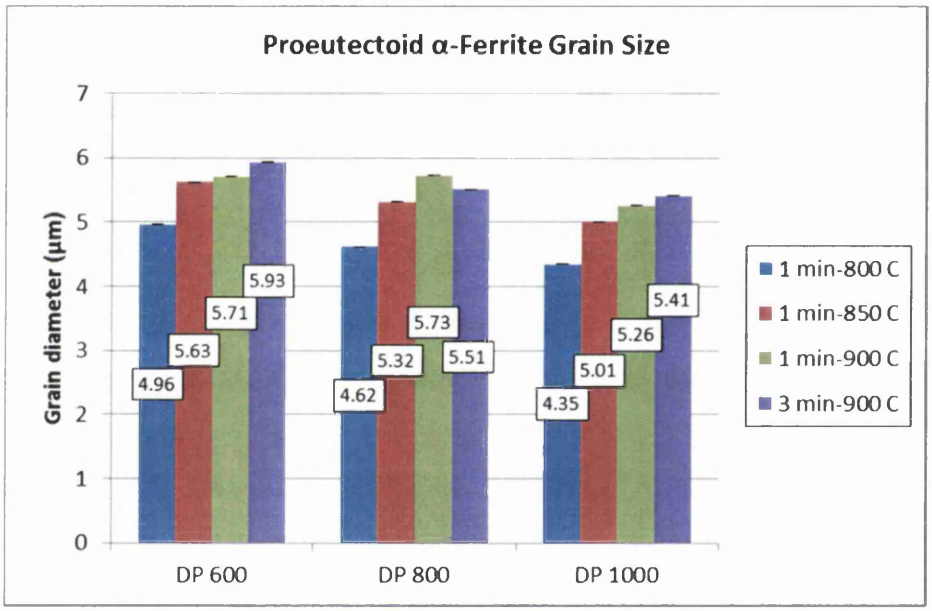


Figure 5.4: Proeutectoid α-ferrite grain size

***Mechanical Properties***

Figures 5.5a-d present tensile properties (proof strength-$R_{p0.2}$, ultimate tensile strength-$R_m$, uniform elongation-$A_u$ and total elongation-$A_{50}$) for each grade following each soak condition. Figures 5.5e-f present Vickers hardness-Hv properties (mean hardness across the specimen and heterogeneity of hardness across the specimen described by the standard deviation) for each grade following each soak condition.

For 22MnB5, mechanical properties were of an order typically resulting from hot stamping treatment. Further discussions are focused on the DP steels.

For DP 600, there was a consistent and positive correlation between soak time-temperature, hardness and proof strength and moreover, generally a positive correlation between soak time-temperature and ultimate tensile strength. This can be largely attributed to increased martensite volume fraction resulting from increased soak temperature or soak time (Figure 5.5g). Further, there was generally a negative correlation between soak time-temperature and uniform elongation or total elongation. This trend can also be attributed to increased martensite volume fraction resulting from increased soak time-temperature. However, there was an anomaly to this trend: the soak condition of 1 min-800 °C failed to provide the highest elongation values (indeed, this soak condition provided the lowest total elongation), despite providing the lowest martensite volume fraction. The relatively low elongation values resulting from the soak condition of 1 min-800 °C can be attributed to relative microstructural heterogeneity, in turn owing to the relatively low soak condition. This is evident from the heterogeneity of hardness value. Moreover, the relatively low elongation values may be attributed to a relatively high carbon concentration in martensite, where an inverse correlation has been reported between martensite volume fraction and martensite carbon concentration [160]. This can be expected from simply observing the iron-iron carbide metastable equilibrium phase diagram (Figure 2.11) and applying the Lever rule principle [11], where during the γ-austenite to proeutectoid α-ferrite transformation, more carbon is progressively rejected from the product phase to the parent phase with further proeutectoid α-ferrite formation. Thus, the γ-austenite carbon concentration increases and hence, so too does the carbon concentration of the product of the subsequent γ-austenite to martensite transformation. Higher martensite carbon concentration could give rise to a relatively brittle martensite microconstituent.

For DP 800, there was generally a positive correlation between soak time-temperature, hardness and proof strength and moreover, consistently a positive correlation between soak time-temperature and ultimate tensile strength. This can

be largely attributed to increased martensite volume fraction resulting from increased soak time-temperature (Figure 5.5g). Moreover, with increased soak temperature or soak time, the martensitic morphology was seen to become increasingly irregular and finer. This martensitic morphological irregularity and refinement with increasing soak time-temperature is also considered to have increased tensile strength. Further, increased soak temperature consistently gave rise to higher total elongation and generally gave rise to higher uniform elongation, despite higher martensite volume fraction. With increased soak temperature, proeutectoid α-ferrite grain size increased and the microstructure generally became more homogenous (evident from the heterogeneity of hardness values). Greater dissolution of precipitates at higher soak temperature can also be suggested. As mentioned above, higher martensite volume fraction can be expected to result in lower martensite carbon concentration. Each of these factors would partially explain higher elongation resulting from increased soak temperature. However, increased soak time from 1 to 3 minutes at the soak temperature of 900 $^{o}$C saw significant decreases to uniform elongation and total elongation.

For DP 1000, increased soak temperature generally gave rise to higher proof strength. This may be attributed to several factors. Firstly, as soak temperature increased, a transition from allotriomorphic inter-granular proeutectoid α-ferrite to Widmanstätten proeutectoid α-ferrite was observed. It has been suggested that in order to achieve low proof strength in the dual phase microstructure, the allotriomorphic inter-granular form should be sought [160]. This is since proof strength of proeutectoid α-ferrite highly influences proof strength of the dual phase microstructure, as this is the softer microconstituent and thus, the first microconstituent to begin yielding [93]. The allotriomorphic inter-granular form has been reported to be softer than the Widmanstätten form [55]. Secondly, it is possible that with increasing soak temperature (and decreasing proeutectoid α-ferrite volume fraction in the final microstructure as quench hardenability was raised), the proeutectoid α-ferrite became increasingly concentrated with carbon at the expense of martensite. Indeed, this phenomenon has been reported [93] and relates to the iron-iron carbide metastable equilibrium phase diagram and

Lever rule principle [11] discussed above. Moreover, the carbon concentration and substitutional solute concentration of proeutectoid α-ferrite could have been increased by higher soak temperature due to greater dissolution of precipitates. Higher dissolved alloy concentration in proeutectoid α-ferrite would provide greater solid solution strengthening, increased proof strength of proeutectoid α-ferrite and hence, increased proof strength of the dual phase microstructure. Thirdly, with increasing soak temperature, the martensitic morphology became less globular, more irregular and finer; eventually needle-like in regions following the 1 min-900 °C soak condition. This may have contributed to increased proof strength through martensitic boundary strengthening and work hardening from martensite-induced dislocation structures [58].

Increased soak time-temperature gave rise to a consistent decrease to ultimate tensile strength, despite increased martensite volume fraction. Coarser microstructure resulting from greater austenitic grain growth, loss of precipitation hardening from greater dissolution of precipitates and ultimately, lower martensite carbon concentration can all account for the decrease to ultimate tensile strength with increasing soak time-temperature. With respect to martensite carbon concentration, this is an important factor since martensitic strength is dramatically increased by increased carbon concentration [39] and moreover, ultimate tensile strength of the dual phase microstructure is highly dependent on martensite [160]. Decreased martensite carbon concentration (decreasing ultimate tensile strength of the dual phase microstructure) with increasing soak temperature, coincides with the suggestion in discussion of proof strength that proeutectoid α-ferrite carbon concentration increased with increasing soak temperature (increasing proof strength of the dual phase microstructure). However, it is acknowledged that the loss of ultimate tensile strength does not exclusively balance the gain of proof strength, since martensite is fundamentally a stronger microconstituent than proeutectoid α-ferrite.

The soak condition of 1 min-800 °C provided the highest uniform elongation and total elongation, with a progressive decrease to uniform elongation and total elongation with increasing soak temperature. It is suggested that the highest

elongation values originated from: 1) highest proeutectoid α-ferrite volume fraction; 2) predominant allotriomorphic inter-granular proeutectoid α-ferrite; 3) relatively low proeutectoid α-ferrite carbon concentration; 4) relatively continuous proeutectoid α-ferrite matrix, where it has been suggested [93] that in order to maximise elongation in the dual phase microstructure, martensitic packets should be isolated so to achieve a continuous proeutectoid α-ferrite matrix; and 5) relatively few dislocation structures resulting from martensite formation (anticipated from the relatively coarse and globular martensitic morphology). With increasing soak time from 1 to 3 minutes at the soak temperature of 900 °C, uniform elongation and total elongation increased. This may be attributed to greater microstructural homogeneity (evident from the heterogeneity of hardness values), proeutectoid α-ferrite coarsening and decreased martensite carbon concentration.

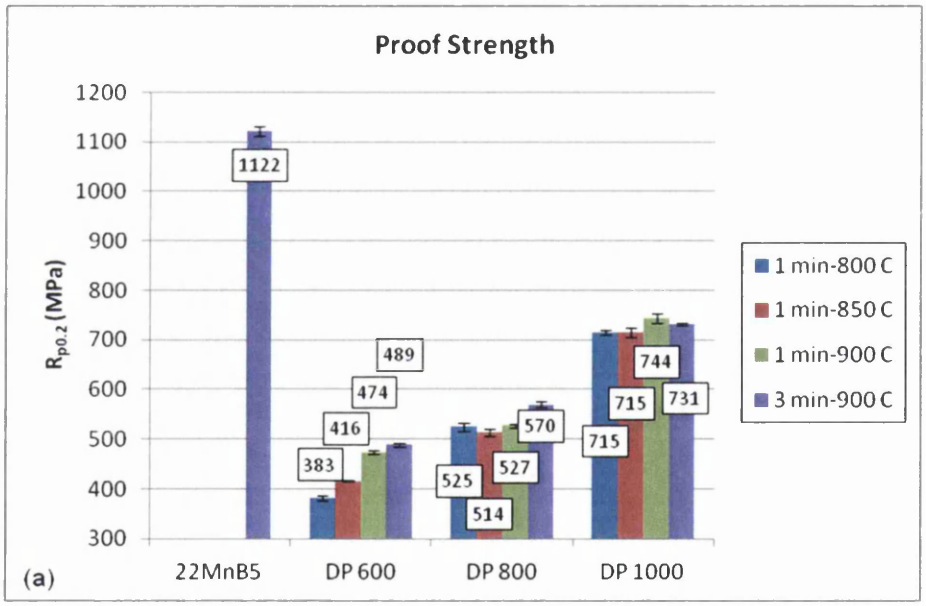

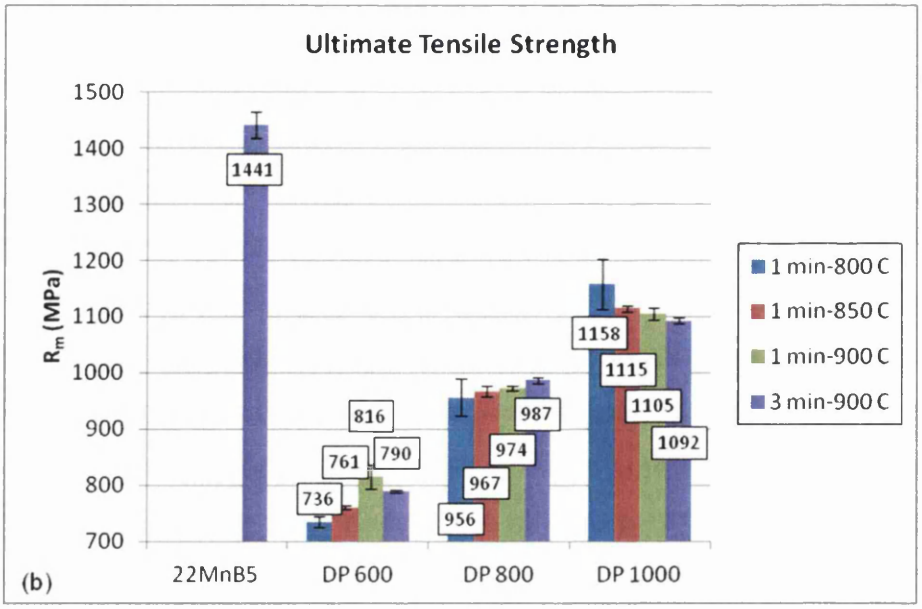
Ultimate Tensile Strength
1500
1400
1300
1200
1100
1000
900
800
700
$R_m$ (MPa)
1441
736
761
816
790
956
967
974
987
1158
1115
1105
1092
1 min-800 C
1 min-850 C
1 min-900 C
3 min-900 C
22MnB5
DP 600
DP 800
DP 1000
(b)

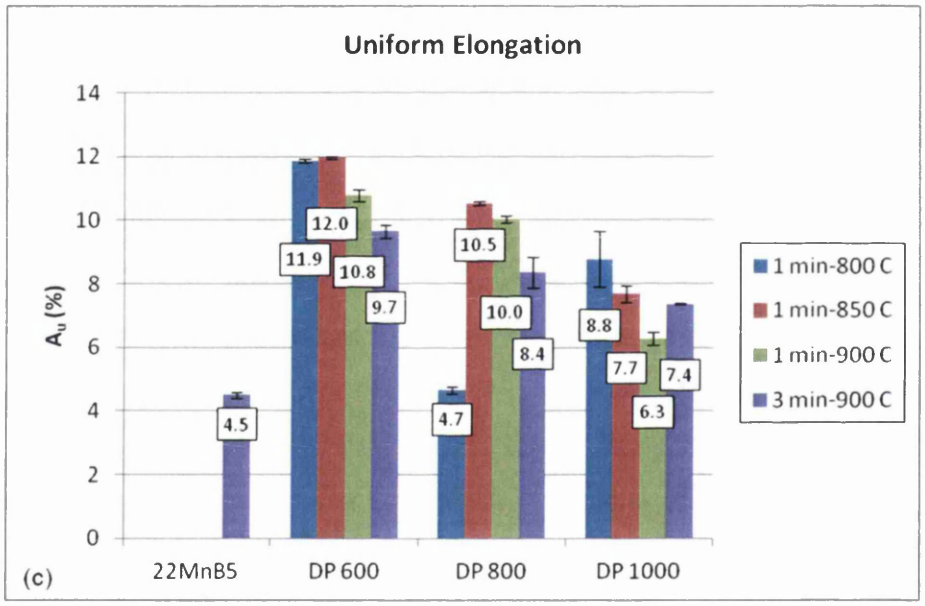
Uniform Elongation
14
12
10
8
6
4
2
0
$A_u$ (%)
4.5
11.9
12.0
10.8
9.7
4.7
10.5
10.0
8.4
8.8
7.7
6.3
7.4
1 min-800 C
1 min-850 C
1 min-900 C
3 min-900 C
22MnB5
DP 600
DP 800
DP 1000
(c)

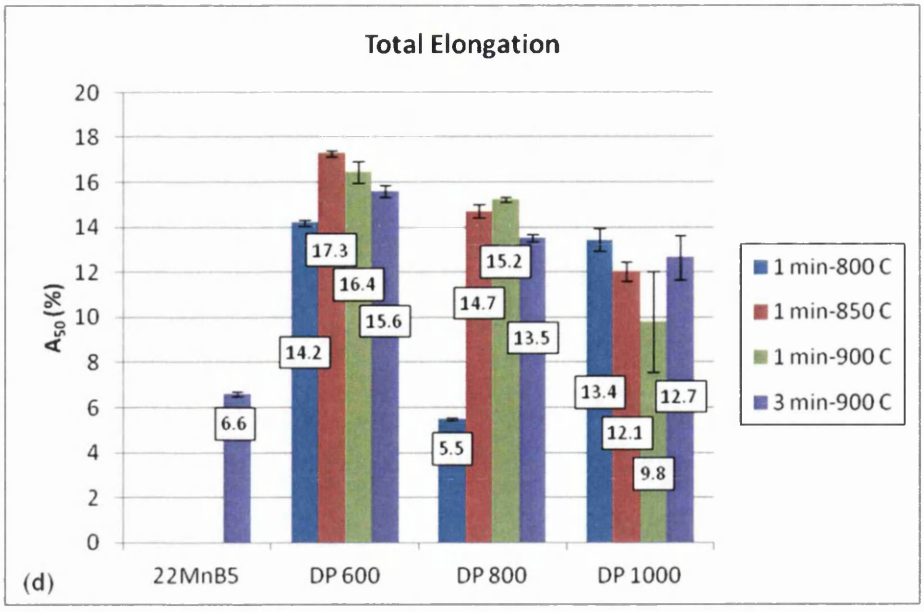
Total Elongation
$A_{50}$ (%)
20
18
16
14
12
10
8
6
4
2
0
6.6
14.2
17.3
16.4
15.6
5.5
14.7
15.2
13.5
13.4
12.1
9.8
12.7
1 min-800 C
1 min-850 C
1 min-900 C
3 min-900 C
22MnB5
DP 600
DP 800
DP 1000
(d)

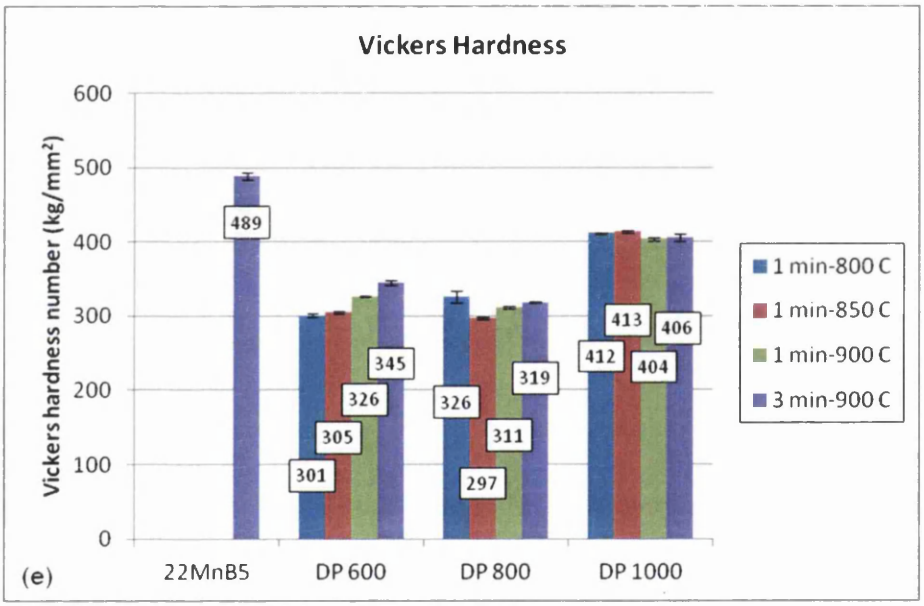
Vickers Hardness
Vickers hardness number (kg/mm²)
600
500
400
300
200
100
0
489
301
305
326
345
326
297
311
319
412
413
404
406
1 min-800 C
1 min-850 C
1 min-900 C
3 min-900 C
22MnB5
DP 600
DP 800
DP 1000
(e)

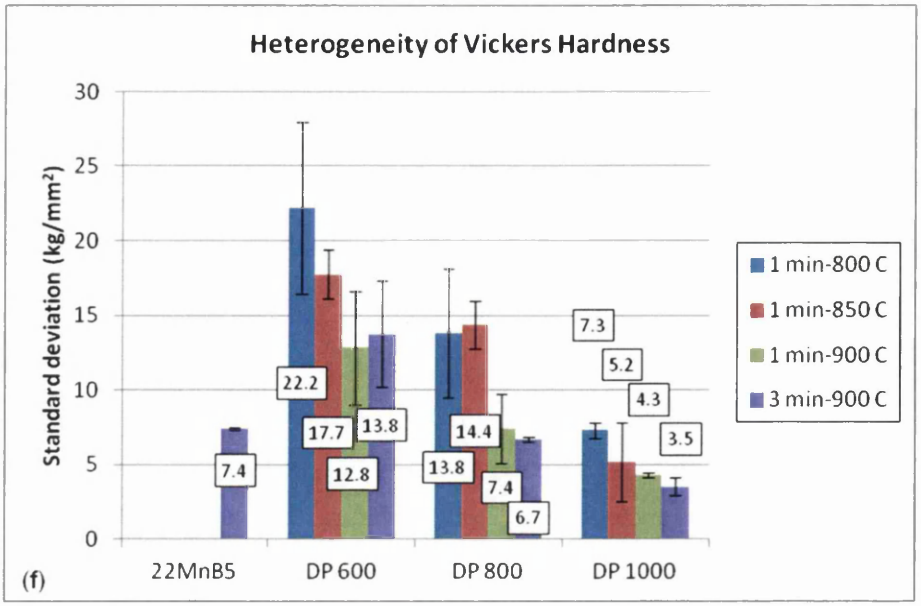


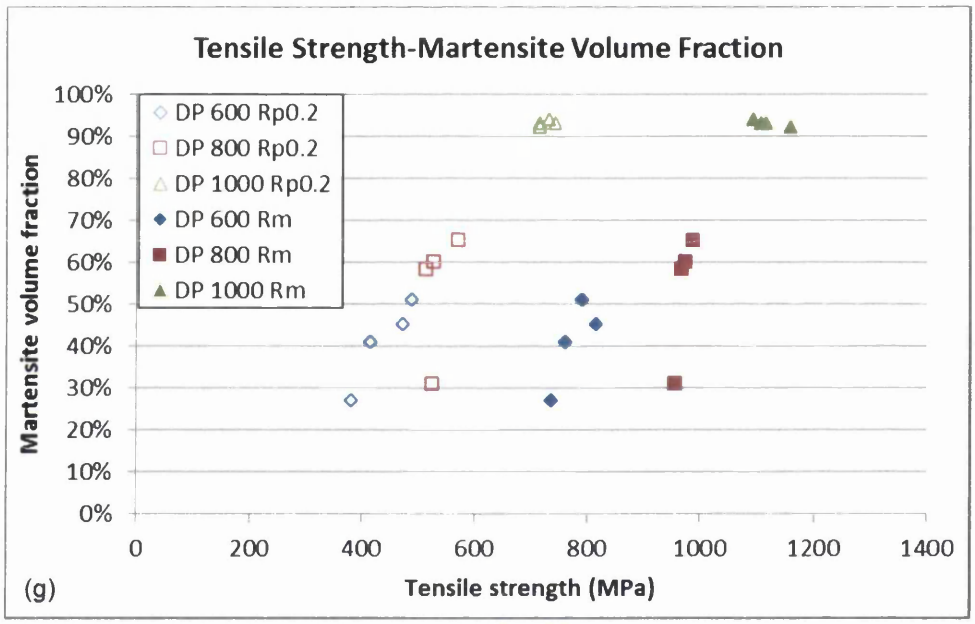


Figure 5.5: Mechanical properties (a) proof strength (b) ultimate tensile strength (c) uniform elongation (d) total elongation (e) Vickers hardness (f) heterogeneity of Vickers hardness (g) tensile strength-martensite volume fraction

### *Hot Stamping Potential*

For DP 600, the soak condition of 1 min-900 °C can be considered optimal, providing the third lowest proof strength of 474 MPa, the highest ultimate tensile strength of 816 MPa and the second highest total elongation of 16.4 %.

For DP 800, the soak condition of 1 min-900 °C can also be considered optimal, providing the third lowest proof strength of 527 MPa, the second highest ultimate tensile strength of 974 MPa and the highest total elongation of 15.2 %.

For DP 1000, the soak condition of 1 min-800 °C can be considered optimal, providing the equal lowest proof strength of 715 MPa, the highest ultimate tensile strength of 1158 MPa and the highest total elongation of 13.4 %.

The DP steels failed to compete with the ultrahigh strength of 22MnB5 (1122 MPa proof strength and 1441 MPa ultimate tensile strength) and therefore, cannot be considered advantageous for anti-intrusive crash performance. The higher tensile strength of 22MnB5 can be attributed to the completely martensitic microstructure and the higher carbon content, where carbon is reported to increase the strength/hardness of martensite more dramatically than any other element on a weight-for-weight basis [39]. Attainment of the completely martensitic microstructure in 22MnB5, but not in the DP steels, illustrates the supreme quench hardenability raising effect of boron addition.

However, the DP steels can be considered advantageous for impact energy absorptive crash performance, providing lower proof strength, substantially higher uniform elongation and total elongation, yet with a relatively small loss to ultimate tensile strength. Figure 5.6 presents a comparison of tensile properties (proof strength, ultimate tensile strength, uniform elongation and total elongation) between each of the DP steels (treated to their as-determined optimal hot stamping soak conditions) and 22MnB5. Here, each tensile property of the DP steels was divided by the corresponding value of 22MnB5, so to give a ratio of comparison. For example, DP 600 provided 0.6 times the ultimate tensile strength of 22MnB5, yet with 2.5 times the total elongation. Figure 5.6 clearly illustrates the substantially higher elongation values of the DP steels, yet with relatively small losses to ultimate tensile strength compared to 22MnB5. In turn, this clearly illustrates the improvement to impact energy absorptive crash performance.

Each of the DP steels provided higher ultimate tensile strength, yet similar (or even higher) total elongation compared to its as-delivered condition, as illustrated by Table 5.1 [161] [162]. Moreover, the tensile properties of as-delivered DP 800 were produced from heat treated DP 600, while the tensile properties of as-delivered DP 1000 were produced from heat treated DP 800. The significance of this is that a given heat treated DP steel can provide the tensile properties of a 'richer' as-delivered DP steel. This demonstrates the suitability of the DP steels to hot stamping, where equivalent tensile properties to a traditionally cold formed DP steel could be obtained from a leaner hot stamped DP steel. This could provide cost savings and improved weldability (subject to surface oxidation minimisation) for the automotive manufacturer if it chooses hot stamped DP steels rather than traditionally cold formed DP steels.

With the exception of DP 1000, each of the DP steels exhibits a lower carbon equivalent than 22MnB5 (Figure 4.1). Thus, DP 800 and especially DP 600 can be considered to provide superior weldability to 22MnB5. Weldability of the DP steels is further aided compared to martensitic 22MnB5 by their dual phase ferritic-martensitic microstructures. Thus, DP 800 and especially DP 600 offer opportunities for use in the tailor welded blank concept.

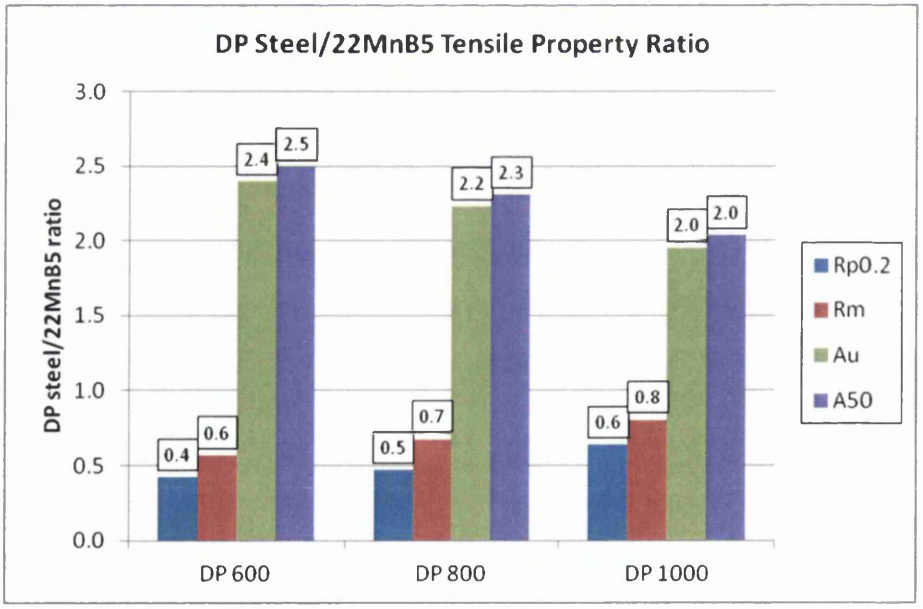


Figure 5.6: DP steel/22MnB5 tensile property ratio

Table 5.1: Comparison between as-delivered DP steels and heat treated DP steels (adapted from [161] [162])

| Grade | $R_{p0.2}$ (MPa) | | $R_m$ (MPa) | | A (%) | |
|---|---|---|---|---|---|---|
| | As-delivered (range) | Heat treated | As-delivered (typical) | Heat treated | As-delivered (typical) | Heat treated |
| DP 600 | 340-420 | 474 ± 4 | 600 | 816 ± 21 | 20.0 | 16.4 ± 0.1 |
| DP 800 | 450-560 | 527 ± 3 | 780 | 974 ± 4 | 14.0 | 15.2 ± 0.5 |
| DP 1000 | 590-740 | 715 ± 4 | 980 | 1158 ± 44 | 10.0 | 13.4 ± 0.1 |

**Heating Curves & Water Quenching**

Figures 5.7a-c present time-temperature heating curves given furnace/soak temperatures of 800, 850 and 900 °C respectively. The heating curve for each grade-thickness-soak temperature combination was used to calculate the furnace heating time and mean heating rate to soak temperature (Table 5.2). The heating time to soak temperature was then used in the Laboratory Hot Stamping experimental.

Conversion of the raw time-temperature data to mean temperature-mean heating rate data was used to estimate critical phase transformation temperatures on heating (Figure 5.8). For each grade, there was generally a positive correlation between soak temperature (heating rate) and the $Ac_1$ and $Ac_3$ temperatures. This can be attributed to superheating [11]. Moreover, the effect of superheating was more pronounced on the $Ac_3$ temperature [33]. There was generally an inverse correlation between carbon equivalent and $Ac_3$ temperature, while the $Ac_1$ temperature was relatively insensitive to carbon equivalent. These observations reflect the nature of the iron-iron carbide metastable equilibrium phase diagram (Figure 2.11). Each grade presented an $Ac_3$ temperature of below 800 °C given furnace temperatures of 800 or 850 °C. Moreover, each grade presented an $Ac_3$ temperature of below 850 °C given the maximum furnace temperature of 900 °C. Therefore, during laboratory hot stamping with each grade-thickness-soak temperature combination, the blank can be considered to have been completely austenitic at the moment of removal from the furnace.

Conversion of the raw time-temperature data on cooling to mean temperature-mean cooling rate data was used to estimate the probability of phase transformations during the 8-10 second transfer stage of laboratory hot stamping. No phase transformations were identified on cooling. Thus, for each grade-

thickness-soak temperature combination, it can be suggested that adequate austenitic grain growth and in turn, adequate quench hardenability was achieved so to prevent reconstructive phase transformations during the transfer stage of laboratory hot stamping.

By combining the last two paragraphs, it can be suggested that during laboratory hot stamping with each grade-thickness-soak temperature combination, the blank was completely austenitic at the commencement of the hot stamping/die quenching stage.

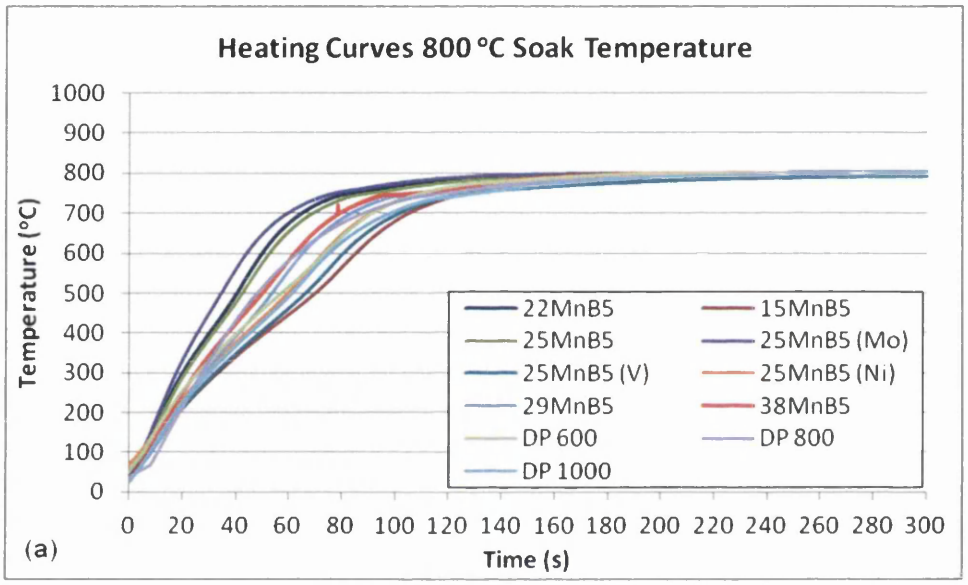


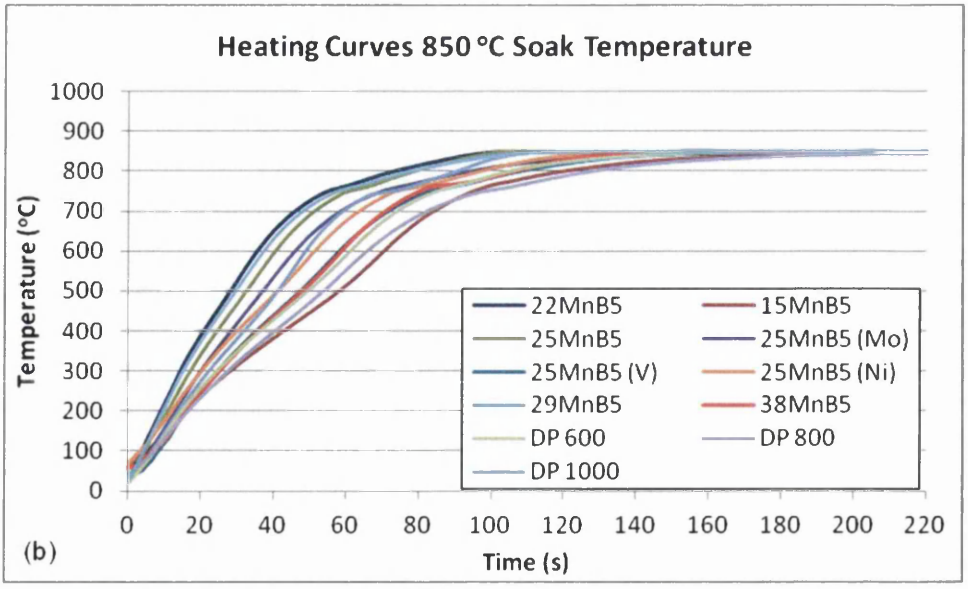

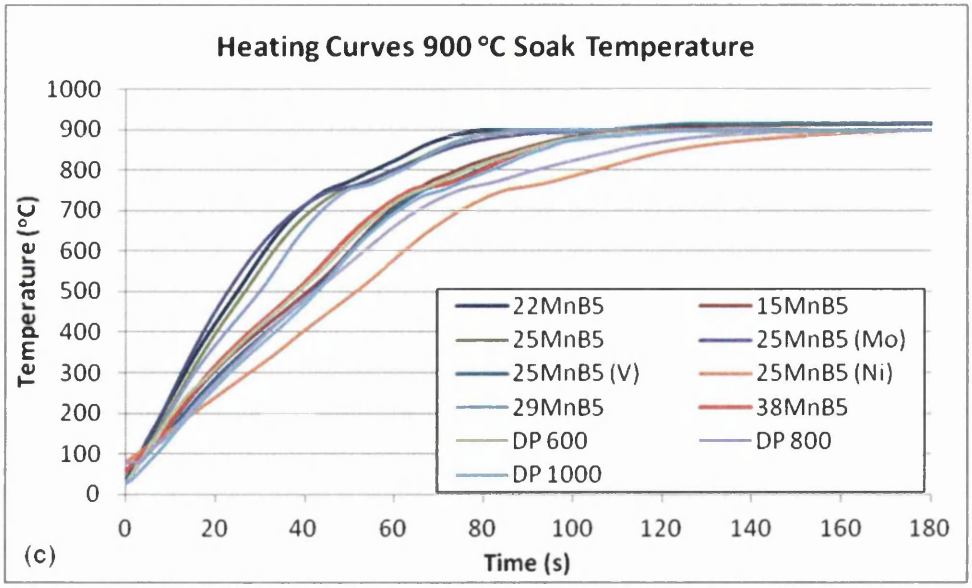


Figure 5.7: Time-temperature heating curves (a) 800 °C soak temperature (b) 850 °C soak temperature (c) 900 °C soak temperature

Table 5.2: Mean heating rates to soak temperature

| *Grade* | *Mean heating rate (°C/s) to soak temperature* | | |
|---|---|---|---|
| | *800 °C soak temperature* | *850 °C soak temperature* | *900 °C soak temperature* |
| 22MnB5 | 4.1 | 8.0 | 10.9 |
| 15MnB5 | 2.7 | 2.9 | 5.0 |
| 25MnB5 | 4.0 | 6.5 | 10.0 |
| 25MnB5 (Mo) | 4.6 | 5.5 | 7.8 |
| 25MnB5 (V) | 2.6 | 3.4 | 6.9 |
| 25MnB5 (Ni) | 2.6 | 3.6 | 4.4 |
| 29MnB5 | 3.5 | 7.3 | 10.0 |
| 38MnB5 | 4.0 | 5.1 | 6.7 |
| DP 600 | 3.9 | 5.0 | 6.8 |
| DP 800 | 2.8 | 3.1 | 4.8 |
| DP 1000 | 2.5 | 7.0 | 6.9 |

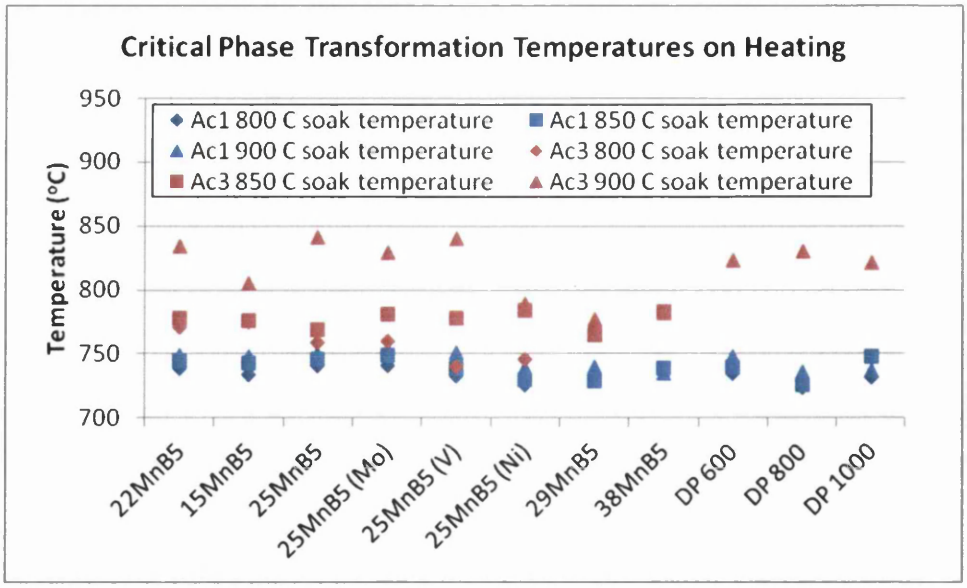


Figure 5.8: Critical phase transformation temperatures on heating

**Dilatometry**

Figure 5.9 presents austenisation curves. There was general agreement with the critical phase transformation temperatures of Figure 5.8, where each grade (except 15MnB5) exhibited more than 90 vol. % γ-austenite at 850 °C. Therefore, this supports that each grade presented an $Ac_3$ temperature of below 850 °C, regardless of the furnace temperature (heating rate) and that during laboratory hot stamping with each furnace/soak temperature, the blank would have been completely austenitic at the moment of removal from the furnace. Moreover, it is necessary to consider that the austenisation curves of Figure 5.9 do not illustrate the effect of γ-austenite volume fraction as a function of isothermal heat treatment at a given temperature. For example, according to Figure 5.9, at 800 °C, 15MnB5 exhibited ~ 25 vol. % γ-austenite. However, this is not to say that with isothermal heat treatment at 800 °C for 5, 3 or even 1 minute, the volume fraction of γ-austenite would not increase. Indeed, it can be anticipated that with such isothermal heat treatment, the volume fraction of γ-austenite would increase (Figure 2.25).

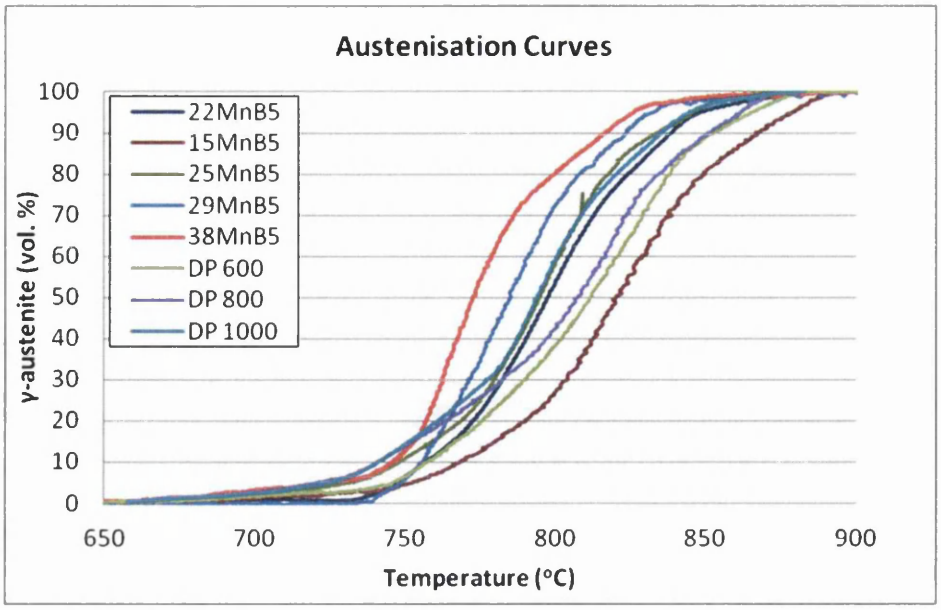


Figure 5.9: Austenisation curves

**Laboratory Hot Stamping**

***Microstructural Analysis***

Figure 5.10 presents retained γ-austenite volume fraction determined by XRD for 22MnB5 and 38MnB5 following each soak condition. Following a given soak condition, 38MnB5 consistently exhibited equal or higher retained γ-austenite volume fraction than 22MnB5 (except for 5 min-850 °C, although this is debatable when considering the associated error). This can be attributed to the higher carbon content of 38MnB5 lowering the Ms and Mf temperatures. However, for both grades following each soak condition, the retained γ-austenite volume fraction was marginal, reaching a maximum of just 3.6 vol. % for 22MnB5 and 4.5 vol. % for 38MnB5. Due to the marginal presence of retained γ-austenite and moreover, errors associated with the XRD measurements that were on occasion greater than the measured retained γ-austenite values, further discussions are focused exclusively on the dominant microconstituents, namely proeutectoid α-ferrite and martensite.

Throughout the Laboratory Hot Stamping Results & Discussion, results are presented graphically and are grouped into the categories of XMnB5, 25MnB5 (X) and Dual Phase. For example, Figures 5.11a-c present martensite volume fraction following each soak condition for the XMnB5 category, the 25MnB5 (X) category

and the Dual Phase category, respectively. Moreover, tabulated results are presented as appendices. For example, Appendix 1 presents martensite volume fraction for each grade following each soak condition.

With respect to microconstituent volume fractions, note that in each case where the martensite volume fraction was less than 100 vol. %, the remainder of the microstructure was considered to be constituted entirely by proeutectoid α-ferrite. In all cases, the possible minute volume fraction of retained γ-austenite (discussed above) and possible presence of intermetallic compounds/inclusions (discussed below) is ignored.

Figures 5.12a-c present proeutectoid α-ferrite grain size. Appendix 2 presents tabulated results.

For 22MnB5, the completely martensitic microstructure was achieved given the soak condition equal to and above 1 min-850 °C (Figure 5.11a): Figure 5.13a presents a micrograph. Given a soak condition below 1 min-850 °C, a significant volume fraction of proeutectoid α-ferrite was present. Moreover, with increasing soak time given the soak temperature of 800 °C, the martensite volume fraction generally increased. Indeed, for each grade, there was generally a positive correlation between soak time-temperature and martensite volume fraction (Figures 5.11a-c). The above observations illustrate the widely known relationship between increasing soak time-temperature, increasing austenitic grain growth, decreasing austenitic grain boundary surface area, decreasing heterogeneous nucleation sites for reconstructive phase transformations on cooling, increasing quench hardenability and ultimately, increasing martensite volume fraction in the final quenched microstructure [62] [63] [64].

The relationship between increasing soak time and increasing austenitic grain growth for 22MnB5 is supported by increasing proeutectoid α-ferrite grain size with increasing soak time given the soak temperature of 800 °C (Figure 5.12a), where the grain size of the product phase (proeutectoid α-ferrite) is proportional to the grain size of the parent phase (γ-austenite) [39]. However, the positive

correlation between soak time-temperature and proeutectoid α-ferrite grain size was not consistent for all grades, where quite frequently, proeutectoid α-ferrite grain size decreased with increasing soak time-temperature (Figures 5.12a-c). This can be related to quench hardenability, discussed above. With increasing soak time-temperature, the reduction to heterogeneous nucleation sites for reconstructive phase transformations on cooling delays nucleation of proeutectoid α-ferrite and moreover, limits opportunity for proeutectoid α-ferrite nucleation and growth. This can be appreciated from envisaging the CCT diagram where the proeutectoid α-ferrite curve is shifted to the right (Figure 2.8). Thus, although greater austenitic grain growth resulting from increasing soak time-temperature provides potential for a larger proeutectoid α-ferrite grain size, the simultaneous increase to quench hardenability may prevent the larger proeutectoid α-ferrite grain size from being achieved. It has also been reported [163] that increasing austenisation (soak) temperature with boron steels promotes segregation of solute boron atoms at γ-austenite grain boundaries, which can increase quench hardenability further.

For 15MnB5, the completely martensitic microstructure was not achieved across all nine soak conditions (Figure 5.11a). Instead, a dual phase ferritic-martensitic microstructure was presented following each soak condition, even up to the maximum soak condition of 5 min-900 °C: Figure 5.13b presents a micrograph.

In contrast to the above, 38MnB5 achieved the completely martensitic microstructure given the soak condition equal to and above 5 min-800 °C (Figure 5.11a): Figure 5.13h presents a micrograph.

For DP 600 and DP 800, the completely martensitic microstructure was achieved given the soak condition equal to and above 3 min-900 °C; while for DP 1000, the completely martensitic microstructure was achieved given the soak condition equal to and above 1 min-850 °C (Figure 5.11c): Figures 5.13i-k present micrographs.

Given a soak condition from which each grade presented a ferritic-martensitic microstructure (e.g. 1 min-800 °C), there was generally a positive correlation between carbon concentration or carbon equivalent and martensite volume fraction (Figures 5.11a-c).

The above observations illustrate the widely reported positive influence of carbon on quench hardenability [39]. Quench hardenability may be increased by chemical or physical characteristics, with chemical characteristics represented by carbon or alloy additions; and with physical characteristics represented by austenitic grain growth (as described above) [39] [62] [63] [64]. Increasing carbon concentration and thus, increasing quench hardenability via the chemical characteristics, allows for a complete transformation to martensite without such a great requirement for austenitic grain growth (the physical characteristics). Thus, the complete transformation to martensite can be achieved given a lower soak condition.

The positive influence of carbon concentration (or carbon equivalent) on quench hardenability is clearly illustrated by Figure 5.11d, which presents carbon concentration and carbon equivalent (CEN) against mean martensite volume fraction resulting from the nine soak conditions.

Given a soak condition from which each 25MnB5 (X) grade presented a ferritic-martensitic microstructure (e.g. 1 min-800 °C), 25MnB5 (Mo) and 25MnB5 (V) consistently demonstrated lower martensite volume fractions than 25MnB5 (Figure 5.11b). In isolation, molybdenum and vanadium additions would be expected to increase quench hardenability [39]. Molybdenum has also been reported [72] [164] [165] to have a synergistic effect with boron on quench hardenability. Moreover, it has been reported [164] that molybdenum addition to boron steel suppresses nucleation of boron carbide $M_{23}(C,B)_6$ by retardation of carbon diffusion and thus, maintains solute boron concentration at γ-austenite grain boundaries (in addition to solute carbon concentration), thereby enhancing quench hardenability. However, it has also been reported [163] that molybdenum addition to boron steel may impair quench hardenability under certain austenisation conditions by promoting boron carbide nucleation at γ-austenite

grain boundaries. Not only does such boron carbide nucleation reduce the solute boron concentration at γ-austenite grain boundaries and reduce the solute carbon concentration, but moreover, it has been suggested [73] [74] [165] [166] that boron carbide can provide a heterogeneous nucleation site for proeutectoid α-ferrite formation. Thus, the impairment to quench hardenability from boron carbide nucleation can be considered multi-fold. It may also be noted that the impairment to quench hardenability was greatest from the vanadium addition and second greatest from the molybdenum addition, while the nickel addition apparently had little influence on quench hardenability (although may be considered to have increased quench hardenability if the errors associated with the volume fraction measurements are taken into account). It is then worthy to consider that nickel is not a carbide former, while molybdenum and vanadium are carbide formers, with vanadium exhibiting a stronger carbide forming affinity than molybdenum [39]. Thus, perhaps a positive correlation can be drawn between carbide forming affinity and impairment to quench hardenability.

25MnB5 (Mo) exhibited intermetallic compounds (Figures 5.14a-i). EDX demonstrated that these species were rich in iron, titanium, aluminium, nitrogen, manganese and sulphur (Figures 5.15a-f). Therefore, it can be suggested that these species were mostly ferro- titanium nitride, aluminium nitride and manganese sulphide intermetallic compounds.

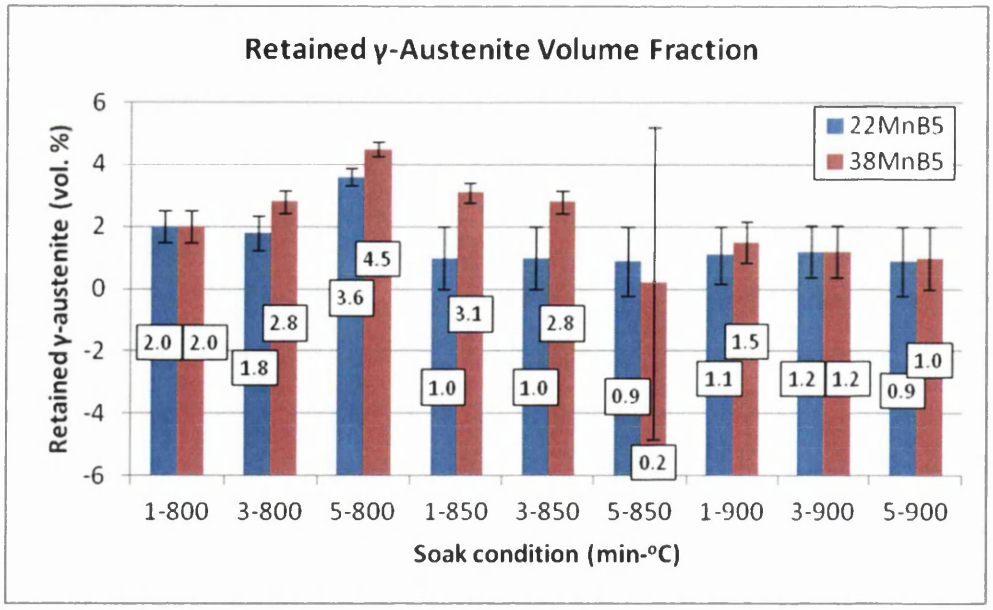


Figure 5.10: Retained γ-austenite volume fraction determined by XRD

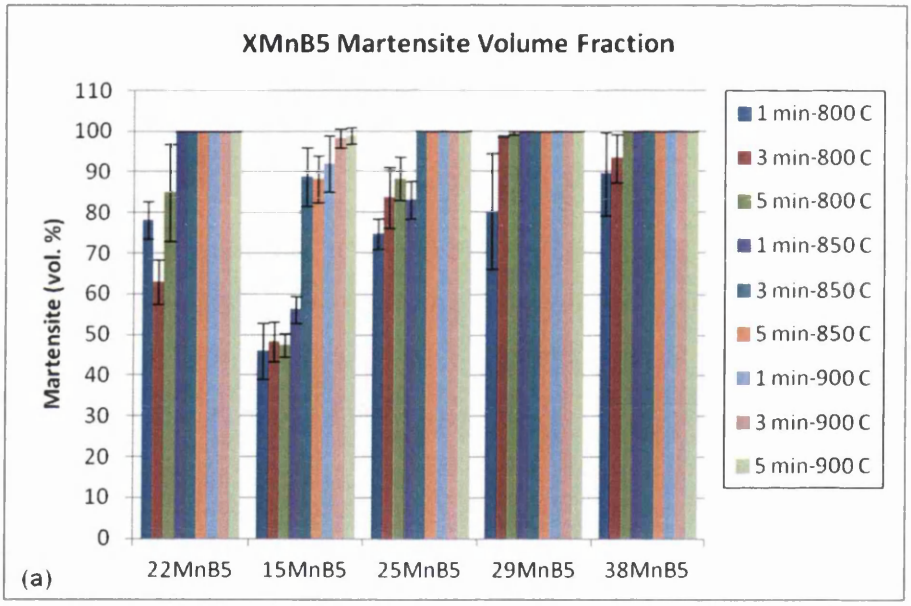

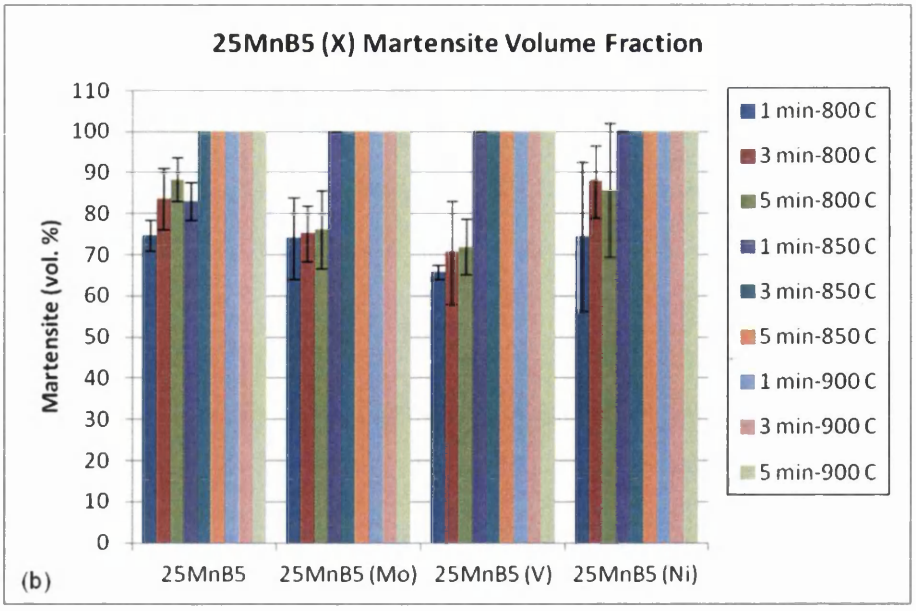
25MnB5 (X) Martensite Volume Fraction
Martensite (vol. %)
110
100
90
80
70
60
50
40
30
20
10
0
25MnB5
25MnB5 (Mo)
25MnB5 (V)
25MnB5 (Ni)
1 min-800 C
3 min-800 C
5 min-800 C
1 min-850 C
3 min-850 C
5 min-850 C
1 min-900 C
3 min-900 C
5 min-900 C
(b)

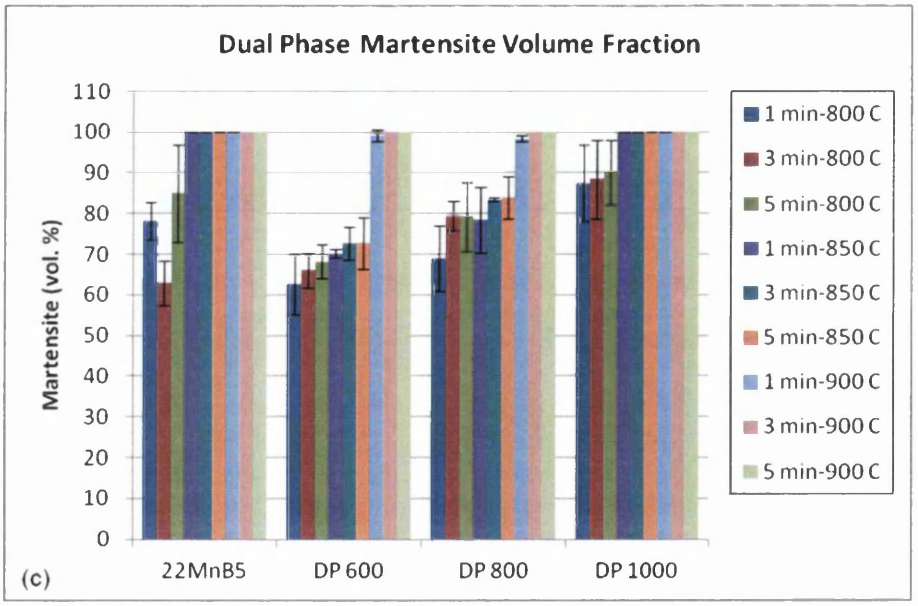
Dual Phase Martensite Volume Fraction
Martensite (vol. %)
110
100
90
80
70
60
50
40
30
20
10
0
22MnB5
DP 600
DP 800
DP 1000
1 min-800 C
3 min-800 C
5 min-800 C
1 min-850 C
3 min-850 C
5 min-850 C
1 min-900 C
3 min-900 C
5 min-900 C
(c)

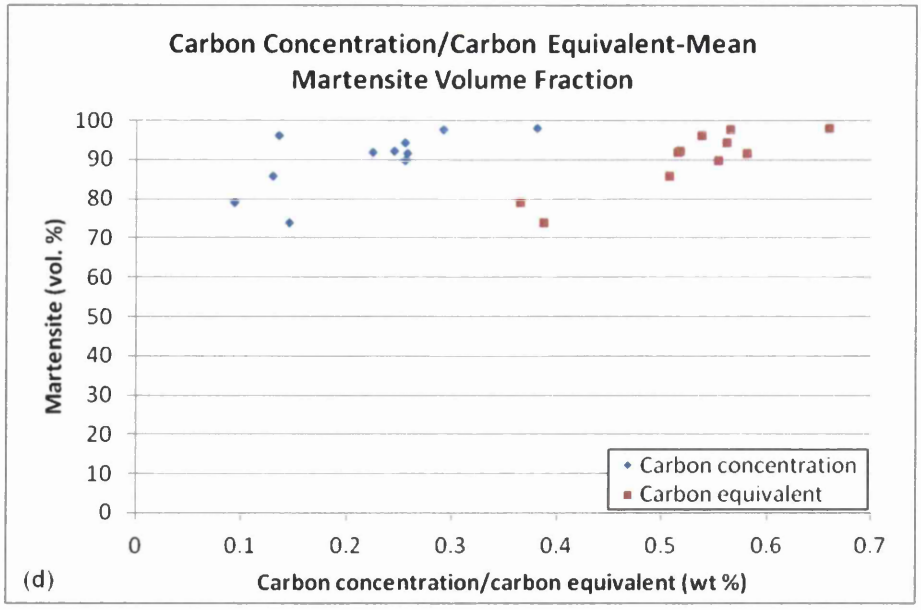


Figure 5.11: Martensite volume fraction (a) XMnB5 (b) 25MnB5 (X) (c) Dual Phase (d) carbon concentration/carbon equivalent-mean martensite volume fraction

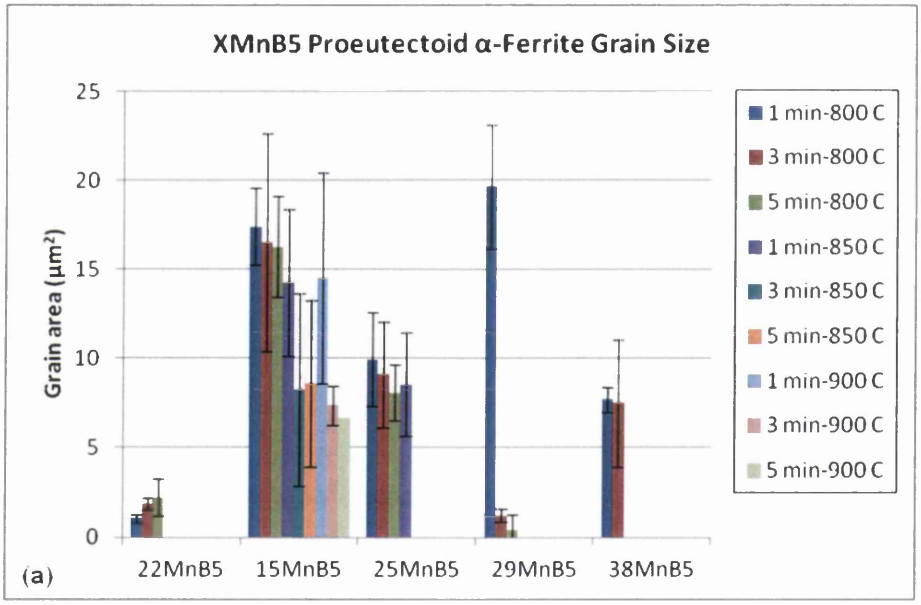

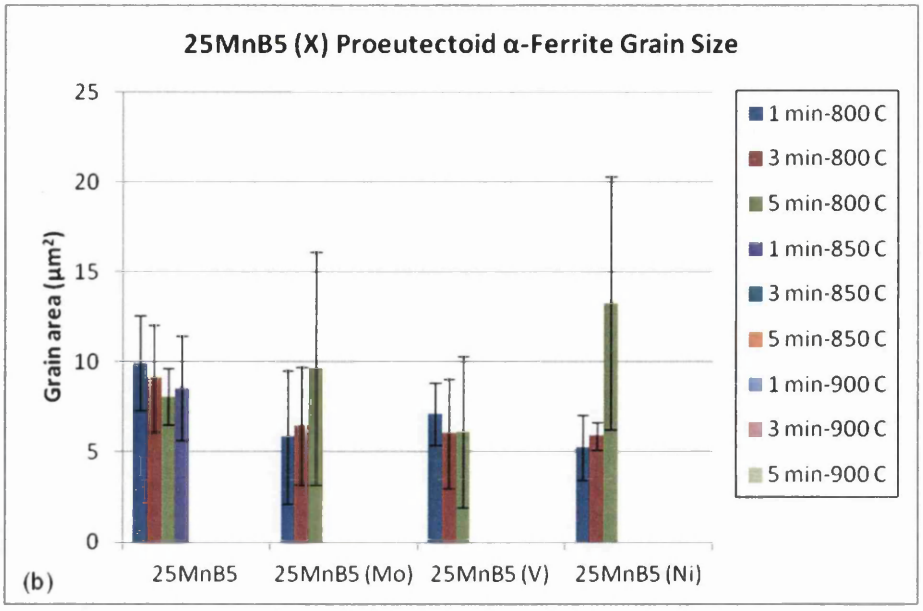


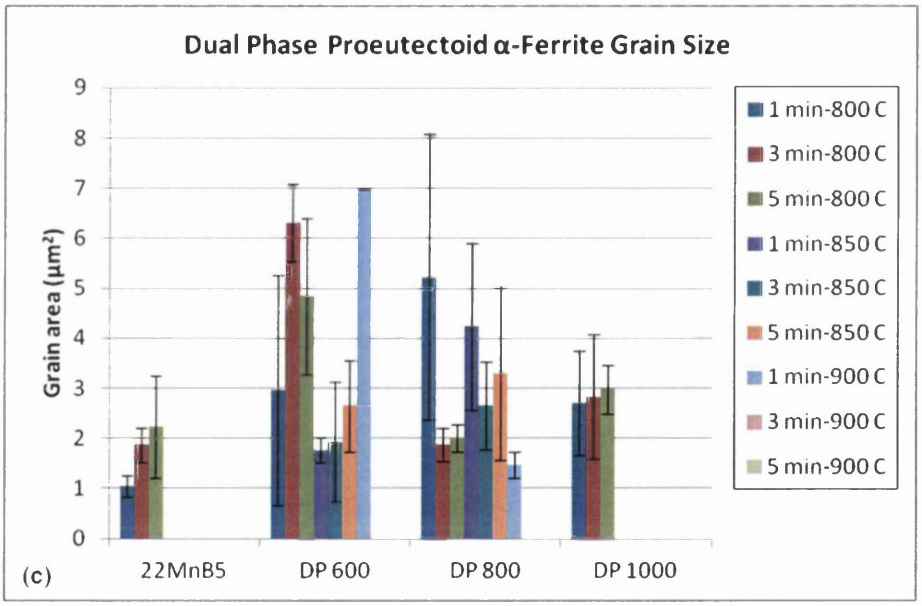


Figure 5.12: Proeutectoid α-ferrite grain size (a) XMnB5 (b) 25MnB5 (X) (c) Dual Phase

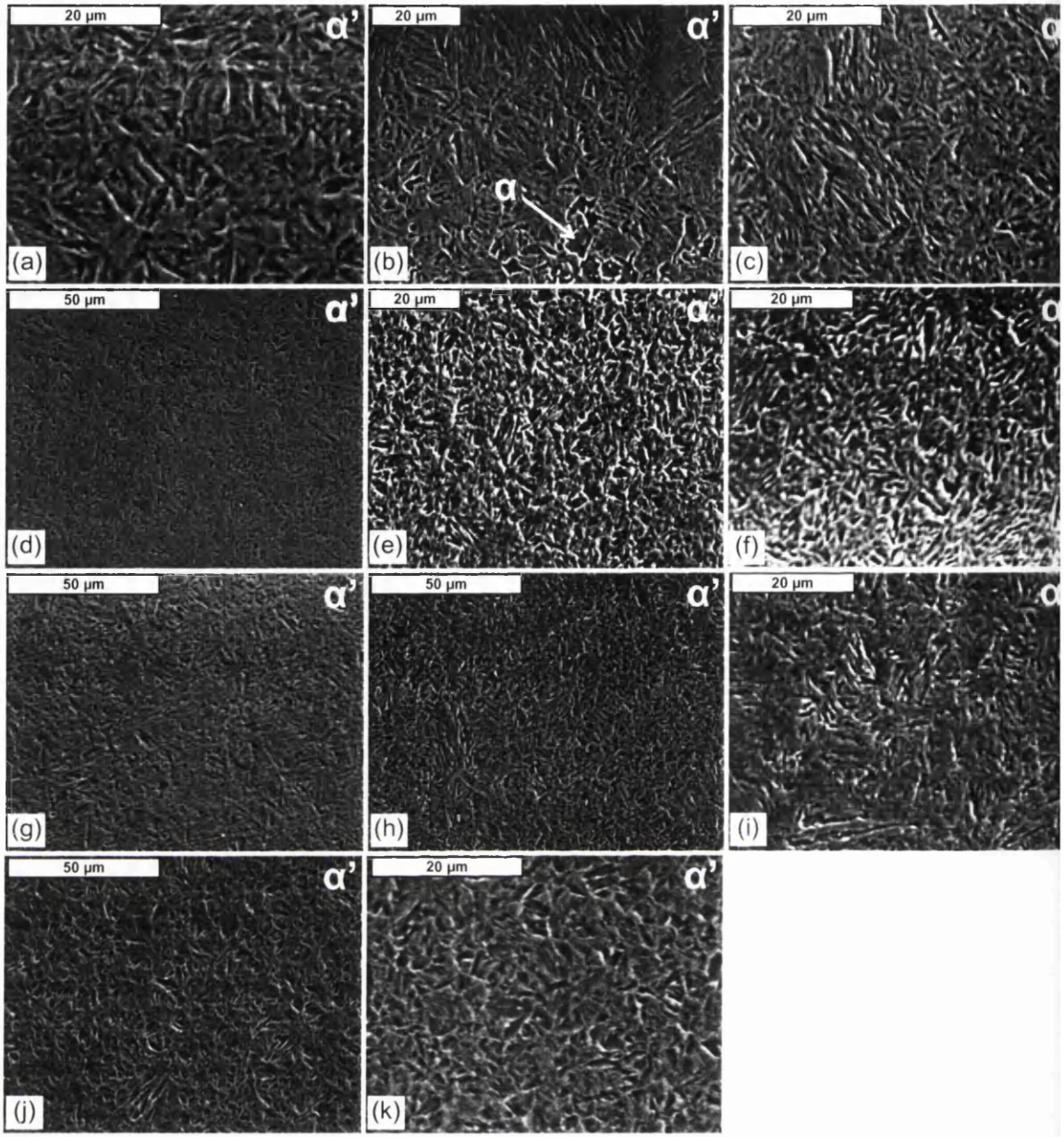


Figure 5.13: SEM micrographs taken at ¾ specimen thickness and with soak condition equal to the lowest soak condition from which a completely martensitic microstructure was achieved (except 15MnB5 for which the soak condition represents that which achieved the maximum martensite volume fracton) (a) 22MnB5 1 min-850 °C (b) 15MnB5 5 min-900 °C (c) 25MnB5 3 min-850 °C (d) 25MnB5 (Mo) 1 min-850 °C (e) 25MnB5 (V) 1 min-850 °C (f) 25MnB5 (Ni) 1 min-850 °C (g) 29MnB5 1 min-850 °C (h) 38MnB5 5 min-800 °C (i) DP 600 3 min-900 °C (j) DP 800 3 min-900 °C (k) DP 1000 1 min-850 °C

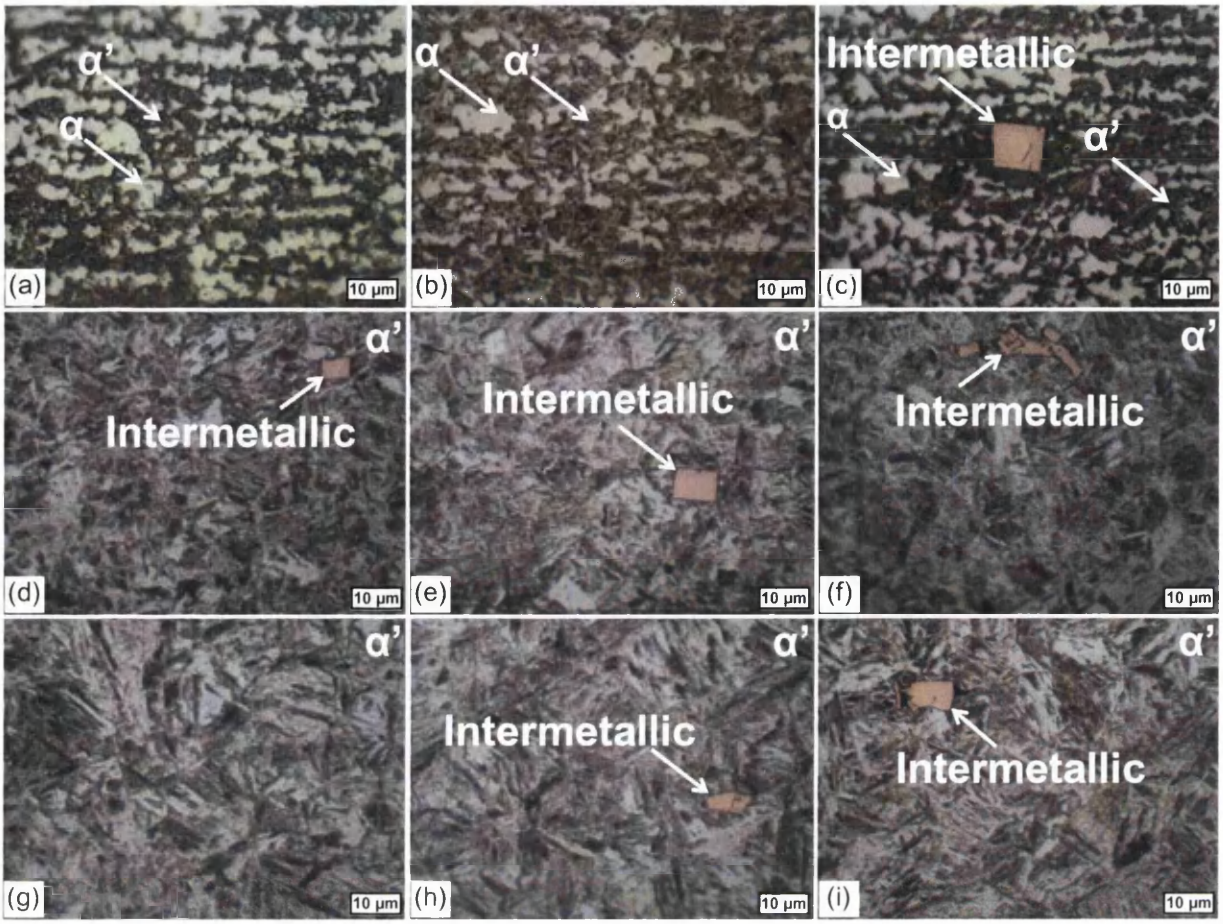


Figure 5.14: 25MnB5 (Mo) LOM micrographs taken at ¼ specimen thickness (a) 1 min-800 °C (b) 3 min-800 °C (c) 5 min-800 °C (d) 1 min-850 °C (e) 3 min-850 °C (f) 5 min-850 °C (g) 1 min-900 °C (h) 3 min-900 °C (i) 5 min-900 °C

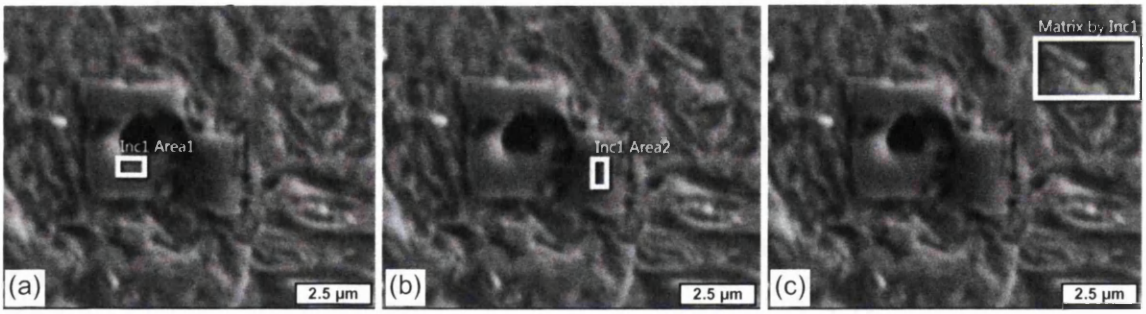


| *Element* | *Wt %* |
|---|---|
| Ti | 51.71 |
| N | 28.20 |
| Fe | 19.02 |
| Zr | 0.39 |
| Mn | 0.35 |
| Mo | 0.33 |
| Total: | 100.00 |

| *Element* | *Wt %* |
|---|---|
| Ti | 60.76 |
| N | 23.97 |
| Fe | 12.13 |
| Mn | 1.60 |
| S | 0.93 |
| Zr | 0.43 |
| Cr | 0.19 |
| Total: | 100.00 |

| *Element* | *Wt %* |
|---|---|
| Fe | 98.06 |
| Mn | 1.23 |
| Cr | 0.41 |
| Si | 0.29 |
| Total: | 100.00 |

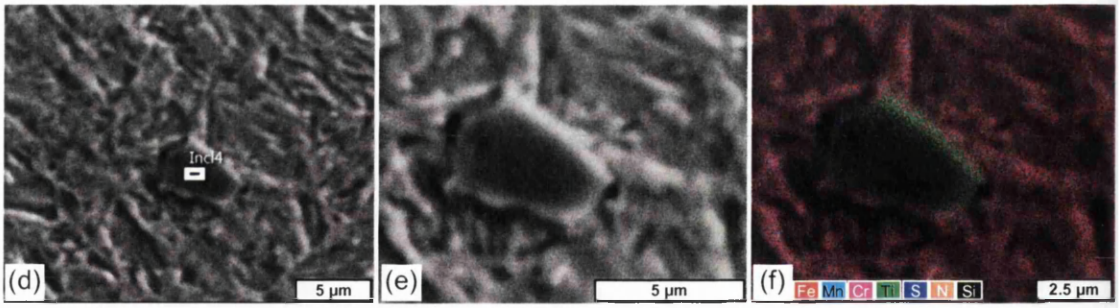


| *Element* | *Wt %* |
|---|---|
| Ti | 48.11 |
| Fe | 29.32 |
| N | 21.91 |
| Mn | 0.45 |
| Cr | 0.21 |
| Total: | 100.00 |

Figure 5.15: 25MnB5 (Mo) 5 min-850 °C EDX (a) inclusion 1-area 1 illustrating titanium nitride (b) inclusion 1-area 2 illustrating titanium nitride (c) matrix near inclusion 1 for comparison (d) inclusion 4 illustrating titanium nitride (e) inclusion 4 at higher magnification (f) 'layered map' of inclusion 4 illustrating titanium nitride (green/orange) and manganese sulphide (turquoise/blue)

***Mechanical Properties***

Figures 5.16a-c present proof strength-$R_{p0.2}$. Figures 5.17a-c present ultimate tensile strength-$R_m$. Figures 5.18a-c present uniform elongation-$A_u$. Figures 5.19a-c present total elongation-$A_{50}$. Figures 5.20a-c present Vickers hardness-Hv. Figures 5.21a-c present heterogeneity of Vickers hardness. Appendices 3-8 present tabulated results.

22MnB5 achieved maximum proof strength, ultimate tensile strength and hardness given the soak condition of 1 min-850 °C. Given a soak condition below 1 min-850 °C, the above properties were compromised by the proeutectoid α-ferrite volume fraction. Given a soak condition above 1 min-850 °C, it can be suggested that the above properties were compromised by greater coarseness of the martensitic microstructure (larger packet size), resulting from excessive austenitic grain growth. Conversely, the proeutectoid α-ferrite volume fraction resulting from a soak condition below 1 min-850 °C gave rise to higher uniform elongation and total elongation. It can be suggested that greater coarseness of the martensitic microstructure, in addition to greater microstructural homogeneity (indicated by greater homogeneity of hardness) resulting from a soak condition above 1 min-850 °C, also gave rise to higher uniform elongation and particularly higher total elongation. Further, it has been suggested [124] that

carbides/inclusions (found to be most abundantly precipitated with a soak condition of 5 min-850 °C) may scavenge free hydrogen molecules from the primary microconstituent(s) (martensite), giving rise to higher impact toughness and elongation.

15MnB5 achieved maximum proof strength and ultimate tensile strength given the soak condition of 1 min-900 °C. Given a soak condition below 1 min-900 °C, the above properties were compromised by greater proeutectoid α-ferrite volume fraction. Given a soak condition above 1 min-900 °C, it can be suggested that the above properties were compromised by greater martensitic coarseness resulting from excessive austenitic grain growth, with the deficit to strength from greater martensitic coarseness proving to be a more influential factor than the strength gain from the small increase to martensite volume fraction. Moreover, it is likely that the lower martensite volume fraction presented a higher carbon martensite of higher strength [11] [93]. Thus, the soak condition of 1 min-900 °C can be considered to have provided the optimal degree of austenitic grain growth, providing the optimal balance between quench hardenability and grain boundary strengthening. Greater proeutectoid α-ferrite volume fraction resulting from the soak temperature of 800 °C gave rise to higher uniform elongation and total elongation. The lower total elongation resulting from the soak temperature of 850 °C, despite higher proeutectoid α-ferrite volume fraction can be related to microstructural refinement, microstructural heterogeneity and possibly higher martensite carbon concentration. It can be suggested that greater martensitic coarseness, greater microstructural homogeneity and lower martensite carbon concentration resulting from a soak condition above 1 min-900 °C, also gave rise to higher uniform elongation and total elongation.

25MnB5 achieved maximum proof strength and ultimate tensile strength given the soak condition of 3 min-850 °C. Given a soak condition below 3 min-850 °C, the above properties were compromised by the proeutectoid α-ferrite volume fraction. Given a soak condition above 3 min-850 °C, it can be suggested that the above properties were compromised by greater coarseness of the martensitic microstructure, resulting from excessive austenitic grain growth. The proeutectoid

α-ferrite volume fraction resulting from the soak temperature of 800 °C gave rise to higher uniform elongation and total elongation. However, the proeutectoid α-ferrite volume fraction resulting from the soak condition of 1 min-850 °C did not result in higher uniform elongation or total elongation than the soak condition of 3 min-850 °C. This can be related largely to extreme microstructural heterogeneity resulting from the soak condition of 1 min-850 °C. It can be suggested that greater coarseness of the martensitic microstructure, in addition to greater microstructural homogeneity resulting from a soak condition above 3 min-850 °C, gave rise to higher uniform elongation and total elongation.

29MnB5 achieved maximum proof strength, ultimate tensile strength and hardness given the soak condition of 3 min-800 °C. Given the soak condition below 3 min-800 °C, the above properties were compromised by higher proeutectoid α-ferrite volume fraction. It can also be suggested that excessive microstructural heterogeneity resulting from the soak condition of 1 min-800 °C (related to the relatively high carbon content of 29MnB5) gave rise to premature fracture, limiting elongation and tensile strength. Indeed, given the soak condition of 1 min-800 °C, the recorded uniform elongation value equalled the recorded total elongation value. This is a strong indication of premature fracture, since the specimen fractured at the ultimate tensile strength (or even before the theoretical ultimate tensile strength) rather than persisting to a characteristic failure strength. Given a soak condition above 3 min-800 °C, it can be suggested that tensile strength and hardness were compromised by greater martensitic coarseness, resulting from excessive austenitic grain growth. Conversely, it can be suggested that greater martensitic coarseness in addition to greater microstructural homogeneity resulting from a soak condition above 3 min-800 °C, gave rise to higher total elongation.

38MnB5 achieved maximum proof strength given the soak condition of 3 min-850 °C, yet maximum ultimate tensile strength given the soak condition of 5 min-850 °C. Given a soak condition below 5 min-850 °C, ultimate tensile strength was compromised by the proeutectoid α-ferrite volume fraction and/or in particular, by excessive microstructural heterogeneity (related to the relatively high carbon

content of 38MnB5). All soak conditions below 5 min-850 °C (except for 1 min-800 °C) resulted in higher hardness than the soak condition of 5 min-850 °C. Given a soak condition below 5 min-850 °C, uniform elongation and total elongation were extremely low. Indeed, for a given soak condition below 5 min-850 °C, the recorded uniform elongation value equalled the recorded total elongation value. As mentioned in discussion of 29MnB5, this is a strong indication of premature fracture. Thus, it is suggested that the finer martensitic microstructure resulting from a soak condition below 5 min-850 °C provided potential for maximum ultimate tensile strength. However, excessive microstructural heterogeneity resulted in premature fracture that prevented the maximum ultimate tensile strength potential from being reached. Given the soak condition of 5 min-850 °C, excessive microstructural heterogeneity resulting in premature fracture that limited ultimate tensile strength, was overcome.

As a general rule, ultimate tensile strength is reported [167] [168] [169] to be approximately 3.0 times the Vickers hardness. Given a soak condition equal to and above 5 min-850 °C, the approximation was consistent for 38MnB5 (Figure 5.22). However, given a soak condition below 5 min-850 °C, the approximation was inconsistent, with ultimate tensile strength just 2.2 to 2.6 times the hardness. It is also worthy to note the change of fracture mode (Figure 5.23). Given all soak times at the soak temperature of 800 °C, the fracture surface was at approximately 90 ° to the gauge length, indicating a brittle pure shear fracture [11]. With increasing soak time at the soak temperature of 850 °C, the fracture surface gradually became closer to 45 ° to the gauge length, indicating a more ductile plane nominal-shear fracture [11]. Given all soak times at the soak temperature of 900 °C (except for 5 min-900 °C which should be considered an anomaly) the fracture surface was at approximately 45 ° to the gauge length.

25MnB5 (Mo) achieved maximum proof strength (and hardness) given the soak condition of 5 min-850 °C, yet maximum ultimate tensile strength given the soak condition of 1 min-850 °C. Given a soak condition below 1 min-850 °C, both properties were compromised by the proeutectoid α-ferrite volume fraction. Given a soak condition above 1 min-850 °C, it can be suggested that ultimate tensile

strength was compromised by: 1) greater coarseness of the martensitic microstructure resulting from excessive austenitic grain growth; and 2) lesser solid solution strengthening due to greater precipitation of intermetallic compounds (mostly ferro-titanium nitride). Conversely, increased precipitation of intermetallic compounds with increased soak condition up to 5 min-850 °C provided the highest proof strength. Thus, precipitation of intermetallic compounds can be considered beneficial to proof strength since intermetallic compounds may strongly restrict dislocation movement in the manner of precipitation hardening, delaying the onset of permanent deformation (this is most true for nano-sized intermetallic compounds [170]). However, precipitation of intermetallic compounds beyond a critical threshold can be considered detrimental to ultimate tensile strength since intermetallic compounds take solute atoms out of solid solution, where such solute atoms dissolved in solid solution may relatively weakly, but persistently to failure, restrict dislocation movement in the manner of solid solution strengthening. As a simplified example, if all solute atoms were bound in (nano-sized) intermetallic compounds, the initial restriction to dislocation movement would be at the maximum, hence proof strength would be at the maximum. However, once the dislocation breaks free from the temporarily restricting intermetallic compound and permanent deformation is permitted to begin, there would be no solute atoms in solid solution to persistently restrict dislocation movement to failure, hence ultimate tensile strength and the failure strength would be at the minimum. The proeutectoid α-ferrite volume fraction resulting from the soak temperature of 800 °C gave rise to higher uniform elongation and total elongation than the martensitic microstructure resulting from the soak temperature of 850 °C. However, maximum total elongation was achieved from the soak condition of 1 min-900 °C. This can be suggested to have arisen from the combination of: 1) greater martensitic coarseness resulting from greater austenitic grain growth at the higher soak temperature; 2) less precipitation of intermetallic compounds (than at the soak temperature of 850 °C), where intermetallic compounds may restrict austenitic grain growth; and 3) greater microstructural homogeneity. Further, by making comparison between 25MnB5 and 25MnB5 (Mo) for a given soak condition, it is apparent that molybdenum dissolved in solid solution is beneficial to proof strength, ultimate tensile strength, uniform

elongation, total elongation, hardness and homogeneity of hardness, with each of these properties increased by the molybdenum addition across all nine soak conditions.

25MnB5 (V) achieved maximum proof strength (and hardness) given the soak condition of 1 min-900 °C, yet maximum ultimate tensile strength given the soak condition of 3 min-850 °C. It can be suggested that similar intermetallic compound-related phenomena as described for 25MnB5 (Mo) may also have taken place in 25MnB5 (V). Although intermetallic compounds were not observed in 25MnB5 (V), it is worthy to note that such species may have been present on a scale that was too fine to observe with LOM or SEM. Moreover, the sub-micro-scale intermetallic compounds can have stronger interactions with dislocations [170]. It is also worthy to note that the soak condition of 5 min-800 °C gave rise to surprisingly high proof strength, despite the significant proeutectoid α-ferrite volume fraction. It is possible that intermetallic compounds were responsible for this rather high proof strength. Given a soak condition below 1 min-900 °C, proof strength was compromised by the proeutectoid α-ferrite volume fraction and possibly lesser precipitation of intermetallic compounds. Given a soak condition above 1 min-900 °C, it can be suggested that proof strength was compromised by greater coarseness of the martensitic microstructure. The proeutectoid α-ferrite volume fraction resulting from the soak temperature of 800 °C failed to give rise to higher uniform elongation or total elongation than the martensitic microstructure resulting from soak temperatures of 850 and 900 °C. Moreover, equal maximum total elongation was achieved from the soak condition of 1 min-900 °C. In a similar fashion to 25MnB5 (Mo), this can be suggested to have arisen from the combination of: 1) greater martensitic coarseness resulting from greater austenitic grain growth at the higher soak temperature; 2) less precipitation of intermetallic compounds, where intermetallic compounds may restrict austenitic grain growth; and 3) greater microstructural homogeneity. Further, by making comparison between 25MnB5 and 25MnB5 (V) for a given soak condition, it is apparent that vanadium dissolved in solid solution is beneficial to proof strength, ultimate tensile strength, total elongation and hardness, with each of these properties increased by the vanadium addition across all nine soak conditions. Additionally, uniform

elongation was increased by the vanadium addition given the soak temperatures of 850 or 900 °C. However, given the soak temperature of 800 °C, uniform elongation was greatly impaired by the vanadium addition. This can be related to microstructural heterogeneity, where given the soak temperature of 800 °C, heterogeneity of hardness for 25MnB5 (V) was very high.

25MnB5 (Ni) achieved maximum proof strength given the soak condition of 3 min-800 °C, yet maximum ultimate tensile strength given the soak condition of 5 min-850 °C. Given a soak condition below 5 min-850 °C, ultimate tensile strength was compromised by the proeutectoid α-ferrite volume fraction and/or particularly, by excessive microstructural heterogeneity. All soak conditions below 5 min-850 °C gave rise to equal or higher proof strength and higher hardness, possibly due to a finer microstructure. Thus, in a similar fashion as posed for 38MnB5, it can be suggested that the potential for maximum ultimate tensile strength was present given a soak condition below 5 min-850 °C. However, excessive microstructural heterogeneity resulted in premature fracture that not only limited elongation, but also limited ultimate tensile strength. Given the soak condition of 5 min-850 °C, excessive microstructural heterogeneity resulting in premature fracture that limited ultimate tensile strength, was overcome. The above suggestion is supported by generally increasing total elongation with increasing soak condition and moreover, the maximum soak condition of 5 min-900 °C giving rise to maximum total elongation. It can then be suggested that microstructural heterogeneity was more of a consideration for 25MnB5 (Ni) than for 25MnB5, 25MnB5 (Mo) or 25MnB5 (V), due to the higher dissolved alloy content. Nevertheless, by making comparison between 25MnB5 and 25MnB5 (Ni) for a given soak condition, it is apparent that nickel dissolved in solid solution is beneficial to proof strength, ultimate tensile strength, total elongation and hardness, with each of these properties increased by the nickel addition across all nine soak conditions. Additionally, uniform elongation was generally increased by the nickel addition given the soak temperatures of 850 or 900 °C. However, given the soak temperature of 800 °C, uniform elongation was impaired by the nickel addition. This can be related to microstructural heterogeneity, where across nearly all nine

soak conditions, but especially given the soak temperature of 800 °C, heterogeneity of hardness for 25MnB5 (Ni) was higher than that for 25MnB5.

DP 600 achieved maximum proof strength and ultimate tensile strength given the soak condition of 1 min-900 °C. Given a soak condition below 1 min-900 °C, the above properties were compromised by greater proeutectoid α-ferrite volume fraction. Given a soak condition above 1 min-900 °C, it can be suggested that the above properties were compromised by greater coarseness of the martensitic microstructure resulting from excessive austenitic grain growth. Conversely, the greater proeutectoid α-ferrite volume fraction resulting from a soak condition below 1 min-900 °C gave rise to higher uniform elongation and higher total elongation. It can be suggested that greater coarseness of the martensitic microstructure, in addition to greater microstructural homogeneity resulting from a soak condition above 1 min-900 °C, also gave rise to higher uniform elongation and higher total elongation.

DP 800 achieved maximum proof strength, ultimate tensile strength and hardness given the soak condition of 1 min-900 °C. Given a soak condition below 1 min-900 °C, the above properties were compromised by greater proeutectoid α-ferrite volume fraction. Given a soak condition above 1 min-900 °C, it can be suggested that the above properties were compromised by greater coarseness of the martensitic microstructure resulting from excessive austenitic grain growth. Conversely, the greater proeutectoid α-ferrite volume fraction resulting from a soak condition below 1 min-900 °C gave rise to higher uniform elongation and higher total elongation. It can be suggested that greater coarseness of the martensitic microstructure, in addition to greater microstructural homogeneity resulting from a soak condition above 1 min-900 °C, also gave rise to higher uniform elongation and higher total elongation.

DP 1000 achieved maximum proof strength and hardness given the soak condition of 1 min-850 °C, yet maximum ultimate tensile strength given the soak condition of 5 min-850 °C. Given a soak condition below 1 min-850 °C, the above properties were compromised by the proeutectoid α-ferrite volume fraction. Given

a soak condition above 5 min-850 °C, it can be suggested that the above properties were compromised by greater coarseness of the martensitic microstructure resulting from excessive austenitic grain growth. However, the proeutectoid α-ferrite volume fraction resulting from the soak temperature of 800 °C did not give rise to the highest uniform elongation or total elongation, with both of these properties relatively low following the soak temperature of 800 °C. This can be attributed to relative microstructural heterogeneity and possibly a relatively high martensite carbon concentration. Indeed, the soak condition of 5 min-850 °C gave rise to the equal highest uniform elongation and the second highest total elongation. Conversely, it can be suggested that greater coarseness of the martensitic microstructure, in addition to greater microstructural homogeneity resulting from a soak condition above 5 min-850 °C, gave rise to higher total elongation.

There was generally a positive correlation between carbon concentration or carbon equivalent and ultimate tensile strength (Figures 5.17a-c). Moreover, there was generally an inverse correlation between carbon concentration or carbon equivalent and total elongation (Figures 5.19a-c). These observations illustrate the widely reported strengthening mechanisms introduced by carbon or alloy additions, such as interstitial solid solution strengthening (carbon), substitutional solid solution strengthening (manganese, chromium, vanadium, niobium, molybdenum and nickel), precipitation hardening (carbon, manganese, chromium, vanadium, niobium and molybdenum) grain boundary strengthening (intermetallic compounds) and quench hardenability (carbon and boron).

The positive influence of carbon concentration (or carbon equivalent) on ultimate tensile strength and moreover, the negative influence of carbon concentration (or carbon equivalent) on total elongation, is clearly illustrated by Figures 5.17d and 5.19d, which present carbon concentration and carbon equivalent (CEN) against mean ultimate tensile strength (Figure 5.17d) and mean total elongation (Figure 5.19d) resulting from the nine soak conditions. However, the notable exception to the negative influence of carbon equivalent on total elongation is presented by the molybdenum, vanadium and nickel additions to 25MnB5.

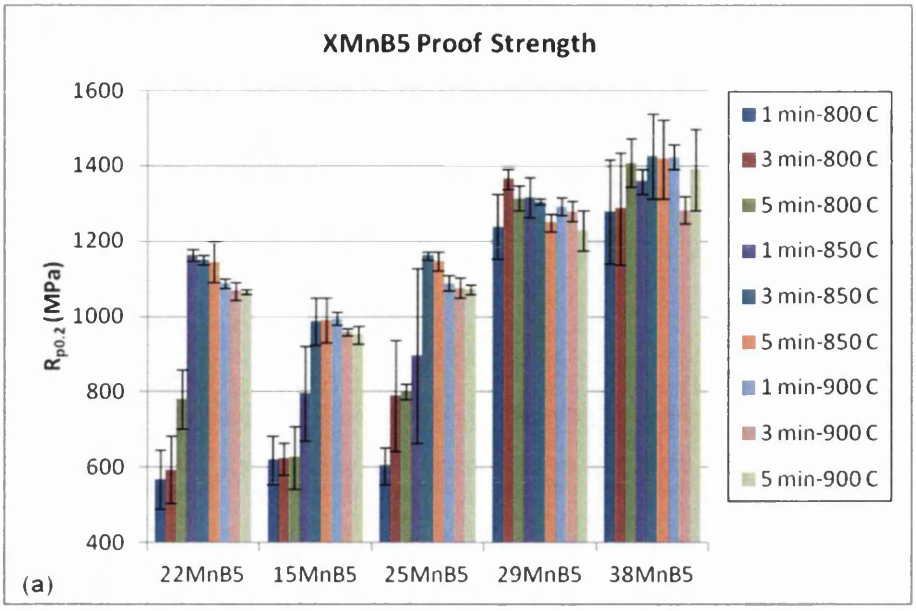
XMnB5 Proof Strength
1600
1400
1200
1000
800
600
400
$R_{p0.2}$ (MPa)
22MnB5
15MnB5
25MnB5
29MnB5
38MnB5
1 min-800 C
3 min-800 C
5 min-800 C
1 min-850 C
3 min-850 C
5 min-850 C
1 min-900 C
3 min-900 C
5 min-900 C
(a)

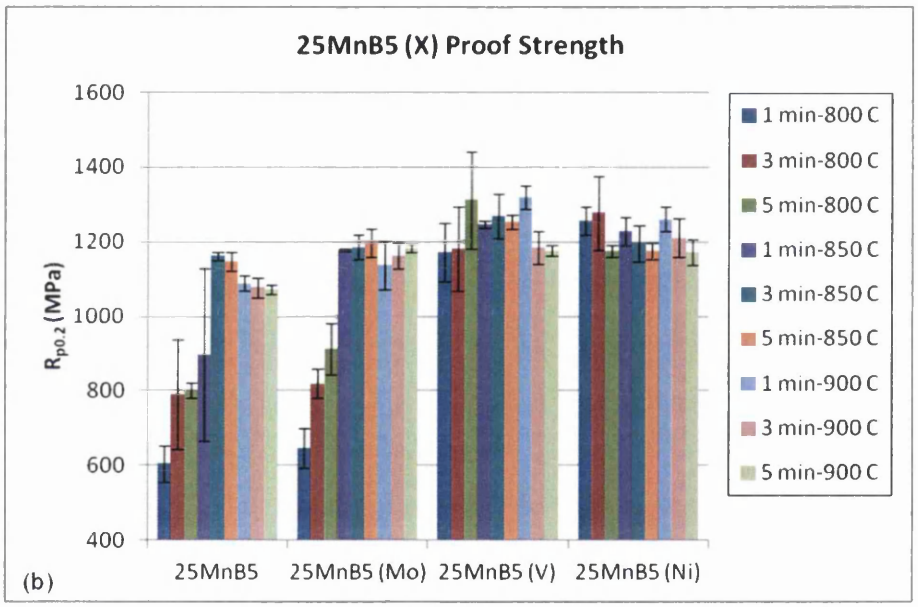
25MnB5 (X) Proof Strength
1600
1400
1200
1000
800
600
400
$R_{p0.2}$ (MPa)
25MnB5
25MnB5 (Mo)
25MnB5 (V)
25MnB5 (Ni)
1 min-800 C
3 min-800 C
5 min-800 C
1 min-850 C
3 min-850 C
5 min-850 C
1 min-900 C
3 min-900 C
5 min-900 C
(b)

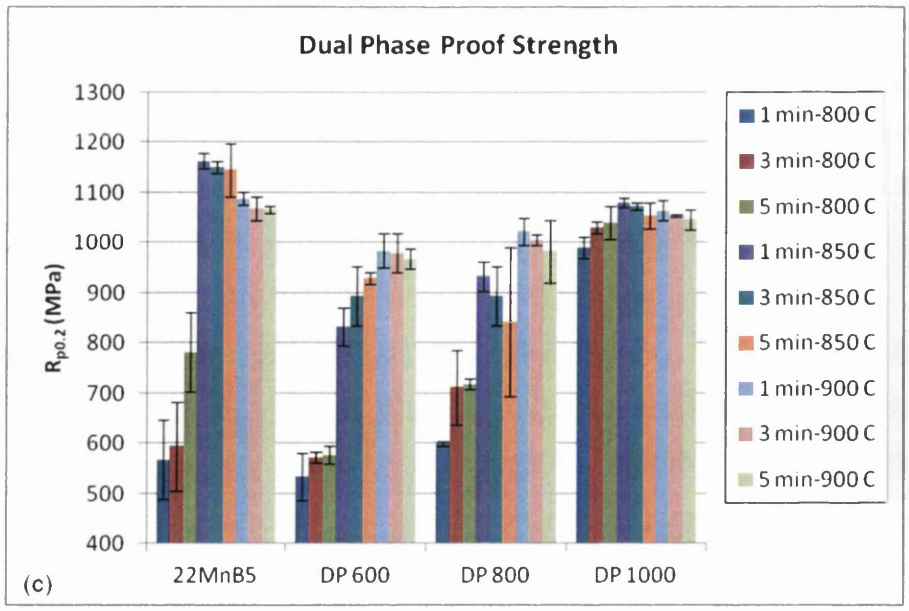


Figure 5.16: Proof strength (a) XMnB5 (b) 25MnB5 (X) (c) Dual Phase

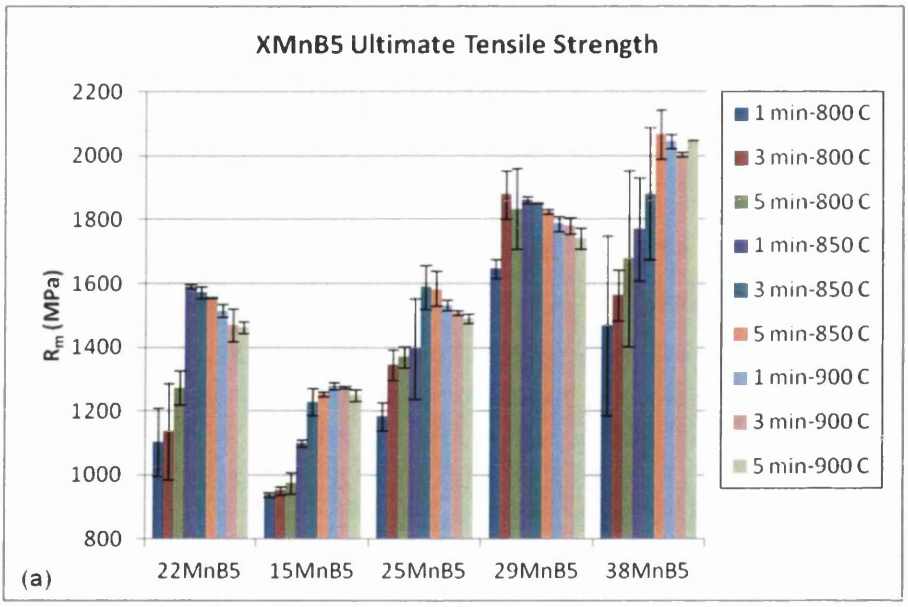

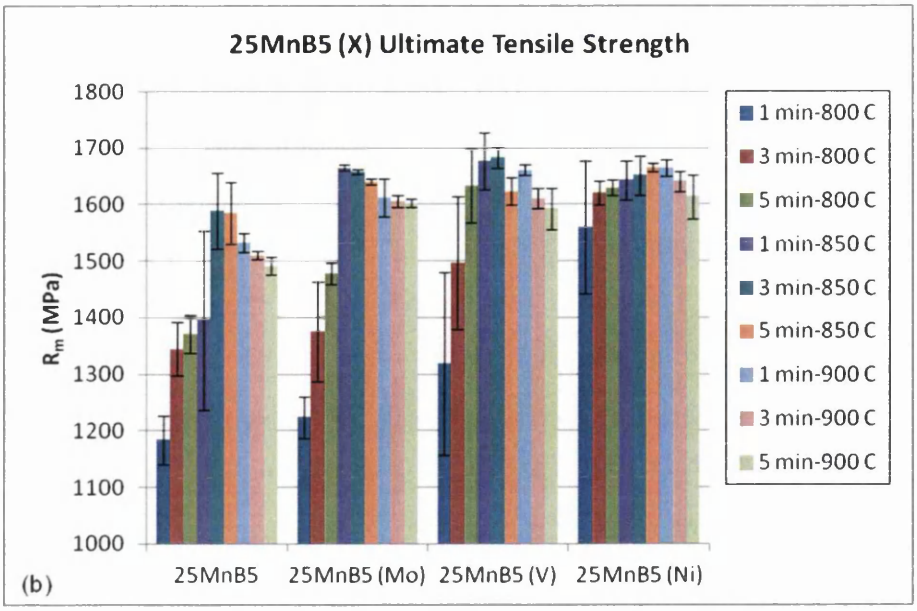
25MnB5 (X) Ultimate Tensile Strength
1800
1700
1600
1500
1400
1300
1200
1100
1000
$R_m$ (MPa)
25MnB5
25MnB5 (Mo)
25MnB5 (V)
25MnB5 (Ni)
1 min-800 C
3 min-800 C
5 min-800 C
1 min-850 C
3 min-850 C
5 min-850 C
1 min-900 C
3 min-900 C
5 min-900 C
(b)

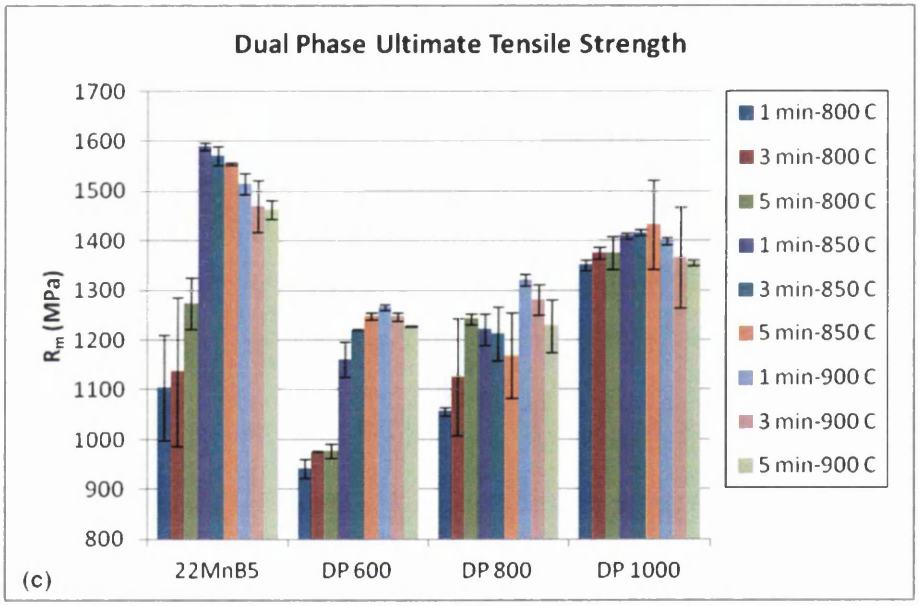
Dual Phase Ultimate Tensile Strength
1700
1600
1500
1400
1300
1200
1100
1000
900
800
$R_m$ (MPa)
22MnB5
DP 600
DP 800
DP 1000
1 min-800 C
3 min-800 C
5 min-800 C
1 min-850 C
3 min-850 C
5 min-850 C
1 min-900 C
3 min-900 C
5 min-900 C
(c)

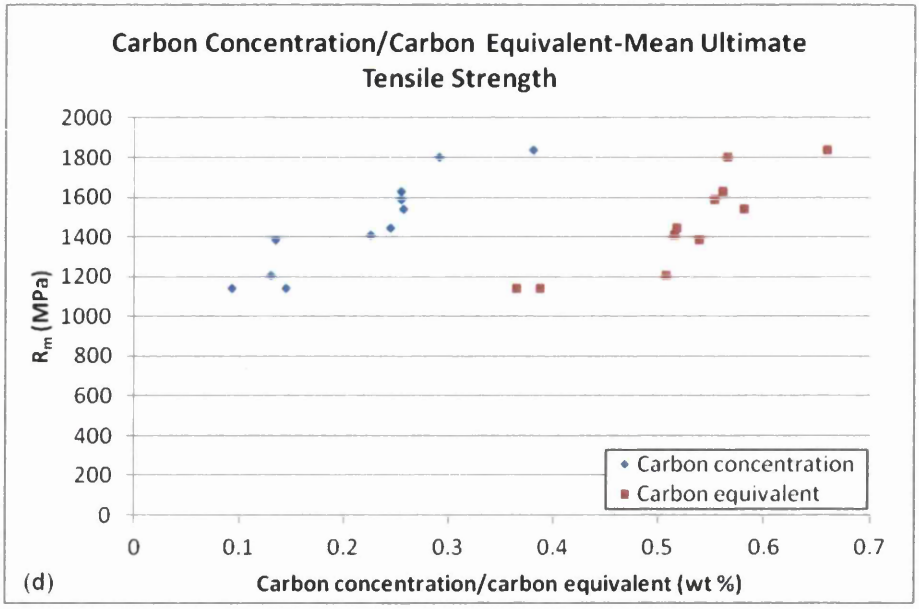


Figure 5.17: Ultimate tensile strength (a) XMnB5 (b) 25MnB5 (X) (c) Dual Phase (d) carbon concentration/carbon equivalent-mean ultimate tensile strength

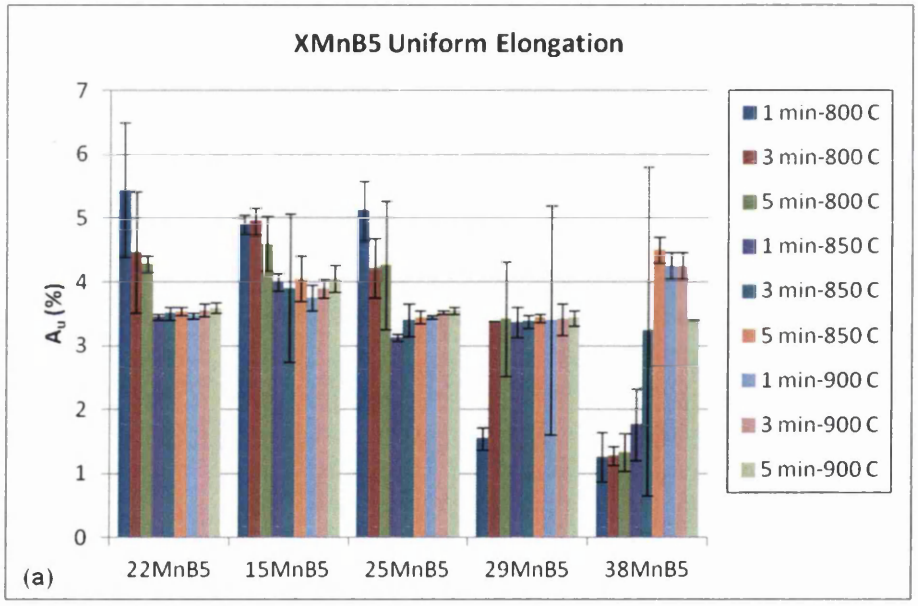

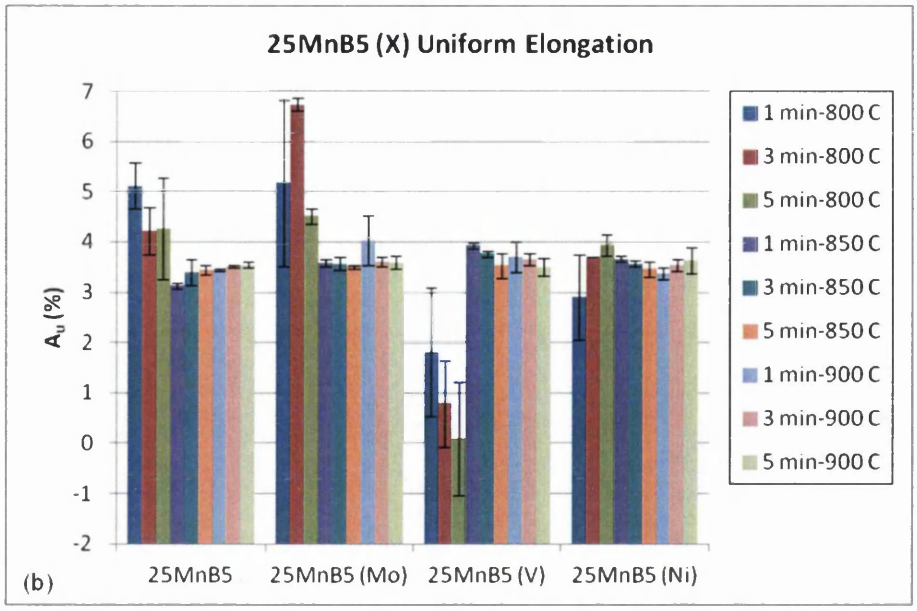


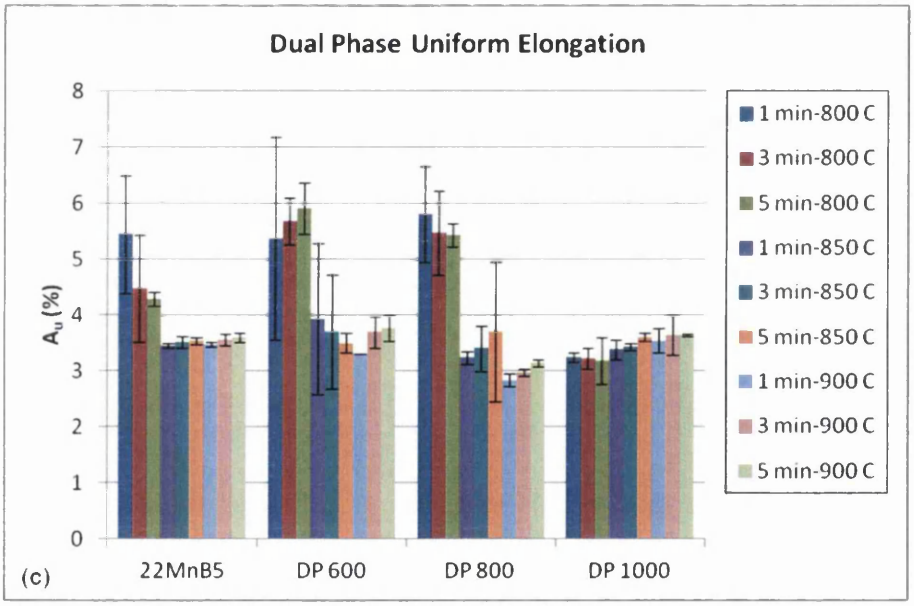


Figure 5.18: Uniform elongation (a) XMnB5 (b) 25MnB5 (X) (c) Dual Phase

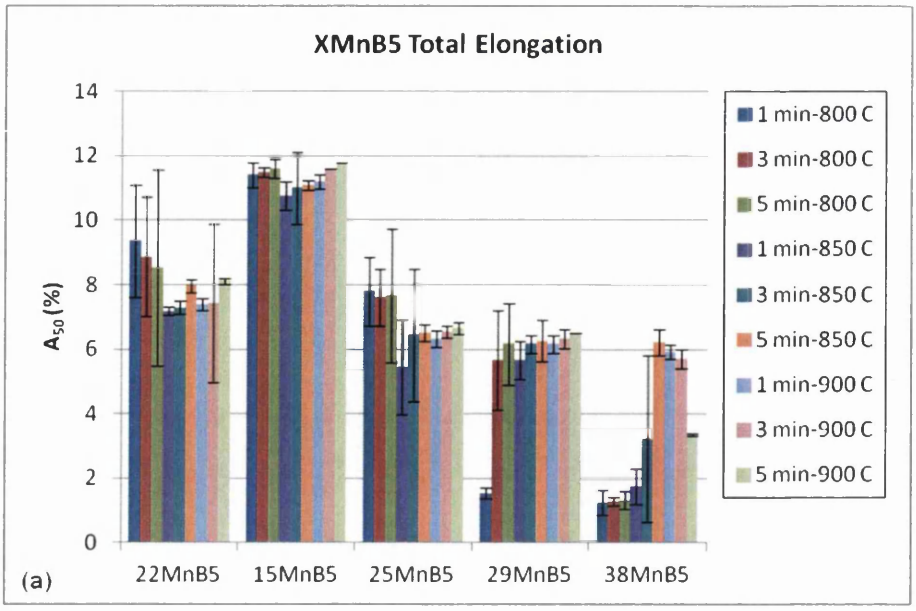
XMnB5 Total Elongation
14
12
10
8
6
4
2
0
$A_{50}$ (%)
1 min-800 C
3 min-800 C
5 min-800 C
1 min-850 C
3 min-850 C
5 min-850 C
1 min-900 C
3 min-900 C
5 min-900 C
22MnB5
15MnB5
25MnB5
29MnB5
38MnB5
(a)

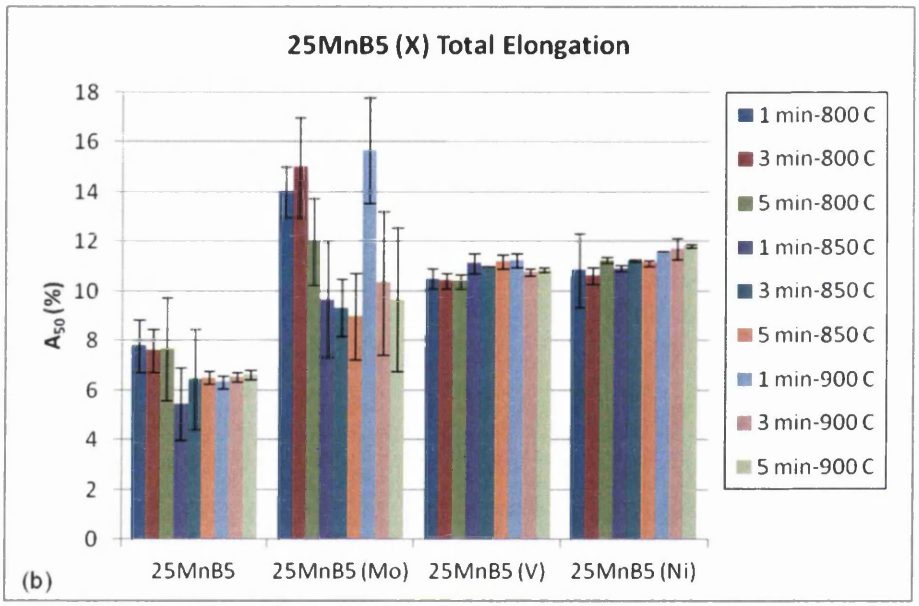
25MnB5 (X) Total Elongation
18
16
14
12
10
8
6
4
2
0
$A_{50}$ (%)
1 min-800 C
3 min-800 C
5 min-800 C
1 min-850 C
3 min-850 C
5 min-850 C
1 min-900 C
3 min-900 C
5 min-900 C
25MnB5
25MnB5 (Mo)
25MnB5 (V)
25MnB5 (Ni)
(b)

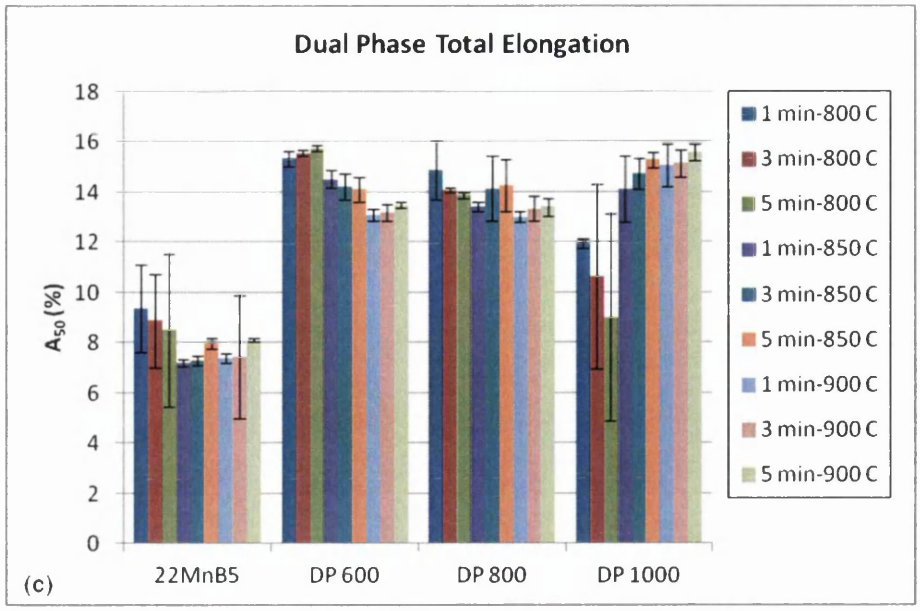


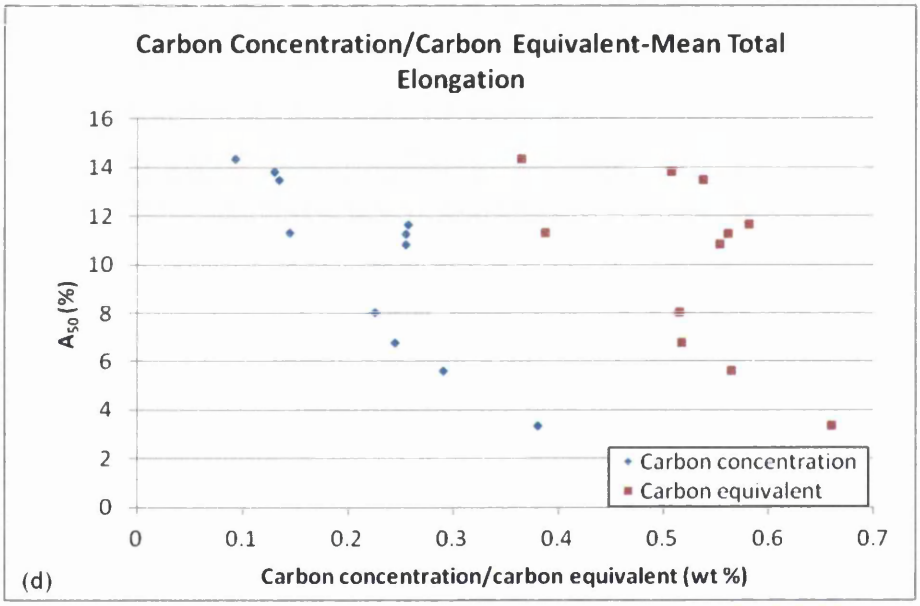


Figure 5.19: Total elongation (a) XMnB5 (b) 25MnB5 (X) (c) Dual Phase (d) carbon concentration/carbon equivalent-mean total elongation

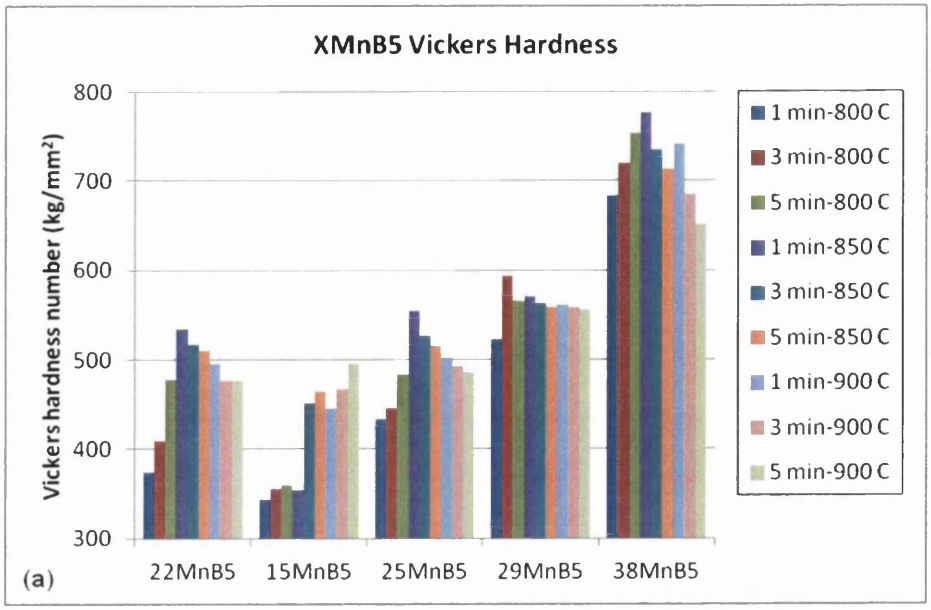
XMnB5 Vickers Hardness
Vickers hardness number (kg/mm²)
800
700
600
500
400
300
22MnB5
15MnB5
25MnB5
29MnB5
38MnB5
1 min-800 C
3 min-800 C
5 min-800 C
1 min-850 C
3 min-850 C
5 min-850 C
1 min-900 C
3 min-900 C
5 min-900 C
(a)

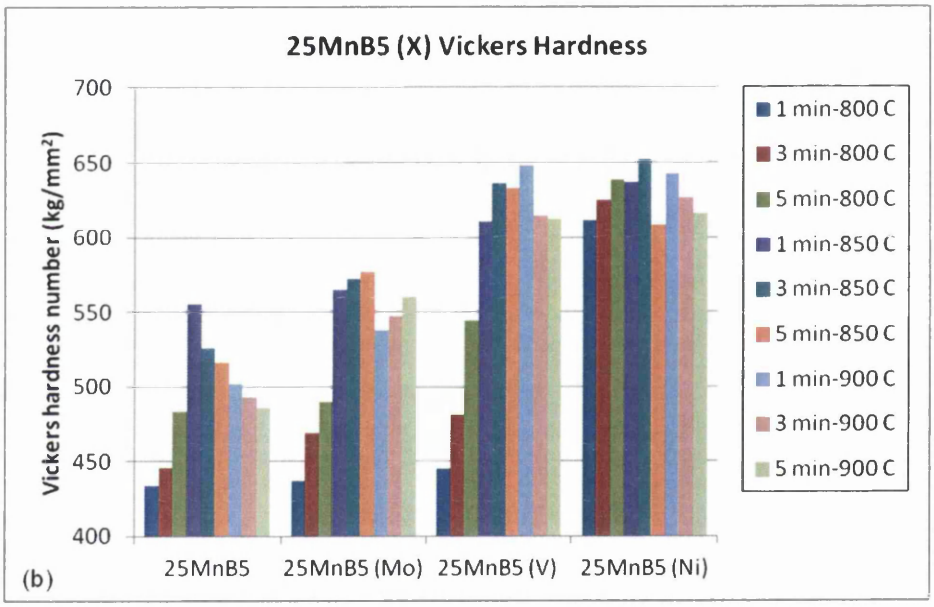
25MnB5 (X) Vickers Hardness
Vickers hardness number (kg/mm²)
700
650
600
550
500
450
400
25MnB5
25MnB5 (Mo)
25MnB5 (V)
25MnB5 (Ni)
1 min-800 C
3 min-800 C
5 min-800 C
1 min-850 C
3 min-850 C
5 min-850 C
1 min-900 C
3 min-900 C
5 min-900 C
(b)

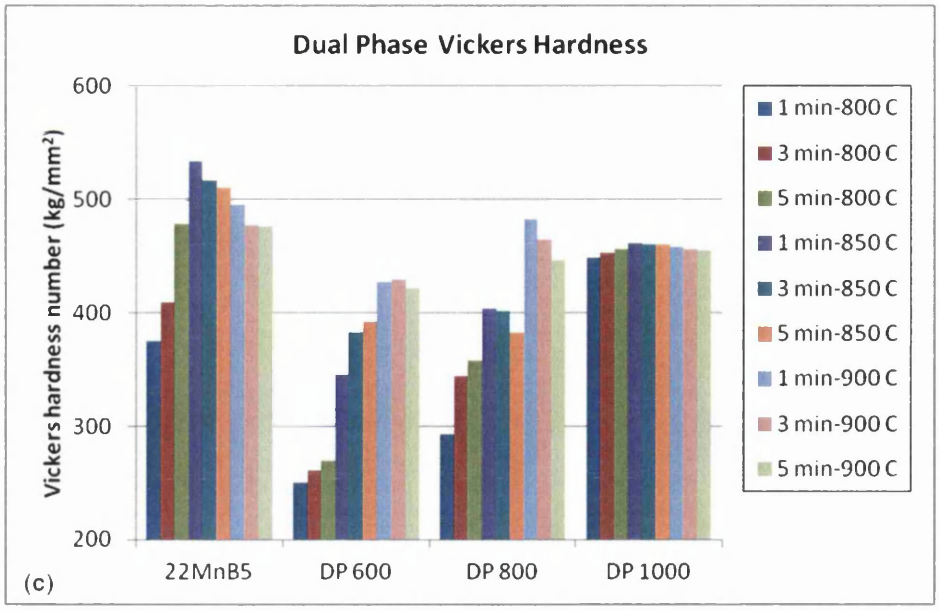


Figure 5.20: Vickers hardness (a) XMnB5 (b) 25MnB5 (X) (c) Dual Phase

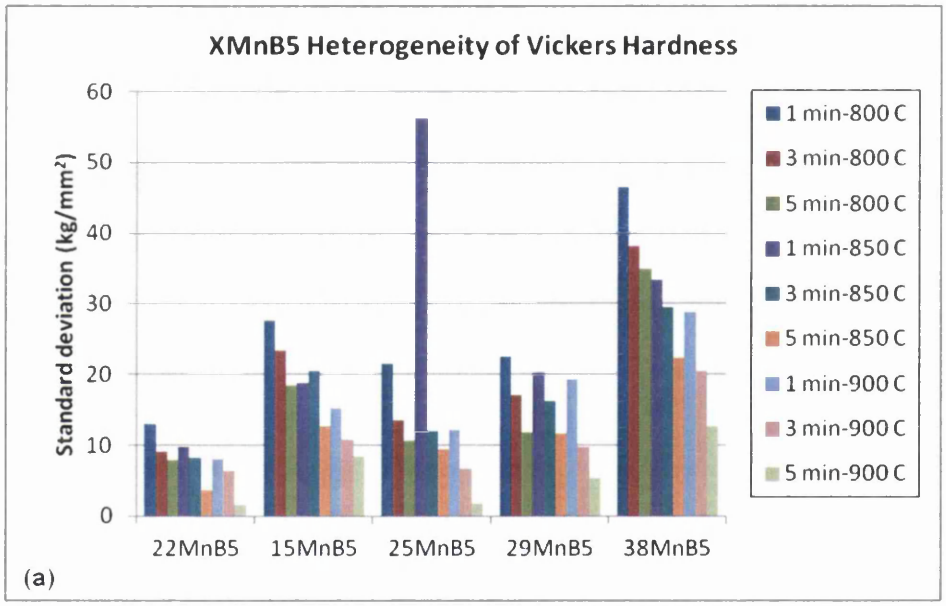

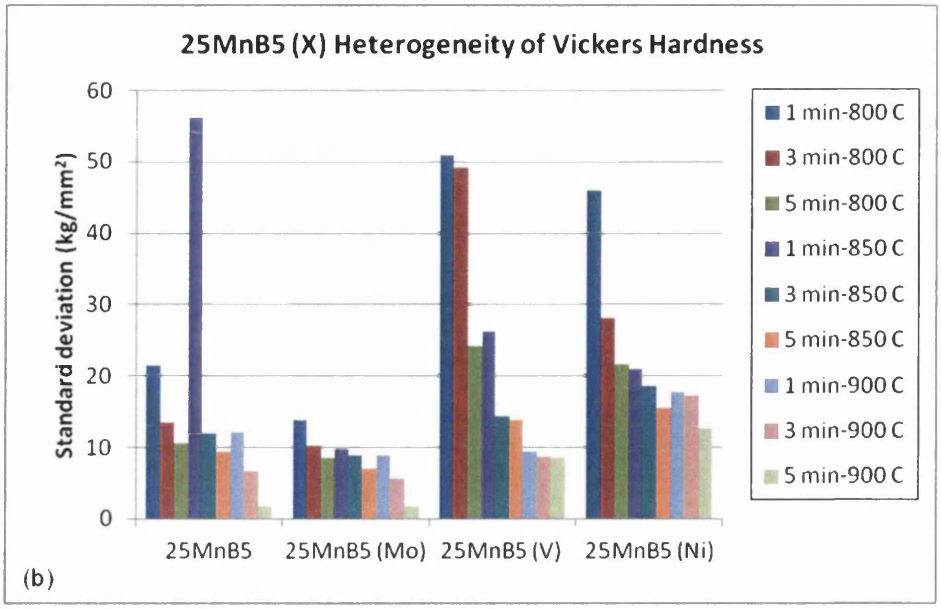


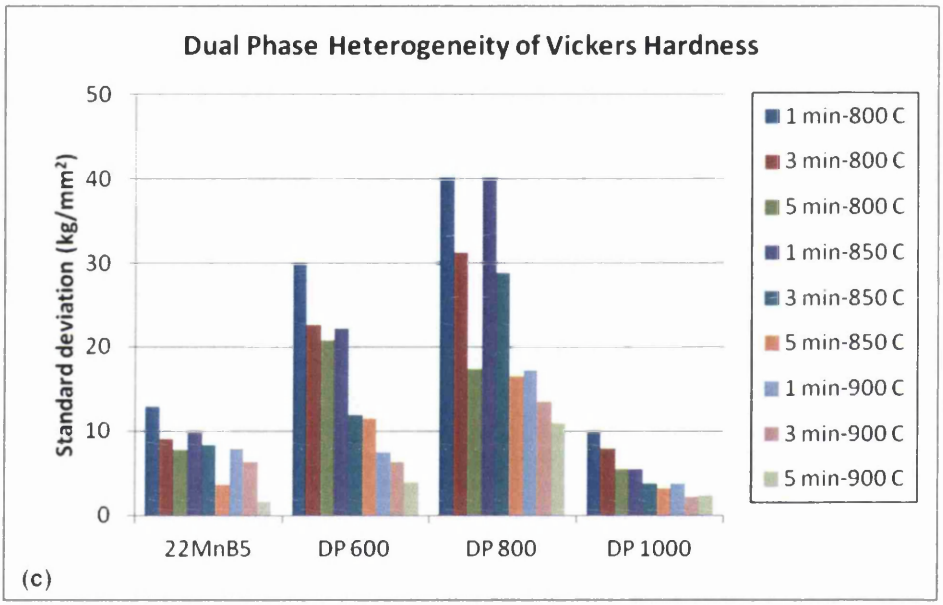


Figure 5.21: Heterogeneity of Vickers hardness (a) XMnB5 (b) 25MnB5 (X) (c) Dual Phase

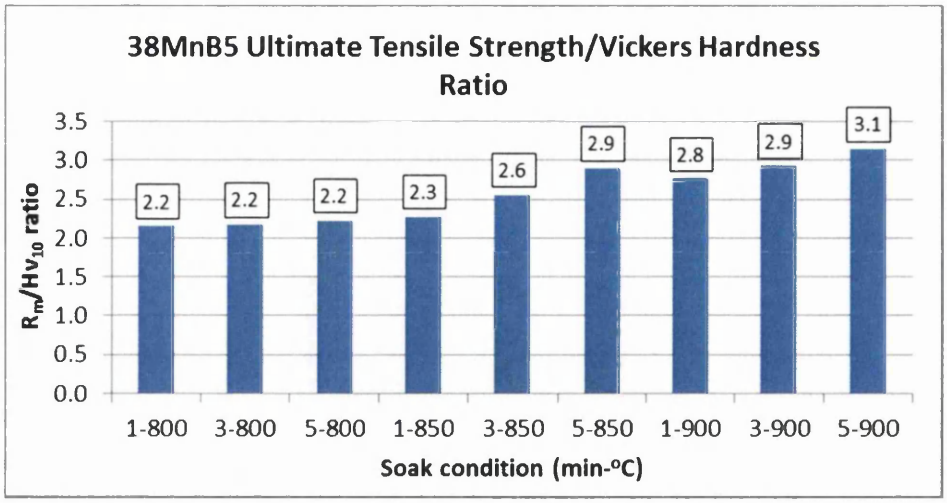


Figure 5.22: 38MnB5 ultimate tensile strength/Vickers hardness ratio

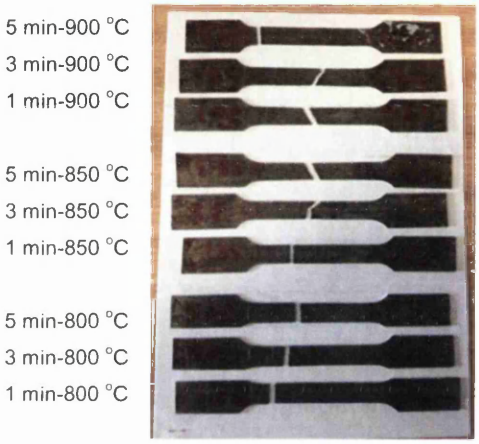


Figure 5.23: 38MnB5 fractured tensile specimens illustrating change of fracture mode

***Optimal Soak Condition***

The optimal soak condition for each grade is presented in Table 5.3 together with corresponding tensile properties, Vickers hardness and martensite volume fraction. The optimal soak condition for each grade was determined principally by maximum ultimate tensile strength, with maximum proof strength and adequate total elongation also important considerations. The exceptions were 15MnB5 and the three DP steels, for which more of a compromise on tensile strength was made for higher elongation.

The 22MnB5 control grade provided properties in the order of those widely reported for hot stamped 22MnB5. This validates the experimental procedures employed. However, it is worthy to note that the optimal soak condition of 1 min-

850 °C is lower than the typical soak condition employed of 3 to 5 minutes at 900 to 950 °C. This highlights potential energy, time and ultimately, cost savings.

Compared to 22MnB5, the lower carbon content, lower quench hardenability and in turn, dual phase ferritic-martensitic microstructure, in addition to less interstitial solid solution strengthening of 15MnB5, provided lower proof strength (-204 MPa) and lower ultimate tensile strength (-315 MPa), but with a relatively large gain to total elongation (+4.4 %). Moreover, 15MnB5 compared favourably to ArcelorMittal's Ductibor 1000 and Ductibor 1300 grades [20] discussed in Literature Review.

Compared to 22MnB5, the slightly higher carbon content of 25MnB5 failed to provide any appreciable difference in tensile properties.

Compared to 25MnB5, the molybdenum addition provided higher proof strength (+17 MPa), higher ultimate tensile strength (+77 MPa) and higher total elongation (+3.3 %). Similar tensile strength and elongation advantages were provided over 22MnB5. The tensile strength gain may be attributed to the dual actions of intermetallic compound-induced precipitation hardening and substitutional solid solution strengthening. Intermetallic compounds were found to be mostly ferro-titanium nitride. The precipitation of which may be aided by the molybdenum addition, where it is known that the addition of carbide/nitride former's such as molybdenum, can encourage stronger carbide/nitride formers present (such as titanium) to form carbides/nitrides [39]. Substitutional solid solution strengthening would have been provided by dissolved molybdenum. There is also the consideration of microstructural refinement owing to: 1) intermetallic compounds pinning γ-austenite grain boundaries during austenisation; and 2) greater quench hardenability [31]. Explanation to the elongation gain is unclear. However, it is apparent that molybdenum is beneficial to elongation when dissolved in solid solution.

Compared to 25MnB5, the vanadium addition provided higher proof strength (+108 MPa), higher ultimate tensile strength (+95 MPa) and higher total

elongation (+4.6 %). Similar tensile strength and elongation advantages were provided over 22MnB5. Explanation to the tensile strength gain can be suggested to be much the same as that explanation posed for molybdenum. Moreover, explanation to the elongation gain is also unclear. However, in common with molybdenum, it is apparent that vanadium is beneficial to elongation when dissolved in solid solution.

Compared to 25MnB5, the nickel addition provided higher proof strength (+99 MPa), higher ultimate tensile strength (+75 MPa) and higher total elongation (+5.2 %). Similar tensile strength and elongation advantages were provided over 22MnB5. The tensile strength gain can be attributed largely to substitutional solid solution strengthening. There is also the consideration of microstructural refinement owing to greater quench hardenability [31]. Explanation to the elongation gain is once more unclear. However, in common with molybdenum and vanadium, it is apparent that nickel is beneficial to elongation. All three grades 25MnB5 (Mo), 25MnB5 (V) and 25MnB5 (Ni) compared favourably to Naderi et al's hot stamped and tempered 37MnB4 grade [89] and Benteler's EP 1881083-A1 grade [90] discussed in Literature Review.

Compared to 22MnB5, the higher carbon content of 29MnB5 provided higher proof strength (+202 MPa) and higher ultimate tensile strength (+288 MPa), yet with similar total elongation (-1.5 %). The tensile strength gain can be attributed largely to interstitial solid solution strengthening. There are also the considerations of additional carbide-induced precipitation hardening and moreover, microstructural refinement owing to: 1) carbides pinning γ-austenite grain boundaries during austenisation; and 2) greater quench hardenability [31].

Compared to 22MnB5, the significantly higher carbon content of 38MnB5 provided higher proof strength (+256 MPa) and higher ultimate tensile strength (+476 MPa), yet with similar total elongation (-1.0 %). The tensile strength gain can be attributed to the same factors posed for 29MnB5. For both 29MnB5 and 38MnB5, the insignificant loss of elongation compared to 22MnB5 may be attributed to greater auto-tempering of martensite during quenching [31], which has been

reported to enhance elongation and impact toughness while maintaining strength [31]. Both 29MnB5 and particularly 38MnB5 compared favourably to ThyssenKrupp's reported MBW 1900 grade [87] discussed in Literature Review.

Compared to 22MnB5, the lower carbon equivalent, absence of boron, lower quench hardenability and in turn, dual phase ferritic-martensitic microstructure, in addition to less interstitial solid solution strengthening of DP 600, provided lower proof strength (-234 MPa) and lower ultimate tensile strength (-341 MPa), but with a relatively large gain to total elongation (+6.9 %). Moreover, compared to 15MnB5, DP 600 provided slightly lower proof strength (-30 MPa), slightly lower ultimate tensile strength (-26 MPa), but with a relatively large gain to total elongation (+2.5 %).

Compared to 22MnB5, the lower carbon equivalent, absence of boron, lower quench hardenability and in turn, dual phase ferritic-martensitic microstructure, in addition to less interstitial solid solution strengthening of DP 800, also provided lower proof strength (-445 MPa) and lower ultimate tensile strength (-347 MPa), but with a relatively large gain to total elongation (+6.7 %). Moreover, compared to 15MnB5, DP 800 provided lower proof strength (-241 MPa), slightly lower ultimate tensile strength (-32 MPa), but with a relatively large gain to total elongation (+2.3 %). Both DP 600 and DP 800 compared favourably to ArcelorMittal's Ductibor 1000 and Ductibor 1300 grades [20] discussed in Literature Review.

Compared to 22MnB5, DP 1000 provided slightly lower proof strength (-109 MPa) and slightly lower ultimate tensile strength (-158 MPa), but with a large gain to total elongation (+8.1 %). Indeed, DP 1000 provided the highest total elongation of all grades. DP 1000 compared favourably to Benteler's EP 1881083-A1 grade [90] and Yi et al's DP-PF grade [93] discussed in Literature Review.

The Laboratory Hot Stamping experimental reinforced findings from the preliminary CASIM experimental, where the DP steels were considered advantageous for impact energy absorptive crash performance compared to

22MnB5, providing lower proof strength, substantially higher uniform elongation and total elongation, yet with a relatively small loss to ultimate tensile strength.

It was anticipated that the mechanical properties to be obtained from the DP steels could be obtained from 15MnB5, where the latter exhibits a more economical chemical composition. However, it is apparent that the richer chemical compositions (manganese, chromium, vanadium, niobium and/or nickel additions) of the DP steels do provide mechanical advantages following hot stamping and therefore, the DP steels may be considered to justify their greater expense.

Figure 5.24 illustrates where the investigated grades treated to their optimal hot stamping soak conditions lay with respect to ultimate tensile strength-total elongation ranges of current automotive steels. Moreover, Figure 5.24 illustrates where the investigated grades lay with respect to the ultimate tensile strength-total elongation range targeted by the steel and automotive industries (as first presented in Figure 1.1). 38MnB5, DP 1000 and 25MnB5 (V) reach into the target range. Further, compared to the 22MnB5 control grade, 38MnB5 meets the higher tensile strength objective, DP 1000 meets the higher elongation objective and 25MnB5 (V) meets the higher tensile strength-higher elongation objective. Thus, these three grades, treated to their as-determined optimal hot stamping soak conditions, were selected for further evaluation, including dynamic tensile testing, three-point bend testing and FEM crash simulation.

Table 5.3: Laboratory hot stamping optimal soak conditions

| *Grade* | *Soak condition (min-°C)* | $R_{p0.2}$ *(MPa)* | $R_m$ *(MPa)* | $A_u$ *(%)* | $A_{50}$ *(%)* | *Hv* $(kg/mm^2)$ | *Martensite (vol. %)* |
|---|---|---|---|---|---|---|---|
| 22MnB5 | 1-850 | 1163 ± 15 | 1590 ± 7 | 3.5 ± 0.5 | 7.2 ± 0.1 | 534 | 100.0 ± 0.0 |
| 15MnB5 | 3-900 | 959 ± 9 | 1275 ± 4 | 3.9 ± 0.1 | 11.6 ± 0.0 | 467 | 98.3 ± 2.3 |
| 25MnB5 | 3-850 | 1162 ± 12 | 1589 ± 68 | 3.4 ± 0.3 | 6.4 ± 2.0 | 526 | 100.0 ± 0.0 |
| 25MnB5 (Mo) | 1-850 | 1179 ± 3 | 1666 ± 5 | 3.6 ± 0.1 | 9.7 ± 2.3 | 565 | 100.0 ± 0.0 |
| 25MnB5 (V) | 3-850 | 1270 ± 59 | 1684 ± 18 | 3.8 ± 0.1 | 11.0 ± 0.0 | 636 | 100.0 ± 0.0 |
| 25MnB5 (Ni) | 1-900 | 1261 ± 32 | 1664 ± 15 | 3.4 ± 0.1 | 11.6 ± 0.0 | 642 | 100.0 ± 0.0 |
| 29MnB5 | 3-800 | 1365 ± 28 | 1878 ± 76 | 3.4 ± 0.0 | 5.7 ± 1.5 | 594 | 98.8 ± 0.1 |
| 38MnB5 | 5-850 | 1419 ± 64 | 2066 ± 77 | 4.5 ± 0.2 | 6.2 ± 0.4 | 713 | 100.0 ± 0.0 |
| DP 600 | 5-850 | 929 ± 12 | 1249 ± 6 | 3.5 ± 0.2 | 14.1 ± 0.5 | 392 | 72.8 ± 6.3 |
| DP 800 | 5-800 | 718 ± 11 | 1243 ± 11 | 5.4 ± 0.2 | 13.9 ± 0.1 | 358 | 79.2 ± 8.5 |
| DP 1000 | 5-850 | 1054 ± 25 | 1432 ± 89 | 3.6 ± 0.1 | 15.3 ± 0.3 | 460 | 100.0 ± 0.0 |

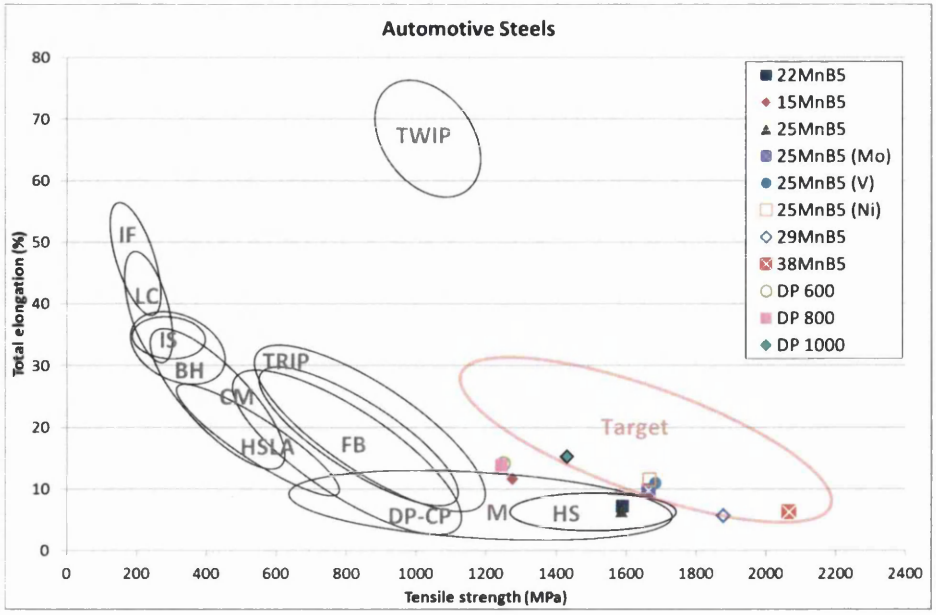


Figure 5.24: Where the investigated grades treated to their optimal hot stamping soak conditions lay with respect to the ultimate tensile strength-total elongation range targeted by the steel and automotive industries

## Dynamic Tensile Testing

### *Tensile Properties*

Figures 5.25a-f present tensile properties ((true) proof strength-$R_{p0.2}$, (true) ultimate tensile strength-$R_m$, uniform (plastic) elongation-$A_u$, total (plastic) elongation-A, toughness (2 % plastic strain) and toughness (total plastic strain)).

For 22MnB5, increasing strain rate from 0.001 to 1 $s^{-1}$ resulted in increasing proof strength and ultimate tensile strength, but decreasing uniform elongation and total elongation. Conversely, increasing strain rate from 1 to 100 and to 200 $s^{-1}$ resulted in generally decreasing proof strength and ultimate tensile strength, but generally increasing uniform elongation and total elongation. The contradictory responses between tensile strength and elongation (particularly proof strength and uniform elongation) to increasing strain rate resulted in similar toughness (2 % plastic strain) across all four strain rates. However, increasing elongation (particularly total elongation) with increasing strain rate from 1 to 100 and to 200 $s^{-1}$ resulted in significantly higher toughness (total plastic strain). These observations illustrate the strong influence of proof strength on toughness (2 % plastic strain) and moreover, the very strong influence of total elongation on toughness (total plastic strain). The latter is clearly evident from the manner in

which the 'total elongation' chart is almost an exact replica (depicts exactly the same trends) of the 'toughness (total plastic strain)' chart.

For DP 1000, increasing strain rate from 0.001 to 1 $s^{-1}$ resulted in increasing proof strength, but decreasing total elongation. Conversely, increasing strain rate from 1 to 100 and to 200 $s^{-1}$ resulted in consistently decreasing proof strength, but consistently increasing total elongation. Ultimate tensile strength and uniform elongation demonstrated variable and anomalous responses to increasing strain rate. The very strong influence of total elongation on toughness (total plastic strain) is again apparent.

For 25MnB5 (V), increasing strain rate from 0.001 to 1 $s^{-1}$ resulted in increasing proof strength. Conversely, increasing strain rate from 1 to 100 and to 200 $s^{-1}$ resulted in consistently decreasing proof strength. Increasing strain rate across all four strain rates resulted in generally increasing ultimate tensile strength, uniform elongation and total elongation. Consequently, increasing strain rate across all four strain rates resulted in consistently increasing toughness (2 % plastic strain) and particularly, consistently increasing toughness (total plastic strain).

For 38MnB5, increasing strain rate across all four strain rates resulted in generally increasing proof strength and consistently increasing ultimate tensile strength. Increasing strain rate from 0.001 to 1 $s^{-1}$ resulted in decreasing uniform elongation and total elongation. Conversely, increasing strain rate from 1 to 100 and to 200 $s^{-1}$ resulted in generally increasing uniform elongation and total elongation. Consequently, the highest strain rates of 100 and 200 $s^{-1}$ resulted in significantly higher toughness (total plastic strain).

Strain rate sensitivity values are presented in Table 5.4. Each grade demonstrated positive strain rate sensitivity with increasing strain rate from 0.001 to 1 $s^{-1}$. However, each grade demonstrated negative strain rate sensitivity with increasing strain rate from 1 to 100 $s^{-1}$. Moreover, DP 1000 and 25MnB5 (V) also demonstrated negative strain rate sensitivity with increasing strain rate from 100 to 200 $s^{-1}$.

Positive strain rate sensitivity with increasing strain rate from 0.001 to 1 $s^{-1}$ can be attributed to the breakdown of dislocation cell structures. It has been reported [3] [129] that under low strain rates, plastic deformation takes place with dislocations forming ordered dislocation cell structures. However, under high strain rates, dislocation cell structures demonstrate a tendency to breakdown, leading to more dislocation nucleation sites for the subsequent generation of dislocations within the plastic deformation process. Thus, the final dislocation density is relatively large. The increase in dislocation density then gives rise to strengthening through work hardening. This characteristic of dislocation cell structures forming and being maintained under low strain rates, but dislocation cell structures breaking down under high strain rates, has been reported [3] [129] [133] [136] to be particularly common in mild carbon ferritic steels, such as CM and HSLA steels, giving rise to relatively high strain rate sensitivity values of typically 0.07. However, in multiphase steels such as DP and TRIP steels, it has been reported [3] [129] [133] that dislocation cell structures are inhibited from forming regardless of the strain rate, due to interactions between dislocations and hard secondary phases or precipitates. It is for this reason that DP and TRIP steels have been reported [3] [129] [133] to demonstrate lower strain rate sensitivity values than ferritic steels, typically in the order of 0.02-0.03. It is proposed that here for the hot stamped martensitic steels, greater breakdown of dislocation cell structures and thus, higher dislocation density under higher strain rates was a factor, leading to positive strain rate sensitivity with increasing strain rate from 0.001 to 1 $s^{-1}$. However, the magnitude of greater dislocation cell structure breakdown with increasing strain rate was relatively small, with dislocation cell structures inhibited from forming (to some extent) regardless of the strain rate, due to interactions between dislocations and the numerous boundaries found in lath martensite, namely packet, block and lath boundaries.

The possible occurrence of dynamic strain aging should also be considered. Dynamic strain aging is defined as the presence of mechanical deformation together with thermal aging [171], giving rise to the Luders front and Portevin-Le-Chatelier effects [172].

During plastic deformation, dislocations migrate through the crystal until their movement is inhibited by obstacles, such as forest dislocations, grain boundaries or precipitates. While the dislocation is immobile, interstitial solutes such as carbon and nitrogen and to a lesser extent, substitutional solutes such as chromium, can diffuse through the crystal to the dislocation, introduce a strain field (or Cottrell Atmosphere) around the dislocation and thereby, further restrict the dislocation's movement and provide a marked strengthening effect in addition to a characteristic serrated stress-strain curve. Indeed, the phenomenon of dynamic strain aging shares very close similarities with the yield point elongation phenomenon. However, the distinction to dynamic strain aging is the occurrence of this 'discontinuous yielding' behaviour throughout the deformation process as a consequence of mechanical deformation at elevated temperature, whereas the yield point elongation phenomenon occurs exclusively around the yield point and at ambient temperature. It may be considered that with the introduction of adiabatic heating under high strain rates (discussed below), the dynamic strain aging phenomenon took place.

Negative strain rate sensitivity with increasing strain rate from 1 to 100 and to 200 $s^{-1}$ can be attributed to adiabatic heating [3] [129] [131]. During plastic deformation a portion of mechanical energy is transferred to heat energy. It has been reported [3] [129] [131] that under low strain rates, the heat energy generated has opportunity to dissipate from the deformed region to the external atmosphere. However, under high strain rates, the heat energy does not have opportunity to dissipate rapidly enough. Thus, the heat energy remains concentrated in the deformed region throughout the plastic deformation process, leading to adiabatic heating and in turn, weakening of inter-atomic bonds. It has been reported [3] [129] [131] that the weakening of inter-atomic bonds resulting from adiabatic heating can be responsible for negative strain rate sensitivity. Here for the hot stamped martensitic steels, it was proposed that with increasing strain rate, adiabatic heating became a larger factor. Moreover, at the higher strain rates of 100 and 200 $s^{-1}$, softening from adiabatic heating was a more significant factor than hardening from dislocation density increase. It is for this reason that the hot stamped martensitic steels exhibited relatively low (even negative) mean strain

rate sensitivity values, with the highest mean strain rate sensitivity value of just 0.012 provided by 38MnB5. This compares to strain rate sensitivity values of 0.07 reported [3] [129] [133] [136] for ferritic steels and 0.02-0.03 reported [3] [129] [133] for DP and TRIP steels.

With the exception of DP 1000, each grade demonstrated maximum uniform elongation and total elongation given the higher strain rates of 100 and 200 $s^{-1}$. The adiabatic heating theory at higher strain rates may also explain this trend, where it has been reported [134] that DP and TRIP steels exhibit higher elongation values under dynamic strain rates compared to under quasi-static strain rates.

38MnB5 was the only grade to demonstrate positive mean strain rate sensitivity across all four strain rates and moreover, the only grade to demonstrate consistently increasing ultimate tensile strength across all four strain rates. Further, 38MnB5 demonstrated a relatively large increase to total elongation at the higher strain rates of 100 and 200 $s^{-1}$. For example, the difference between the minimum and maximum total elongation of 22MnB5 was 2.7 %, whereas the difference between the minimum and maximum total elongation of 38MnB5 was 8.1 %. The relatively large increase to total elongation at the higher strain rates demonstrated by 38MnB5 may be attributed to the higher carbon content and in turn, greater rise of adiabatic heating. The proposed theory being that a greater concentration of interstitial solute carbon atoms are present to interact and generate heat.

Repeat quasi-static and dynamic tensile testing across all four strain rates of 0.001, 1, 100 and 200 $s^{-1}$ for 22MnB5 and 38MnB5 with the addition of thermocouple data logging, demonstrated the adiabatic heating theory (Figure 5.26), where it was proposed that with increasing strain rate, adiabatic heating became a larger factor, leading to: 1) negative strain rate sensitivity values; and 2) each grade (with the exception of DP 1000) demonstrating maximum uniform elongation and total elongation given the higher strain rates of 100 and 200 $s^{-1}$. Moreover, Figure 5.26, which plots strain rate against (maximum) change in

temperature during the tensile test, illustrates that 38MnB5 demonstrated a greater rise of adiabatic heating at the higher strain rates of 100 and 200 $s^{-1}$, compared to 22MnB5, where 22MnB5 demonstrated a temperature rise of 27.7 °C under the strain rate of 0.001 $s^{-1}$ and a temperature rise of 35.6 °C under the strain rate of 200 $s^{-1}$, but in contrast, 38MnB5 demonstrated a temperature rise of 29.1 °C under the strain rate of 0.001 $s^{-1}$ and a temperature rise of 55.9 °C under the strain rate of 200 $s^{-1}$. Thus, it can be considered that the greater rise of adiabatic heating at the higher strain rates, owing to the higher carbon content, was responsible for the relatively large increase to total elongation at the higher strain rates demonstrated by 38MnB5.

The response of 38MnB5 to increasing strain rate gave rise to significantly higher toughness compared to 22MnB5 at the higher strain rates. Moreover, by making comparison to results presented by other researchers [3] [129] (Figure 5.27), each of the hot stamped martensitic steels demonstrated higher toughness (2 % plastic strain) under the lowest strain rate of 0.001 $s^{-1}$ than a selection of as-delivered automotive steels, including XF 450 (HSLA), CMn 800, DP 600, DP 800, DP 1400, TRIP 600, TRIP 800, TRIP 950 and TRIP 1000. Under the highest strain rate of 200 $s^{-1}$, only as-delivered DP 1400 competes with the toughness (2 % plastic strain) of the hot stamped martensitic steels.

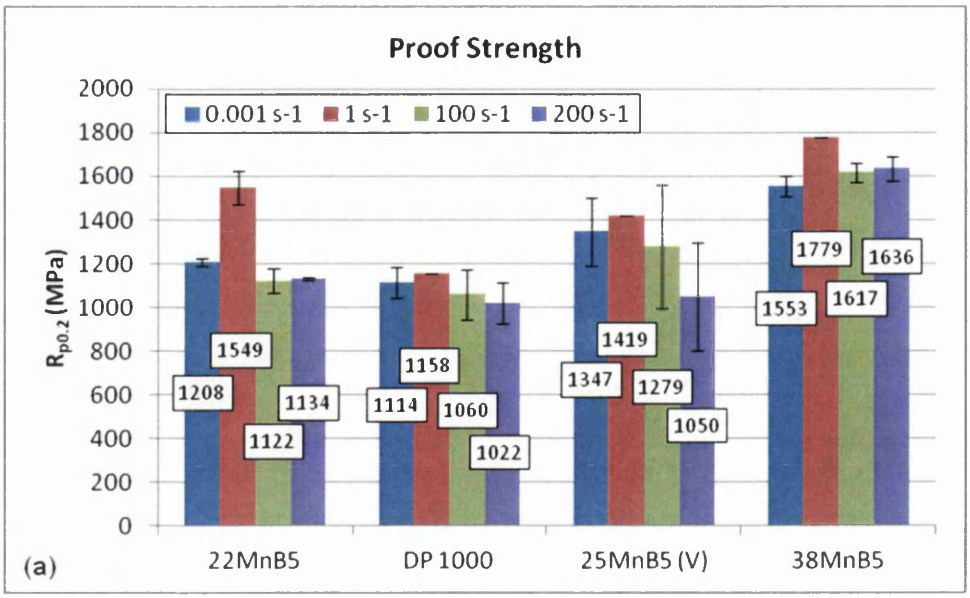
Proof Strength
0.001 s-1
1 s-1
100 s-1
200 s-1
$R_{p0.2}$ (MPa)
2000
1800
1600
1400
1200
1000
800
600
400
200
0
1208
1549
1122
1134
1114
1158
1060
1022
1347
1419
1279
1050
1553
1779
1617
1636
(a)
22MnB5
DP 1000
25MnB5 (V)
38MnB5

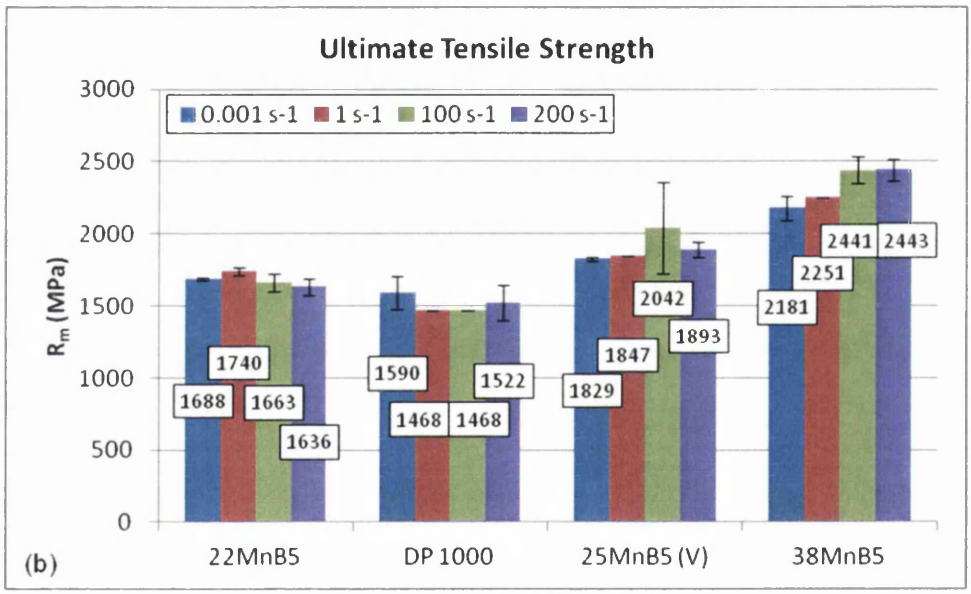
Ultimate Tensile Strength
0.001 s-1
1 s-1
100 s-1
200 s-1
$R_m$ (MPa)
3000
2500
2000
1500
1000
500
0
1688
1740
1663
1636
1590
1468
1468
1522
1829
1847
2042
1893
2181
2251
2441
2443
(b)
22MnB5
DP 1000
25MnB5 (V)
38MnB5

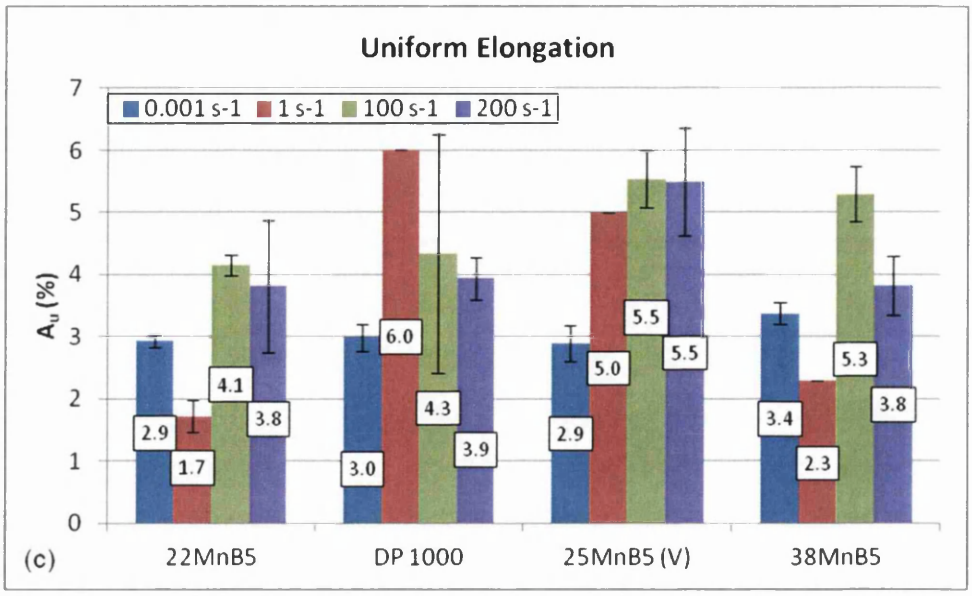
Uniform Elongation
0.001 s-1
1 s-1
100 s-1
200 s-1
$A_u$ (%)
0
1
2
3
4
5
6
7
2.9
1.7
4.1
3.8
3.0
6.0
4.3
3.9
2.9
5.0
5.5
5.5
3.4
2.3
5.3
3.8
(c)
22MnB5
DP 1000
25MnB5 (V)
38MnB5

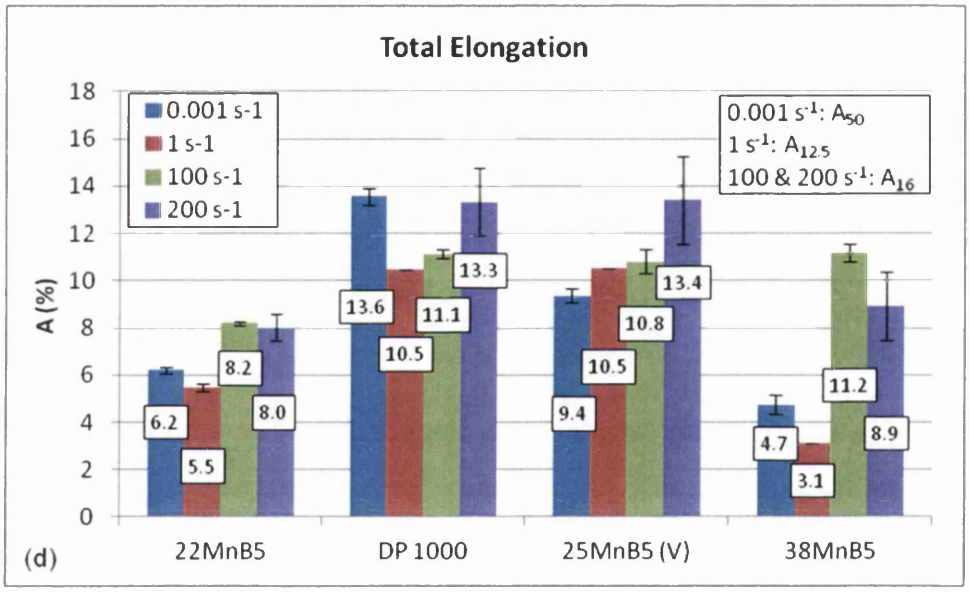
Total Elongation
0.001 s-1
1 s-1
100 s-1
200 s-1
0.001 $s^{-1}$: $A_{50}$
1 $s^{-1}$: $A_{12.5}$
100 & 200 $s^{-1}$: $A_{16}$
A (%)
0
2
4
6
8
10
12
14
16
18
6.2
5.5
8.2
8.0
13.6
10.5
11.1
13.3
9.4
10.5
10.8
13.4
4.7
3.1
11.2
8.9
(d)
22MnB5
DP 1000
25MnB5 (V)
38MnB5

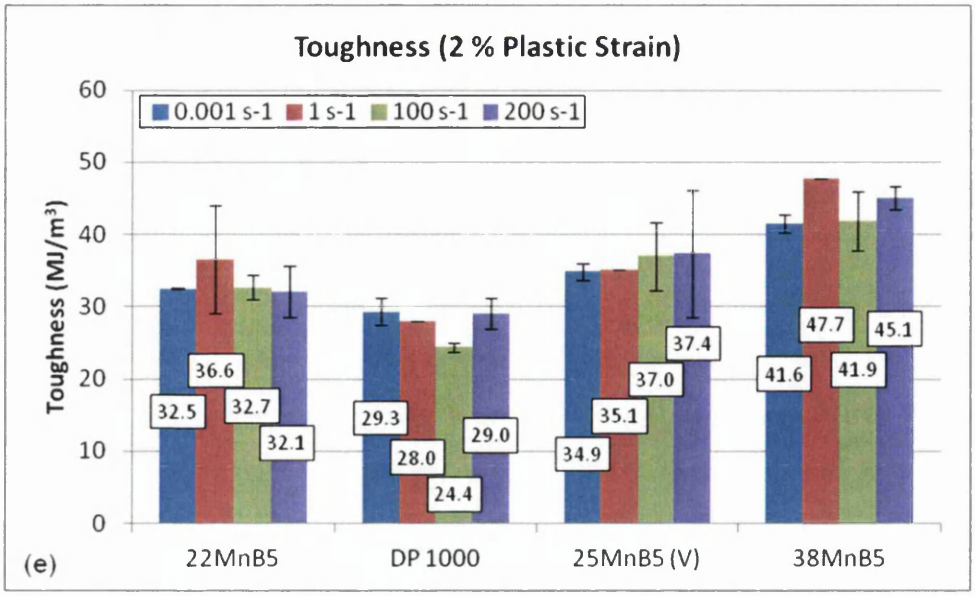


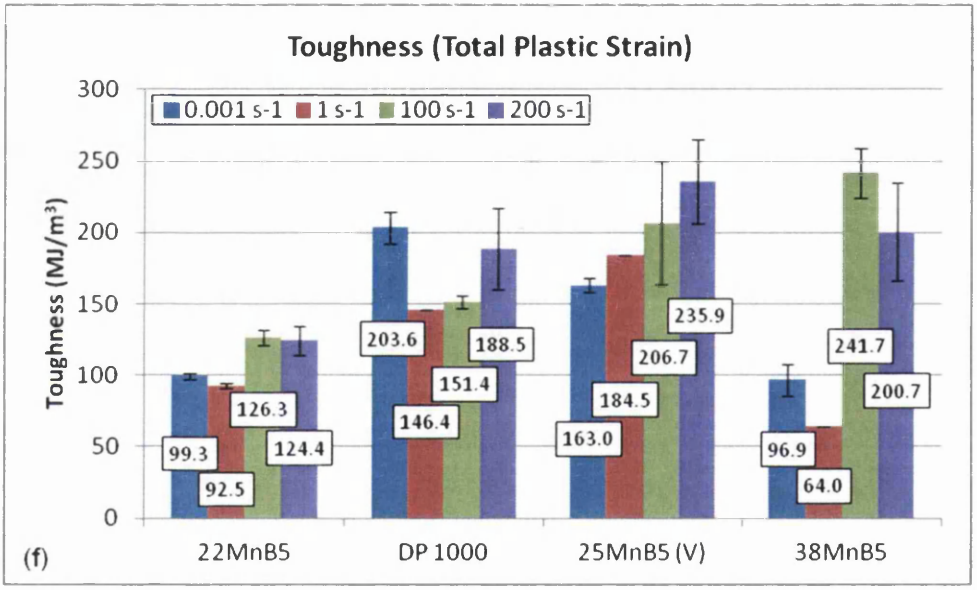


Figure 5.25: Dynamic tensile properties (a) proof strength (b) ultimate tensile strength (c) uniform elongation (d) total elongation (e) toughness (2 % plastic strain) (f) toughness (total plastic strain)

Table 5.4: Strain rate sensitivity

| *Grade* | $m_{0.001\text{-}1}$ | $m_{1\text{-}100}$ | $m_{100\text{-}200}$ | $m_{mean}$ |
|---|---|---|---|---|
| 22MnB5 | 0.083 | -0.161 | 0.033 | -0.015 |
| DP 1000 | 0.013 | -0.044 | -0.121 | -0.051 |
| 25MnB5 (V) | 0.017 | -0.052 | -0.658 | -0.231 |
| 38MnB5 | 0.045 | -0.048 | 0.037 | 0.012 |

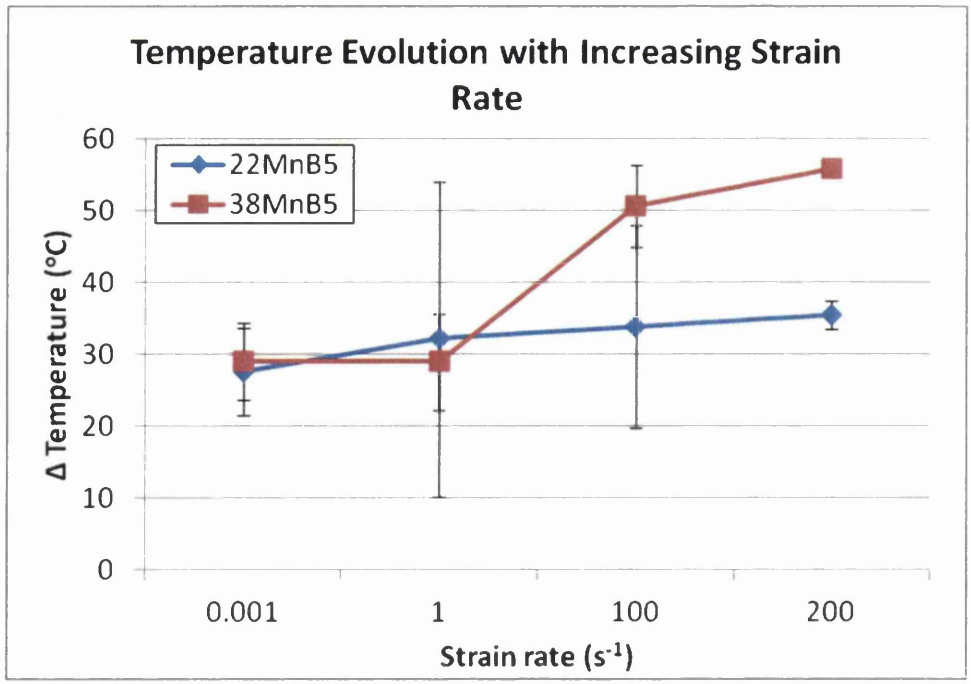


Figure 5.26: Temperature evolution with increasing strain rate

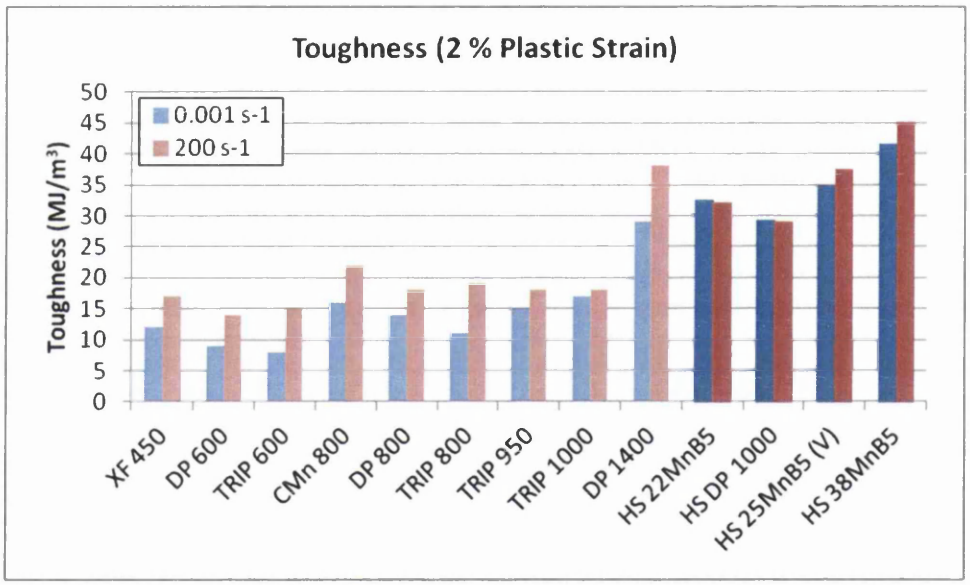


Figure 5.27: Comparison of toughness (2 % plastic strain) between the hot stamped (HS) martensitic steels and select as-delivered automotive steels researched by S. Oliver et al [3] [129]

***Hardness Properties***

Figure 5.28 presents change in Vickers hardness (ΔHv) from the shoulders to the fracture point of the dynamic tensile specimen. 38MnB5 demonstrated consistently increasing ΔHv with increasing strain rate. This demonstrates increasing work hardening along the reduced section to the fracture point with increasing strain rate. Moreover, this supports the increasing dislocation density theory proposed above. DP 1000 demonstrated variable ΔHv with increasing strain rate. This coincides with the variable response of ultimate tensile strength to increasing strain rate.

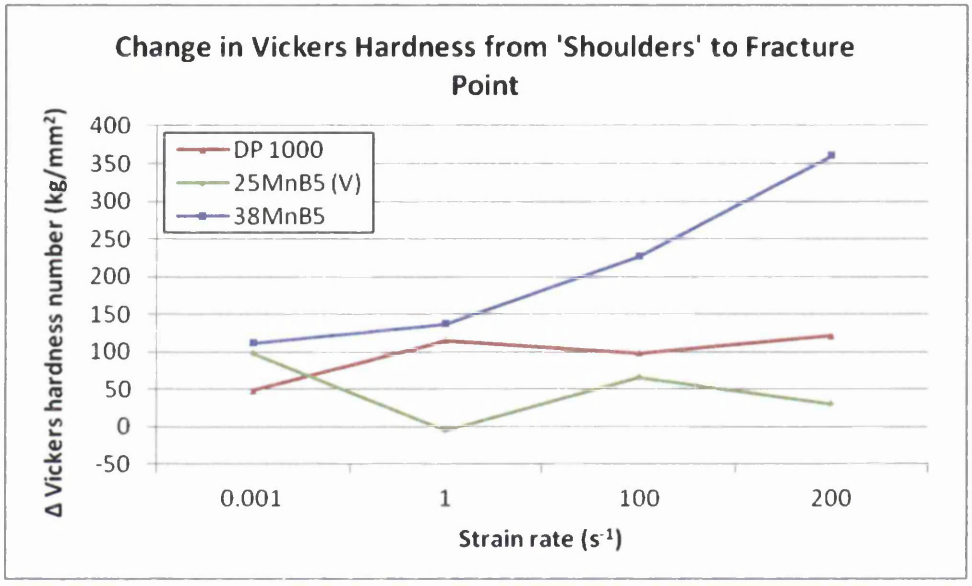


Figure 5.28: Change in Vickers hardness from shoulders to fracture point

***Microstructural Analysis***

Figures 5.29a-l present SEM micrographs of the fractured dynamic tensile specimen reduced sections.

Each grade exhibited a transition from ductile fracture to brittle fracture (or visa-versa) with increasing strain rate. Note that in most cases, the fracture mode was not pure ductile or pure brittle, but rather, a combination of both fracture modes. Here, the balance between the two fracture modes shifted with increasing strain rate.

For each grade, there was generally a correlation between fracture mode and total elongation. The most notable example was perhaps provided by DP 1000. The fracture surface demonstrated a significant ductile component across all four strain rates, marked by the characteristic 'cup and cone' appearance [11]. With increasing strain rate from 0.001 to 1 $s^{-1}$, the fracture surface demonstrated a greater brittle component, marked by the characteristic planar appearance [11]. With increasing strain rate from 1 to 100 $s^{-1}$, the fracture surface demonstrated a pure ductile fracture. The transition of fracture mode reflects the total elongation values: as the fracture mode became more brittle, total elongation decreased; as the fracture mode became more ductile, total elongation increased. These observations support the increasing dislocation density and adiabatic heating theories proposed above.

Figures 5.30a-l present SEM micrographs of the fracture points taken at ½ specimen thickness. In all cases, the microstructure was completely martensitic. Moreover, there was seldom (or even no) observable modification to the microstructure with increasing deformation along the reduced section to the fracture point.

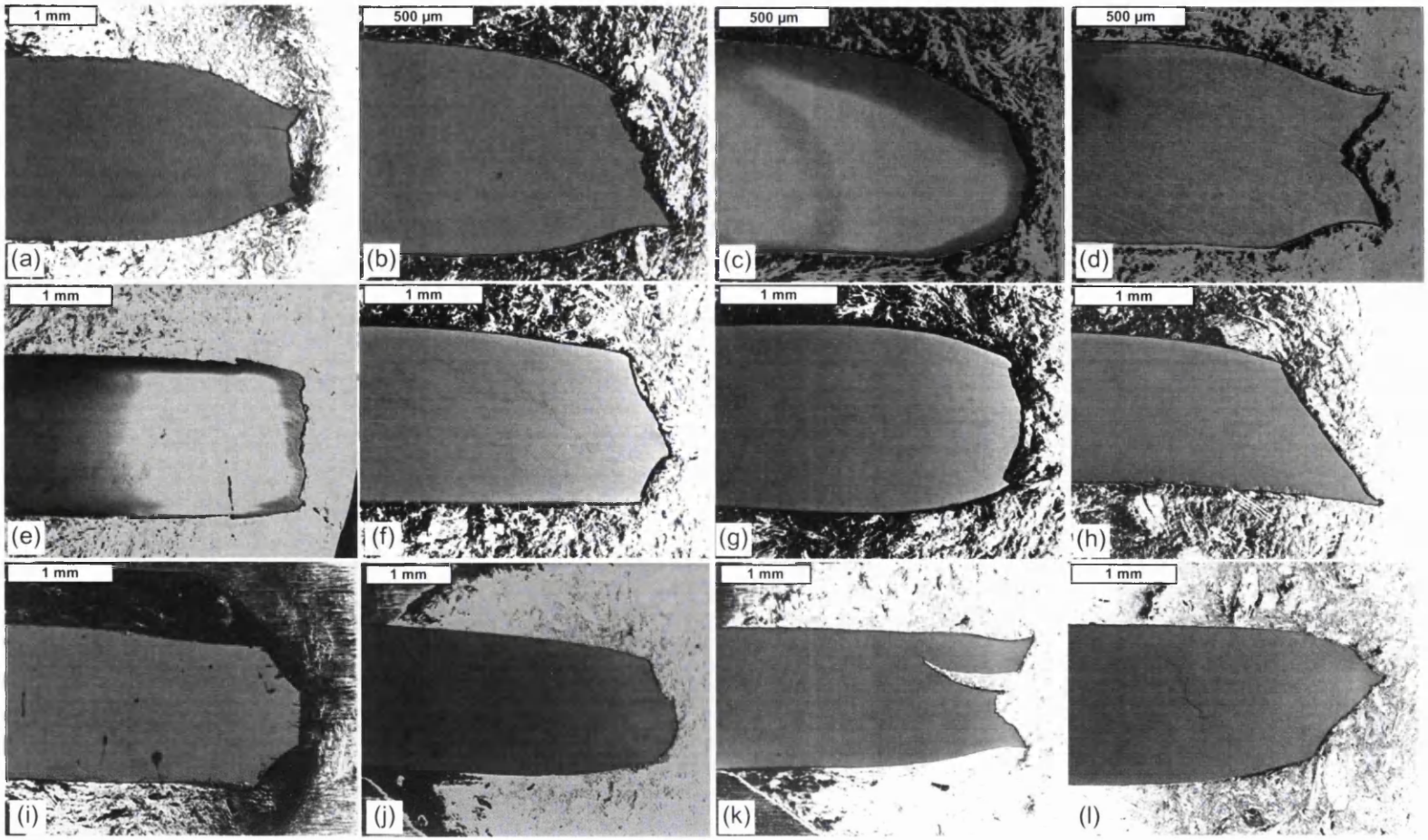


Figure 5.29: SEM micrographs of fractured dynamic tensile specimen reduced sections (a) DP 1000 0.001 $s^{-1}$ (b) DP 1000 1 $s^{-1}$ (c) DP 1000 100 $s^{-1}$ (d) DP 1000 200 $s^{-1}$ (e) 25MnB5 (V) 0.001 $s^{-1}$ (f) 25MnB5 (V) 1 $s^{-1}$ (g) 25MnB5 (V) 100 $s^{-1}$ (h) 25MnB5 (V) 200 $s^{-1}$ (i) 38MnB5 0.001 $s^{-1}$ (j) 38MnB5 1 $s^{-1}$ (k) 38MnB5 100 $s^{-1}$ (l) 38MnB5 200 $s^{-1}$

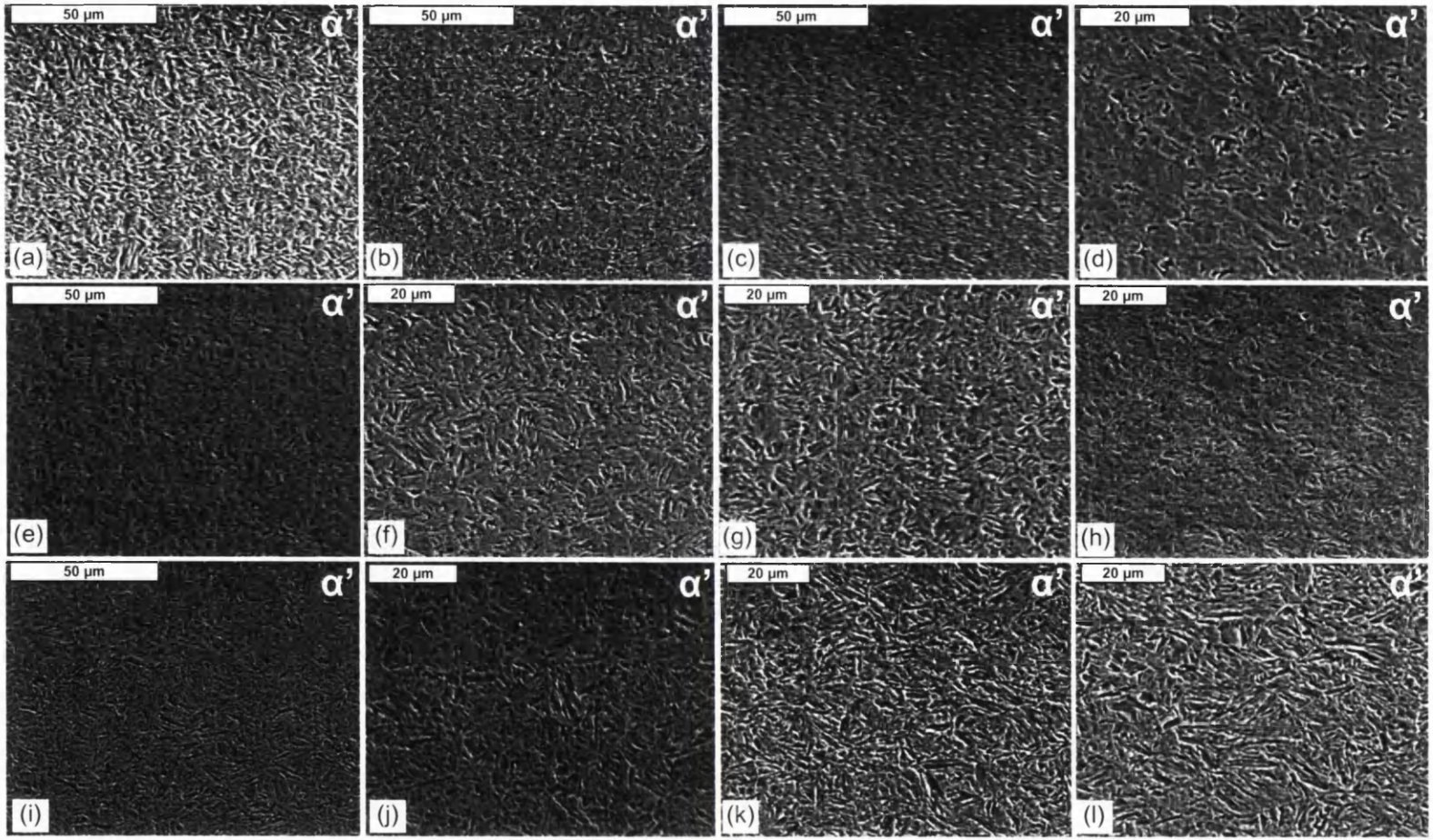


Figure 5.30: SEM micrographs of fracture points taken at ½ specimen thickness (a) DP 1000 0.001 $s^{-1}$ (b) DP 1000 1 $s^{-1}$ (c) DP 1000 100 $s^{-1}$ (d) DP 1000 200 $s^{-1}$ (e) 25MnB5 (V) 0.001 $s^{-1}$ (f) 25MnB5 (V) 1 $s^{-1}$ (g) 25MnB5 (V) 100 $s^{-1}$ (h) 25MnB5 (V) 200 $s^{-1}$ (i) 38MnB5 0.001 $s^{-1}$ (j) 38MnB5 1 $s^{-1}$ (k) 38MnB5 100 $s^{-1}$ (l) 38MnB5 200 $s^{-1}$

**Three-Point Bend Testing**

Figure 5.31a presents maximum force. Figure 5.31b presents maximum displacement and displacement at maximum force. Figure 5.31c presents final bend angle. Figures 5.32a-d present photographs of the specimens following three-point bend testing.

22MnB5, in addition to 25MnB5 (V) and DP 1000, each withstood the bend test to the maximum displacement of 30 mm, evident from 'the absence of cracks visible without the use of magnifying aids' [157]. However, 38MnB5 failed to withstand the bend test, sustaining fracture at a maximum force of just -1.3 kN and a displacement of just -2.5 mm. Although 38MnB5 demonstrated comparable uniform and total elongation values to 22MnB5 during quasi-static tensile testing, greater brittleness of 38MnB5, exhibiting significantly higher carbon content, was thus clear from three-point bend testing. This demonstrates the influence that complex stress-strain states and bending moments (that are not considered in the tensile test) can have on the specimen and moreover, demonstrates the result of subjecting a 'higher carbon' and inherently more brittle grade, to such complex stress-strain states and bending moments.

22MnB5 sustained a maximum force of -3.5 kN, while 25MnB5 (V) sustained a maximum force of -3.8 kN. Although the difference between the two grades was slight, the trend of increasing force sustained from 22MnB5 to 25MnB5 (V), indicating improved anti-intrusive and impact energy absorptive crash performance, was apparent. Moreover, 22MnB5 demonstrated a displacement of -23.0 mm at the maximum force, while 25MnB5 (V) demonstrated a displacement of -19.6 mm at the maximum force. Again, although the difference between the two grades was slight, the trend of decreasing displacement and thus improved anti-intrusive crash performance from 22MnB5 to 25MnB5 (V), was apparent. The three-point bend test results, demonstrating higher force sustainment and lower displacement, correlate with the tensile results presented previously, where the combined carbon and vanadium addition of 25MnB5 (V) provided higher tensile strength and higher elongation. It may be particularly worthy to note the higher uniform elongation of 25MnB5 (V) (3.8 ± 0.1 %) compared to 22MnB5 (3.5 ±

0.5 %). When considering 22MnB5 to take the uniform elongation value at the lower end of its range (3.0 %) and 25MnB5 (V) to take the value at the higher end of its range (3.9 %), the difference between the two grades becomes significant. Moreover, it has been suggested [15] [34] that bendability can be evaluated by local elongation, where local elongation (in the region of the specimen undergoing bending) can be equated to the uniform elongation. The three-point bend test results support the previously suggested benefits of vanadium addition to boron steel.

DP 1000 sustained a maximum force of -3.8 kN, corresponding to a displacement of -22.8 mm. Although the difference was once again slight, these figures represent improved anti-intrusive and impact energy absorptive crash performance compared to 22MnB5.

22MnB5, 25MnB5 (V) and DP 1000 each exhibited similar final bend angles of 95.0 to 101.7 ° (correlating with the fact that each grade withstood the maximum 30 mm displacement). 38MnB5 exhibited a final bend angle of just 24.0 °, corresponding to the moment of fracture.

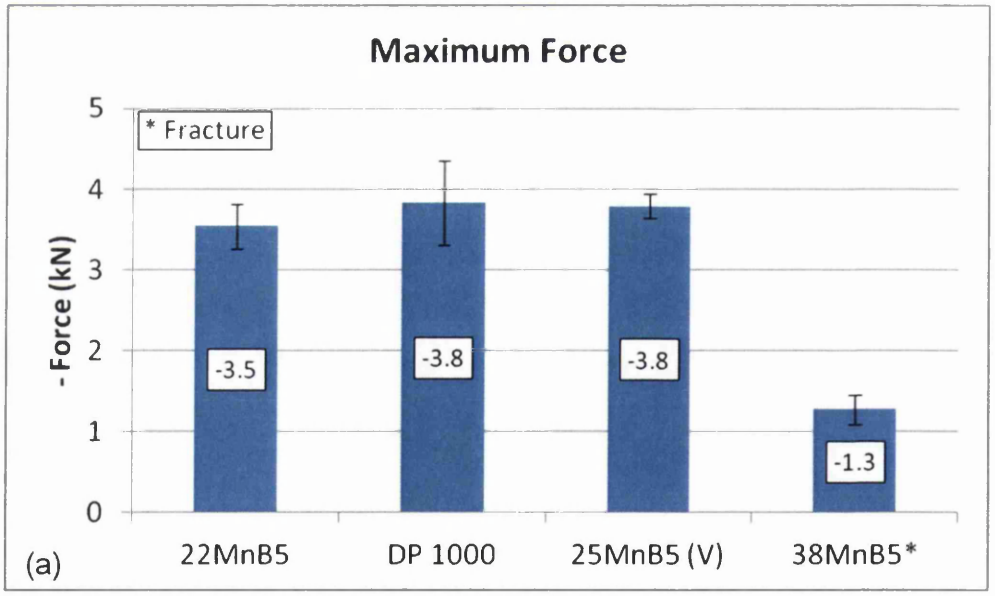

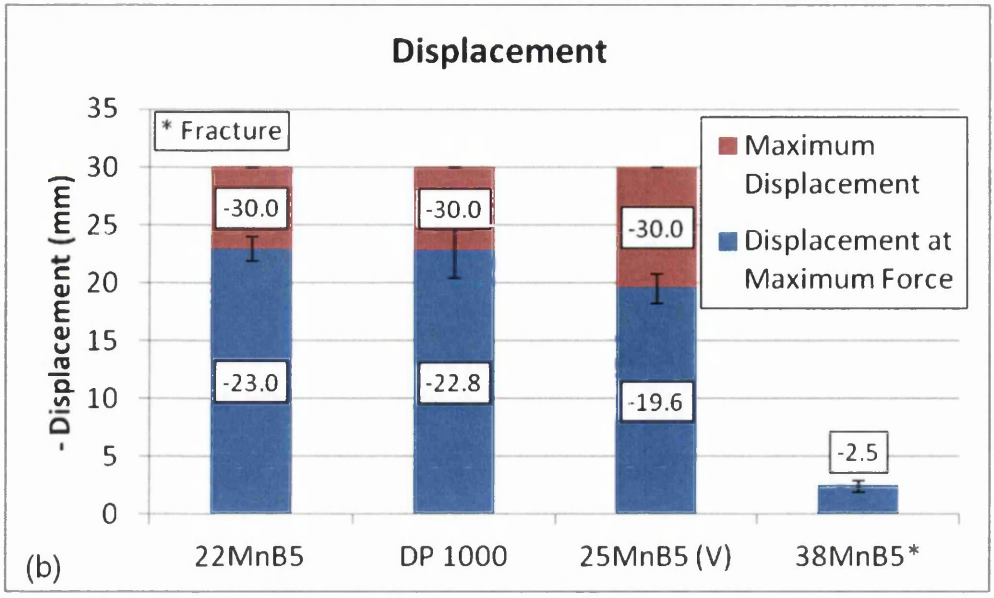


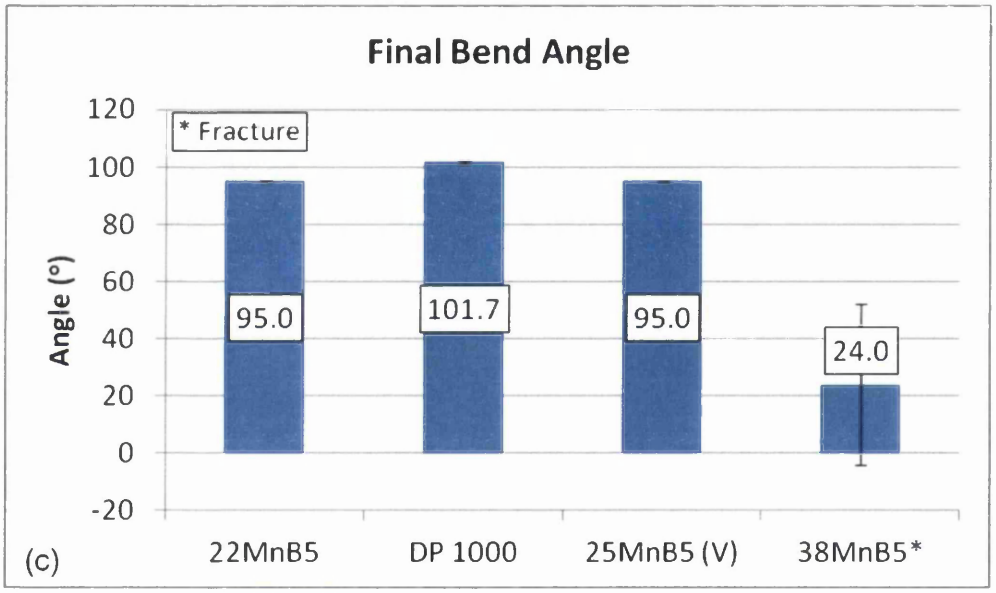


Figure 5.31: Three-point bend testing (a) maximum force (b) maximum displacement and displacement at maximum force (c) final bend angle

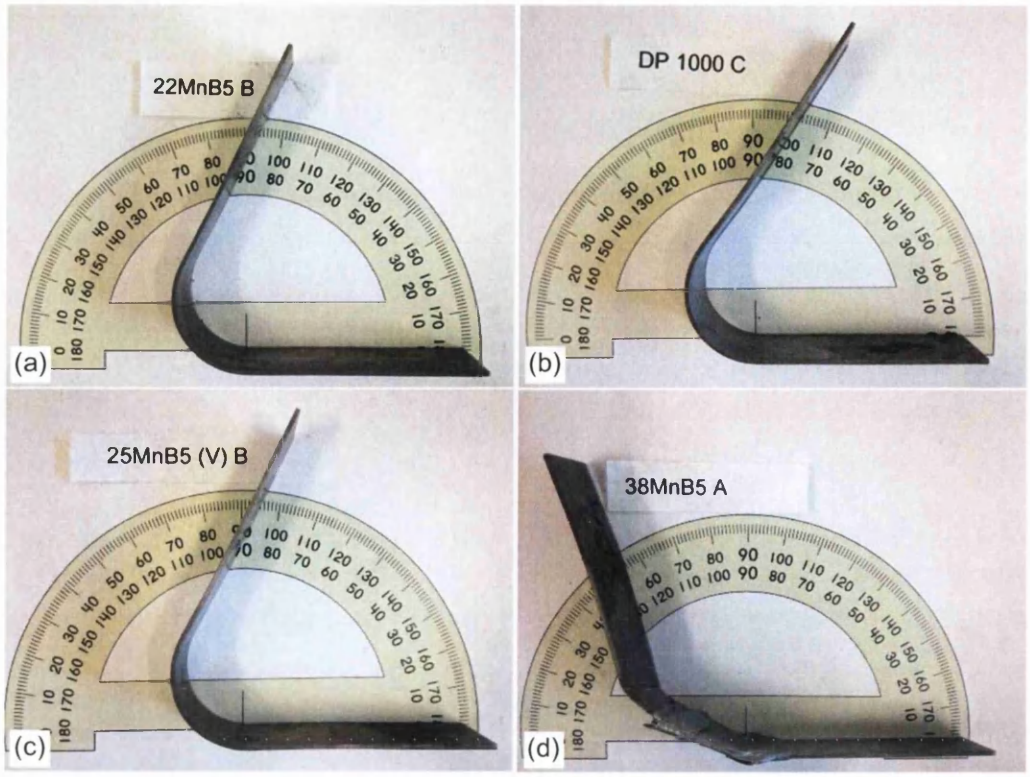


Figure 5.32: Specimens following three-point bend testing (a) 22MnB5 (b) DP 1000 (c) 25MnB5 (V) (d) 38MnB5

### *Plastic Strain*

Figures 5.33a-d present the full deformed vehicle. Figures 5.34a-d present full outer vehicle final plastic strain. Figures 5.35a-d present B-pillar reinforcement final plastic strain. Although subtle, decreasing plastic strain from DP 1000, to 22MnB5, to 25MnB5 (V) and to 38MnB5 is apparent. This reflects displacement, internal energy and material tensile strength-elongation trends discussed below.

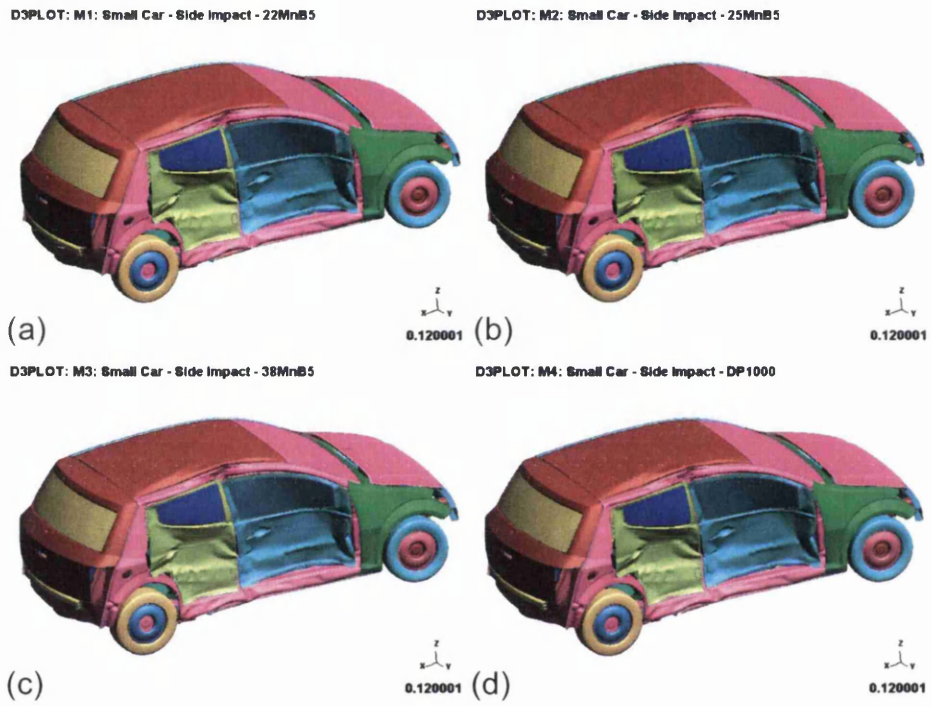


Figure 5.33: Full deformed vehicle (a) 22MnB5 (b) 25MnB5 (V) (c) 38MnB5 (d) DP 1000

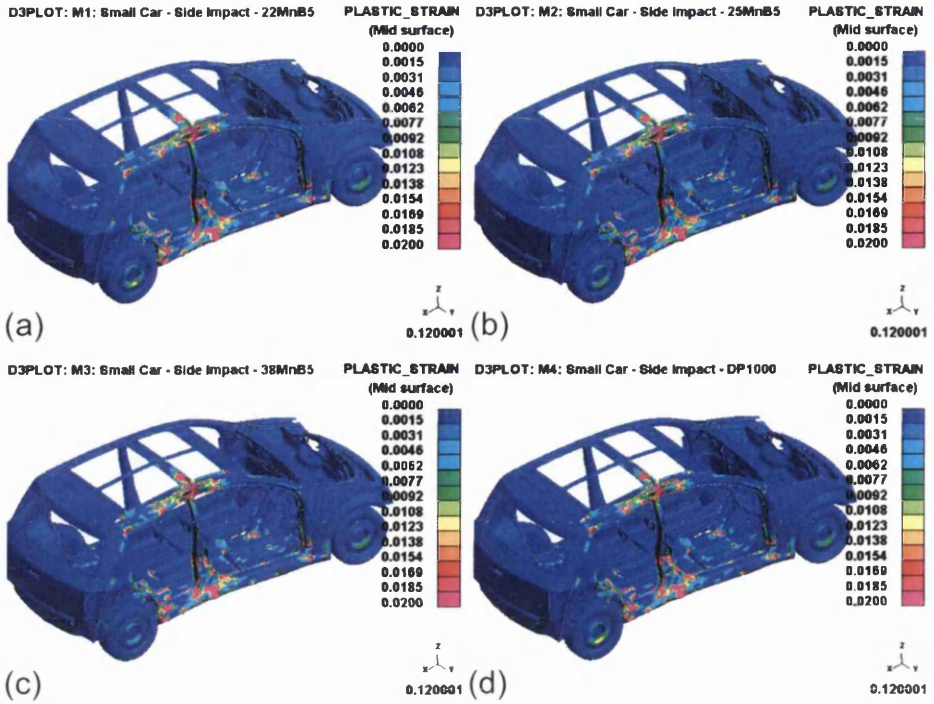


Figure 5.34: Full outer vehicle final plastic strain (a) 22MnB5 (b) 25MnB5 (V) (c) 38MnB5 (d) DP 1000

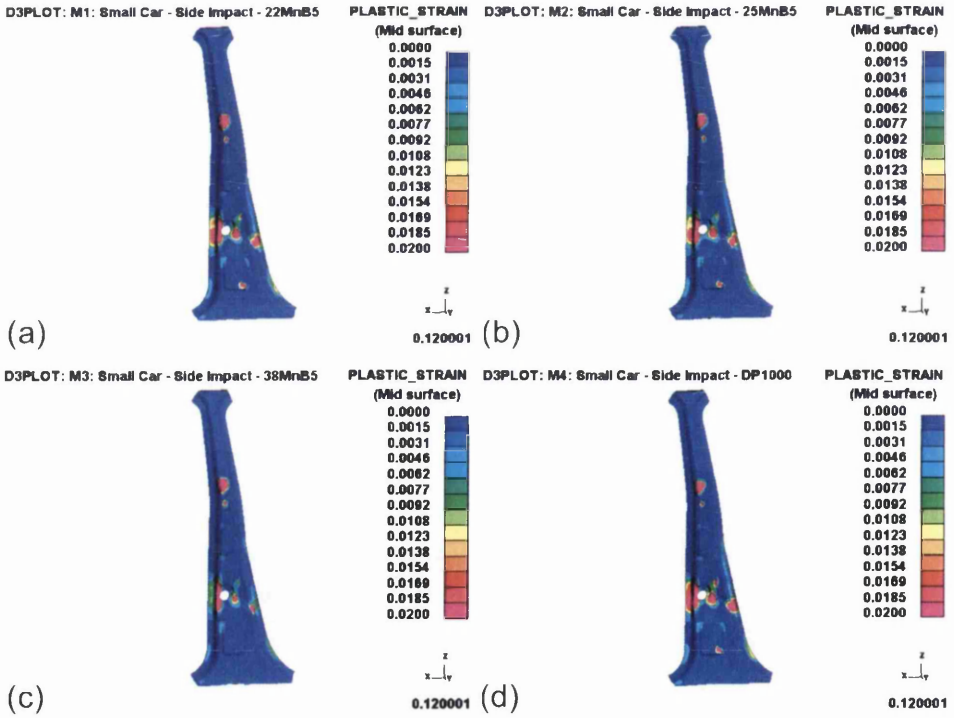


Figure 5.35: B-pillar reinforcement final plastic strain (a) 22MnB5 (b) 25MnB5 (V) (c) 38MnB5 (d) DP 1000

***Displacement***

Figures 5.36a-d present full vehicle final displacement. While discrepancies between the four grades are difficult to distinguish from these figures, Figures 5.37a-d present final displacement of the cross-section immediately behind the B-pillar, which clearly depict decreasing displacement of the B-pillar reinforcement from 22MnB5, to 25MnB5 (V) and to 38MnB5.

Figure 5.38a presents impact time against central B-pillar reinforcement displacement. This figure clearly depicts decreasing displacement from DP 1000, to 22MnB5, to 25MnB5 (V) and to 38MnB5. Figure 5.38b presents central B-pillar reinforcement final displacement against material (true) ultimate tensile strength ($R_m$), from which the above trend is highlighted even more clearly (note that in Figure 5.38b, displacement has been plotted as absolute positive values in order to facilitate appreciation of the following inverse relationship). Moreover, a consistent inverse correlation is apparent between displacement and ultimate tensile strength i.e. the highest ultimate tensile strength of 38MnB5 resulted in the smallest displacement and thus, the best anti-intrusive crash performance. Quantitatively, 38MnB5 resulted in 11 mm less displacement than 22MnB5.

From further analysis of Figure 5.38b, the following approximate relationship was found with a simple linear fit: $R_m = -31.991 \times displacement + 8198.7$. It can be calculated that to achieve a 10 % reduction to displacement, an increase to ultimate tensile strength of ~ 669 MPa is necessary.

Figure 5.39 presents impact time against front door displacement. This figure illustrates the affect that the experimental grades applied to the B-pillar reinforcement, has on displacement of adjacent components. Although subtle with just 3 mm difference in final displacement between 38MnB5 and 22MnB5, the trend of decreasing displacement from DP 1000, to 22MnB5, to 25MnB5 (V) and to 38MnB5 is again apparent.

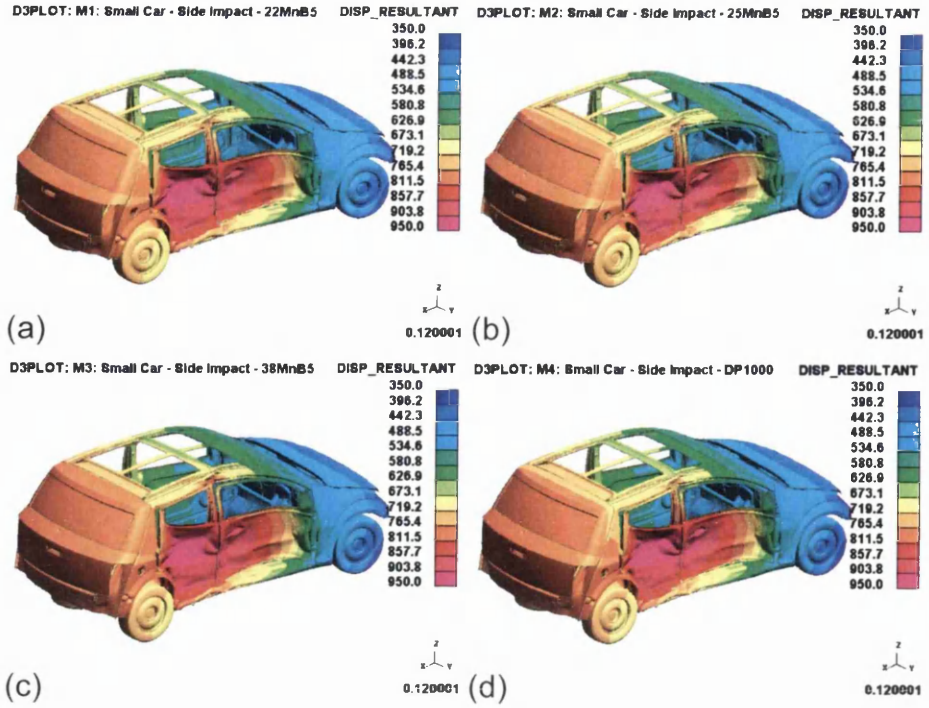


Figure 5.36: Full vehicle final displacement (a) 22MnB5 (b) 25MnB5 (V) (c) 38MnB5 (d) DP 1000

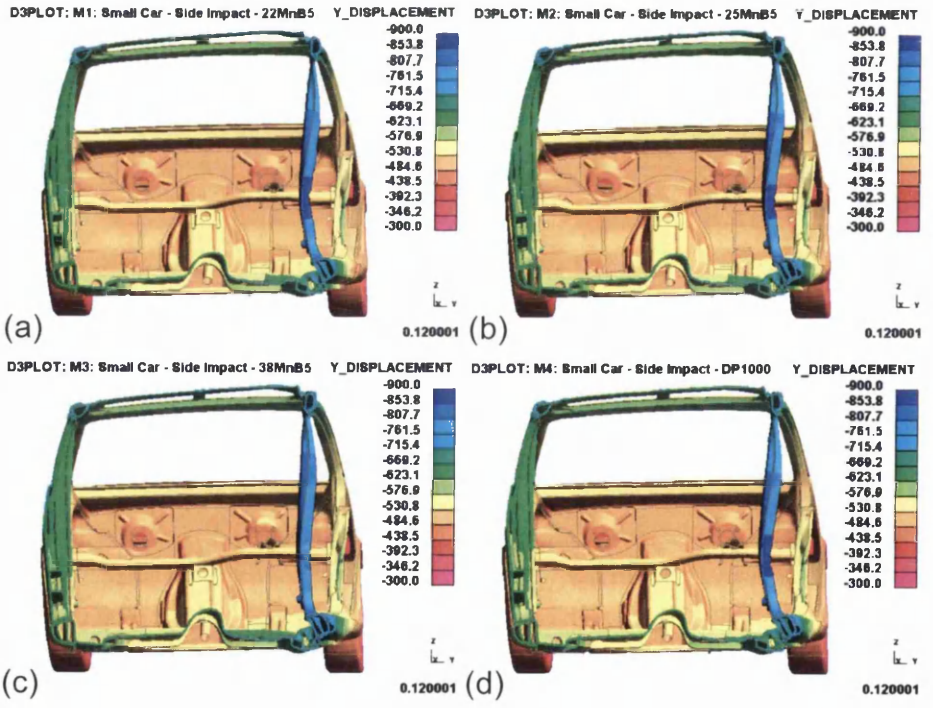


Figure 5.37: Final displacement of cross-section immediately behind B-pillar (a) 22MnB5 (b) 25MnB5 (V) (c) 38MnB5 (d) DP 1000

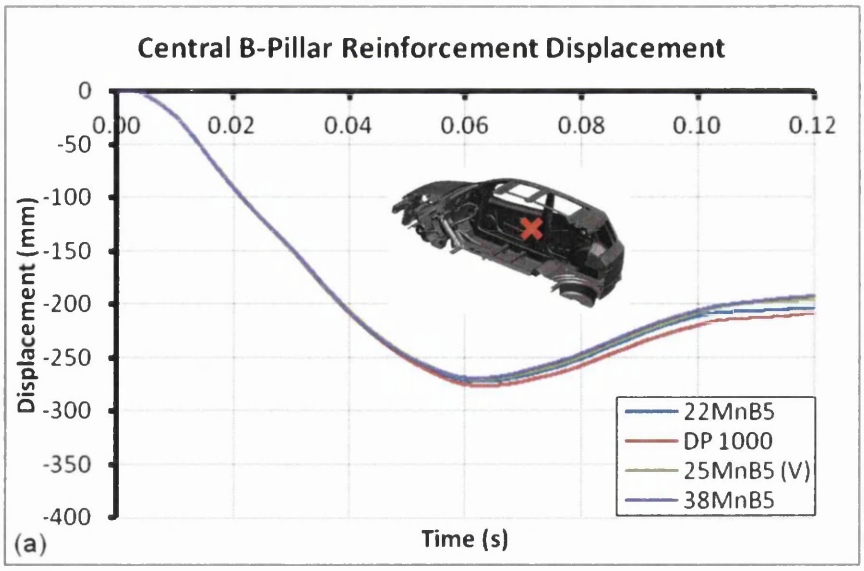


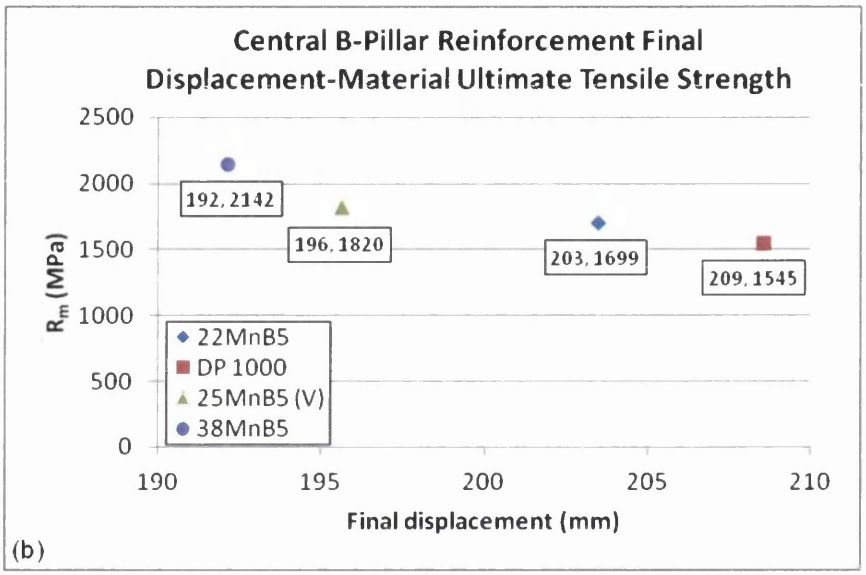


Figure 5.38: Central B-pillar reinforcement (a) impact time-displacement (b) final displacement-material ultimate tensile strength

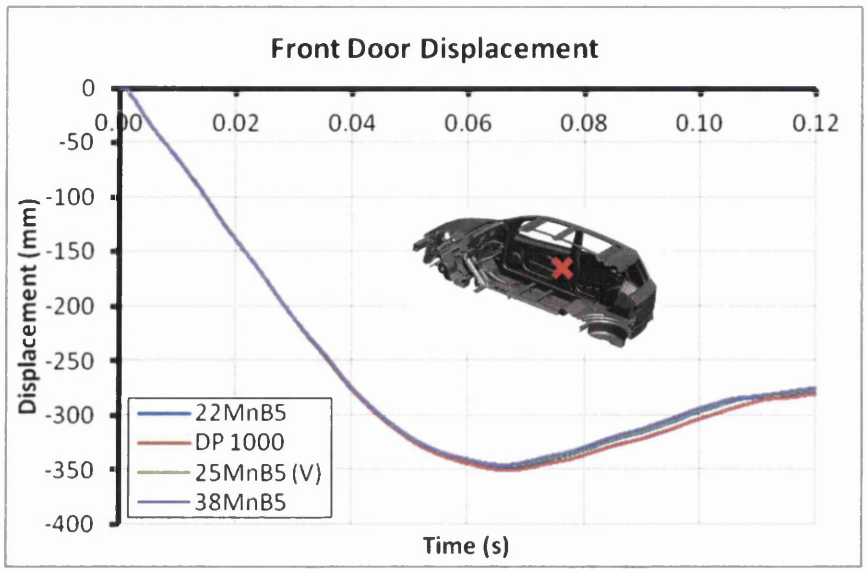


Figure 5.39: Impact time-front door displacement

***Internal Energy***

Figures 5.40a-d present full outer vehicle final internal energy. While discrepancies between the four grades are difficult to distinguish from these figures, Figures 5.41a-d present lower B-pillar reinforcement maximum internal energy, which clearly depict increasing internal energy from 38MnB5, to 25MnB5 (V), to 22MnB5 and to DP 1000.

Figure 5.42a presents impact time against B-pillar reinforcement internal energy. Although the purpose of the B-pillar reinforcement is to provide anti-intrusive crash performance rather than impact energy absorptive crash performance, the results can be considered for their value in an alternative, impact energy absorptive component that has the purpose of providing impact energy absorptive crash performance. Figure 5.42a clearly depicts increasing internal energy from 38MnB5, to 25MnB5 (V), to 22MnB5 and to DP 1000. Figure 5.41b presents B-pillar reinforcement maximum internal energy against material total (plastic) elongation ($A_{50}$), from which the above trend is highlighted even more clearly. Moreover, a general positive correlation is apparent between internal energy and total elongation i.e. the highest total elongation of DP 1000 resulted in the highest internal energy and thus, the best impact energy absorptive crash performance. Quantitatively, DP 1000 resulted in 0.04 kJ greater maximum internal energy and 0.15 kJ greater final internal energy than 22MnB5.

From further analysis of Figure 5.42b, the following approximate relationship was found with a simple linear fit: $A_{50}$ = *34.65* × *internal energy - 34.443*. It can be calculated that to achieve a 10 % increase to internal energy, an increase to total elongation of ~ 3.8 % (ε = 0.038) is necessary given a constant ultimate tensile strength of 1844 MPa.

Figures 5.43 and 5.44 present impact time against rear seat cross member internal energy and inner bodyside reinforcement internal energy. These figures illustrate the affect that the experimental grades applied to the B-pillar reinforcement, has on internal energy of adjacent components. The application of higher tensile strength grades to the B-pillar reinforcement resulted in greater internal energy in the rear seat cross member (Figure 5.45) and the inner bodyside reinforcement. In other words, these components were required to absorb more impact energy, since the higher tensile strength B-pillar reinforcement absorbed less impact energy.

However, in contrast to the above, the door reinforcement (Figure 5.46) demonstrated the same trend as the B-pillar reinforcement, with greater internal energy from 38MnB5, to 25MnB5 (V), to 22MnB5 and to DP 1000. This illustrates the complex interactions between different components in a crash event.

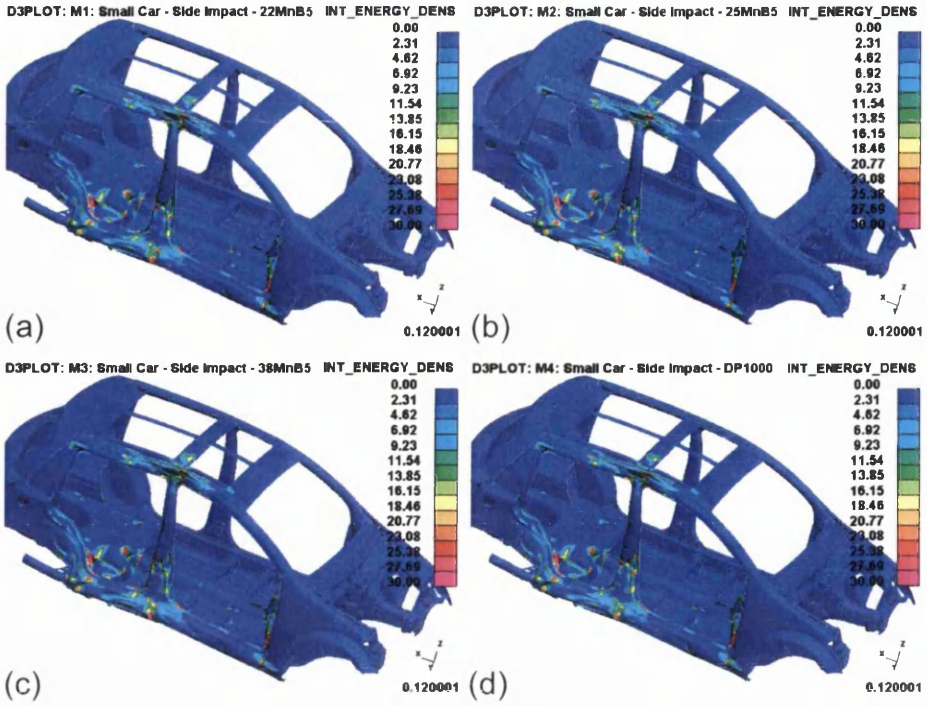


Figure 5.40: Full outer vehicle final internal energy (a) 22MnB5 (b) 25MnB5 (V) (c) 38MnB5 (d) DP 1000

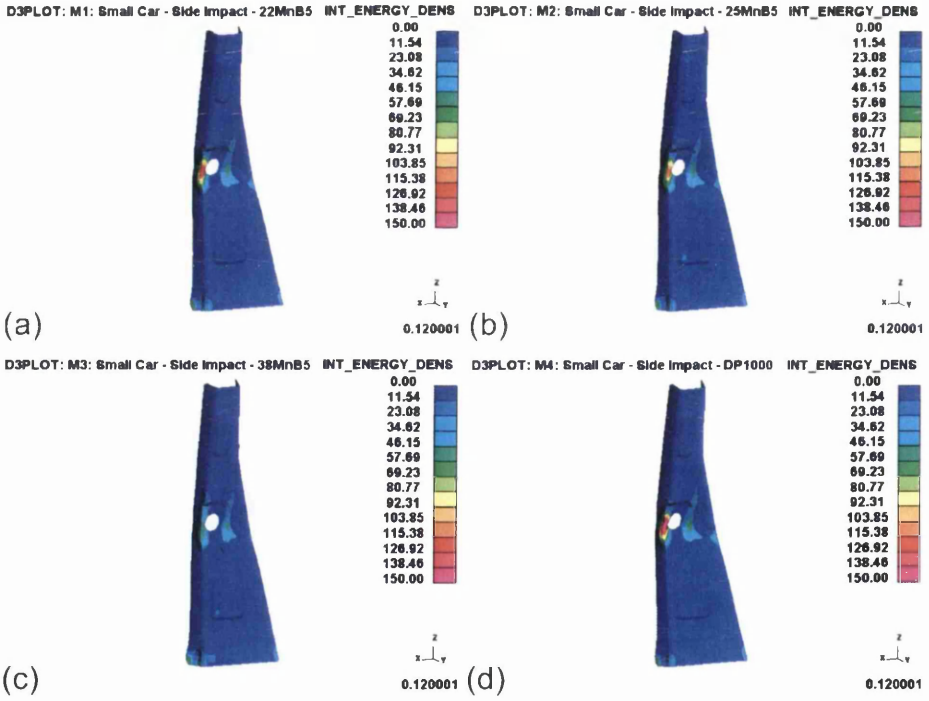


Figure 5.41: Lower B-pillar reinforcement maximum internal energy (a) 22MnB5 (b) 25MnB5 (V) (c) 38MnB5 (d) DP 1000

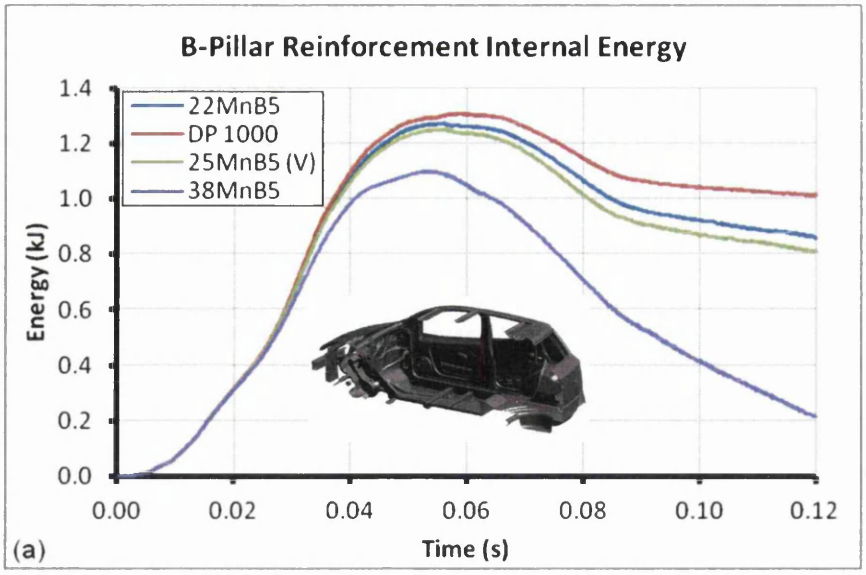


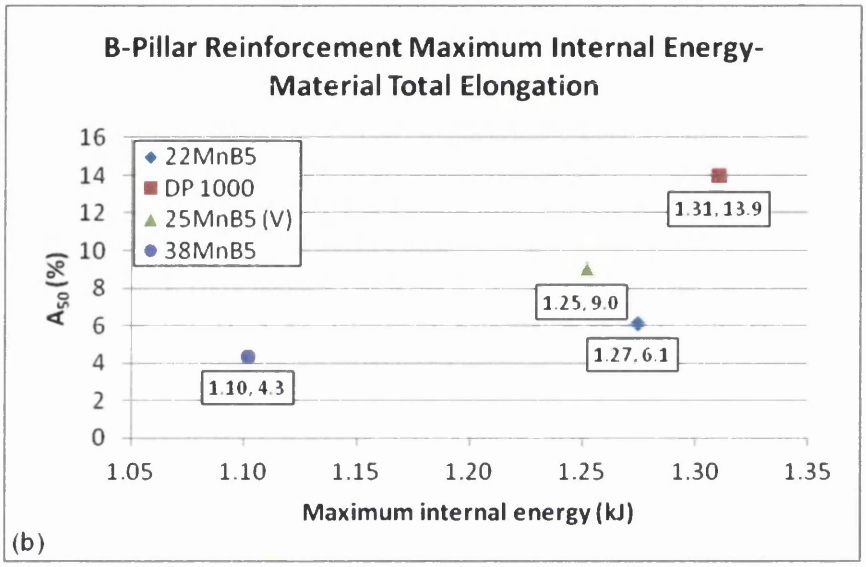


Figure 5.42: B-pillar reinforcement (a) impact time-internal energy (b) maximum internal energy-material total elongation

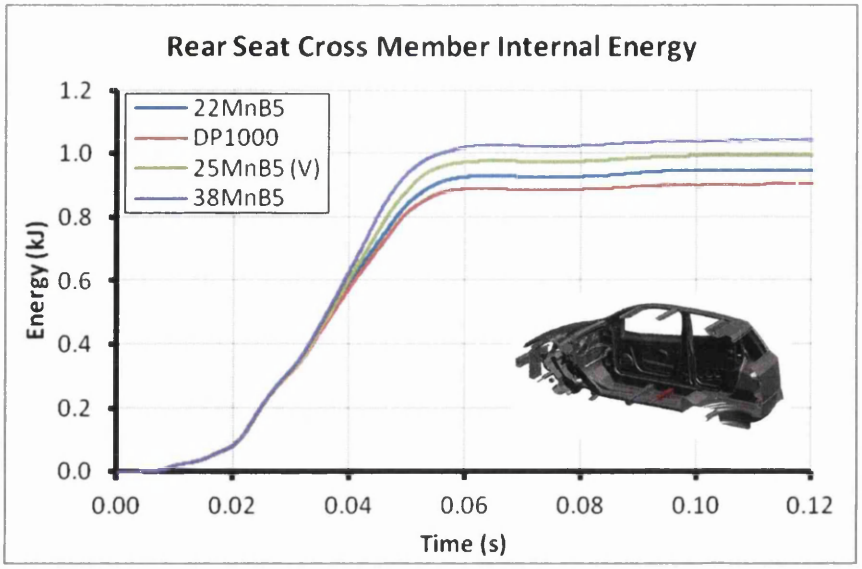


Figure 5.43: Impact time-rear seat cross member internal energy

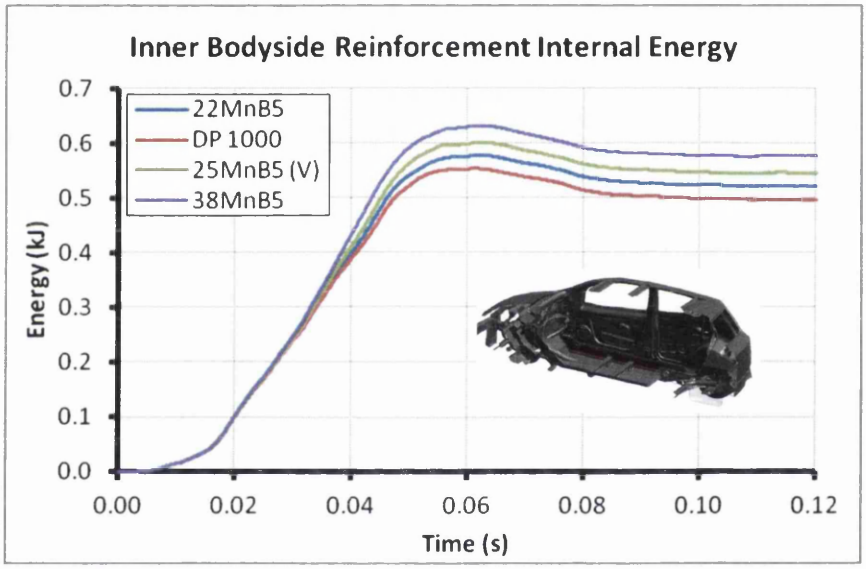


Figure 5.44: Impact time-inner bodyside reinforcement internal energy

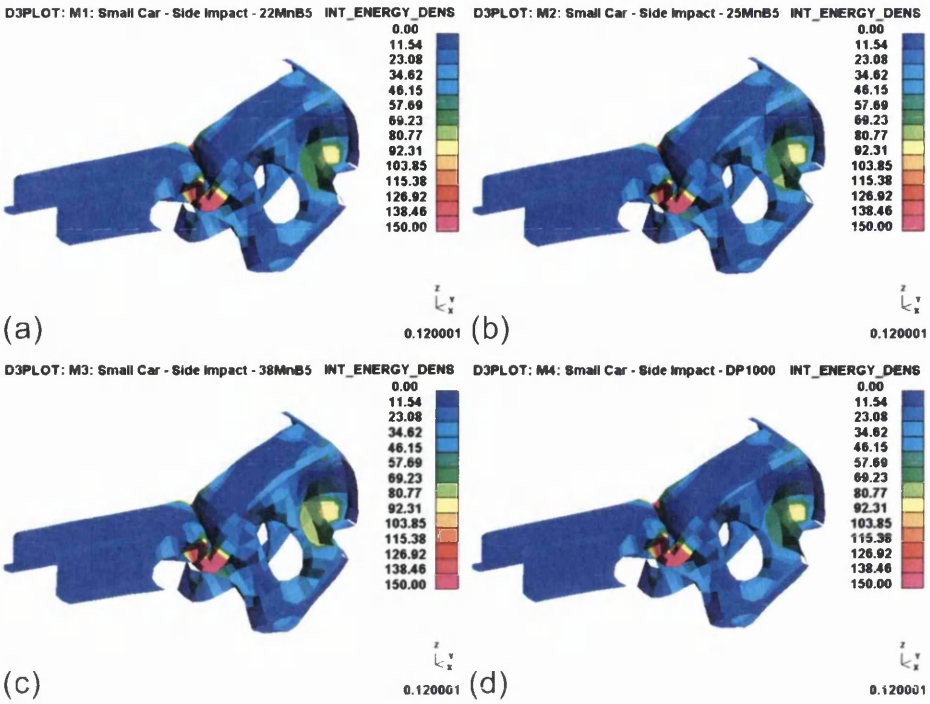


Figure 5.45: Rear seat cross member maximum internal energy (a) 22MnB5 (b) 25MnB5 (V) (c) 38MnB5 (d) DP 1000

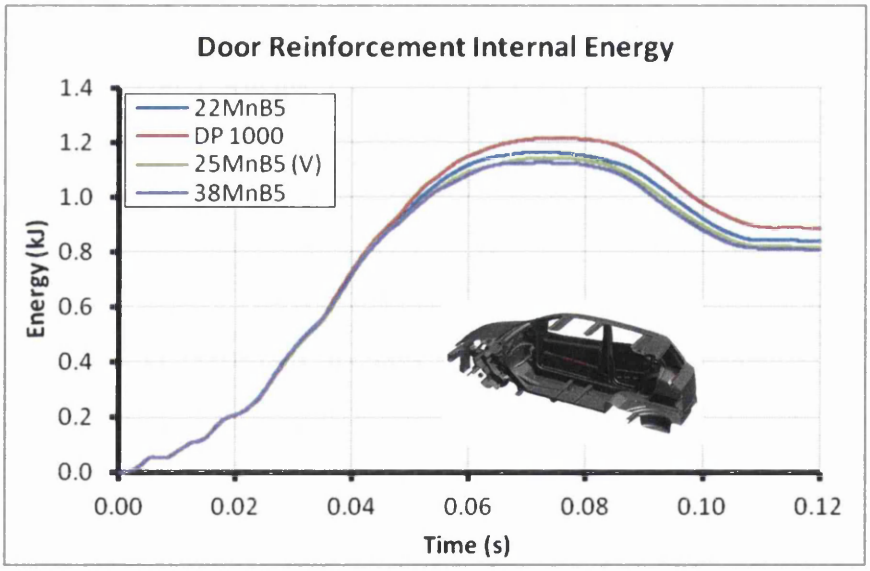


Figure 5.46: Impact time-door reinforcement internal energy

***38MnB5 Down Gauging***

Given the superior anti-intrusive crash performance demonstrated by 38MnB5, down gauging opportunities were investigated with B-pillar reinforcement thicknesses of 1.4 and 1.2 mm, in addition to the original thickness of 1.6 mm.

Figures 5.47a-d present final displacement of the cross-section immediately behind the B-pillar: 1.4 mm 38MnB5 resulted in similar displacement as 1.6 mm 22MnB5.

Figure 5.48 presents impact time against central B-pillar reinforcement displacement. This figure clearly illustrates that 1.4 mm 38MnB5 resulted in similar displacement as 1.6 mm 22MnB5.

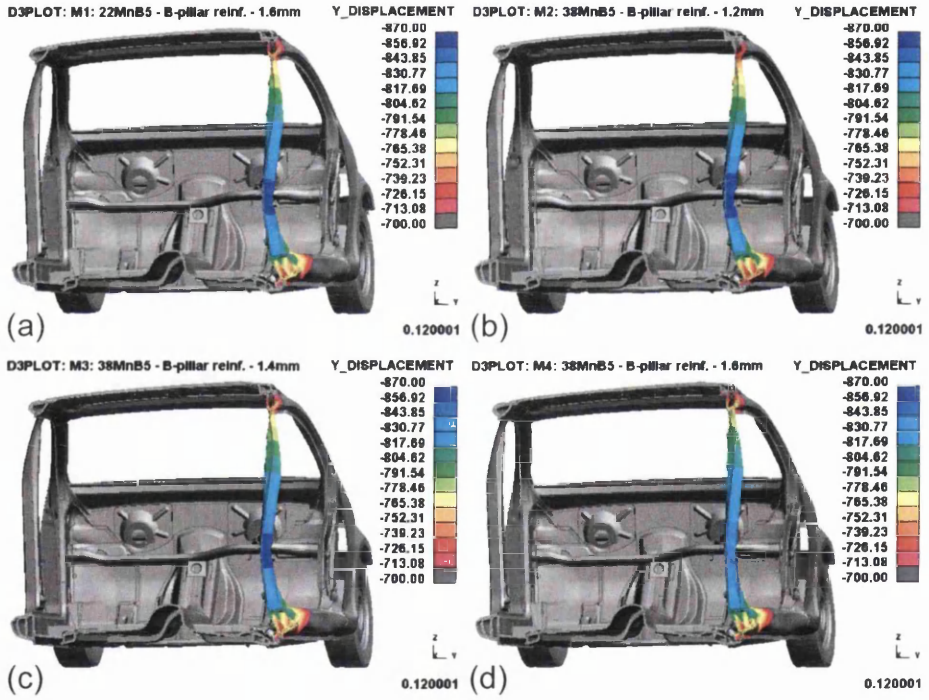


Figure 5.47: Final displacement of cross-section immediately behind B-pillar (a) 22MnB5 – 1.6 mm (b) 38MnB5 – 1.2 mm (c) 38MnB5 – 1.4 mm (d) 38MnB5 – 1.6 mm

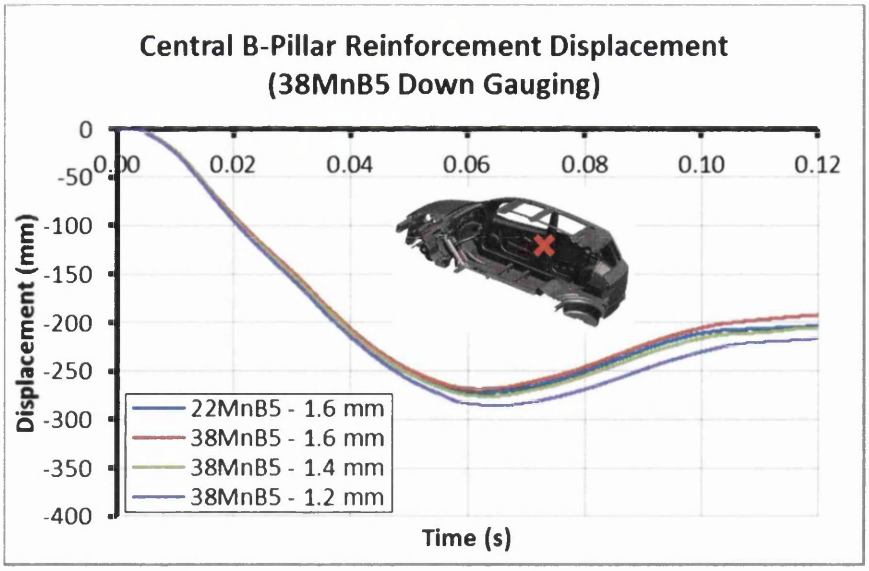


Figure 5.48: Impact time-central B-pillar reinforcement displacement (38MnB5 down gauging)

# CONCLUSIONS

The overall objective of the research reported in this thesis was to develop novel grades for automotive hot stamping technologies that demonstrated novel mechanical properties following hot stamping. Broadly, these properties were divided into three categories: 1) higher tensile strength; 2) higher elongation; and 3) higher tensile strength-higher elongation, compared to 22MnB5. These properties would fill the ultimate tensile strength-total elongation range targeted by the steel and automotive industries. Within the overall research objective of developing novel grades for automotive hot stamping technologies, key sub-objectives of the research included laboratory hot stamping with ten experimental grades in addition to the 22MnB5 control grade; characterisation of the dynamic tensile properties of hot stamped steels; and characterisation of the automotive crash performance of hot stamped steels via FEM crash simulation. These last two sub-objectives represented completely novel research that was not available in the literature.

Conclusions to be drawn from laboratory hot stamping can be listed as follows:

- The DP steels, especially DP 1000, were considered advantageous for impact energy absorptive crash performance, providing lower proof strength, substantially higher uniform elongation and total elongation, yet with a relatively small loss to ultimate tensile strength compared to 22MnB5. DP 1000 met the higher elongation objective.
- The tensile properties of all three DP steels compared favourably to those of ArcelorMittal's Ductibor 1000 and Ductibor 1300 grades, Benteler's EP 1881083-A1 grade and Yi et al's DP-PF grade reported in the literature. For example, compared to ArcelorMittal's Ductibor 1000, hot stamped DP 1000 provided 104 MPa higher proof strength, 132 MPa higher ultimate tensile strength and 7.3 % higher total elongation.
- The DP steels were considered to offer potential application to alternative, impact energy absorptive structural body components, that thus far have been eluded from hot stamped boron steels.

- Each of the hot stamped DP steels provided higher ultimate tensile strength, yet similar (or even higher) total elongation compared to its as-delivered condition.
- Owing to superior weldability of the DP steels compared to 22MnB5, potential use in the hot stamped tailor welded blank concept was highlighted.
- Compared to 22MnB5, the combined carbon and vanadium addition of 25MnB5 (V) provided higher proof strength, higher ultimate tensile strength and higher total elongation. 25MnB5 (V) met the higher tensile strength-higher elongation objective.
- It was apparent that vanadium is beneficial to elongation when dissolved in solid solution. Similar benefits were also found from molybdenum and nickel additions.
- The tensile properties of all three grades 25MnB5 (Mo), 25MnB5 (V) and 25MnB5 (Ni) compared favourably to those of Naderi et al's hot stamped and tempered 37MnB4 grade and Benteler's EP 1881083-A1 grade reported in the literature. For example, compared to Benteler's EP 1881083-A1, hot stamped 25MnB5 (V) provided 484 MPa higher ultimate tensile strength and 3.0 % higher total elongation.
- Compared to 22MnB5, the significantly higher carbon content of 38MnB5 provided higher proof strength and higher ultimate tensile strength, yet with similar total elongation. 38MnB5 met the higher tensile strength objective.
- The tensile properties of 38MnB5 compared favourably to those of ThyssenKrupp's MBW 1900 grade reported in the literature, providing 166 MPa higher ultimate tensile strength and 2.2 % higher total elongation.
- 38MnB5 was considered to offer significant down gauging and weight reduction opportunities to anti-intrusive structural body components.

Conclusions to be drawn from dynamic tensile testing can be listed as follows:

- Each grade selected for dynamic tensile testing, namely 22MnB5, 38MnB5, DP 1000 and 25MnB5 (V), generally demonstrated positive strain rate sensitivity with increasing strain rate from 0.001 to 1 $s^{-1}$, but negative strain rate sensitivity with increasing strain rate from 1 to 200 $s^{-1}$.

- Each grade generally demonstrated maximum elongation given the higher strain rates of 100 or 200 $s^{-1}$.
- The responses of the hot stamped martensitic steels to increasing strain rate were attributed to dislocation cell structure breakdown increasing dislocation density (increasing tensile strength) and adiabatic heating (decreasing tensile strength and increasing elongation).
- The adiabatic heating theory was demonstrated for 22MnB5 and 38MnB5.
- The unique response of 38MnB5 to increasing strain rate, marked by positive mean strain rate sensitivity across all four strain rates, consistently increasing ultimate tensile strength across all four strain rates and significantly higher elongation at the higher strain rates of 100 and 200 $s^{-1}$, gave rise to significantly higher energy absorption compared to 22MnB5 at the higher strain rates.
- The significantly higher elongation of 38MnB5 at the higher strain rates was attributed to the higher carbon content and in turn, greater rise of adiabatic heating. It was considered that 38MnB5 should provide superior anti-intrusive crash performance under low speed impact (owing to significantly higher tensile strength under all strain rates), yet superior impact energy absorptive crash performance under high speed impact (owing to significantly higher tensile strength, elongation and ultimately, energy absorption under the higher strain rates).

Conclusions to be drawn from FEM crash simulation can be listed as follows:

- The consistent inverse correlation was found between central B-pillar reinforcement displacement and material ultimate tensile strength. Thus, the highest ultimate tensile strength of 38MnB5 resulted in the smallest displacement and consequently, the best anti-intrusive crash performance.
- The general positive correlation was found between B-pillar reinforcement internal energy and material total elongation. Thus, the highest total elongation of DP 1000 resulted in the highest internal energy and thus, the best impact energy absorptive crash performance.
- The application of higher tensile strength grades to the B-pillar reinforcement resulted in greater internal energy in certain adjacent

components, yet less internal energy in other adjacent components. This demonstrated the demand to develop novel higher tensile strength and higher elongation grades that can be applied simultaneously throughout the body structure in order to optimise anti-intrusive crash performance and impact energy absorptive crash performance of the full vehicle.

- 38MnB5 of 1.4 mm thickness resulted in similar displacement as 22MnB5 of 1.6 mm thickness. This demonstrated down gauging opportunities resulting from the application of novel hot stamped steels exhibiting higher tensile strength.

It can be concluded that the range of novel hot stamped steels, particular 38MnB5, DP 1000 and 25MnB5 (V), provides a range of tensile properties from higher tensile strength-lower elongation, to lower tensile strength-higher elongation and even, higher tensile strength-higher elongation compared to 22MnB5, that offers significant down gauging and weight reduction opportunities to the automotive industry. Moreover, the range of properties offered by the novel hot stamped steels offers applicability to a range of automotive structural body components requiring different crash performance characteristics. Thus, the automotive industry is granted more freedom to select the material and its properties that are most fit for the intended component.

# RECOMMENDATIONS

It was found that molybdenum, nickel and especially, vanadium addition to boron steel is beneficial to tensile strength and elongation. Thus, it is recommended that molybdenum, nickel or especially, vanadium modified boron steels are commercialised and marketed for automotive hot stamping technologies. Indeed, Tata Steel is planning an industrial trial of molybdenum modified boron steel in collaboration with automotive component manufacturer Benteler. However, explanation behind the elongation gain arising from molybdenum, nickel or vanadium addition is unclear. Thus, further investigation, particularly focusing on intermetallic compound phenomena with transmission electron microscopy, is recommended.

It was found that 38MnB5 provided significantly higher tensile strength than 22MnB5, yet with comparable elongation. Moreover, 38MnB5 demonstrated significantly higher elongation at higher strain rates. However, 38MnB5 performed poorly during three-point bend testing. Thus, further investigation into bending behaviour, particularly of 25MnB5 and 29MnB5 with intermediate carbon contents between 22MnB5 and 38MnB5, is recommended. Additionally, the highlighted benefits of 38MnB5 are purely from an academic perspective. For the highlighted benefits to be translated into industry, manufacturing constraints must be overcome, namely cold rolling to a thickness below 1.5 mm and achievement of customer as-delivered maximum tensile strength specifications. Both of these manufacturing constraints are made more severe by the higher tensile strength intrinsic to 38MnB5. Moreover, weldability of the final hot stamped component is also worthy of consideration. Thus, assessment of manufacturing feasibility and weldability is recommended.

It was found that the DP steels are highly suited to automotive hot stamping technologies, for numerous reasons. Thus, it is recommended that the DP steels are marketed for automotive hot stamping technologies, specifically for application to impact energy absorptive structural body components and the tailor welded blank concept. Indeed, Tata Steel is in the process of doing this.

# REFERENCES


[1] 'Advanced high strength steels (AHSS) application guidelines version 4.1', 2009, WorldAutoSteel (e-book available from http://309fbf2c62e8221fbaf0-b80c17cbaf20104b072d586b316c6210.r88.cf1.rackcdn.com/AHSS_Application_Guidelines_4-1June2009.pdf).

[2] '2nd International conference automotive steels 2013', Automotive Steels 2013, http://www.automotive-steels.com/Default.aspx (cited 16 09 2013).

[3] S. Oliver: 'Development and dynamic performance of high strength and advanced high strength strip steels', EngD thesis, University of Wales Swansea, UK, 2007.

[4] 'Reducing CO2 emissions from passenger cars', European Commission, http://ec.europa.eu/clima/policies/transport/vehicles/cars/index_en.htm (cited 18 09 2013).

[5] 'Calculate vehicle tax rates', GOV.UK, https://www.gov.uk/calculate-vehicle-tax-rates (cited 14 10 2013).

[6] M. Kleiner, M. Geiger and A. Klaus: 'Manufacturing of lightweight components by metal forming', Annals of the CIRP, 2003, 52, 521-542.

[7] J. Yanagimoto and K. Ikeuchi: 'Sheet forming process of carbon fibre reinforced plastics for lightweight parts', CIRP Annals – Manufacturing Technology, 2012, 61, 247-250.

[8] A. Clough: Tata Steel, Warwick, UK, personal communication, 28 03 2012.

[9] 'BMW carbon fibre car launch attracts rivals' attention', BBC News, http://www.bbc.co.uk/news/business-14550710 (cited 10 09 2011).

[10] C. M. Tamarelli: 'AHSS 101: the evolving use of advanced high strength steels for automotive applications', 2011, AUTOSTEEL (e-book available from http://www.autosteel.org/en/sitecore/content/Global/Document%20Types/News/2012/~/media/Files/Autosteel/Research/AHSS/AHSS%20101%20-%20The%20Evolving%20Use%20of%20Advanced%20High-Strength%20Steels%20for%20Automotive%20Applications%20-%20Ir.ashx).

[11] W. D. Callister: 'Materials science and engineering an introduction', 2003, New York, John Wiley & Sons.

[12] D. F. Gordon: Tata Steel, Port Talbot, UK, personal communication, 02 07 2010.

[13] T. B. Jones: Tata Steel, Port Talbot, UK, personal communication, 02 07 2010.

[14] ArcelorMittal: 'Usibor 1500P and hot stamping', AP&T Press Hardening Seminar, Paris, France, 2009, presentation.

[15] M. Naderi: 'Hot stamping of ultrahigh strength steels', PhD thesis, Aachen University, Germany, 2007.

[16] E. Billur and T. Altan: 'Hot stamping of boron steels: progress, state of technology and simulations', Workshop on Advanced Sheet Metal Forming and Stamping Technology, Ohio, USA, 2012, presentation (available from http://nsmwww.eng.ohio-state.edu/2012-11_Hot_Stamping_No_Video.pdf).

[17] A. Clough: 'Boron steel developments at EuroCarBody 2012', Report No. 156313, Tata Steel, Warwick, UK, 2012.

[18] G. Bergland: 'The history of hardening of boron steel in northern Sweden', 1st International Conference on Hot Sheet Metal Forming of High-Performance Steel, Kassel, Germany, 2008, 175-177.

[19] J. Aspacher: 'AHSS capacity on rise', Wards Auto, http://wardsauto.com/ar/ahss_capacity_rise_110909 (cited 12 07 13).

[20] ArcelorMittal: 'Hot stamping with USIBOR1500P', AP&T Advanced Hot Stamping Seminar, Detroit, USA, 2010, presentation.

[21] C. E. Ridderstrale, Norrbottens Järnverk AB: 'Manufacturing a hardened steel article', UK Patent 1490535-A, Sweden, filed 06 11 1973.

[22] 'Saab 9000', New Cars Models, http://www.newcarsmodels.com/2010/03/1992-saab-9000.html (cited 15 03 2011).

[23] H. Karbasian and A. E. Tekkaya: 'A review on hot stamping', Journal of Materials Processing Technology, 2010, 210, 2103-2118.

[24] M. Naderi, M. Ketabchi and M. Abbasi: 'Analysis of microstructure and mechanical properties of different hot stamped B-bearing steels', Steel Research International, 2010, 81, 1-17.

[25] M. Abbasi, M. Naderi and A. Saeed-Akbari: 'Isothermal versus non-isothermal hot compression process: a comparative study on phase transformations and structure–property relationships', Materials & Design, 2013, 45, 1-5.

[26] M. Abbasi, A. Saeed-Akbari and M. Naderi: 'The effect of strain rate and deformation temperature on the characteristics of isothermally hot compressed boron-alloyed steel', Materials Science and Engineering A, 2012, 538, 356-363.

[27] M. Naderi, M. Ketabchi, M. Abbasi and W. Bleck: 'Analysis of microstructure and mechanical properties of different boron and non-boron alloyed steels after being hot stamped', Procedia Engineering, 2011, 10, 460-465.

[28] M. Naderi, M. Ketabchi, M. Abbasi and W. Bleck: 'Semi-hot stamping as an improved process of hot stamping', Journal of Materials Science and Technology, 2007, 27, 369-376.

[29] M. Nikravesh, M. Naderi and G. H. Akban: 'Influence of hot plastic deformation and cooling rate on martensite and bainite start temperatures in 22MnB5 steel', Materials Science and Engineering A, 2012, 540, 24-29.

[30] M. Naderi, A. Saeed-Akbari and W. Bleck: 'The effects of non-isothermal deformation on martensitic transformation in 22MnB5 steel', Materials Science and Engineering A, 2008, 487, 445-455.

[31] G. Hensen: 'Handbook for tailor made mechanical properties through hot forming, hot forming product and process parameters', Report No. 136693, Corus, Ijmuiden, The Netherlands, 2009.

[32] F. J. Lenze, S. Sikora, J. Banik and O. Straube: 'Hot forming - new potentials for innovative manufacturing', Steel Grips: Journal of Steel and Related Materials, 2009, 6, 427-432.

[33] F. L. G. Oliveira, M. S. Andrade and A. B. Cota: 'Kinetics of austenite formation during continuous heating in a low carbon steel', Materials Characterization, 2007, 58, 256-261.

[34] K. Yamazaki: 'Current situation and properties of ultrahigh strength steel for automotive use in Japan', La Revue de Metallurgie, 2003, 100, 779-786.

[35] J. Tungtrongpairoj, V. Uthaisangsuk and W. Bleck: 'Determination of yield behaviour of boron alloy steel at high temperature', Journal of Metals, Materials and Minerals, 2009, 19, 29-38.

[36] J. Yanagimoto, K. Oyamada and T. Nakagawa: 'Springback of high-strength steel after hot and warm sheet formings', CIRP Annals – Manufacturing Technology, 2005, 54, 213-216.

[37] J. Yanagimoto and K. Oyamada: 'Mechanism of springback-free bending of high-strength steel sheets under warm forming conditions', CIRP Annals – Manufacturing Technology, 2007, 56, 265-268.

[38] K. Kusumi, S. Yamamoto, T. Takeshita and M. Abe: 'The effect of martensitic transformation on the spring-back behaviour of the hot stamping', Proceedings of 2nd International Conference of Hot Sheet Metal Forming of High-Performance Steel, Lulea, Sweden, 2009, 97-104.

[39] E. C. Bain: 'The alloying elements in steel', 1939, Pittsburgh, ASM International.

[40] M. Kiani, I. Gandikota, A. Parrish, K. Motoyama and M. Rais-Rohani: 'Surrogate-based optimisation of automotive structures under multiple crash and vibration design criteria', International Journal of Crashworthiness, 2013, 18, 473-482.

[41] K. Adams: 'Pocket book of steel', 2007, Corus Automotive (e-book available from http://www.tatasteelautomotive.com/file_source/StaticFiles/Microsites/Automotive/Publications/Book%20of%20steel/Book%20of%20Steel%203rd%20Ed_lowres.pdf).

[42] 'The car body inner construction', Auto Repair, http://www.auto-maintenance-repair.com/r/Inner-construction.html (cited 12 08 2010).

[43] '2011 Mercedes Benz E-Class wagon body structure', boronextrication, http://boronextrication.com/2011/02/2011-mercedes-benze-e-class-wagon-body-structure/ (cited 06 06 2011).

[44] 'Béla Barényi and the discovery of passive safety', Daimler, http://media.daimler.com/dcmedia/0-921-657486-1-862061-1-0-0-0-0-0-11702-614318-0-1-0-0-0-0-0.html (cited 22 10 2013).

[45] '2011 Ford Fiesta boron body cage', boronextrication, http://boronextrication.com/2010/06/2011-ford-fiesta-boron-body-cage/ (cited 06 06 2011).

[46] 'Steels for hot stamping', ArcelorMittal, http://www.arcelormittal.com/automotive/sheets/catalogue.pl?id_sheet=E&header=&language=EN (cited 13 07 2010).

[47] 'ThyssenKrupp tailored blanks', ThyssenKrupp, http://www.tailored-blanks.com/en/group/a-story-of-success.html (cited 22 05 2013).

[48] 'BMW X5 B-pillar UHSS', boronextrication, http://boronextrication.com/2009/09/bmw-x5-b-pillar-uhss-where-would-you-make-your-cut/ (cited 06 06 2010).

[49] R. Kolleck: 'Press hardening process of boron steel sheets', Auto Focus Asia, http://www.autofocusasia.com/automotive_materials/press_hardening_boron_steel.htm (cited 14 07 2010).

[50] 'Upcoming MQB-platform Volkswagen Golf to be VW's most important launch yet', I Motor Times, http://www.imotortimes.com/articles/1991/20120822/upcoming-mqb-platform-volkswagen-golf-vws-important.htm (cited 26 03 2013).

[51] 'Results released in 2012', EURO NCAP, http://www.euroncap.com/results/2012.aspx (cited 20 05 2013).

[52] 'Steel glossary', American Iron and Steel Institute, http://www.steel.org/AM/Template.cfm?Section=Steel_Glossary&Template=/CM/HTMLDisplay.cfm&ContentID=26163 (cited 21 05 2010).

[53] A. Mejía, C. Bedolla-Jacuinde, J. M. Maldonado and C. Cabrera: 'Hot ductility behaviour of a low carbon advanced high strength steel (AHSS) microalloyed with boron', Materials Science and Engineering A, 2011, 528, 4468-4474.

[54] G. Fourlaris: 'Year 3 lecture notes: physical metallurgy of steels EG-392', University of Wales Swansea, UK, 2006.

[55] V. F. Aaronson and H. I. Zackay: 'Decomposition of austenite by diffusional processes', 1962, Philadelphia, Interscience Publishers.

[56] H. K. D. H. Bhadeshia: 'Bainite in steels', 2001, Cambridge, Institute of Materials.

[57] C. A. Dubé: 'Title not provided', PhD thesis, Carnegie Institute of Technology, USA, 1948.

[58] E. R. Petty: 'Martensite: fundamentals and technology', 1970, London, Longman Group Limited.

[59] H. K. D. H. Bhadeshia: 'The Bain correspondence', University of Cambridge, http://www.msm.cam.ac.uk/phasetrans/2003/Lattices/bain.html (cited 12 06 2010).

[60] P. Evans, A. Gater and A. Brown: '22MnB5 boron hot pressing steel development', Report No. not provided, Corus, Port Talbot, UK, 2010.

[61] M. Maikranz-Valentin, N. Saba, U. Weidig, R. Weißner and K. Steinhoff: 'Hot forming of work hardened steel', Steel GRIPS, 2008, 6, 191-198.

[62] M. Blair and T. L. Stevens: 'Steel castings handbook', 1995, Ohio, ASM International.

[63] B. K. Agrawal: 'Introduction to engineering materials', 1988, New Delhi, Tata McGraw-Hill Education.

[64] R. Abbaschian, L. Abbaschian and R. E. Reed-Hill: 'Physical metallurgy principles', 2009, Michigan, Cengage Learning.

[65] 'Effect of alloying elements on steel properties', Subs Tech, http://www.substech.com/dokuwiki/doku.php?id=effect_of_alloying_elements_on_steel_properties (cited 14 08 2010).

[66] 'Cast steel: influence of alloying elements on steel microstructure', Key to Metals, http://www.keytometals.com/articles/art50.htm (cited 12 08 2010).

[67] M. Barcellona and D. Palmeri: 'The effect of plastic hot deformation on the hardness and continuous cooling transformations of 22MnB5 microalloyed boron steel', Metallurgical and Materials Transactions A, 2009, 40A, 1160-1174.

[68] P. Evans: Tata Steel, Port Talbot, UK, personal communication, 09 01 2012.

[69] B. Qin: 'Crystallography of TWIP steels', Master's thesis, Pohang University of Science and Technology, South Korea, 2007.

[70] J. E. Morral and J. B. Cameron: 'Title not provided', Metallurgical and Materials Transactions A, 1977, 8, 1817.

[71] D. A. Mortimer and M. G. Nicholas: 'Title not provided', Material Science, 1976, 10, 326.

[72] P. Maitrepierre, D. Thivellier and R. Tricot: 'Title not provided', Metallurgical and Materials Transactions A, 1975, 6A, 287.

[73] D. Doane and J. Kirkaldy: 'Hardenability concepts with application to steel', 1978, Warrendale, The Metallurgical Society of AIME.

[74] S. Banerji and J. Morral: 'Boron in steels', 1979, Warrendale, The Metallurgical Society of AIME.

[75] P. Maitrepierre, D. Thivellier, J. Roves-Vernis, D. Rousseau and R. Tricot: 'Hardenability concepts with application to steel', 1978, Warrendale, The Metallurgical Society of AIME.

[76] C. H. Xuan, D. H. Wang, C. L. Zhang, Z. D. Han, B. X. Gu and Y. W. Du: 'Boron's effect on martensitic start temperature and magneto-caloric effect in Ni¬43Mn46Sn11Bx alloys', Applied Physics Letters, 2008, 92, pages not provided.

[77] B. C. de Cooman, J. G. Speer, I. Y. Pyshmintsev and N. Yoshinaga: 'Materials design: the key to modern steel products', 2007, Bad Harzburg, Grips Media.

[78] K. W. Andrews: 'Title not provided', Journal of Iron and Steel Institute, 1965, 203, 721-717.

[79] N. Yurioka: 'Carbon equivalents for hardenability and cold cracking susceptibility of steels', Select Conference on Hardenability of Steels, Derby, UK, 1990, paper 3.

[80] J. Dearden and H. O'Neill: 'A guide to the selection and welding of low alloy structural steel', Transactions of the Institute of Welding, 1940, 3, 203-214.

[81] 'Welding - recommendations for welding of metallic materials - part 2: arc welding of ferritic steels', EN 1011-2, British Standards Institution, 2003.

[82] 'Guideline on alternative methods for determining preheat', AWS D1.1-2010 Annex I.

[83] Y. Ito and K. Bessyo: 'Weldability formula of high strength steels related to heat affected zone cracking', International Institute of Welding, 1968, paper IX-576-68.

[84] N. Bailey: 'Factors influencing weldability - weldability of ferritic steels', 1994, Cambridge, Abington Publishing.

[85] C. F. Düren: 'Prediction of hardness in the HAZ of HSLA steels by means of the C-equivalent', Select Conference on Hardenability of Steels, Derby, United Kingdom, 1990, paper 4.

[86] C. L. N. Cottrell: 'An improved prediction method for avoiding HAZ hydrogen cracking', Welding and Metal Fabrication, 1990, 58, 178-183.

[87] 'Gamma Protect', ThyssenKrupp Steel Europe AG, http://www.thyssenkrupp-steel-europe.com/upload/binarydata_tksteel05d4cms/18/11/79/02/00/00/2791118/GammaProtect_en.pdf (cited 15 03 2013).

[88] 'AHSS Database', Tata Steel, 2009-2013.

[89] M. Naderi, L. Thorsten, U. Vitoon and B. Wolfgang: 'New ultrahigh strength steel grades for hot stamping', 2nd International Conference on Steels in Cars and Trucks, Wiesbaden, Germany, 2008, 154-163.

[90] U. Diekmann, T. Sauberlich, A. Frehn and K. Bake, Benteler Stahl: 'Werkstuck aus seiner hochfesten Stahllegierung und dessen Verwendung', European Patent EP 1881083-A1, Germany, published 23 01 2008.

[91] D. C. Bae, K. G. Chin, S. J. Kim, J. R. Lee, J. K. Oh and Y. J. Park, POSCO: 'Steel sheet for hot press forming having excellent heat treatment and impact property, hot press parts made of it and the method for manufacturing thereof', International Patent WO 2007/064172-A1, South Korea, published 07 06 2007.

[92] M. Azuma, N. Suzuki, N. Maruyama, N. Yoshinaga and A. Murasato: 'High strength steel sheet and galvanised steel having very good balance between hole expansibility and ductility, and also excellent in fatigue resistance and methods of producing the steel sheets', International Patent C22C38/00 02, Japan, published 02 03 2011.

[93] H. J. Yi, S. Ghosh and H. K. D. H. Bhadeshia: 'Dual phase hot press forming alloy', Materials Science and Engineering A, 2010, 527, 4870-4874.

[94] A. Turetta, S. Bruschi and A. Ghiotti: 'Investigation of 22MnB5 formability in hot stamping operations', Journal of Materials Processing Technology, 2006, 177, 396-400.

[95] A. G. Grabe: 'Antifriction bearing and method of manufacturing the same', US Patent 2097878, USA, published 02 11 1937.

[96] R. L. Cairns and J. A. Charles: 'Production of controlled martensite-ferrite microstructures in steel', Journal of the Iron and Steel Institute, 1967, 205, 1044-1050.

[97] R. L. Cairns and J. A. Charles: 'Mechanical properties of steel with controlled martensite-ferrite microstructures', Journal of the Iron and Steel Institute, 1967, 205, 1051-1065.

[98] H. K. D. H. Bhadeshia: 'TRIP-assisted steels?', ISIJ International, 2002, 42, 1059-1060.

[99] D. G. Mumford: 'The continuous annealing of multiphase steels', EngD thesis, University of Wales Swansea, UK, 2010.

[100] F. J. Lenze, J. Banik and S. Sikora: 'Applications of hot formed parts for body in white', International Deep Drawing Research Group, Olofström, Sweden, 2008, 511-519.

[101] F. J. Lenze, S. Sikora, J. Banik and D. Sauer: 'Development tendencies as to processing of press hardening under application of coated steel', 1st International Conference on Hot Sheet Metal Forming of High-Performance Steel, Kassel, Germany, 2008, 15-21.

[102] R. Kolleck, T. Veit, H. Hofmann and F. J. Lenze: 'Alternative heating concepts for hot sheet metal forming', 1st International Conference on Hot Sheet Metal Forming of High-Performance Steel, Kassel, Germany, 2008, 239-246.

[103] A. Behrens, S. Hübner and M. Demir: 'Conductive heating system for hot sheet metal forming', 1st International Conference on Hot Sheet Metal Forming of High-Performance Steel, Kassel, Germany, 2008, 63-68.

[104] B. A. Behrens: 'Schnelle Platinenerwarming fur das Pressharten', IFUM Proceedings Umformtechnisches Kolloquium, Hannover, Germany, 2008, pages not provided.

[105] K. Mori, S. Maki and Y. Tanaka: 'Warm and hot stamping of ultrahigh tensile strength steel sheets using resistance heating', CIRP Annals – Manufacturing Technology, 2009, 54, 209-212.

[106] K. Mori: 'Smart hot stamping of ultra-high strength steel parts', Transactions of Nonferrous Metals Society of China, 2012, 22, 496-503.

[107] R. Kolleck, J. Aspacher and R. Veit: 'Efficiency of hot forming processes', 2nd International Conference on Hot Sheet Metal Forming of High-Performance Steel, Luleå, Sweden, 2009, 173-179.

[108] R. Kolleck, R. Veit, M. Merklein, J. Lechler and M. Geiger: 'Investigation on induction heating for hot stamping of boron alloyed steels', CIRP Annals – Manufacturing Technology, 2009, 58, 275-278.

[109] U. Paar: 'Warmblechumformung ein fertigungsprozess fur die zukunft?', IFUM Proceedings Umformtechnisches Kolloquium, Hannover, Germany, 2009, pages not provided.

[110] L. Gehringhoff and H. J. Knaup, Benteler AG: 'B-Säule für ein Kraftfahrzeug', European Patent EP 1180470-B1, Germany, published 20 02 2008.

[111] M. Geiger, J. Duflou, H. J. J. Kals, B. Shirvani and U. P. Singh: 'Basic investigations on the hot stamping steel 22MnB5', Advanced Materials Research, 2005, 6-8, 795-804.

[112] M. C. Somani, L. P. Karjalainen, M. Oldenburg and M. Eriksson: 'Effects of plastic deformation and stresses on dilatation during the martensitic transformation in B-bearing steel', Journal of Material Science and Technology, 2001, 17, 203-206.

[113] T. V. Rajan, C. P. Sharma and A. Sharma: 'Heat treatment: principles and techniques', 1994, New Delhi, PHI Learning.

[114] M. G. Lee, S. J. Kim, H. N. Han and W. C. Jeong: 'Application of hot press forming process to manufacturer an automotive part and its finite element analysis considering phase transformation plasticity', International Journal of Mechanical Sciences, 2009, 51, 888-898.

[115] K. Ikeuchi and J. Yanagimoto: 'Valuation method for effects of hot stamping process parameters on product properties using hot forming

simulator', Journal of Materials Processing Technology, 2011, 211, 1441-1447.

[116] B. Casas, D. Latre, N. Rodriguez and I. Valls: 'Tailor made tool materials for the present and upcoming tooling solutions in hot sheet metal forming', 1st International Conference on Hot Sheet Metal Forming of High-Performance Steel, Kassel, Germany, 2008, 23-35.

[117] H. Beenken, T. Heller, F. J. Lenze and S. Sikora, ThyssenKrupp Steel AG: 'Verfahren zum herstellen eines metall bauteils mit aneinander angrenzenden abschnitten unterschiedlicher materialeigenschaften, mittels pressharten', International Patent WO 2006/128821-A1, Germany, published 07 12 2006.

[118] K. Mori, T. Maeno and K. Mongkolkaji: 'Tailored die quenching of steel parts having strength distribution using bypass resistance heating in hot stamping', Journal of Materials Processing Technology, 2013, 213, 508-514.

[119] F. A. Horton, B. S. Bradford, L. Hastilow, J. Metz, J. R. Judkins, M. Hansen, S. S. Kotagiri and A. G. Janssen, Magna International Inc: 'Hot stamp die apparatus', US Patent US8215147 B2, USA, published 10 07 2012.

[120] M. P. Arbuzov and Y. E. Bushuev: 'Decomposition of martensite and formation of carbide phases during tempering of chromium steels', Metal Science and Heat Treatment, 1971, 13, 10-13.

[121] H. K. D. H. Bhadeshia: 'Tempered martensite', University of Cambridge, http://www.msm.cam.ac.uk/phase-trans/2004/Tempered.Martensite/tempered.martensite.html (cited 16 05 2010).

[122] B. K. Jha and N. S. Mishra: 'Microstructural evolution during tempering of a multiphase steel containing retained austenite', Materials Science and Engineering A, 1999, 263, 42-55.

[123] T. Laumann: 'Galvanised hot forming steels for the body in white', 10th Global Car Body Benchmarking Conference EuroCarBody, Bad Nauheim, Germany, 2008, presentation.

[124] A. Tokizawa, K. Yamamoto, Y. Takemoto and T. Senuma: 'Development of 2000MPa class hot stamped steel components with good toughness and

high resistance against delayed fracture', 4th International Conference on Hot Sheet Metal Forming of High Performance Steel, Luleå, Sweden, 2013, pages not provided.

[125] K. E. Thelning: 'Steel and its heat treatment', 1984, Michigan, Butterworks.

[126] 'Metallic materials. Tensile testing. Method of test at ambient temperature', BS EN ISO 6892-1:2009.

[127] Y. Gao: 'Quasi-static material properties for FE analysis', Tata Steel Material Data Training Seminar, Warwick, UK, 2006, presentation.

[128] 'Metallic materials — tensile testing at high strain rates part 2: servo-hydraulic and other test systems', EN ISO 26203-2:2011, British Standards Institution.

[129] S. Oliver, T. B. Jones and G. Fourlaris: 'Dual phase versus TRIP strip steels: microstructural changes as a consequence of quasi-static and dynamic tensile testing', Materials Characterization, 2007, 58, 390-400.

[130] D. Choi, D. Bruce and S. Kim: 'Deformation behaviour of low carbon TRIP sheet steels at high strain rates', ISIJ International, 2002, 42, 1483-1489.

[131] T. B. Jones: 'Optimisation of both steel properties and autobody structural designs for axial, side and off-set impact loading', Report No. 7210.PR/052, Corus, Port Talbot, UK, 1997-2000.

[132] N. D. Beynon, S. Oliver, T. B. Jones and G. Fourlaris: 'Tensile and work hardening properties of low carbon dual phase strip steels at high strain rates', Materials Science & Technology, 2005, 21, 771-778.

[133] W. Bleck and I. Schael: 'Determination of crash-relevant material parameters by dynamic tensile testing', Steel Research, 2000, 71, 174.

[134] T. Vuoristo, V. T. Kuokkala, M. Apostol and P. Peura: 'Deformation and work hardening of cold-formed high strength steels at high rates of strain', Materials Science & Technology Conference Proceedings, Louisiana, USA, 2004, 471-480.

[135] S. Carless: 'The relative impact performance of press formed, hydroformed and roll formed structures and the application of patchpiece and tailor welded blank techniques for optimum mass efficiency', Report No. EUR 21631 EN, Corus, Ijmuiden, The Netherlands, 2005.

[136] K. Miura, S. Takagi, T. Hira and O. Furukimi: 'High strain rate deformation of high-strength sheet steels for automotive parts', SAE International Congress & Exposition, Detroit, USA, 1998, paper 980952.

[137] M. Borsutzki, D. Cornette, Y. Kuriyama, A. Uenishi, B. Yan and E. Opbroek: 'Recommendations for dynamic tensile testing of sheet steels', 2005, International Iron and Steel Institute (e-book available from http://c315221.r21.cf1.rackcdn.com/HighStrainRate_Recommended_Procedure.pdf).

[138] 'Work instruction: method for the determination of the dynamic tensile properties of strip materials', 3.399.317, Tata Steel, Rotherham, UK, 2011.

[139] 'Work instruction: operating instruction for analysis program – static to dynamic tensile tests on strip materials', 3.399.318, Tata Steel, Rotherham, UK, 2011.

[140] 'Metallic materials – tensile testing at high strain rates', ISO/TC 164/SC 1, British Standards Institution, 2002.

[141] 'Standard guide for preparation of metallographic specimens', ASTM E3-11.

[142] 'Metallographic etchants', Dace Technologies, http://www.metallographic.com/Etchants/Etchants.htm (cited 13 06 2011).

[143] G. F. Vander Voort: 'Revealing prior austenite grain boundaries in heat treated steels', Vac Aero, http://vacaero.com/Metallography-with-George-Vander-Voort/Metallography-with-George-Vander-Voort/revealing-prior-austenite-grain-boundaries-in-heat-treated-steels.html (cited 13 06 2011).

[144] F. Osmond: 'Microscopic analysis of metals', 1904, Madison, C. Griffin & Company.

[145] 'ASTM committee E-4 and grain size measurements', Metallography, http://www.metallography.com/grain.htm (cited 13 06 2011).

[146] 'Standard recommended practice for determining volume fraction by systematic manual point count', ASTM E562-11.

[147] 'Standard methods for estimating the average grain size of metals', ASTM E112-12.

[148] 'Standard test methods for rating and classifying inclusions in steel using the scanning electron microscope', ASTM E2142-08.

[149] J. I. Goldstein, D. E. Newbury, P. Echlin, D. C. Joy, C. E. Lyman, E. Lifshin, L. Sawyer and J. R. Michael: 'Scanning electron microscopy and X-ray microanalysis', 2003, New York, Kluwer Academic/Plenum Publishers.

[150] R. Priestner and M. H. Saleha: 'Retained austenite in dual-phase silicon steels and its effect on mechanical properties', Journal of Materials Processing Technology, 2011, 113, 587-593.

[151] G. Thomas: 'Retained austenite and tempered martensite embrittlement', Metallurgical Transactions A, 1978, 9A, 439-450.

[152] 'Standard practice for X-ray determination of retained austenite in steel with near random crystallographic orientation', ASTM E 975 – 95.

[153] F. Jatczak, J. A. Larson and S. W. Shin: 'Retained austenite and its measurement by X-ray diffraction', Society of Automotive Engineers, 1980, paper 800426.

[154] 'Metallic materials — Vickers hardness test — Part 1: test method', BS EN ISO 6507-1:2005.

[155] 'Standard test method for linear thermal expansion of solid materials with a push-rod dilatometer', ASTM E228-11.

[156] D. W. Suh, C. S. Oh, H. N. Han and S. J. Kim: 'Dilatometric analysis of austenite decomposition considering the effect of non-isotropic volume change', Acta Materialia, 2007, 55, 659-669.

[157] 'Metallic materials – bend test', BS EN ISO 7438:2005.

[158] W. S. Choi and B. C. De Cooman: 'Characterization of the bendability of press-hardened 22MnB5 steel', Steel Research International, 2014, article in press.

[159] 'The tests explained', EURO NCAP, http://www.euroncap.com/testprocedures.aspx (cited 11 07 2010).

[160] K. Adcock: 'Phase transformation behaviour in vanadium and niobium bearing hot rolled dual phase steels', EngD thesis, University of Wales Swansea, UK, 2009.

[161] 'Advanced high strength steel', Tata Steel, http://www.tatasteeleurope.com/showsteelsection?PRODUCT_ID=1&PRODUCT_TYPE_ID=2&STEEL_ID=24&MARKET_ID=empty&LOCATION_ID

=UK_MLE&COMMON_STATUS=LOCATION_SELECTED&DISPLAY_IPAD_PAGE=NO (cited 05 08 2013).

[162] 'DP1000 CR', Tata Steel, http://www.tatasteelautomotive.com/file_source/StaticFiles/Automotive/new-2013/BIW/DP1000CR%20Final%20CMYK%20data%20sheet.pdf (cited 05 08 2013).

[163] B. Hwang, D. Suh and S. Kim: 'Austenitizing temperature and hardenability of low-carbon boron steels', Scripta Materialia, 2011, 64, 1-12.

[164] H. Asahi: 'Effects of Mo addition and austenitizing temperature on hardenability of low alloy B-added steels', ISIJ International, 2002, 42, 1150-1155.

[165] L. Karlsson and H. Norden: 'Overview no. 63 non-equilibrium grain boundary segregation of boron in austenitic stainless steel—IV. Precipitation behaviour and distribution of elements at grain boundaries', Acta Metallurgica, 1988, 36, 35-48.

[166] D. H. Werner: 'Boron and boron containing steels', 1995, Düsseldorf, Verlag Stahleisen mbH.

[167] H. Czichos, T. Saiato, L. Leslie and R. Smith: 'Springer handbook of materials measurement methods', 2006, New York, Springer.

[168] G. F. Vander Voort: 'Metallography, principles and practice', 1984, Ohio, ASM International.

[169] E. S. Huron, R. C. Reed, M. C. Hardy, M. J. Mills, R. E. Montero, P. D. Portella and J. Telesman: 'Superalloys 2012', 2012, New York, John Wiley & Sons.

[170] J. W. Martin: 'Precipitation hardening: theory and applications', 1998, Oxford, Butterworth-Heinemann.

[171] S. Luo and S. Wu: 'Effect of dynamic strain aging on the microstructure and mechanical properties of a reactor pressure vessel steel', Materials Science and Engineering A, 2014, 596, 25-31.

[172] A. Benallal, T. Borvik, A. Clausen and O. Hopperstad: 'Dynamic strain aging, negative strain-rate sensitivity and related instabilities', Technische Mechanik, 2003, 23, 160-166.

# APPENDIX 1

## Laboratory Hot Stamping Martensite Volume Fraction (vol. %)

| *Soak condition (min-°C)* | *22MnB5* | *15MnB5* | *25MnB5* | *25MnB5 (Mo)* | *25MnB5 (V)* | *25MnB5 (Ni)* | *29MnB5* | *38MnB5* | *DP 600* | *DP 800* | *DP 1000* |
|---|---|---|---|---|---|---|---|---|---|---|---|
| 1-800 | 78.2±4.7 | 46.0±7.0 | 74.7±3.7 | 74.1±9.9 | 65.8±1.8 | 74.5±18.2 | 80.3±14.3 | 89.6±10.2 | 62.6±7.6 | 68.9±8.0 | 87.5±9.2 |
| 3-800 | 62.9±5.4 | 48.4±4.9 | 83.7±7.4 | 75.2±6.8 | 70.7±12.5 | 87.9±8.7 | 98.8±0.1 | 93.3±5.9 | 66.2±4.3 | 79.4±3.6 | 88.4±9.5 |
| 5-800 | 85.0±12.0 | 47.5±2.9 | 88.3±5.3 | 76.1±9.5 | 72.0±6.8 | 85.8±16.3 | 99.6±0.4 | 100.0±0.0 | 68.2±4.2 | 79.2±8.5 | 90.2±7.9 |
| 1-850 | 100.0±0.0 | 56.3±3.3 | 83.0±4.6 | 100.0±0.0 | 100.0±0.0 | 100.0±0.0 | 100.0±0.0 | 100.0±0.0 | 70.3±0.9 | 78.4±8.1 | 100.0±0.0 |
| 3-850 | 100.0±0.0 | 88.8±7.3 | 100.0±0.0 | 100.0±0.0 | 100.0±0.0 | 100.0±0.0 | 100.0±0.0 | 100.0±0.0 | 72.8±4.0 | 83.5±0.5 | 100.0±0.0 |
| 5-850 | 100.0±0.0 | 88.2±5.8 | 100.0±0.0 | 100.0±0.0 | 100.0±0.0 | 100.0±0.0 | 100.0±0.0 | 100.0±0.0 | 72.8±6.3 | 84.1±5.1 | 100.0±0.0 |
| 1-900 | 100.0±0.0 | 92.0±6.9 | 100.0±0.0 | 100.0±0.0 | 100.0±0.0 | 100.0±0.0 | 100.0±0.0 | 100.0±0.0 | 99.1±1.5 | 98.4±0.7 | 100.0±0.0 |
| 3-900 | 100.0±0.0 | 98.3±2.3 | 100.0±0.0 | 100.0±0.0 | 100.0±0.0 | 100.0±0.0 | 100.0±0.0 | 100.0±0.0 | 100.0±0.0 | 100.0±0.0 | 100.0±0.0 |
| 5-900 | 100.0±0.0 | 98.9±1.9 | 100.0±0.0 | 100.0±0.0 | 100.0±0.0 | 100.0±0.0 | 100.0±0.0 | 100.0±0.0 | 100.0±0.0 | 100.0±0.0 | 100.0±0.0 |

# APPENDIX 2

## Laboratory Hot Stamping Proeutectoid α-Ferrite Grain Size ($\mu m^2$)

| *Soak condition (min-°C)* | *22MnB5* | *15MnB5* | *25MnB5* | *25MnB5 (Mo)* | *25MnB5 (V)* | *25MnB5 (Ni)* | *29MnB5* | *38MnB5* | *DP 600* | *DP 800* | *DP 1000* |
|---|---|---|---|---|---|---|---|---|---|---|---|
| 1-800 | 1.0±0.2 | 17.4±2.2 | 9.9±2.6 | 5.8±3.7 | 7.1±1.7 | 5.2±1.8 | 19.7±3.5 | 7.7±0.7 | 3.0±2.3 | 5.2±2.9 | 2.7±1.0 |
| 3-800 | 1.9±0.4 | 16.5±6.1 | 9.1±3.0 | 6.5±3.3 | 6.0±3.0 | 5.9±0.8 | 1.2±0.4 | 7.5±3.5 | 6.3±0.8 | 1.9±0.3 | 2.8±1.2 |
| 5-800 | 2.2±1.0 | 16.3±2.8 | 8.1±1.6 | 9.7±6.5 | 6.1±4.2 | 13.3±7.0 | 0.4±0.9 | N/A | 4.8±1.6 | 2.0±0.3 | 3.0±0.5 |
| 1-850 | N/A | 14.3±4.1 | 8.5±2.9 | N/A | N/A | N/A | N/A | N/A | 1.8±0.2 | 4.2±1.7 | N/A |
| 3-850 | N/A | 8.3±5.4 | N/A | N/A | N/A | N/A | N/A | N/A | 1.9±1.2 | 2.7±0.9 | N/A |
| 5-850 | N/A | 8.6±4.7 | N/A | N/A | N/A | N/A | N/A | N/A | 2.6±0.9 | 3.3±1.7 | N/A |
| 1-900 | N/A | 14.5±5.9 | N/A | N/A | N/A | N/A | N/A | N/A | 7.0±0.0 | 1.5±0.3 | N/A |
| 3-900 | N/A | 7.4±1.1 | N/A | N/A | N/A | N/A | N/A | N/A | N/A | N/A | N/A |
| 5-900 | N/A | 6.7±0.0 | N/A | N/A | N/A | N/A | N/A | N/A | N/A | N/A | N/A |

# APPENDIX 3

## Laboratory Hot Stamping Proof Strength (MPa)

| *Soak condition (min-°C)* | *22MnB5* | *15MnB5* | *25MnB5* | *25MnB5 (Mo)* | *25MnB5 (V)* | *25MnB5 (Ni)* | *29MnB5* | *38MnB5* | *DP 600* | *DP 800* | *DP 1000* |
|---|---|---|---|---|---|---|---|---|---|---|---|
| 1-800 | 568±79 | 620±65 | 605±49 | 646±52 | 1173±78 | 1257±37 | 1239±86 | 1279±137 | 534±48 | 599±5 | 990±22 |
| 3-800 | 595±88 | 624±43 | 791±146 | 819±39 | 1182±114 | 1278±99 | 1365±28 | 1288±149 | 573±11 | 712±73 | 1030±12 |
| 5-800 | 782±79 | 626±83 | 801±20 | 912±68 | 1313±130 | 1175±15 | 1314±32 | 1408±64 | 577±18 | 718±11 | 1040±33 |
| 1-850 | 1163±15 | 797±126 | 898±232 | 1179±3 | 1247±9 | 1228±37 | 1317±54 | 1359±34 | 833±38 | 933±29 | 1080±9 |
| 3-850 | 1151±12 | 988±62 | 1162±12 | 1186±33 | 1270±59 | 1196±49 | 1305±7 | 1426±112 | 895±59 | 893±59 | 1073±7 |
| 5-850 | 1145±53 | 990±59 | 1147±24 | 1197±39 | 1253±18 | 1175±22 | 1250±23 | 1419±105 | 929±12 | 842±148 | 1054±25 |
| 1-900 | 1088±13 | 996±17 | 1089±21 | 1138±66 | 1319±32 | 1261±32 | 1292±24 | 1424±33 | 984±35 | 1022±26 | 1064±20 |
| 3-900 | 1068±23 | 959±8 | 1077±27 | 1163±35 | 1185±44 | 1211±53 | 1280±26 | 1284±37 | 980±39 | 1006±11 | 1053±2 |
| 5-900 | 1066±7 | 953±23 | 1073±11 | 1183±11 | 1176±15 | 1173±35 | 1229±54 | 1390±107 | 968±21 | 982±63 | 1046±20 |

# APPENDIX 4

## Laboratory Hot Stamping Ultimate Tensile Strength (MPa)

| *Soak condition (min-°C)* | *22MnB5* | *15MnB5* | *25MnB5* | *25MnB5 (Mo)* | *25MnB5 (V)* | *25MnB5 (Ni)* | *29MnB5* | *38MnB5* | *DP 600* | *DP 800* | *DP 1000* |
|---|---|---|---|---|---|---|---|---|---|---|---|
| 1-800 | 1104±106 | 940±8 | 1184±43 | 1224±37 | 1318±161 | 1560±117 | 1646±29 | 1469±280 | 942±19 | 1057±9 | 1352±11 |
| 3-800 | 1137±150 | 953±13 | 1344±47 | 1376±88 | 1497±117 | 1621±21 | 1878±76 | 1563±78 | 976±1 | 1126±118 | 1376±12 |
| 5-800 | 1274±52 | 976±32 | 1371±34 | 1477±19 | 1634±65 | 1630±13 | 1833±126 | 1679±274 | 977±15 | 1243±11 | 1376±32 |
| 1-850 | 1590±7 | 1099±11 | 1396±158 | 1666±5 | 1677±50 | 1643±35 | 1861±10 | 1768±161 | 1161±36 | 1221±32 | 1410±5 |
| 3-850 | 1572±19 | 1229±42 | 1589±67 | 1658±4 | 1684±18 | 1651±35 | 1852±3 | 1881±207 | 1221±2 | 1213±54 | 1417±5 |
| 5-850 | 1555±2 | 1254±6 | 1584±54 | 1640±5 | 1623±25 | 1665±8 | 1825±6 | 2066±77 | 1249±6 | 1168±86 | 1432±89 |
| 1-900 | 1515±21 | 1279±11 | 1532±16 | 1613±34 | 1661±10 | 1664±15 | 1787±23 | 2045±22 | 1267±6 | 1321±12 | 1400±7 |
| 3-900 | 1470±52 | 1275±4 | 1510±7 | 1606±11 | 1611±18 | 1641±18 | 1781±26 | 2005±7 | 1247±8 | 1281±30 | 1366±101 |
| 5-900 | 1463±18 | 1250±17 | 1491±15 | 1603±8 | 1593±37 | 1614±38 | 1741±33 | 2049±0 | 1228±2 | 1229±53 | 1356±6 |

# APPENDIX 5

## Laboratory Hot Stamping Uniform Elongation (%)

| *Soak condition (min-°C)* | *22MnB5* | *15MnB5* | *25MnB5* | *25MnB5 (Mo)* | *25MnB5 (V)* | *25MnB5 (Ni)* | *29MnB5* | *38MnB5* | *DP 600* | *DP 800* | *DP 1000* |
|---|---|---|---|---|---|---|---|---|---|---|---|
| 1-800 | 5.4±1.1 | 4.9±0.1 | 5.1±0.5 | 5.2±1.6 | 1.8±1.3 | 2.9±0.8 | 1.5±0.2 | 1.3±0.4 | 5.4±1.8 | 5.8±0.9 | 3.2±0.1 |
| 3-800 | 4.5±1.0 | 5.0±0.2 | 4.2±0.5 | 6.7±0.1 | 0.8±0.9 | 3.7±0.0 | 3.4±0.0 | 1.3±0.1 | 5.7±0.4 | 5.5±0.8 | 3.2±0.2 |
| 5-800 | 4.3±0.1 | 4.6±0.4 | 4.3±1.0 | 4.5±0.2 | 0.1±1.1 | 3.9±0.2 | 3.4±0.9 | 1.3±0.3 | 5.9±0.5 | 5.4±0.2 | 3.2±0.4 |
| 1-850 | 3.5±0.0 | 4.0±0.1 | 3.1±0.1 | 3.6±0.1 | 3.9±0.1 | 3.7±0.1 | 3.4±0.2 | 1.8±0.6 | 3.9±1.4 | 3.2±0.1 | 3.4±0.2 |
| 3-850 | 3.5±0.1 | 3.9±1.2 | 3.4±0.3 | 3.6±0.1 | 3.8±0.1 | 3.6±0.1 | 3.4±0.1 | 3.2±2.6 | 3.7±1.0 | 3.4±0.4 | 3.4±0.1 |
| 5-850 | 3.5±0.1 | 4.1±0.4 | 3.4±0.1 | 3.5±0.0 | 3.5±0.3 | 3.5±0.2 | 3.4±0.1 | 4.5±0.2 | 3.5±0.2 | 3.7±1.2 | 3.6±0.1 |
| 1-900 | 3.5±0.1 | 3.8±0.2 | 3.5±0.0 | 4.0±0.5 | 3.7±0.3 | 3.4±0.1 | 3.4±1.8 | 4.3±0.2 | 3.3±0.0 | 2.8±0.1 | 3.5±0.2 |
| 3-900 | 3.6±0.1 | 3.9±0.1 | 3.5±0.0 | 3.6±0.1 | 3.7±0.1 | 3.5±0.1 | 3.4±0.3 | 4.3±0.2 | 3.7±0.3 | 3.0±0.1 | 3.6±0.4 |
| 5-900 | 3.6±0.1 | 4.1±0.2 | 3.5±0.0 | 3.6±0.1 | 3.5±0.2 | 3.6±0.3 | 3.4±0.1 | 3.4±0.0 | 3.8±0.2 | 3.1±0.1 | 3.6±0.0 |

# APPENDIX 6

## Laboratory Hot Stamping Total Elongation (%)

| *Soak condition (min-°C)* | *22MnB5* | *15MnB5* | *25MnB5* | *25MnB5 (Mo)* | *25MnB5 (V)* | *25MnB5 (Ni)* | *29MnB5* | *38MnB5* | *DP 600* | *DP 800* | *DP 1000* |
|---|---|---|---|---|---|---|---|---|---|---|---|
| 1-800 | 9.4±1.7 | 11.4±0.4 | 7.8±1.1 | 14.0±1.0 | 10.5±0.4 | 10.9±1.5 | 1.5±0.2 | 1.3±0.4 | 15.3±0.3 | 14.9±1.2 | 11.9±0.2 |
| 3-800 | 8.9±1.9 | 11.5±0.1 | 7.6±0.9 | 15.0±2.0 | 10.4±0.3 | 10.6±0.3 | 5.7±1.5 | 1.3±0.1 | 15.5±0.1 | 14.1±0.1 | 10.6±3.7 |
| 5-800 | 8.5±3.0 | 11.6±0.3 | 7.7±2.1 | 12.0±1.7 | 10.4±0.3 | 11.3±0.1 | 6.2±1.3 | 1.3±0.3 | 15.7±0.1 | 13.9±0.1 | 9.0±4.1 |
| 1-850 | 7.2±0.1 | 10.8±0.4 | 5.4±1.5 | 9.7±2.3 | 11.1±0.4 | 10.9±0.1 | 5.7±0.6 | 1.8±0.6 | 14.5±0.4 | 13.4±0.2 | 14.1±1.3 |
| 3-850 | 7.3±0.2 | 11.0±1.1 | 6.4±2.0 | 9.3±1.2 | 11.0±0.0 | 11.2±0.1 | 6.2±0.3 | 3.2±2.6 | 14.2±0.5 | 14.1±1.3 | 14.7±0.6 |
| 5-850 | 8.0±0.2 | 11.1±0.1 | 6.5±0.3 | 9.0±1.7 | 11.2±0.3 | 11.1±0.1 | 6.3±0.6 | 6.2±0.4 | 14.1±0.5 | 14.3±1.0 | 15.3±0.3 |
| 1-900 | 7.4±0.2 | 11.2±0.2 | 6.3±0.2 | 15.7±2.1 | 11.2±0.3 | 11.6±0.0 | 6.2±0.3 | 5.9±0.2 | 13.1±0.2 | 13.0±0.2 | 15.1±0.8 |
| 3-900 | 7.4±2.5 | 11.6±0.0 | 6.5±0.2 | 10.3±2.9 | 10.8±0.2 | 11.7±0.4 | 6.3±0.3 | 5.7±0.3 | 13.2±0.3 | 13.3±0.5 | 15.1±0.5 |
| 5-900 | 8.1±0.1 | 11.8±0.0 | 6.6±0.2 | 9.7±2.9 | 10.9±0.1 | 11.9±0.1 | 6.5±0.0 | 3.4±0.0 | 13.5±0.1 | 13.4±0.3 | 15.6±0.3 |

# APPENDIX 7

## Laboratory Hot Stamping Vickers Hardness ($kg/mm^2$)

| *Soak condition (min-°C)* | *22MnB5* | *15MnB5* | *25MnB5* | *25MnB5 (Mo)* | *25MnB5 (V)* | *25MnB5 (Ni)* | *29MnB5* | *38MnB5* | *DP 600* | *DP 800* | *DP 1000* |
|---|---|---|---|---|---|---|---|---|---|---|---|
| 1-800 | 375 | 343 | 434 | 437 | 445 | 611 | 522 | 683 | 250 | 293 | 449 |
| 3-800 | 409 | 355 | 446 | 469 | 481 | 625 | 594 | 720 | 261 | 345 | 453 |
| 5-800 | 478 | 359 | 483 | 490 | 544 | 638 | 565 | 754 | 270 | 358 | 456 |
| 1-850 | 534 | 354 | 555 | 565 | 610 | 637 | 571 | 776 | 345 | 404 | 462 |
| 3-850 | 517 | 451 | 526 | 572 | 636 | 652 | 562 | 735 | 382 | 402 | 460 |
| 5-850 | 510 | 464 | 516 | 577 | 633 | 608 | 559 | 713 | 392 | 382 | 460 |
| 1-900 | 496 | 446 | 502 | 538 | 648 | 642 | 561 | 741 | 428 | 482 | 458 |
| 3-900 | 477 | 467 | 493 | 547 | 614 | 626 | 559 | 685 | 430 | 465 | 456 |
| 5-900 | 476 | 495 | 486 | 560 | 612 | 616 | 556 | 651 | 422 | 446 | 455 |

# APPENDIX 8

## Laboratory Hot Stamping Heterogeneity of Vickers Hardness (kg/mm$^2$)

| *Soak condition (min-°C)* | *22MnB5* | *15MnB5* | *25MnB5* | *25MnB5 (Mo)* | *25MnB5 (V)* | *25MnB5 (Ni)* | *29MnB5* | *38MnB5* | *DP 600* | *DP 800* | *DP 1000* |
|---|---|---|---|---|---|---|---|---|---|---|---|
| 1-800 | 12.9 | 27.7 | 21.4 | 13.8 | 51.0 | 45.9 | 22.5 | 46.5 | 30.0 | 40.2 | 9.8 |
| 3-800 | 9.1 | 23.3 | 13.5 | 10.3 | 49.1 | 28.1 | 17.0 | 38.1 | 22.6 | 31.2 | 7.9 |
| 5-800 | 7.8 | 18.4 | 10.6 | 8.5 | 24.2 | 21.6 | 11.8 | 35.0 | 20.7 | 17.4 | 5.5 |
| 1-850 | 9.8 | 18.8 | 56.1 | 9.8 | 26.3 | 21.0 | 20.2 | 33.3 | 22.2 | 40.3 | 5.5 |
| 3-850 | 8.3 | 20.5 | 11.9 | 8.8 | 14.3 | 18.6 | 16.1 | 29.5 | 12.0 | 28.8 | 3.8 |
| 5-850 | 3.6 | 12.6 | 9.4 | 7.1 | 13.8 | 15.5 | 11.6 | 22.3 | 11.4 | 16.4 | 3.2 |
| 1-900 | 8.0 | 15.1 | 12.1 | 8.9 | 9.3 | 17.7 | 19.2 | 28.7 | 7.4 | 17.2 | 3.8 |
| 3-900 | 6.3 | 10.7 | 6.7 | 5.6 | 8.8 | 17.3 | 9.7 | 20.5 | 6.4 | 13.5 | 2.2 |
| 5-900 | 1.6 | 8.4 | 1.7 | 1.7 | 8.6 | 12.6 | 5.3 | 12.5 | 4.0 | 11.0 | 2.4 |

# APPENDIX 9

## Publications

**Articles In-Press (Accepted for Publication)**

T. Taylor, G. Fourlaris, P. Evans and G. Bright: 'New generation ultrahigh strength boron steel for automotive hot stamping technologies', Materials Science and Technology, article in-press.

T. Taylor, G. Fourlaris and P. Evans: 'New generation boron steels for automotive hot stamping technologies', Materials and Design, article in-press.

T. Taylor, G. Fourlaris and P. Evans: 'Dynamic tensile testing of ultrahigh strength hot stamped martensitic steels', Materials and Design, article in-press.

**Articles under Peer-Review (Awaiting Acceptance for Publication)**

T. Taylor, G. Fourlaris and P. Evans: 'Development of dual phase steels for automotive hot stamping technologies', Materials Processing Technology, article under peer-review.

T. Taylor, G. Fourlaris, P. Evans and J. Cafolla: 'Finite element modelling full vehicle side impact with ultrahigh strength hot stamped steels', Materials Processing Technology, article under peer-review.